

**CRACK INTERACTION WITH A FRICTIONAL INTERFACE IN A
ROCK-MODEL MATERIAL: AN EXPERIMENTAL AND NUMERICAL
INVESTIGATION**

by

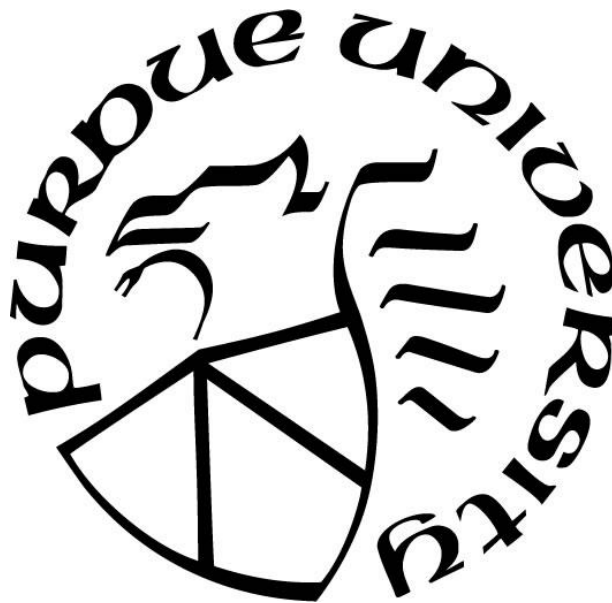
Danielli de Melo Moura

A Dissertation

Submitted to the Faculty of Purdue University

In Partial Fulfillment of the Requirements for the degree of

Doctor of Philosophy



Lyles School of Civil Engineering

West Lafayette, Indiana

May 2021

THE PURDUE UNIVERSITY GRADUATE SCHOOL
STATEMENT OF COMMITTEE APPROVAL

Dr. Antonio Bobet, Chair

School of Civil Engineering

Dr. Philippe Bourdeau

School of Civil Engineering

Dr. Laura Pyrak-Nolte

School of Physics and Astronomy

Dr. Jie Shan

School of Civil Engineering

Dr. Sergio Fontoura

School of Civil Engineering – PUC RIO

Approved by:

Dr. Dulcy M. Abraham

To my beloved grandparents Josete and Umbelino

ACKNOWLEDGMENTS

First of all, I would like to thank Professor Antonio Bobet for his endless support and for being my rock throughout the years of my PhD program at Purdue University. He is not only a knowledgeable Professor but a true mentor. It is beautiful to see how he goes above and beyond to help his students succeed. His guidance has made a major impact in my life as it helped me build up more confidence to continue pursuing a successful career in civil engineering, which is the field that I have always been tremendously passionate about.

I am also extremely thankful to my committee members: Professors Jie Shan, Laura Pyrak-Nolte, Sergio Fontoura and Phillippe Bourdeau. They have always been generous, kind and willing to support me. I feel honored to have these talented professionals whom I look up to as part of my committee.

I have been fortunate to have my studies partially funded by the Science without Borders fellowship and this would not have been possible without the investments in higher education made by Presidents Lula and Dilma. In addition, I have had the support from Purdue University through the awarded positions that I held as Lyles Teaching Assistant and Lyles Teaching Fellow. These opportunities not only allowed me to gain experience in research and teaching, but also contributed to the completion of my PhD program.

Furthermore, I would like to thank my close friends and family. I will be forever grateful for their love, kindness and for being a great support to me.

Special thanks to my favorite artist of all time and friend Chad Gray. His words of encouragement will never be forgotten.

I have no words to describe how much I appreciate everyone who crossed my way during my PhD journey and selflessly made a positive impact that I will take with me for the rest of my life. Their support has made me feel even more determined, resilient and stronger.

TABLE OF CONTENTS

LIST OF TABLES.....	10
LIST OF FIGURES	11
ABSTRACT	17
1. CHAPTER 1: INTRODUCTION	19
1.1 Problem Statement and Motivation.....	19
1.2 Research Objectives	20
1.3 Thesis Organization	21
2. CHAPTER 2. EXPERIMENTAL INVESTIGATION: BACKGROUND	24
3. CHAPTER 3. EXPERIMENTAL INVESTIGATION: METHODOLOGY AND RESULTS .	
.....	36
3.1 Experimental Procedures	36
3.1.1 Introduction.....	36
3.1.2 Specimen geometry	36
3.1.3 Specimen Preparation	37
3.1.3.1 Intact Specimens.....	37
3.1.3.2 Pre-cracked Specimens without interface	38
3.1.3.3 Pre-cracked Gypsum Specimens with an interface	39
3.1.4 Experimental Setup and Testing	40
3.2 Experimental Results	41
3.2.1 Introduction.....	41
3.2.2 Material Properties.....	42
3.2.3 Gypsum specimens without an interface.....	43
3.2.3.1 Specimen with geometry 0-2a30°	43
1.2.3.2 Specimen with geometry 3a030°	44
3.2.3.3 Specimen with geometry 2aa30°	44
3.2.4 Gypsum specimens with an interface	45
3.2.4.1 Specimen with geometry 0-2a30° containing a smooth interface ($\phi=35^\circ$) inclined 90° with the loading direction.....	45

3.2.4.2 Specimen with geometry 0-2a30° containing a rough interface ($\phi=50^\circ$) inclined 90° with the loading direction.....	46
3.2.4.3 Specimen with geometry 0-2a30° containing a smooth interface ($\phi=35^\circ$) inclined 80° with the loading direction.....	46
3.2.4.4 Specimen with geometry 0-2a30° containing a rough interface ($\phi=50^\circ$) inclined 80° with the loading direction.....	47
3.2.4.5 Specimen with geometry 3a030° containing a smooth interface ($\phi=35^\circ$) inclined 90° with the loading direction.....	48
3.2.4.6 Specimen with geometry 3a030° containing a rough interface ($\phi=50^\circ$) inclined 90° with the loading direction.....	48
3.2.4.7 Specimen with geometry 3a030° containing a smooth interface ($\phi=35^\circ$) inclined 80° with the loading direction.....	49
3.2.4.8 Specimen with geometry 3a030° containing a rough interface ($\phi=50^\circ$) inclined 80° with the loading direction.....	49
3.2.4.9 Specimen with geometry 3a030° containing a smooth interface ($\phi=35^\circ$) inclined 70° with the loading direction.....	50
3.2.4.10 Specimen with geometry 3a030° containing a rough interface ($\phi=50^\circ$) inclined 70° with the loading direction.....	51
3.2.4.11 Specimen with geometry 2aa30° with smooth interface ($\phi=35^\circ$) inclined 90° with the loading direction	51
3.2.4.12 Specimen with geometry 2aa30° with rough interface ($\phi=50^\circ$) inclined 90° with the loading direction	52
3.2.4.13 Specimen with geometry 2aa30° with smooth interface ($\phi=35^\circ$) inclined 80° with the loading direction	53
3.2.4.14 Specimen with geometry 2aa30° with rough interface ($\phi=50^\circ$) inclined 80° with the loading direction	53
3.2.4.15 Specimen with geometry 2aa30° with smooth interface ($\phi=35^\circ$) inclined 70° with the loading direction	54
3.2.4.16 Specimen with geometry 2aa30° with rough interface ($\phi=50^\circ$) inclined 70° with the loading direction	55
3.2.5 Analyses of the results.....	55

3.2.5.1	Crack initiation	55
3.2.5.2	Interaction between cracks and the interface	56
3.2.5.3	Coalescence	57
3.2.5.4	General observations	58
4.	CHAPTER 4. NUMERICAL INVESTIGATION: BACKGROUND	102
4.1	Introduction	102
4.2	Fracture mechanics.....	102
4.3	Criteria for crack initiation and propagation at flaw tips.....	105
4.3.1	Maximum tangential stress criterion ($\sigma\theta$ – criterion)	105
4.3.2	Maximum strain energy release rate (G - criterion)	106
4.3.3	Minimum strain energy density criterion (S-criterion)	107
4.3.4	Bobet’s criterion (Stress independent failure criterion)	108
4.3.5	Goncalves da Silva’s criterion	109
4.3.5.1	Goncalves da Silva’s evaluation of existing crack initiation criteria	109
4.3.5.2	Strain based criterion	111
4.3.5.3	Exact stress dependent criterion	111
4.4	Criteria for cracks interacting with an interface.....	112
4.4.1	Energy release rate criterion for crack penetration or deflection at the interface (He and Hutchinson’s criterion)	112
4.4.2	Stress-based crack re-initiation criterion (Lemaitre’s criterion).....	113
4.4.3	Stress-based criterion for orthogonal and non-orthogonal crack propagation across unbonded frictional interfaces.....	115
4.4.4	Maximum principal tensile stress criterion for predicting step-over cracks at the interface	119
4.4.5	Traction-separation criterion (cohesive zone model)	120
5.	CHAPTER 5. NUMERICAL INVESTIGATION: METHODOLOGY AND RESULTS ..	138
5.1	Introduction	138
5.2	Methodology.....	138
5.2.1	Model Description for XFEM simulations in ABAQUS	138
5.2.2	Methodology used in the numerical analysis	140
5.3	Numerical Simulation Results.....	142

5.3.1 Geometry 0-2a30° with interface inclined 90° with the vertical and contact friction angle of 50°	143
5.3.1.1 Tensile cracks initiating from flaws	143
5.3.1.2 Shear cracks initiating from flaws.....	143
5.3.1.3 Tensile cracks initiating (or crossing) the interface	144
5.3.1.4 Shear cracks crossing the interface	145
5.3.2 Geometry 0-2a30° with interface inclined 90° with the vertical and contact friction angle of 35°	145
5.3.2.1 Tensile cracks initiating from flaws	145
5.3.2.2 Tensile cracks initiating (or crossing) the interface	146
5.3.3 Geometry 0-2a30° with interface inclined 80° with the vertical and contact friction angle of 50°	146
5.3.3.1 Tensile cracks initiating from flaws	146
5.3.3.2 Shear cracks initiating from flaws.....	147
5.3.3.3 Tensile cracks initiating (or crossing) the interface	147
5.3.4 Geometry 0-2a30° with interface inclined 80° with the vertical and contact friction angle of 35°	147
5.3.4.1 Tensile cracks initiating from flaws	147
5.3.4.2 Shear cracks initiating from flaws.....	148
5.3.4.3 Tensile cracks initiating (or crossing) the interface	148
5.3.4.4 Shear cracks crossing the interface	148
5.3.5 Discussion	149
5.3.5.1 Effects of interface roughness and inclination angle on the initial stress state	149
5.3.5.2 Effects of interface roughness and inclination angle on the initiation of tensile cracks at the flaw tips	150
5.3.5.3 Effects of roughness and inclination angle on shear crack initiation at the flaw tips	151
5.3.5.4 Effects of roughness and inclination angle on the initiation of cracks at the interface	152
5.3.5.5 Effects of roughness and inclination angle on cracks approaching the interface...	152
5.3.5.6 Summary	153

6. CHAPTER 6. CONCLUSIONS AND RECOMMENDATIONS	191
6.1 Conclusions	191
6.1.1 Experimental Work.....	192
6.1.2 Numerical work	193
6.2 Recommendations for future research	194
REFERENCES	195
VITA.....	202

LIST OF TABLES

Table 2.1. Crack coalescence categories observed by Wong and Einstein (2008) & Park and Bobet (2010)	33
Table 3.1. Mechanical properties of intact gypsum 43	
Table 3.2. Crack initiation and coalescence stresses for the different tested specimens.	86
Table 3.3. Crack initiation and coalescence stresses for the specimens tested for repeatability. ..	87
Table 3.4. Smallest angle between cracks initiated at the interface and interface plane	88
Table 3.5. Angle at which tensile and shear cracks reach the interface from the interface plane and interaction with the interface (i.e. Arrest at interface – A, Cross the interface– C, Arrest right after crossing the interface - CA)	92
Table 3.6. Coalescence patterns for specimens with interface	93
Table 5.1. Geometry 0-2a30° with interface inclined 90° from the vertical and friction angle of 50°	174
Table 5.2. Geometry 0-2a30° with interface inclined 90° from the vertical and friction angle of 35°	179
Table 5.3. Geometry 0-2a30° with interface inclined 80° from the vertical and friction angle of 50°	183
Table 5.4. Geometry 0-2a30° with interface inclined 80° from the vertical and friction angle of 35°	187
Table 5.5. Effects of interface roughness and inclination angle on the initiation of tensile cracks at an inside flaw tip. Maximum principal stress for a crack path radius of 0.2mm from the internal crack tip of the bottom flaw for different interface roughness and inclination angles in a specimen with geometry 0-2a30°	190
Table 5.6. Effects of interface roughness and inclination angle on the initiation of tensile cracks at an outside flaw tip. Maximum principal stress for a crack path radius of 0.2mm from the internal crack tip of the bottom flaw for different interface roughness and inclination angles in a specimen with geometry 0-2a30°	190

LIST OF FIGURES

Figure 1.1. Carbonate rock mass with 1-2m thick bedding layers (adapted from Larsen et al, 2010)	22
Figure 1.2. A shear fracture crossing an interface with an offset of 0.2m (adapted from Larsen, 2010).....	23
Figure 2.1. Types of cracks observed in pre-cracked rock-model specimens subjected to uniaxial compression.....	30
Figure 2.2. Flaws geometry	30
Figure 2.3. Bilayered PMMA specimen. (a) Specimen configuration; (b) Crack penetration; (c) Crack deflection	31
Figure 2.4. Behavior of a crack approaching a bonded interface between dissimilar elastic materials. a) Deflecting crack; b) Penetrating crack.	32
Figure 3.1. Geometry of (a) specimen and (b) flaws.	59
Figure 3.2. Preparation of pre-cracked specimens with interface. (a) mold with pvc block; (b) sandpaper attached to block; (c) greased steel shim inserted through one of the PMMA slits; (d) specimen with rough interface.	60
Figure 3.3. Flaw geometries with smooth interface for 70°, 80° and 90° interface inclination angles. (a) $S=0$, $C=-2a$, $\beta=30^\circ$; (b) $S=3a$, $C=0$, $\beta=30^\circ$; (c) $S=2a$, $C=a$, $\beta=30^\circ$	61
Figure 3.4. Flaw geometries with rough interface (made with sandpaper grit #36) for 70°, 80° and 90° interface inclination angles. (a) $S=0$, $C=-2a$, $\beta=30^\circ$; (b) $S=3a$, $C=0$, $\beta=30^\circ$; (c) $S=2a$, $C=a$, $\beta=30^\circ$	61
Figure 3.5. Gypsum specimen	62
Figure 3.6. Experimental setup	63
Figure 3.7. Crack path detected and interpreted from DIC data for the specimen with geometry 0-2a30° without interface, at different uniaxial compression loads. (a) 11.88MPa; (b) 25.05MPa; (c) 27.47MPa; (d) 28.14MPa; (e) 30.22MPa; (f) After coalescence.	64
Figure 3.8. Crack path detected and interpreted from DIC data for the specimen with geometry 3aa30° without interface, at different uniaxial compression loads. (a) 11.19 MPa; (b) 12.18 MPa; (c) 23.94 MPa; (d) 24.06 MPa; (e) 34.21 Mpa.	65
Figure 3.9. Crack path detected and interpreted from DIC data for the specimen with geometry 2aa30° without interface, at different uniaxial compression loads. (a) 14MPa; (b) 30.28MPa; (c) 34.96MPa; (d) 35.28MPa.	66
Figure 3.10. Crack path detected and interpreted from DIC data for the specimen with geometry 0-2a30° containing a smooth interface ($\phi=35^\circ$) inclined 90° with the loading direction, at different	

uniaxial compression loads. (a) 8.60MPa; (b) 16.39MPa; (c) 19.13MPa; (d) 25.47MPa; (e) 28.37MPa; (f) 28.94MPa; (g) 30.23MPa; (h) 31.36MPa.67

Figure 3.11. Crack path detected and interpreted from DIC data for the specimen with geometry 0-2a30° containing a rough interface ($\phi=50^\circ$), inclined 90° with the loading direction, at different uniaxial compression loads. (a) 6.95 MPa; (b) 15 MPa; (c) 18.94 MPa; (d) 22.79 MPa; (e) 25.5 MPa; (f) 25.88 MPa; (g) 26.79 MPa; (h) 27.5 MPa; (i) 27.6MPa.68

Figure 3.12. Crack path detected and interpreted from DIC data for the specimen with geometry 0-2a30° containing a smooth interface ($\phi=35^\circ$), inclined 80° with the loading direction, at different uniaxial compression loads. (a) 8.5 MPa; (b) 16.98MPa; (c) 20.87MPa; (d) 23.05MPa; (e) 23.92MPa; (f) 23.95MPa.69

Figure 3.13. Crack path detected and interpreted from DIC data for the specimen with geometry 0-2a30° containing a rough interface ($\phi=50^\circ$), inclined 80° with the loading direction, at different uniaxial compression loads. (a) 6.6 MPa; (b) 9.38 MPa; (c) 16.11MPa; (d) 18 MPa; (e) 19.30 MPa; (f) 21.58 MPa; (g) 22.46 MPa; (h) 22.85 MPa.70

Figure 3.14. Crack path detected and interpreted from DIC data for the specimen with geometry 3aa30° containing a smooth interface ($\phi=35^\circ$), inclined 90° with the loading direction, at different uniaxial compression loads. (a) 9.28 MPa; (b) 11.95 MPa; (c) 18.01 MPa; (d) 18.61 MPa; (e) 19.55MPa; (f) 24.68 MPa.71

Figure 3.15. Crack path detected and interpreted from DIC data for the specimen with geometry 3aa30° containing a rough interface($\phi=50^\circ$), inclined 90° with the loading direction, at different uniaxial compression loads. (a) 5.45 MPa; (b) 6.78 MPa; (c) 16.14 MPa; (d) 16.15 MPa; (e) 16.29 MPa; (f) 18.06 MPa; (g) 22.38 MPa; (h) 22.34 MPa.72

Figure 3.16. Crack path detected and interpreted from DIC data for the specimen with geometry 3aa30° containing a smooth interface ($\phi=35^\circ$), inclined 80° with the loading direction, at different uniaxial compression loads. (a) 7.75 MPa; (b) 8.26 MPa; (c) 11.53 MPa; (d) 15.23 MPa; (e) 17.12 MPa; (f) 26 MPa.73

Figure 3.17. Crack path detected and interpreted from DIC data for the specimen with geometry 3aa30° containing a rough interface ($\phi=50^\circ$), inclined 80° with the loading direction, at different uniaxial compression loads. (a) 5.08 MPa; (b) 7.34 MPa; (c) 8.13 MPa; (d) 8.81 MPa; (e) 9.33 MPa; (f) 11.75 MPa.74

Figure 3.18. Crack path detected and interpreted from DIC data for the specimen with geometry 3aa30° containing a smooth interface ($\phi=35^\circ$), inclined 70° with the loading direction, at different uniaxial compression loads. (a) 6.68 MPa; (b) 9.21 MPa; (c) 10.5 MPa; (d) 10.5 MPa; (e) 11.5 MPa; (f) 14.34 MPa.75

Figure 3. 19. Crack path detected and interpreted from DIC data for the specimen with geometry 3aa30° containing a rough interface ($\phi=50^\circ$), inclined 70° with the loading direction, at different uniaxial compression loads. (a) 5 MPa; (b) 6.06 MPa; (c) 7.73 MPa; (d) 8.11 MPa; (e) 10.58 MPa; (f) 13.56 MPa.76

Figure 3.20. Crack path detected and interpreted from DIC data for a specimen with geometry 2aa30°, with a smooth interface ($\phi=35^\circ$) inclined 90° with the loading direction, at uniaxial

compression loads: (a)11.6 MPa; (b) 15.51MPa; (c) 17.44MPa; (d) 19.34MPa; (e) 23.67MPa; (f) 24.24MPa; (g) 27.2 MPa; (h) 30.36MPa.....	77
Figure 3.21. Crack path detected and interpreted from DIC data for the specimen with geometry 2aa30° with a rough interface($\phi=50^\circ$), inclined 90° with the loading direction, at different uniaxial compression loads. (a) 10.53 MPa; (b) 15.45MPa; (c) 19.72MPa; (d) 26.99 MPa; (e) 27.85MPa; (f) 30.79 MPa; (g) 31.29 MPa; (h) 31.31 MPa.	78
Figure 3.22. Crack path detected and interpreted from DIC data for the specimen with geometry 2aa30° with a smooth interface ($\phi=35^\circ$), inclined 80° with the loading direction, at different uniaxial compression loads. (a)11.14MPa; (b) 13.11MPa; (c) 14.09 MPa; (d) 14.78 MPa; (e) 27.02 MPa; (f) 30.86 MPa.	79
Figure 3.23. Crack path detected and interpreted from DIC data for the specimen with geometry 2aa30° with a rough interface ($\phi=50^\circ$), inclined 80° with the loading direction, at different uniaxial compression loads. (a) 10.06 MPa; (b) 17.73 MPa; (c) 25.75MPa; (d) 32.4 MPa.	80
Figure 3.24. Crack path detected and interpreted from DIC data for the specimen with geometry 2aa30° with a smooth interface ($\phi=35^\circ$), inclined 70° with the loading direction, at different uniaxial compression loads. (a) 10.58 MPa; (b) 15.31 MPa; (c) 21.11 MPa; (d) 26.56 MPa; (e) 29.42 MPa; (f) 29.43 MPa.....	81
Figure 3.25. Crack path detected and interpreted from DIC data for the specimen with geometry 2aa30° with a rough interface ($\phi=50^\circ$), inclined 70° with the loading direction, at different uniaxial compression loads. (a) 9.94 MPa; (b) 16.67 MPa; (c) 21.78 MPa; (d) 29.94 MPa.....	82
Figure 3.26. Crack initiation stresses in specimens with interface and without interface for different geometries (including repeatability specimens)	83
Figure 3.27. Angle between crack path and the interface	84
Figure 3.28. Crack coalescence stresses in specimens with interface for different geometries (including repeatability specimens)	85
Figure 4.1 Infinite plate with a central elliptical crack.....	124
Figure 4.2 The three modes of loading. a) mode I; b) mode II; mode III	125
Figure 4.3 Cylindrical stresses of an element near crack tip	125
Figure 4.4 Specimen length L and crack length a in a single edge crack	126
Figure 4.5 Tangential stresses around a flaw tip	126
Figure 4.6 Bobet's investigation in gypsum under uniaxial compression. (a) Experimental and (b) Numerical results for a flaw geometry $S=0$ $C=-2a$ $\beta=45^\circ$; (c) Experimental and (d) Numerical results for a flaw geometry $S=-2a$ $C=-2a$ $\beta=45^\circ$; (e) Failure envelope for Bobet's criterion Adapted from Bobet, 1997	127
Figure 4.7 Goncalves da Silva (2013)'s investigation. (a) path and point IDs; (b) Areas considered in the studied path. Source: Adapted from Goncalves da Silva (2013)	128

Figure 4.8 Strain field around a crack tip/ cylindrical strains of an element radial to the flaw tip	129
Figure 4.9 Failure envelope for: (a) Bobet's criterion; (b) Goncalves da Silva's criterion (after Goncalves da Silva, 2012).....	129
Figure 4.10 Schematic problem of a crack reaching an interface investigated by Lemaitre et al. (1996)	130
Figure 4.11 PMMA Specimen investigated by Lemaitre et al. (1996)	130
Figure 4.12 Interface geometry and coordinate system used to describe the stresses near a crack tip impinging upon a frictional interface in Renshaw and Pollard's criterion. All stresses are drawn as positive.....	131
Figure 4.13 Continuous vs discontinuous propagation across an interface. In the top model, propagation across the interface is continuous (i.e. as if the interface was not there). In the bottom model, crossing occurs when the stresses ahead of the approaching crack tip reinitiate a new crack on the other side of the interface. In Renshaw and Pollard's criterion, crossing is a discontinuous process.	132
Figure 4.14 Geometry and stresses of the fracture process zone. Stresses within this zone are assumed to be equal or less than the stresses calculated from the stress field (Equation 4.7) at a distance $rc(\theta)$. The approximate maximum magnitude of the components of stress $\sigma_{ij}(max)$ acting along the interface can thus be calculated using the stress field equations with $\theta = \pm \pi/2$ and $r = rc(\pm \pi/2)$	133
Figure 4.15 Schematic of fracture approaching interface in Gu and Weng (2010)'s criterion ...	134
Figure 4.16 Maximum tension (principal stress) around the tip of a 1m vertical crack under 5MPa remote isotropic tension. Contours range from 2 to 24 MPa (tension is positive). Along a bonded interface 2 cm ahead of the crack, the greatest value of maximum tension occurs about 1.5 cm to either side of the parent fracture. Two hypothetical daughter fractures are sketched perpendicular to the maximum tension in these locations ahead of the parent fracture tip.	135
Figure 4.17 Maximum tensile stress along a bonded interface. Maximum tension increases as the crack approaches the interface. The greatest tension occurs to either side of the parent fracture and moves closer to $x=0$ as the fracture approaches the interface.	136
Figure 4.18 Cohesive Zone ahead of a crack	136
Figure 4.19 The laminated geometry used to study crack deflection in this paper. A layer of thickness h and with an elastic modulus of E_f and a Poisson's ratio of ν_f is bonded to a substrate of thickness d , where $d \geq 10h$. The substrate has an elastic modulus of E_s and a Poisson's ratio of ν_s . There is a crack that extends from the top surface to the interface, and is normal to the interface. Sets of cohesive elements exist ahead of the crack in the substrate and along the interface. There is a plane of symmetry along the crack, and the system is loaded by a uniform displacement applied to the ends of the specimen.	137
Figure 4.20 Schematic illustration of the (a) mode I, and (b) mode II traction-separation laws used for the cohesive zone model in Parmigiani and Thouless (2006)'s study.....	137

Figure 5.1. Contour of the tangential stress (MPa) near a pre-existing flaw tip with 45° inclination in a specimen under uniaxial compression of 1 MPa. 154

Figure 5.2. Example of specimen geometry used in ABAQUS155

Figure 5.3. Path used in the investigation of existing crack initiation at the inside tip of the bottom flaw of the $-2a030^\circ$ geometry, with $\phi=50^\circ$ interface inclined 90° from vertical. a) point IDs along the path; b) σI (blue full circles) and τ_{12max} (orange hollow circles) along the path.....156

Figure 5.4. Maximum principal stress around a flaw (top and middle) for a model with geometry $0-2a30^\circ$ with interface inclined 90° with the vertical and interface friction angle 50° . The elliptical area (bottom) indicates the region where tensile cracks are most likely to initiate – lighter gray indicates compression and darker grey tension.157

Figure 5.5. Possible directions of tensile cracks according to the stress field analysis.....158

Figure 5.6. Illustration of the results obtained using the Stress Approach. The dashed lines indicate the order by which the shear cracks are most likely to initiate.158

Figure 5.7. Prediction of tensile crack's direction of initiation after crossing the interface, using the approach described in section 4.4.5 (MPa).159

Figure 5.8. Crack 7 in Table 5.1(c). Maximum principal stress contours at 15MPa, for a model with geometry $0-2a30^\circ$ with interface inclined 90° with the vertical and friction angle 50° . The elliptical area (bottom) indicates the region where a tensile crack is most likely to initiate – lighter gray means compression and darker grey tension.160

Figure 5.9. Crack 7, Table 5.1(c). Prediction of crack 7 initiation, for the geometry $0-2a30^\circ$ with interface inclined 90° with the vertical and friction angle of 50° . Top: Region where crack is more likely to initiate. Bottom: Direction - perpendicular to the maximum principal stress vectors (bottom), MPa.161

Figure 5.10. Crack 6, Table 5.1(d). Prediction of crack 6 direction of initiation after crossing the interface, using the approach described in section 4.4.5. Specimen with geometry $0-2a30^\circ$ with interface inclined 90° with the vertical and contact friction angle 50° (MPa).162

Figure 5.11. Cracks 10 and 11, Table 5.1(e). Maximum principal stress contours at 25.5MPa, for a $0-2a30^\circ$ specimen with interface inclined 90° with the vertical and interface friction angle of 50° . The elliptical areas (bottom) indicate the regions at the interface where a tensile crack is most likely to initiate – lighter gray means compression and darker grey tension. (Crack 10 originates in the region shown on the right and crack 11 on the left).163

Figure 5.12 Crack 10, Table 5.1(e) Prediction of tensile crack 10 for a specimen geometry $0-2a30^\circ$ with interface inclined 90° with the vertical and interface friction angle of 50° . Direction of crack: perpendicular to the maximum principal stress (MPa).164

Figure 5.13. Crack 11, Table 5.1(e). Prediction of tensile crack 11 for a specimen geometry $0-2a30^\circ$ with interface inclined 90° with the vertical and interface friction angle of 50° . Direction of crack: perpendicular to the maximum principal stress (MPa).164

Figure 5.14. Crack 12, Table 5.1(h). Prediction of crack 12 direction of initiation after crossing the interface, using the approach described in section 4.4.5. Specimen with geometry 0-2a30° with interface inclined 90° with the vertical and contact friction angle 50° (MPa).	165
Figure 5.15. Crack 10, Table 5.2(e). Prediction of tensile crack 10 for a specimen 0-2a30° with interface inclined 90° with the vertical and interface friction angle of 35°. Direction of crack: perpendicular to the maximum principal stress vectors (MPa).	166
Figure 5.16. Crack 8, Table 5.3(d). Prediction of tensile crack 8 for 0-2a30° specimen with interface inclined 80° with the vertical and interface friction angle of 50°. Direction of crack: perpendicular to the maximum principal stress vectors (MPa).	167
Figure 5.17. Cracks 7 and 8, Table 5.4(b-c). Maximum principal stress contour at 8.5MPa for a specimen with geometry 0-2a30°, interface inclined 80° with the vertical and interface friction angle of 35°. The elliptical areas (bottom) indicate regions at the interface where a tensile crack is most likely to initiate – lighter gray means compressive stress and darker grey means tensile stresses. (Crack 7 originates in the region shown above the interface and crack 8 originates on the region below the interface).....	168
Figure 5.18. Crack 7, Table 5.4(b-c). Prediction of tensile crack 7 in geometry 0-2a30° with interface inclined 80° with the vertical and interface friction angle of 35°. Direction of crack: perpendicular to the maximum principal stress vectors (MPa).	169
Figure 5.19. Crack 6, Table 5.4(f). Prediction of crack direction of re-initiation after crossing the interface with an offset, using the approach described in section 4.4.5. Specimen with geometry 0-2a30° with interface inclined 80° with the vertical and contact friction angle 35° (MPa).	170
Figure 5.20. Effects of interface roughness and inclination angle. Tension and Compression zones in specimen 0-2a30°. a) horizontal interface with 50° friction angle; b) horizontal interface with 35° friction angle; c) inclined interface with 50° friction angle; d) inclined interface with 35° friction angle.	171
Figure 5.21. Effects of interface roughness and inclination angle. Tension and Compression zones in the area of interest for specimen 0-2a30° with interface inclined 90° with the vertical and interface friction angle of 50° (at a compression of 6.64MPa).....	172
Figure 5.22. Effects of interface roughness and inclination angle. Tension and Compression zones in the area of interest for specimen 0-2a30° with interface inclined 90° with the vertical and interface friction angle of 35° (at a compression of 6.64MPa).....	172
Figure 5.23. Effects of interface roughness and inclination angle. Tension and Compression zones in the area of interest for specimen 0-2a30°, interface inclined 80° and friction angle 50° (at a compression of 6.64MPa)	173
Figure 5.24. Effects of interface roughness and inclination angle. Tension and Compression zones in the area of interest for specimen 0-2a30°, interface inclined 80° friction angle 35°	173

ABSTRACT

Different rock formations may appear within the same mass, or even within the same formation there may exist layers of different materials, creating interfaces between layers (an interface may be defined, in more general terms, as a frictional contact that separates two similar or dissimilar materials). Currently, there is no well-established experimental work that investigates the influence of frictional interfaces, interface orientation and flaw geometries on crack behavior (i.e. initiation, propagation and coalescence) in brittle specimens under compressive loading. A series of experiments on homogeneous gypsum specimens, used as a rock-model material, containing two pre-existing open flaws and a frictional interface has been performed under uniaxial compression. The experiments investigate how cracks interact with interfaces and how different variables (i.e. flaw geometry, interface inclination angle and interface roughness) affect crack behavior in homogeneous materials separated by an interface. The specimens are 203.2mm high, 101.6mm wide, and 25.4mm thick. The two flaws, with 0.1mm aperture and 12.7mm length (2a), are created through the thickness of the specimen. The spacing (S) between flaws, continuity (C), and inclination angle, measured from the horizontal, (β) define the geometry of the flaws. Three flaw geometries are tested: $S=0$, $C=-2a=-12.7\text{mm}$, $\beta=30^\circ$ (i.e. a left-stepping geometry); $S=2a=12.7\text{ mm}$, $C=a=6.35\text{ mm}$, $\beta=30^\circ$ (i.e. an overlapping geometry) and $S=3a=19.05\text{mm}$, $C=0$, $\beta=30^\circ$ (i.e. a right-stepping geometry). Smooth and rough unbonded interfaces are created by casting the specimen in two parts. The first half of the specimen is cast against a PVC block with an inclined face (i.e. 90° , 80° or 70°) with respect to the vertical axis of the specimen. The second half is then cast against the first one. Sandpaper may be attached to the PVC block to provide different roughness to the interface; a debonding agent applied to the interface ensures a cohesionless contact. In the experiments, digital image correlation (DIC) is used to monitor crack propagation on the specimen surface. The experiments indicate that the interface itself is an important contributor to new cracks and its presence in the specimens reduce crack initiation stress. Furthermore, the increase in roughness and inclination of the interface (i.e. from horizontal to 70° from the vertical) causes crack initiation stress to decrease. It was also observed that the angle between the incident crack plane and the interface affects whether an incident crack will penetrate an interface or be arrested: Tensile cracks that meet the interface at 30° to 60° angle get arrested, while those at or above 70° cross the interface with an offset of 0 – 1.2 mm. While shear cracks

that meet the interface at 20° to 63° angles get arrested at the interface, while those at or above 70° cross the interface with an offset in the range of 0 – 1.76 mm. Another relevant finding is the fact that changes in interface roughness or inclination angle did not affect the angles at which cracks initiate or reinitiate at the interface.

A numerical study was conducted using the Extended Finite Element Method (XFEM) capability in ABAQUS, to further investigate the fracture behavior observed in the experiments and, more specifically, the influence of the different types of interfaces. An extensive investigation of the stress fields around the tips of the flaws and of the new cracks, as well as along the interface in the specimens, was conducted to determine the relationship between stresses and crack initiation and propagation (i.e. type and direction of cracks). The stress-based approach yields predictions of tensile and shear cracks location and initiation direction that are in good agreement with experimental results. The numerical investigation indicated that rougher horizontal interfaces induced slightly higher tensile stresses around the interior and exterior flaw tips than smoother interfaces, which may explain why tensile cracks at these locations initiated earlier in specimens with a rough interface. Moreover, inclined interfaces induced higher tensile stresses around the interior and exterior flaw tips than horizontal interfaces, which may justify that, in the experiments, inclined interfaces promoted crack initiation earlier than horizontal interfaces.

1. INTRODUCTION

1.1 Problem Statement and Motivation

Failure of structures in rock (such as tunnels, foundations and excavations) may be produced by the presence of pre-existing discontinuities or by new discontinuities created by the stress state imposed by the structures. These discontinuities are of different types, e.g. bedding, joints, faults, and occur at different scales (from microfissures to kilometer-size faults). They may appear in sets or groups with similar orientation and characteristics. An additional complication is the fact that rock masses are not continuous. Different rock formations may appear within the same mass, or even within the same formation there may exist layers of different materials, creating interfaces between layers (See Fig. 1.1). An interface may be defined, in more general terms, as a frictional contact that separates two similar or dissimilar materials. The presence of an interface in rocks may affect fracture behavior. This can be seen in Fig. 1.2, in which the existence of an interface caused an approaching shear crack to jump 0.2 m after crossing the interface.

Sedimentary rocks, especially clay shales, are known for having bedding planes (i.e. interfaces) which may interact with natural or induced cracks. In many branches of geomechanical engineering, the mechanical behavior of clay shales is of great interest, including nuclear waste disposal, underground excavations, and deep well drilling (Amann et al, 2011), as well as for natural resources. Therefore, a better understanding of the continuity of cracks from one rock layer to another is of great importance for oil and gas extraction, for water resources and contaminant migration. Also, for rock slope stability, it is crucial to know if and how cracks connect with each other and with interfaces, or coalesce to create a continuous fracture surface.

In addition, the behavior of a layered rock mass is determined by both intact rock properties and the presence and characteristics of interfaces and cracks within the rock. The continuity, orientation, size and orientation of cracks and interfaces influence the deformability and strength of rock masses. Therefore, understanding fracturing processes in layered rocks, especially initiation and coalescence, is very relevant in rock mechanics.

Fracture mechanics provides a theoretical framework to analyze cracks in rocks. There is an increasing body of experimental and numerical research in the literature on crack initiation and propagation in pre-cracked brittle materials. However, the previous research has concentrated on

homogeneous pre-cracked brittle materials without interfaces (e.g. Bobet and Einstein 1998; Wong et al. 2001; Wong and Einstein 2009; Park and Bobet 2010; Zhou, Cheng and Feng 2014), subjected to mixed-mode loading (mode I, opening or tensile, and mode II, in-plane shear). Therefore, there is a pressing need to investigate the behavior of crack interaction with interfaces. The knowledge of the cracking processes across an interface will lead to better and more economical designs in layered rock masses.

1.2 Research Objectives

This research aims at investigating the effects of an interface on the fracturing mechanisms (i.e. crack initiation, propagation and coalescence) in a pre-cracked rock-model material. The objectives are reached through a comprehensive series of experiments, to observe the cracking mechanisms, and extensive numerical simulations of the experiments to investigate the interaction between new and pre-existing cracks and the interface.

Specimens of gypsum containing two pre-existing cracks, or flaws, and an unbonded interface (with either a smooth or rough contact) inclined at different angles with the loading direction are tested in uniaxial compression. The objectives of the tests are:

1. Understand how cracks interact with an interface (i.e. if cracks arrest or cross the interface; propagation of the cracks as they reach the interface);
2. Observe crack coalescence in specimens separated by an interface as a function of flaws geometry;
3. Investigate the influence of different interface inclination angles and roughness on crack behavior.

A numerical study is conducted using the Extended Finite Element Method (XFEM) capability in ABAQUS, to further investigate the fracture behavior observed in the experiments and, more specifically, the influence of the different types of interfaces on the cracking observed. An extensive investigation of the stress fields around the tips of the flaws and of new cracks, as well as along the interface in the modeled specimens, is conducted to determine whether there is

any relationship between stresses and crack initiation and propagation (i.e. type and direction of cracks).

1.3 Thesis Organization

The thesis includes six chapters, including the Introduction, and is organized as follows:

Chapter 2 provides a background on fracture mechanisms (i.e. initiation, propagation and coalescence) in rock-model materials, natural rocks and other materials.

Chapter 3 describes the experimental investigation conducted to characterize tensile and shear cracks and their interaction with an interface through surface imaging using digital image correlation (DIC). The chapter includes observations of tensile and shear crack initiation and growth for different interface characteristics (i.e. inclination angle and roughness) and pre-existing flaw geometries (i.e. non-overlapping right-stepping, non-overlapping left-stepping and overlapping).

Chapter 4 provides a background on theoretical fracture mechanics, specifically existing crack initiation and propagation criteria.

Chapter 5 explains the stress-based crack initiation approach used for the numerical simulations. Those are done using the XFEM capability in ABAQUS. The numerical models duplicate the experiments described in Chapter 3 and the results are analyzed to provide further insight into the experimental observations.

Chapter 6 highlights the major conclusions reached from the research and suggests recommendations for future research.

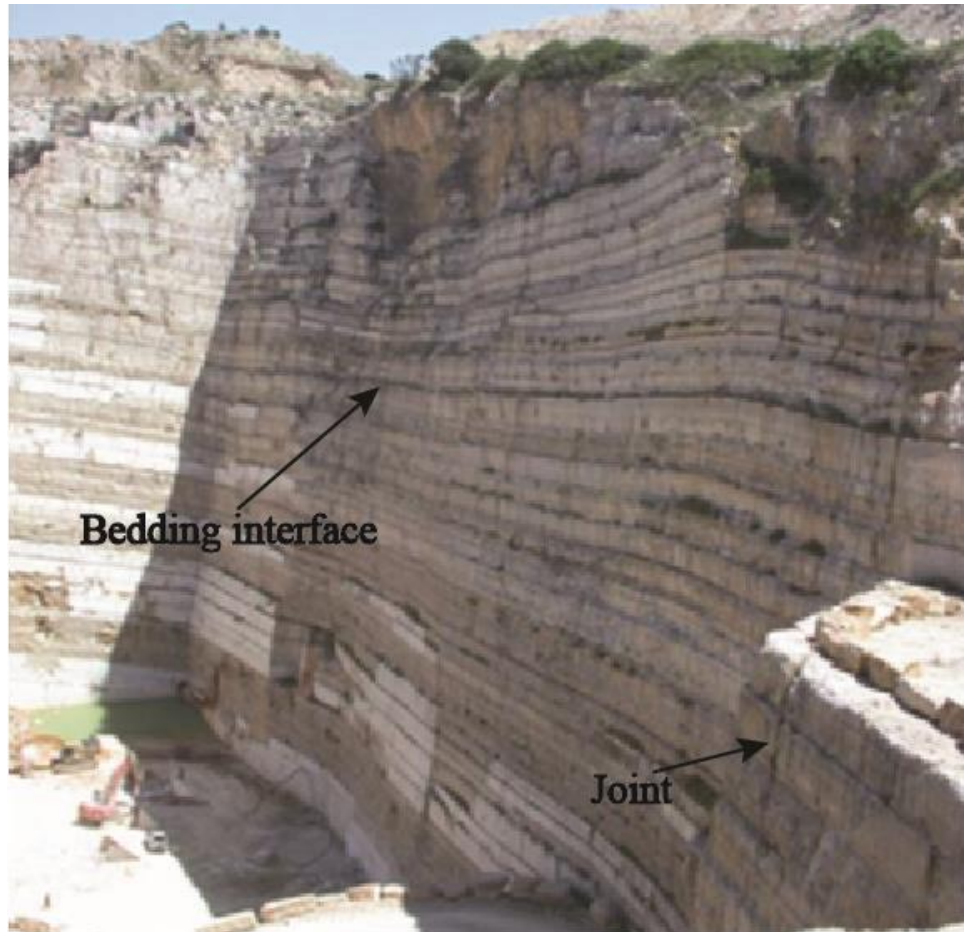


Figure 1.1. Carbonate rock mass with 1-2m thick bedding layers (adapted from Larsen et al, 2010)

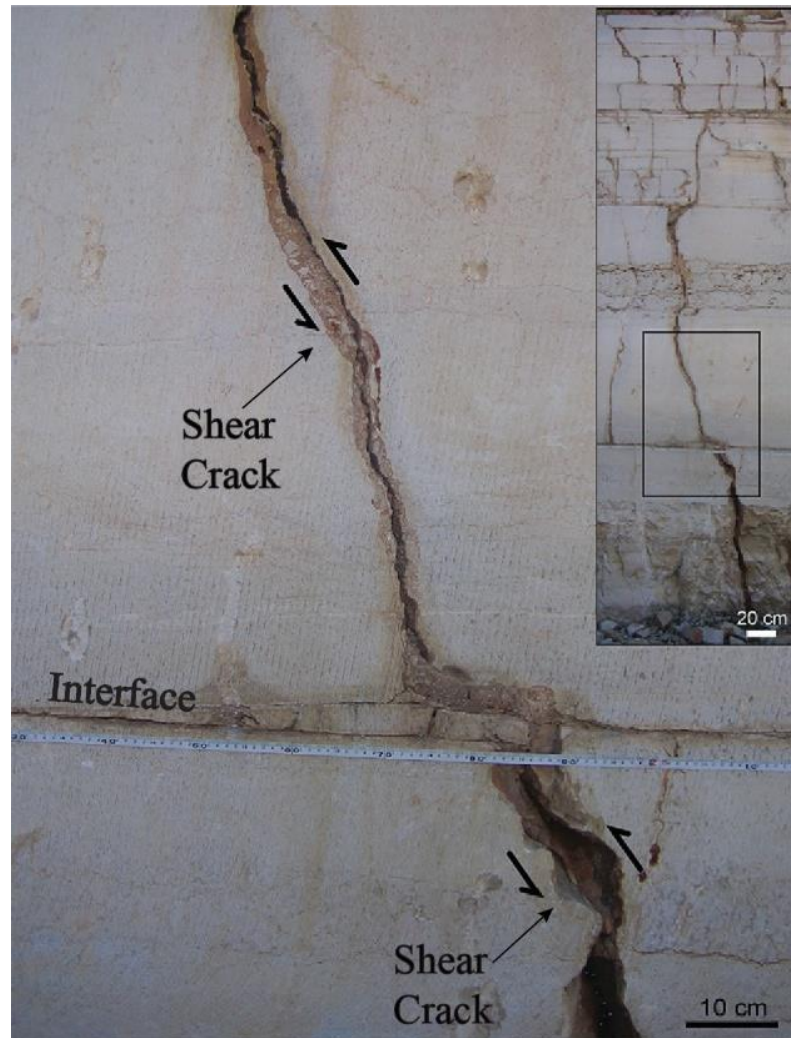


Figure 1.2. A shear fracture crossing an interface with an offset of 0.2m (adapted from Larsen, 2010)

2. EXPERIMENTAL INVESTIGATION: BACKGROUND

A summary of the state of art is provided for crack behavior on: (i) homogeneous materials without interface; (ii) homogeneous and heterogeneous materials with an interface.

Extensive research has been conducted on crack initiation, propagation and coalescence in homogeneous brittle materials containing pre-existing flaws in mixed mode I-II compression loading by a number of investigators such as Park and Bobet (2010) on gypsum; Wong and Einstein (2009) on marble; Morgan et al. (2013) on granite; Yang (2012) on sandstone; Haeri (2014) on Portland cement.

The coalescence patterns observed in the laboratory have been classified into different categories, but according to the particular findings of each researcher (e.g. Bobet and Einstein 1998; Wong and Einstein 2009; Park and Bobet 2010). For example, Park and Bobet (2010) studied crack coalescence of gypsum specimens containing three closed or open flaws and identified seven types of coalescence patterns. Some of the categories observed by different researches are similar to one another, others are not. Aiming at unifying the most relevant coalescence categories, Table 2.1 was developed by gathering observations made by Park and Bobet (2010) and Wong and Einstein (2009). The table shows cases of no coalescence as well as direct and indirect coalescence. There is no coalescence when cracks initiate from the flaw tips or near the tips, but there is no linkage between them. When cracks do link inside the bridge region, coalescence is said to be direct. On the other hand, when cracks link outside bridge region, coalescence is indirect.

The coalescence categories shown in Table 2.1 may occur in experiments performed in both closed and open flaws. Closed flaws have the internal faces in contact (i.e. friction and cohesion are present) while open flaws have an aperture so that the internal faces do not touch each other. Park and Bobet (2009), interestingly, concluded from their research that the cracking pattern and the cracking processes that occur in specimens with closed flaws are the same as with open flaws, meaning that the fracture mechanisms and principles that apply to both types of flaws are the same. However, for the same geometry, the coalescence type observed on specimens with open flaws may not be the same as the coalescence observed on closed flaws. Furthermore, the main difference observed between experiments with open and closed flaws was that initiation and coalescence stresses were higher for closed than for open flaws. This was explained by the

presence of friction along closed flaws that needed to be overcome before a crack initiated, as well as by the capability of closed flaws to transmit normal or shear stresses since the internal faces of the flaws touched each other.

Previous studies have indicated that the cracking processes and coalescence patterns are closely related to the inclination angle (β), continuity (C) and spacing (S) of the pre-existing flaws – See Fig. 2.2. Spacing is defined as the distance between the two flaws measured along the direction perpendicular to the flaws. Continuity is the distance between the right tip of a flaw and the left tip of the other flaw, measured along the direction parallel to the flaws. Finally, flaw geometries can be classified into left and right stepping, and overlapping and non-overlapping. A geometry is characterized as “right stepping” when one moves, along the direction of the loading, from the top to the bottom flaw stepping to the right; likewise, left stepping geometry is when, along the direction of loading, one moves from the top to the bottom flaw stepping to the left (Sagong and Bobet 2002).

Wong and Einstein (2009) investigated the crack behavior of rock-like materials (i.e. marble and gypsum) containing two initial open flaws and, based on their experimental observations, the coalescence types were classified into nine different categories. They observed that, in marble, the development of macroscopic cracks was preceded by multiple white patches, but not in gypsum. The authors also summarized similarities between marble and gypsum. For instance, longer ligament lengths (L) reduced the chance of coalescence. Moreover, for coplanar flaw pairs, i.e. Spacing (S) = 0, low flaw angles (β) favored shear coalescence, while higher values of β favored tensile coalescence. For stepped flaw pairs, as the flaw geometry changed from right-stepping to left-stepping, the coalescence changed from no coalescence, to indirect coalescence, and then to direct coalescence. Regarding direct coalescence, the coalescence categories progressed from shear, to mixed shear-tensile, and then to tensile as the flaws arrangement switched from right-stepping to left-stepping.

Morgan et al. (2013) carried out uniaxial compression tests on barre granite specimens with pre-existing flaw pairs with different geometries. The authors indicated that white patches were spotted on granite previously to crack initiation. Similar to gypsum, as the ligament length (L) between the flaws increased, indirect coalescence tended to occur. Crack coalescence changed from indirect to direct shear and combined shear-tensile to direct tensile as the flaw geometry changed from right-stepping to left-stepping or when the flaw angle (β) increased. However, shear

cracks occurred less often in barre granite when compared to other brittle materials (i.e. gypsum and marble) and tensile cracks were typically much more jagged in shape due to the larger size and higher strength of the mineral grains of the granite. Consequently, more indirect tensile coalescence was observed in granite compared to other materials.

Yang et al. (2012) analyzed crack behavior on sandstone specimens containing three flaws under uniaxial compression and found that crack initiation stress was non-linearly related to the ligament angle (α). Ligament length is the distance between the two internal flaws tips and the angle of connection between them is the ligament angle (α). They observed that as α increased from 75° to 90° , the crack initiation stress slightly decreased, whereas it increased linearly as α increased from 90° to 120° .

Regarding experimental work that has been performed in rock-like specimens, Haeri et al. (2014) observed that, in Portland cement specimens and in compression, tensile cracks were the first type of cracks produced and they propagated toward the direction of uniaxial compression. They also pointed out that shear cracks were produced as quasicoplanar and/or oblique cracks. These observations regarding the tensile and shear cracks is in agreement to the findings obtained in other rock-model materials such as gypsum.

Although there are a few differences in the crack patterns found in brittle materials in compression, the research shows that two types of cracks are commonly observed: tensile and shear cracks (Figure 2.1). Tensile cracks initiate at or near the tips of the flaws and usually propagate in a stable manner following a curvilinear path that aligns with the most compressive load; their surfaces are clean and do not contain any pulverized material. In contrast to the tensile cracks, shear cracks, which always initiate at the tips of the flaws, are characterized by the presence of crushed material and powder on their surfaces, and propagate in a stable manner, at least initially since they may become unstable near coalescence. Shear cracks may be classified as quasi-coplanar or coplanar and oblique, depending on the angle of initiation with respect to the plane of the flaw from which they originate. Coplanar cracks make an angle of 45° or less with the flaw plane, while oblique cracks make an angle higher than 45° (Park and Bobet 2009).

For pre-cracked homogeneous or heterogeneous materials containing an interface, many researchers have focused on deflection or penetration of a tensile crack approaching the interface, for similar (Lemaitre et al. 1996; Roi Xu et al. 2003; Sundaram and Tippur 2016) and dissimilar (He and Hutchinson 1989; Liu et al. 2011; Chang et al. 2015) materials across the interface. Crack

penetration occurs when an incident crack meets the interface and crosses it, while crack deflection takes place when an incident crack is trapped by the interface. The strength of the interface and the properties of the material on each side of the interface are important parameters governing crack deflection/penetration phenomena (Suo and Hutchinson 1990). This can be ascertained from the study performed by Siegmund et al. (1997) who looked into the role of interface strength on crack penetration versus deflection at an interface located perpendicular to the direction of crack growth. The authors observed that a higher strength of the interface favored crack penetration, whereas a weaker strength led the crack to deflect.

Sundaram and Tippur (2016) tested pre-notched homogeneous specimens of PMMA containing an interface oriented perpendicular to an incoming mode-I crack, as depicted in Fig. 2.3. The results showed that the crack behavior at the interface was greatly influenced by the distance between the interface and the incident crack (masked as “d” in Fig. 2.3a). When the interface was located near the pre-existing flaw, the mode-I crack penetrated the interface (See Fig. 2.3b). On the other hand, when the pre-existing flaw was located farther away from the interface, the mode I crack bifurcated into two interfacial cracks, that propagated in opposite directions by nearly equal length into the material across the interface (See Fig. 2.3c). The investigators also tested two different interface toughness (identified as weak and strong). They observed that, for a weak interface, the mode-I crack transitioned to an interface crack before penetrating the material across the interface. For a strong interface, the crack crossed the interface without such transition along the interface. Another interesting finding was that a weaker interface facilitated crack arrest.

According to Roy Xu et al. (2003), the angle between the incident crack plane and the interface affects whether an incident crack will penetrate an interface or be deflected. They investigated failure mechanisms of bonded Homalite layers subjected to projectile impact, and their results showed that deflection took place when incident angles ranged from 0 to 59°, while penetration occurred for incident angles from 59° to 90°.

He and Hutchinson (1989) conducted a comprehensive analytical work in which they examined the competition between penetration and deflection of a tensile crack approaching a bonded interface between dissimilar elastic materials. The ratios G_i/G_1 and G_d/G_p were used by the authors to assess the tendency of a tensile crack to be deflected by the interface or to pass through it. G_1 is the mode I toughness of material 1 (Figure 2.4), G_i is the toughness of the interface, and G_p and G_d are the energy release rates of the penetrating and of the deflected cracks,

respectively. The toughness of an interface is basically the energy required to separate two adjoining materials, usually quantified in terms of a critical energy release rate for crack extension along the interface, measured in units of energy per unit area. When $G_i/G_1 < G_d/G_p$ the crack will likely be deflected (Figure 2.4a); while when $G_i/G_1 > G_d/G_p$ the crack will tend to penetrate and cross the interface (Figure 2.4b). Two types of pre-existing cracks were considered in this study: a crack perpendicular to the interface and an oblique crack. The more oblique the crack approaching the interface is, the more likely deflection will occur.

Debonding and slippage of interfaces have also been studied by researchers such as Leguillon (1999), Cooke and Underwood (2001), and Hou et al. (2016). Debonding is caused by an incident crack that deflects along the interface, leading the materials at both sides of the interface to detach. The mechanism of debonding depends on the elastic mismatch between the two materials as well as the strength of the interface and of the material in which the incident crack is located (Leguillon 2000). On the other hand, interface slippage occurs when the material on each side of the interface slides along the interface (Hou et al. 2015). Slip may be promoted by a crack approaching the interface that imposes shear stresses along the interface. The influence of both sliding and opening, as a crack approaches the interface, was explored by Cooke and Underwood (2000) through their investigation on fracture interaction with bedding planes. The authors tested the case of interface slip with no opening (sliding-only) and then the case of debonding and subsequent opening along the interface with no sliding (opening-only). They found that sliding-only interfaces encouraged propagation of fractures straight through the modeled interface. In contrast, opening-only interfaces yielded either fracture termination or initiation of a new fracture in the material across the interface at a distance from the point where the incident crack met the interface. Their results indicated that debonding rather than slipping was responsible for fracture termination (i.e. arrest) and step-over of fractures (i.e. when a crack deflects along the interface before penetrating the material across the interface). Furthermore, they also observed that a weak interface begins to slip at a smaller distance from the tip of a perpendicular incident crack than a strong interface.

Another relevant finding was pointed out by Renshaw and Pollard (1995). The authors observed that increased interface normal compression encourages crack propagation through the interface.

At present, there is no well-established experimental work that investigates the influence of frictional interfaces, interface angles and flaw geometries on crack behavior (i.e. initiation, propagation and coalescence) in homogeneous specimens under compressive loading. This research is expected to improve the understanding of the crack-and-interface interaction. This understanding may be useful to improve our analytical tools for the stability of structures in layered rocks such as underground excavations, slopes, or tunnels, where pre-existing discontinuities in the rock mass play a crucial role for the integrity of such structures.

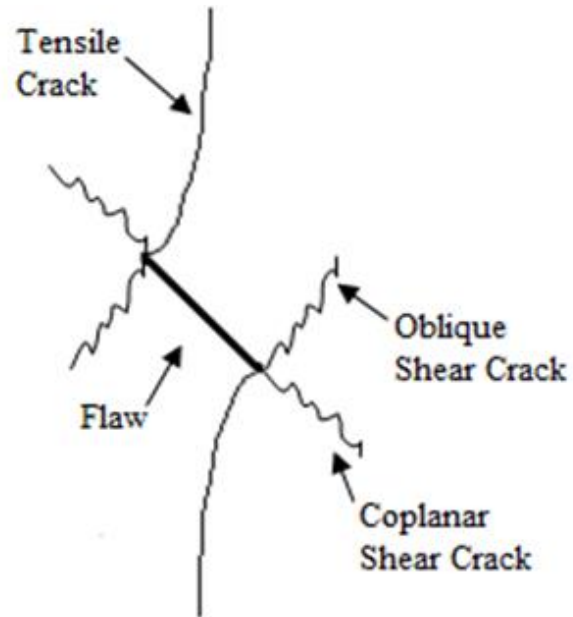


Figure 2.1. Types of cracks observed in pre-cracked rock-model specimens subjected to uniaxial compression

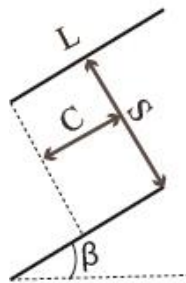


Figure 2.2. Flaws geometry

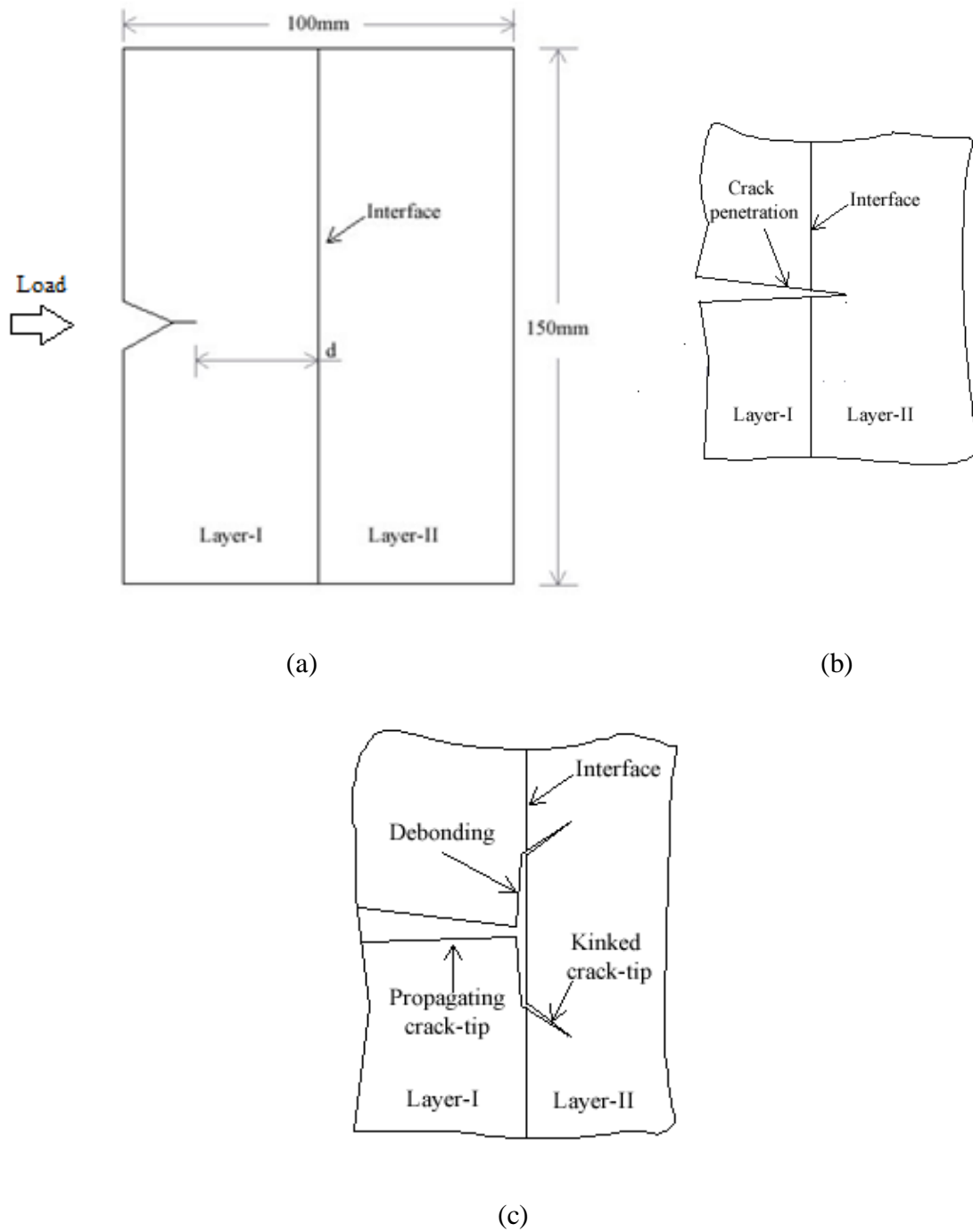
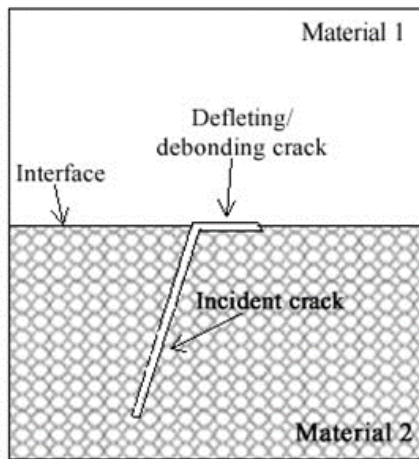
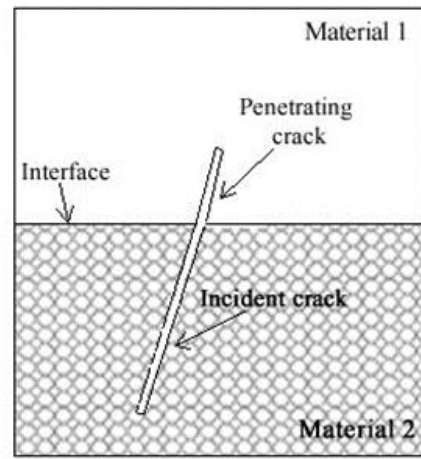


Figure 2.3. Bilayered PMMA specimen. (a) Specimen configuration; (b) Crack penetration; (c) Crack deflection



(a)



(b)

Figure 2.4. Behavior of a crack approaching a bonded interface between dissimilar elastic materials. a) Deflecting crack; b) Penetrating crack.

Table 2.1. Crack coalescence categories observed by Wong and Einstein (2008) & Park and Bobet (2010)

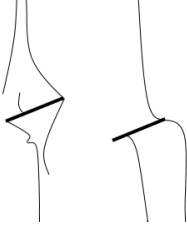
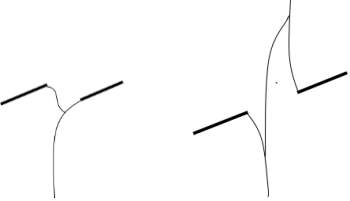

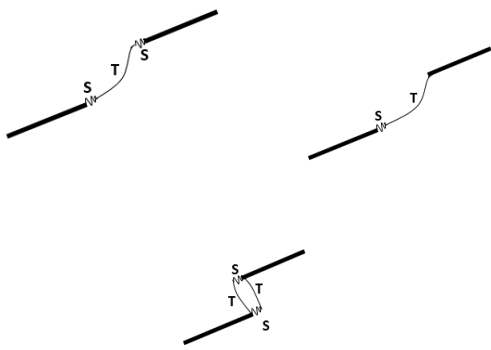
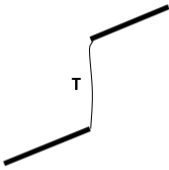
Category	Coalescence patterns	Description
No coalescence (1)		Cracks initiate from the flaw tips or near the tips, but there is no linkage between them.
Indirect coalescence (2)		Cracks link outside bridge region.
Coplanar (or quasi-coplanar) shear cracks (3)		Linkage of two coplanar (or quasi-coplanar) shear cracks, which initiated from the flaw tips.
One or more coplanar (or quasi-coplanar) shear cracks and a tensile crack (4)		Linkage through a combination of shear from the internal tips of the flaws and a tensile crack.
One or two tensile cracks (5)		The inner flaw tips are linked up by a tensile crack.

Table 2.1. continued

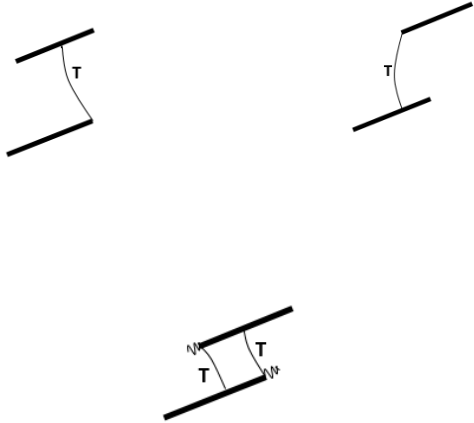
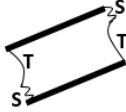
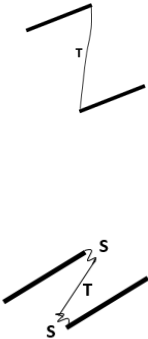

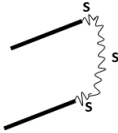
Category	Coalescence patterns	Description
<p>Tensile crack(s) from flaw tip to face of the other flaw (or vice-versa)</p> <p>(6)</p>		<p>The two pre-existing flaws are connected by one or more tensile cracks. The coalescence crack can initiate from the tip of one flaw and then propagate towards the face of the other flaw, at a distance from the flaw tip, or it can initiate from the face of one flaw at a distance from the flaw tip and then propagate towards the tip of the other flaw; or both.</p>
<p>Curvilinear tensile crack (and short shear crack segments) linking flaw tips at the same side</p> <p>(7)</p>		<p>The flaw tips of the two flaws are connected by a tensile crack. Short shear segments may be observed at the tips.</p>
<p>Right tip linked to left tip of flaw by a tensile crack (oblique shear cracks may develop close to the tips)</p> <p>(8)</p>		<p>The tips of flaws are connected by a tensile crack. This tensile crack either initiates as a single continuous crack or forms due to the linkage of multiple short crack segments initiated earlier in the central bridging region. Oblique shear cracks may be observed at the tips.</p>

Table 2.1 continued

Category	Coalescence patterns	Description
Oblique shear cracks (9)		The inner tips are linked through an oblique shear crack.
Quasi-coplanar shear cracks at the flaws tips linked by shear crack (10)		Two quasi-coplanar shear cracks initially propagate from the tips of the flaws in a stable manner. At a certain moment, an out-of-plane shear crack propagates in an unstable manner and links the two quasi-coplanar shear cracks.

* Categories 3 to 10 are classified as direct coalescence

3. EXPERIMENTAL INVESTIGATION: METHODOLOGY AND RESULTS

3.1 Experimental Procedures

3.1.1 Introduction

Prismatic specimens using gypsum were prepared and tested under uniaxial compression. In general, two types of specimens were manufactured: intact and pre-cracked, containing two pre-existing open flaws. Pre-cracked specimens were prepared with and without an interface through their center. The procedures for preparing the specimens are described in section 3.1.3. The fabrication process was precisely followed to prepare all the specimens to ensure repeatability and to diminish, to the maximum extent possible, any manufacturing errors.

Gypsum was initially used for the specimens since it provides good repeatability of results and it has been used extensively for the investigation of rock-model materials by various researchers (Einstein and Hirschfeld 1970, Reyes 1991, Takeuchi 1991, Shen et al. 1995, Bobet and Einstein 1998, Wong and Einstein 2006, and Ko et al. 2006).

The experimental procedures section consists of 4 sub-sections, in addition to the Introduction. Section 3.1.2 presents details of the flaw geometries tested. Section 3.1.3 describes the preparation of specimens. Section 3.1.4 contains the description of the experimental setup and how the tests were performed.

3.1.2 Specimen geometry

The dimensions of the finished specimens were 203.2 mm high, 101.6 mm wide, and 25.4 mm thick. Intact specimens did not contain any pre-existing flaws nor interfaces. Two pre-existing open flaws were created in the pre-cracked specimens (Figure 3.1.a). The aperture of the flaws

was 0.1 mm which is the thickness of the steel shims used during specimen preparation (discussed later). The flaws all had a constant length (L) of 12.7 mm and were parallel to each other. The spacing (S) between flaws, continuity (C), and inclination angle (β) define the geometry of the flaws (Figure 3.1.b).

Spacing is defined as the distance between the two flaws measured along the direction perpendicular to the flaws. Continuity is the distance between the right tip of a flaw and the left tip of the other flaw, measured along the direction parallel to the flaws. Continuity is considered positive when the two flaws overlap and negative when they do not overlap.

Experiments were performed on specimens containing the following flaw geometries: $S=0$, $C=-2a=-12.7\text{ mm}$, $\beta=30^\circ$; $S=2a=12.7\text{ mm}$, $C=a=6.35\text{ mm}$, $\beta=30^\circ$ and $S=3a=19.05\text{ mm}$, $C=0$, $\beta=30^\circ$, where 'a' is the half length of the flaw.

3.1.3 Specimen Preparation

3.1.3.1 Intact Specimens

Uniaxial compression loading tests were conducted on intact gypsum prismatic specimens to obtain the unconfined compression strength and stiffness of these materials. The mold in which the specimens were cast was composed of an assemblage of four steel plates. A PMMA plate was attached to the bottom of the steel mold with packaging tape and grease added between them to avoid leaks.

The gypsum specimen preparation is described as follows:

1. 11.43 g of diatomaceous earth and 400 cc of tap water were placed in a blender and mixed at high speed for 30 seconds;
2. 1000 g of Hydrocal B-11 was added to the mixture and blended for 30 seconds at low speed and then for 4 minutes at high speed;

3. The mixture was poured into the steel mold and was vibrated for 4 minutes on a vibrating table;

Diatomaceous earth was used to prevent water bleeding through the specimen surface during preparation. The water/hydrocal and water/diatomaceous earth ratios were 0.4 and 35.0, respectively. Those proportions had been also used by other researchers (e.g. Bobet 1998, Sagong, 2002 and Park 2009).

The gypsum was Hydrocal B-11, made by U.S. Gypsum Company. Diatomaceous earth was manufactured by Eagle-Picher Minerals Inc. as the commercial product Celatom.

After fabrication, the steel molds containing gypsum were placed on a horizontal table for 24 hours at room temperature. After that, the mold and bottom PMMA plate were disassembled and the specimens were placed in an oven to cure at 40°C for 4 days. The specimens were then polished using a gantry sheer router machine and finally tested in compression.

3.1.3.2 Pre-cracked Specimens without interface

The same procedure as that described in Section 3.1.3.1 was followed; the only difference is that two identical PMMA plates containing slits with the desired flaw arrangement were attached to the top and bottom of the mold. One steel shim per flaw, placed through the slits of the PMMA plates and perpendicular to the top and bottom faces of the mold, created the flaws once the gypsum inside the model hardened. The 0.1mm thick shims were greased to facilitate extraction from the specimen after 24 hours.

3.1.3.3 Pre-cracked Gypsum Specimens with an interface

The specimens consisted of two halves separated through a frictional interface. Each half of the specimen contained 50% of the amount of Hydrocal B-11, diatomaceous earth and tap water mentioned in section 3.1.3.1.

As described in section 3.1.3.2, two PMMA plates with slits corresponding to the desired flaw geometry were attached to the top and bottom of the mold; through the slits, steel shims were placed to form the flaws.

The specimens were manufactured in two steps: first, only half of the specimen was prepared. Once the first half had hardened, the second half was cast against the first half.

A solid block made of PVC was placed inside the steel mold to serve as a cast for the first half of the specimen. The surface of the block against which the gypsum was cast was either perpendicular to the sides of the block or with an angle of 70° or 80° from the vertical, to produce an inclined contact surface between the two halves, as shown in Fig.3.2 (a-d). To produce a rough interface (i.e. interface with friction angle $\phi=50^\circ$), a sandpaper with grit #36 was attached to the inclined surface of the PVC block. To produce a smooth interface (i.e. interface with friction angle $\phi=35^\circ$), no sandpaper was attached. The specimens with interface tested in this study are depicted in Fig. 3.3 and 3.4.

For the preparation of the specimens, steps (1) through (3) in section 3.1.3.1 were followed. The rest of the fabrication process is described below:

4. The mold was placed on a horizontal table and the first half of the specimen containing one steel shim was cured at room temperature for 24 hours;

5. The PVC block and sand paper, if placed, were removed from the steel block and, to prevent bonding at the interface, a debonding agent (i.e. product of Dow Corning) was applied;
6. A second shim was inserted through the second slit of the PMMA top and bottom plates;
7. A new gypsum mixture was poured into the mold against the first half of the specimen;
8. The mold was placed on a horizontal table and cured at room temperature for 24 hours;
9. The steel shims were pulled out of the gypsum;
10. The steel mold and PMMA plates were disassembled and the specimen was placed in an oven at 40°C for 4 days;
11. Finally, the specimen was polished using a fly cutter in a gantry sheet router machine.

3.1.4 Experimental Setup and Testing

Uniaxial compression tests were run using a multipurpose 100 kN Instron loading machine. The load was applied to the specimen using displacement control at a rate of 0.04 mm/s. Petroleum jelly and a stripe of Teflon film were placed between the specimen and the loading platens to reduce both friction and stress concentrations on the surface of the specimen. The vertical load was measured using the load cell of the machine and the vertical displacements with the LVDT of the machine. The load applied to the specimen was recorded by a data acquisition system, controlled with the Labview software.

The region of interest (ROI=50.8 x 50.8 mm) around the flaws had a random speckle pattern (dark area in Fig. 3.5) so that the surface displacements could be monitored with a DIC imaging system.

DIC is a continuous measurement technique that computes surface displacement fields by comparing digital images of a specimen surface acquired before (i.e. reference image) and during

deformation. A neighborhood of points around the point of interest (pixel), called a subset, is tracked between the deformed and the reference image (Sutton et al., 2009).

The DIC images were taken at a rate of 2 frames/sec by a Grasshopper (Point Grey) CCD camera with a focal length of 50 mm throughout the loading process. Focus and aperture of the lens were adjusted before each test. Once the test was completed, the images recorded during the experiment were analyzed using the software DaVis, which uses a Zero Normalized Correlation Criteria - ZNNC to obtain the displacements and strains. A crack on the surface was deemed present when the DIC displacement jump across the crack was at least 5 μm . This minimum threshold is based on a sensitive analysis that correlated direct surface observations with DIC measurements.

The experimental setup is depicted in Fig. 3.6.

3.2 Experimental Results

3.2.1 Introduction

This section comprises four major subsections, in addition to the introduction. First, the material properties of gypsum are shown in Section 3.2.2. The description of the crack behavior for the gypsum specimens tested with and without interfaces are presented, respectively, in Sections 3.2.3 and 3.2.4. Finally, the analyses of the influence of different interface flaw geometries, interface roughness and inclination angles on crack behavior are stated in Section 3.2.5.

It is relevant to mention that, in Sections 3.2.3 and 3.2.4, the classification of the cracks into tensile or shear was carried out by doing a visual assessment of the cracks after the tests and using the knowledge obtained from previous researchers, as well as by checking the tangential (i.e. shear contribution) and normal (i.e. opening contribution) displacements of the cracks.

Regarding the visual assessment, cracks are classified as ‘tensile cracks’ when they propagate in a stable manner following a curvilinear path that aligns with the most compressive load or when their surfaces are clean and characterized by a plumose structure that do not contain any pulverized material. Cracks are classified as ‘shear cracks’ when they are characterized by the presence of crushed material and powder on their surfaces, and propagate in a stable manner, at least initially, but may become unstable near coalescence. Shear cracks may be classified as ‘quasi-coplanar or coplanar’ and ‘oblique’, depending on the angle of initiation with respect to the plane of the flaw from which they originate. Coplanar cracks make an angle of 45° or less with the flaw plane, while oblique cracks make an angle higher than 45° (See Fig. 2.1 in Chapter 2).

In theory, tensile cracks that propagate along their own plane present only a mode I contribution (i.e. displacement normal to the plane of the crack) while shear cracks that propagate along their plane present a mode II contribution (i.e. displacement parallel to the plane of the crack and perpendicular to the crack length). However, as cracks deviate from their own plane, they are loaded in mixed mode I-II. Therefore, as other researchers have observed (e.g. Modiriasari, 2017), tensile cracks may also display spots with tangential displacements; and shear cracks may also display spots with normal displacements. For those cases, visual assessment and knowledge obtained from previous researchers were crucial to crack classification.

3.2.2 Material Properties

Uniaxial compression tests performed on intact specimens were used to find the unconfined compression strength (UCS) and Young’s modulus (E_{50}) of gypsum, as presented in Table 3.1. The E_{50} values correspond to the stiffness of the material at 50% of the peak strength. The tensile strength (σ_t) of gypsum is 3.2MPa (Bobet, 1997).

Table 3.1. Mechanical properties of intact gypsum

Gypsum		
UCS (MPa)	E50 (MPa)	σ_t (MPa)
37.3	13,768	3.2

Previous observations by Hedayat (2013) showed that the peak friction angle at rough contact surfaces (i.e. rough interface created with sandpaper #36) in homogeneous gypsum specimens following a similar procedure as that described previously in this chapter was 50°. Biaxial shear tests were carried out to confirm the peak friction angle value obtained by Hedayat (2013) for a rough interface as well as to obtain the peak friction angle for a smooth interface. The peak friction angles for rough and smooth interfaces were found to be $\phi=50^\circ$ and $\phi=35^\circ$, respectively.

3.2.3 Gypsum specimens without an interface

3.2.3.1 Specimen with geometry 0-2a30°

Figure 3.7 displays the crack behavior observed on the surface of a specimen with geometry 0-2a30°, at different loading stages. In Fig. 3.7 (a), it is possible to observe that crack initiation occurs at 11.88MPa when tensile cracks (1), (2), (3) and (4) emanates from all flaws tips. At 25.05MPa, an oblique shear crack (5) is detected at the inside tip of the upper flaw (Fig. 3.7 (b)). Cracks (1), (2), (3) and (5) propagate with further loading while crack (4) does not. New cracks originate at 27.47MPa, as shown in Fig. 3.7 (c): a quasi-coplanar shear crack (6) at the outside tip of the bottom flaw, a coplanar shear crack (7) at the inside tip of the bottom flaw, a tensile crack (8) near the inside tip of the upper flaw, and an oblique shear crack (9) at the outside tip of the upper flaw. When the stress reaches 28.14MPa, three tensile cracks (10), (11) and (12) appear in

the ROI (See Fig. 3.7 (d)). Finally, coalescence is produced indirectly at 30.22MPa when crack (7) reaches crack (5) and propagates towards the loading direction (marked as crack 13 in Fig. 3.7 (d)). At this point, a tensile crack (14) is observed near the outside tip of the bottom flaw.

1.2.3.2 Specimen with geometry 3a030°

Snapshots of the DIC images showing the cracking process on a gypsum specimen with flaw geometry 3a030° are provided in Fig. 3.8. Crack initiation takes place at 11.19 MPa when tensile cracks (1) and (2) originate at the inside tips of both flaws (Fig. 3.8 (a)). Shortly, at 12.18 MPa, two tensile cracks (3) and (4) appear at the outside tips of both flaws (Fig. 3.8 (b)). At 22.09 MPa, an oblique shear crack (5) originates at the inside tip of the upper flaw. In Fig. 3.8 (c), one can observe that cracks (1), (2), (3) and (4) propagate towards the most compressive load direction. In addition, crack (5) propagates towards the inside tip of the bottom flaw. At this point, oblique shear cracks (6) and (7) initiate at both tips of the bottom flaw. In Fig. 3.8 (d), at 24.06 MPa, coalescence occurs when the oblique shear crack (5) reaches the inside tip of the bottom flaw. Failure takes place at 34.21 MPa, as shown in Fig. 3.8 (e).

3.2.3.3 Specimen with geometry 2aa30°

Snapshots of the DIC images showing the cracking process on a gypsum specimen with flaw geometry 2aa30° are provided in Fig. 3.9. Crack initiation takes place when two tensile cracks (1) and (2) originate at both tips of the upper flaw at 14MPa, as depicted in Fig. 3.9 (a). Shortly, two tensile cracks (3) and (4) appear at both tips of the bottom flaw, respectively, at 14.63MPa and 16.93MPa. With further loading, those four tensile cracks propagate in the direction of the loading, showing a curvilinear path, which can be observed in Fig. 3.9 (b). When the stress reaches 34.96MPa, crack (4) closes and an oblique shear crack (5) originates at the inside tip of the bottom

flaw and immediately reaches the outside tip of the upper flaw. Therefore, coalescence occurs through the linkage of the flaw tips by the shear crack (5) at 34.96MPa (See Fig. 3.9 (c)). Right after coalescence, crack (2) reaches the bottom flaw, and a few other cracks can be observed in the ROI, as shown in Fig. 3.9 (d).

3.2.4 Gypsum specimens with an interface

3.2.4.1 Specimen with geometry 0-2a30° containing a smooth interface ($\phi=35^\circ$) inclined 90° with the loading direction

Fig. 3.10 presents crack behavior on the surface of a specimen with geometry 0-2a30° containing an unbonded smooth interface inclined 90° with the loading direction, at various loading stages. Crack initiation takes place at 9.5 MPa with a tensile crack (marked as 1) originating at the outside tip of the upper flaw, and another tensile crack (2) at the interface, as observed in Fig. 3.10 (a). When the stress reaches 16.39MPa, three new tensile cracks (3), (4) and (5) originate, respectively, at the crack tips of the pre-existing flaws (Fig. 3.10 (b)). With further loading, one can observe that cracks (1) and (5) propagate towards the loading direction while cracks (3) and (4) arrest. Furthermore, new tensile cracks originate at the interface: crack (6) at 19.13MPa in Fig. 3.10 (c), crack (7) at 25.47MPa in Fig. 3.10 (d), and crack (8) at 28.37MPa in Fig. 3.10 (e). At 28.94 MPa, shown in Fig. 3.10 (f), the top tip of the tensile crack (2) connects to the outside tip of the upper flaw and the bottom tip connects with tensile crack (7), before propagating towards the loading direction. Also, one can observe that the crack (8) reaches the inside tip of the upper flaw at 28.94 MPa. At this point, new tensile cracks (9) and (10) originate at the interface. At 30.23MPa, a tensile crack (11) originates at the interface with an offset of 2.39 mm from crack (10) and propagates in a direction parallel to the loading (Fig. 3.10 (g)). Plus, the tensile crack (6) reaches the inside tip of the bottom flaw, a crack (12) is spotted near the interface and the tensile crack (13) propagates inside the ROI, respectively. In Fig. 3.10 (h), it is possible to observe that crack (13) bifurcates, originating the tensile crack (14) that propagates towards the inside tip of the bottom flaw. Crack (13) then reaches crack (12) and crosses the interface without any offset. Coalescence occurs indirectly through cracks (8), (9), (13) and (14) at 31.36 MPa.

3.2.4.2 Specimen with geometry 0-2a30° containing a rough interface ($\phi=50^\circ$) inclined 90° with the loading direction

Figure 3.11 provides snapshots of the crack behavior observed on the surface of a specimen with geometry 0-2a30° containing a rough interface inclined 90° with the vertical, at different loading stages. In Fig. 3.11 (a), one can observe that crack initiation occurs at 6.95 MPa when tensile cracks (1), (2), (3) and (4) originate at the tips of both flaws. In Fig. 3.11 (b), at 15 MPa, one can notice that a coplanar shear crack (5) originates at the inside tip of the upper flaw. An oblique shear crack (6) is then detected at the outside tip of the upper flaw, and a tensile crack (7) originates at the interface, both at 18.94 MPa as depicted in Fig. 3.11 (c). Crack (6) reaches the interface at 22.79 MPa (Fig. 3.11 (d)), and crosses it (marked as 8 in the figure), without any offset at 25.5MPa (Fig. 3.11 (e)). At a latter stress stage, the coplanar shear crack (5) reaches and crosses the interface with an offset of 0.95mm; another oblique shear crack (9) can be noticed at the outside tip of the upper flaw. Shortly, at 25.8MPa, two tensile cracks (10) and (11) initiate at the interface, as shown in Fig. 3.11 (f). As the stress increases to 26.79 MPa, new cracks are detected, as seen in Fig. 3.11 (g): an oblique shear crack (12) at the inside tip of the bottom flaw, and two other oblique shear cracks (13) and (14) at the inside tips of the upper flaw. Furthermore, cracks (7) and (12) connect with each other, and also cracks (9) and (10). In Fig. 3.11 (h), one can observe that crack (14), which initiates as a shear crack, propagates as a tensile crack towards the loading direction. In addition, the shear crack (12) crosses the interface without an offset (15). Three new tensile cracks (16), (17) and (18) originate and abruptly propagate with loading. Crack (16) appears at the inside tip of the bottom flaw, and cracks (17) and (18) appear at the interface. Coalescence does not occur.

3.2.4.3 Specimen with geometry 0-2a30° containing a smooth interface ($\phi=35^\circ$) inclined 80° with the loading direction

Fig. 3.12 depicts crack behavior on the surface of a specimen with geometry 0-2a30° containing an unbonded smooth interface inclined 80° from the loading direction, at various loading stages. In Fig. 3.12 (a), one can observe that crack initiation occurs at 8.5 MPa when tensile cracks (1) and (2) originate at the outside tips of both flaws, one tensile crack (3) initiates at the inside tip of the bottom flaw, and two other cracks (4) and (5) initiate at the interface. With further loading, cracks (1) and (2) continue to propagate towards the direction of the load while crack (3)

seems to be insensitive to the load. At 16.98MPa, shear crack (6) originates at the inside tip of the upper flaw. At this point, as shown in Fig. 3.12 (b), a new tensile crack (7) is observed at the interface. In Fig. 3.12 (c), it is possible to notice another tensile crack (8) at the interface at 20.87 MPa. The figure also shows oblique shear cracks (9) and (10) originating at the inside tip of the bottom flaw and at the outside tip of the upper flaw, respectively. Cracks (7), (8) and (9) seem to be sensitive to the load while crack (10) does not. Shear crack (9) turns into a tensile crack with further loading. Furthermore, a coplanar shear crack (11) appears at the inside tip of the bottom flaw. Fig. 3.12 (d) shows the moment at which crack (11) reaches crack (4), at 23.05MPa. At this loading stage, tensile cracks (12) and (13) originate at the interface and on the top left side of the ROI, respectively. In Fig. 3.12 (e), at 23.92MPa, crack (12) reaches the outside tip of the bottom flaw. At this point, two new tensile cracks (14) and (15) originate and propagate from the interface. Also, tensile crack (13) reaches the outside tip of the upper flaw and an oblique shear crack (17) propagates from the inside tip of the upper flaw in the loading direction. Indirect coalescence occurs through the tensile crack (9) and the shear cracks (6) that crossed the interface with an offset of 1.756mm at 23.95 MPa (See Fig. 3.12 (f)).

3.2.4.4 Specimen with geometry 0-2a30° containing a rough interface ($\phi=50^\circ$) inclined 80° with the loading direction

Figure 3.13 depicts the crack behavior observed on the surface of a specimen with geometry 0-2a30° containing a rough interface inclined 80° with the vertical, at different loading stages. At 6.6 MPa, one can notice the initiation of tensile cracks (1) and (2) at the outside tips of both flaws as well as two other tensile cracks (3) and (4) at the interface, as shown in Fig. 3.13 (a). In Fig. 3.13 (b), at 9.38 MPa, a crack (5) originate at the interface. Later on, at 16.11 MPa, a coplanar shear crack (7) is observed at the inside tip of the bottom flaw (Fig. 3.13 (c)). Cracks (1) and (2) propagate toward the vertical direction with further loading. In Fig. 3.13 (d), at 18 MPa, one can observe that the coplanar shear crack (7) reaches the interface. Furthermore, a tensile crack (8) initiates at the interface. In Fig. 3.13 (e), a tensile crack (9) initiates at the interface at 19.30 MPa. At this load stage, the tensile crack (4) reaches the outside tip of the upper flaw. At 21.58 MPa, a coplanar shear crack (10) and an oblique shear crack (11) originate at the outside tip of the bottom flaw, as show in Fig. 3.13 (f). Moreover, the tensile crack (9) reaches the inside tip of the upper flaw, and the tensile crack (3) propagates towards the most compressive loading direction.

At 22.46 MPa, a subtle tensile crack (12) originates at the same point where crack (5) is located and propagates the vertical direction. Crack (13) crossed the interface without any offset. No coalescence takes place.

3.2.4.5 Specimen with geometry 3a030° containing a smooth interface ($\phi=35^\circ$) inclined 90° with the loading direction

Figure 3.14 provides snapshots of the crack behavior observed on the surface of a specimen with geometry 3a030°, containing a smooth interface inclined 90° with the vertical. i.e. with the loading direction, at different loading stages. As observed in Fig. 3.14 (a), crack initiation takes place at 9.28MPa with tensile cracks (1), (2), (3) and (4) at all flaws tips, as well as tensile cracks (5) and (6) at the interface. When the stress reaches 11.48 MPa, one can observe that a tensile crack (7) initiates at the interface. Shortly, at 11.95MPa, another tensile crack (8) originates at the interface with an offset of 0.32 mm from crack (7), as shown in Fig. 3.14 (b). Later on, at 18.01MPa, three other cracks are observed: tensile cracks (10) and (11) at the interface, and an oblique shear crack (12) at the outside tip of the upper flaw. At this stage, cracks (2) and (4) propagate towards the loading direction. In Fig. 3.14 (c), it is possible to notice that cracks (7) and (8) propagate with further loading. At 18.61MPa, depicted in Fig. 3.14 (d), crack (12) propagates towards the interface and a new tensile crack (13) originates at the interface. At 19.55MPa, an oblique shear crack (14) initiates at the inside tip of the bottom flaw and abruptly reaches the interface. Coalescence occurs when the tensile crack (7) connects with the oblique shear crack (12) above the interface; at the same time, tensile crack (8) links with the oblique shear crack (14) below the interface, as shown in Fig. 3.14 (e). Failure takes place at 24.68MPa, which is observed in Fig. 3.14 (f).

3.2.4.6 Specimen with geometry 3a030° containing a rough interface ($\phi=50^\circ$) inclined 90° with the loading direction

Fig. 3.15 provides snapshots of the crack behavior observed on the surface of the specimen with an unbonded rough interface, at different loading stages. As seen in Fig. 3.15 (a), crack initiation starts at both tips of the upper flaw (two tensile cracks marked as 1 and 2 in the figure) at 5.45 MPa. At 6.78 MPa, tensile cracks (3) and (4) originate at the interface without any offset between them, while tensile cracks (5) and (6) initiate near the middle and at the inside tip of the bottom flaw, respectively (Fig. 3.15 (b)). With further loading, cracks (1) and (6) propagate

towards the vertical direction, as shown in Fig. 3.15 (c). At 16.15 MPa, depicted in Fig. 3.15 (d), an oblique shear crack (7) originates at the inside tip of the upper flaw and abruptly connects with the tensile crack (3). When the stresses reach 16.29 MPa (Fig. 3.15 (e)), a tensile crack (8) initiates at the interface, and an oblique shear crack (9) originates at the inside tip of the bottom flaw. Later on, a tensile crack (10) appears at the interface at 20.7 MPa. Coalescence occurs at 18.06 MPa through the oblique shear crack (7) connecting with tensile crack (3), and tensile crack (4) that reaching the inside tip of the bottom flaw (Fig. 3.15 (f)). Failure takes place at 22.38 MPa, which is shown in Fig. 3.15 (g).

3.2.4.7 Specimen with geometry 3a030° containing a smooth interface ($\phi=35^\circ$) inclined 80° with the loading direction

For the specimen with geometry 3a030° with the smooth interface inclined 80° with the vertical, which is shown in Fig. 3.16, crack initiation occurs at 7.75 MPa when tensile cracks (1), (2), (3) and (4) originate at the flaws tips. In addition, a tensile crack (5) initiates at the interface (See Fig. 3.16 (a)). At 8.26 MPa, depicted in Fig. 3.16 (b), another tensile crack (6) initiates at the interface with an offset of 0.95 mm from crack (5). As it can be observed in Fig. 3.16 (c), all cracks propagate with further loading. At 11.53MPa, new cracks originate: two tensile cracks (7) and (8) at the interface, an oblique shear crack (9) at the inside tip of the upper flaw, a tensile crack (10) at the middle of the upper flaw, and a tensile crack (11) at the interface. When the stress reaches 15.23 MPa, which is shown in Fig. 3.16 (d), an oblique shear crack (12) initiates at the inside tip of the bottom flaw and suddenly crosses the interface (13). At 16.29MPa, crack (5) connects to crack (9). Coalescence is produced through cracks (5), (9) and (12) at 17.12 MPa, depicted in Fig. 3.16 (e). Fig. 3.16 (f) shows that failure occurs at 26MPa.

3.2.4.8 Specimen with geometry 3a030° containing a rough interface ($\phi=50^\circ$) inclined 80° with the loading direction

Figure 3.17 depicts the crack behavior observed on the surface of a specimen with geometry 3aa30° containing a rough interface inclined 80° with the vertical, at different loading stages. As depicted in Fig. 3.17 (a), one can notice the initiation of tensile cracks (1) and (2) at the interface at 5.08 MPa. In addition, a tensile crack (3) at the inside tip of the upper flaw and tensile crack (4) near the outside tip of the upper flaw also appear. At 7.34 MPa, a tensile crack (5) initiates

at the inside tip of the bottom flaw (Fig. 3.17 (b)). Cracks (3) and (5) propagate towards the most compressive loading direction with further loading. In Fig. 3.17 (c), a tensile crack (6) originates at the inside tip of the bottom flaw, and a tensile crack (7) initiates at the interface at 8.13 MPa. In Fig. 3.17 (d), at 8.81 MPa, a tensile crack (8) initiates at the middle of the bottom flaw. At 9.33 MPa, new cracks can be observed: tensile cracks (9), (11) and (12) at the interface; and oblique shear crack (10) at the inside tip of the upper flaw (Fig. 3.17 (e)). Coalescence takes place through cracks (2), (7), (10) and (12) at 11.75 MPa.

3.2.4.9 Specimen with geometry 3a030° containing a smooth interface ($\phi=35^\circ$) inclined 70° with the loading direction

Figure 3.18 provides snapshots of the crack behavior observed on the surface of a specimen with geometry 3a030° containing a smooth interface inclined 70° with the vertical, at different loadings. In Fig. 3.18 (a), one can observe that crack initiation occurs at 6.68 MPa when a tensile crack (1) originates at the outside tip of the upper flaw. At 7.82MPa, a tensile crack (2) originates at the inside tip of the upper flaw. Shortly, at 9.21MPa, tensile cracks (3) and (4) initiate, respectively, at the outside and inside tips of the bottom flaw (Fig. 3.18 (b)). In Fig. 3.18 (c), tensile cracks (5), (6), (7) and (8) are observed originating at the interface at 10.17MPa. Also, cracks (2) and (4) propagate toward the loading direction with further loading. In Fig. 3.18 (d), it is possible to notice a tensile crack (9) that originates at 10.5MPa at the interface, at the same location where crack (6) initiated, and propagates towards the inside tip of the bottom flaw. Also, a tensile crack (10) is observed at the middle of the upper flaw and an oblique shear crack (11) initiates at the inside tip of the upper flaw. Furthermore, crack (5) reaches the outside tip of the upper flaw and a tensile crack (12) originates at the same location where crack (5) initiated, and propagates towards the loading direction. At 11.5 MPa, a coplanar shear crack (14) originates at the inside tip of the upper flaw. Crack coalescence is produced when the tensile crack (6) connects with the coplanar shear crack (15), and the tensile crack (9) reaches the inside tip of the bottom flaw, as shown in Fig. 3.18 (e). Failure of the specimen occurs at 14.34 MPa (Fig. 3.18 (f)).

3.2.4.10 Specimen with geometry 3a030° containing a rough interface ($\phi=50^\circ$) inclined 70° with the loading direction

Figure 3.19 depicts the crack behavior observed on the surface of a specimen with geometry 3aa30° containing a rough interface inclined 70° with the vertical, at different loading stages. Crack initiation occurs at 5 MPa when tensile cracks (1) originates at the outside tip of the upper flaw, shown in Fig. 3.19 (a). Under 6.06 MPa, tensile cracks (2), (3) and (4) initiate at the other flaws tips (See Fig. 3.19 (b)). With further loading, tensile cracks (5) and (6) appear at the interface, respectively, at 6.91 MPa and 7.73 MPa (See Fig. 3.19 (c)). At 8.11MPa, three other tensile cracks (7), (8) and (9) are observed at the interface. In addition, one can observe that tensile crack (5) reaches the inside tip of the bottom flaw, which is depicted in Fig. 3.19 (d). At 8.45MPa, a tensile crack (10) appears at the length of the bottom flaw. Later on, at 8.88MPa, a tensile crack (11) is observed at the interface. With further loading, another tensile crack (12) initiates at the interface and an oblique shear crack (13) abruptly originated and propagated from the inside tip of the upper flaw, which are depicted in the crack path for a load of 10.58MPa in Fig. 3.19 (e). At this point, coalescence is observed through the connection of cracks (5), (6) and (13). Failure takes place at 13.56MPa, shown in Fig. 3.19 (f). Crack (13) crosses the interface with an offset of 1.5 mm.

3.2.4.11 Specimen with geometry 2aa30° with smooth interface ($\phi=35^\circ$) inclined 90° with the loading direction

Figure 3.20 provides snapshots of the crack behavior observed on the surface of a specimen with geometry 2aa30° containing a smooth interface inclined 90° with the vertical, and at different loading stages. As observed in Fig. 3.20 (a), crack initiation takes place with an oblique shear crack at the inside tip of the bottom flaw, and with two tensile cracks at the interface and at the outside tip of the upper flaw at 11.6MPa (marked as 1, 2 and 3 in the figure, respectively). With loading, the cracks grow. At 15.51MPa, the oblique shear crack (1) reaches the interface (Fig. 3.20 (b)). In Fig. 3.20 (c), at 17.44MPa, one can observe that the tensile cracks (2) and (3) start propagating with further loading and a coplanar shear crack (4) initiates at the inside tip of the upper flaw. At this point, a new tensile crack (5) initiates with an offset of 1.51 mm from crack (1) and propagates towards the outside tip of the upper flaw. Also, a tensile crack (6) initiates at the outside tip of the bottom flaw and propagates in the loading direction with further loading. When the stress reaches

19.34MPa, the tensile crack (2) and the coplanar shear crack (4) connect to one another, as shown in Fig. 3.20 (d). In Fig. 3.20 (e), at 23.67 MPa, crack (1) crosses the interface, denoted as crack (7) in the figure, without any offset. At this point of the experiment, a tensile crack (8) originates at the interface. Plus, cracks (2) and (4) cross the interface without offset. Crack (9) propagates towards the outside tip of the bottom flaw. In Fig. 3.20 (f), the tensile crack (10) initiates at the interface at 24.24MPa, and moves towards crack (5). Plus, an oblique shear crack (11) initiates from the outside tip of the bottom flaw and propagates with further loading (Fig. 3.20 (g)). At 27.2 MPa, coalescence occurs through the oblique shear cracks (1) and (7), as shown in Fig 3.20 (g). Failure takes place at 30.36 MPa, which is shown in Fig. 3.20 (h). New tensile cracks (12) and (13) are observed at the interface at this point.

3.2.4.12 Specimen with geometry 2aa30° with rough interface ($\phi=50^\circ$) inclined 90° with the loading direction

Figure 3.21 provides snapshots of the crack behavior observed on the surface of a specimen with geometry 2aa30° containing a rough interface inclined 90° from the vertical, at different loading stages. As observed in Fig. 3.21 (a), crack initiation takes place at the outside tip of the upper flaw at 10.53 MPa with a tensile crack (1). Shortly, at 15.45MPa, two more tensile cracks (2) and (3) are detected at the inside tips of both flaws (See Fig. 3.21 (b)). When the stress reaches 19.72MPa, shown in Fig. 3.21 (c), one can observe that a tensile crack (4) originates at the outside tip of the bottom flaw, and other two tensile cracks (5) and (6) originate at the interface. With further loading, crack (5) propagates towards the outside tip of the upper flaw and crack (6) reaches the inside tip of the bottom flaw at 26.99MPa as depicted in Fig. 3.21 (d). At 27.85MPa, two tensile cracks (7) and (8) originate at the interface with an offset of 2.14mm from one another (Fig. 3.21 (e)). In Fig. 3.21 (f), it is possible to notice that a tensile crack (9) originates in the ROI and propagates towards crack (7). Once the stress reaches 31.29MPa, a tensile crack (10) can be observed originating at the middle of the upper flaw length, which is illustrated in Fig. 3.21 (g). Moreover, cracks (1) and (4) propagate in the direction of the loading while cracks (2) and (3) seem to be insensitive to the load; crack (8) reaches the inside tip of the upper flaw at this point of the experiment. Finally, coalescence occurs through the tensile cracks (5) and (6) that connect the outside tip of the upper flaw and the inside tip of the bottom flaw at 31.31MPa, as shown in Fig. 3.21 (h). At coalescence, a tensile crack (11) appears in the ROI and suddenly crosses the interface

with an offset of 0.87mm. Also, a coplanar shear crack (12) originates at the inside tip of the bottom flaw, instantly crosses the interface, and propagates towards the outside tip of the upper flaw.

3.2.4.13 Specimen with geometry 2aa30° with smooth interface ($\phi=35^\circ$) inclined 80° with the loading direction

Fig. 3.22 provides snapshots of the crack behavior observed on the surface of the specimen with an unbonded smooth interface, at different loading stages. As observed in Fig. 3.6 (a), crack initiation takes place near the inside tip of the bottom flaw at 11.14 MPa (a tensile crack marked as 1 in the figure). In Fig. 3.22 (b), one can observe that this tensile crack (1) does not propagate with further loading. Also, a tensile crack (2) is originated at the interface at 13.11 MPa, and propagates towards the outside tip of the bottom flaw. In addition, a tensile crack (3) initiates at the outside tip of the bottom flaw and a tensile crack (4) originates in the middle of the upper flaw and propagates towards the interface. An oblique shear crack (5) that originated at the inside tip of the bottom flaw at 13.7 MPa reaches the interface at 14.09 MPa (See Fig. 3.22 (c)). In Fig. 3.22 (e), with further loading, it is possible to notice that the shear crack (5) reaches the interface, crosses the interface at 18.06 MPa with an offset of 1.56 mm, and continues to propagate in the loading direction; this is denoted as crack (8) in the figure. New tensile cracks originate at the interface at around 25.41MPa; these are cracks (9) and (10). Also, an oblique shear crack (11), originates at the outside tip of the upper flaw at 26.69 MPa, and propagates towards the interface. At this point, the tensile crack (4) is arrested at the interface. In Fig. 3.22 (f), new tensile cracks (12) and (13) are originated at the interface at 27.02 MPa and 29.82 MPa, respectively. Cracks (5) and (11) ultimately produce coalescence at 30.86 MPa.

3.2.4.14 Specimen with geometry 2aa30° with rough interface ($\phi=50^\circ$) inclined 80° with the loading direction

The specimen has an unbonded rough interface inclined 80° with the loading direction. Figure 3.23 depicts the cracking process during loading. The first crack initiated at the outside tip of the bottom flaw at 10.06 MPa (marked as 1) (Fig. 3.23 (a)). As depicted in Fig. 3.23 (b), this crack (1) propagates with further loading and is identified as tensile. At 11.24 MPa, a tensile crack (2) initiates in the middle of the bottom flaw. Also, tensile cracks (3) and (4) initiate from both tips

of the upper flaw at around 14.78 MPa. At this point, tensile cracks (5), (6), (7) and (8) originate at the interface. In Fig. 3.23 (c), one can observe that most cracks propagate with loading, i.e. (1), (3), (5), (6) and (8), while others seem insensitive to the load, e.g. they arrest. This is the case for cracks (4) and (7). The figure also shows new cracks: crack (9), a tensile crack, at the interface, originates at 17.73 MPa and propagates towards the inside tip of the upper flaw; crack (10), also a tensile crack, originates at the interface at that same load and propagates towards the outside tip of the bottom flaw; crack (11), also tensile, starts from the interface at 24.44 MPa; and finally, crack (12), tensile, is observed at the inside tip of bottom flaw at 24.67 MPa. In Fig. 3.23 (d), it is possible to observe an oblique shear crack (13) that originates at the inside tip of the bottom flaw, which occurs at 26.34 MPa. One can also notice the initiation of a tensile crack (14) near the middle of the upper flaw at 27.63 MPa and two tensile cracks (15) and (16) at the interface, at 28.05 MPa and 29.49 MPa, respectively. Most of the cracks propagate with the load. Coalescence is produced by the linkage of crack (12), from the bottom flaw, propagating across the interface as crack (17) and reaching the upper flaw. Crack coalescence is observed at 32.4 MPa. Crack (12) crosses the interface with an offset of 1.2 mm.

3.2.4.15 Specimen with geometry 2aa30° with smooth interface ($\phi=35^\circ$) inclined 70° with the loading direction

Figure 3.24 provides snapshots of the crack behavior observed on the surface of a specimen with geometry 2aa30° containing a smooth interface inclined 70° from the vertical, at different loading stages. As observed in Fig. 3.24 (a), crack initiation takes place at the outside tip of the bottom flaw with tensile crack (1) at 10.58 MPa. At 12.96 MPa, tensile cracks (2), (3) and (4) initiate at the other flaws tips. In Fig. 3.24 (b), one can observe the initiation of a tensile crack (5) at the interface when the load reaches 15.31 MPa. Shortly after, at 15.58 MPa, another tensile crack (6) appears at the interface. Crack (5) reaches the inside tip of the bottom flaw at 20.08 MPa. Later on, at 21.11 MPa, two other tensile cracks (7) and (8) are spotted at the interface (See Fig. 3.24 (c)). Crack (7) reaches the inside tip of the upper flaw at 22.76 MPa. At 25.77 MPa, a coplanar shear crack (9) initiates at the inside tip of the bottom flaw, reaching the interface at 26 MPa and crossing it at 26.56 MPa, without offset. (See Fig. 3.24 (d)). In Fig. 3.24 (e), one can observe two other tensile cracks (10) and (11) originating at the interface. Finally, coalescence occurs through the connection of cracks (5) and (11) at 29.43 MPa.

3.2.4.16 Specimen with geometry 2aa30° with rough interface ($\phi=50^\circ$) inclined 70° with the loading direction

Figure 3.25 depicts the crack behavior observed on the surface of a specimen with geometry 2aa30° containing a rough interface inclined 70° with the vertical, at different loading stages. Crack initiation occurs at 9.94 MPa with tensile cracks (1) and (2) initiating at the outside tip of the upper and bottom flaw, respectively (See Fig. 3.25 (a)). At 10.35 MPa, tensile crack (3) appears at the length of the bottom flaw. Shortly after, at 12.78 MPa, tensile crack (4) originates at the inside tip of the upper flaw. With further loading, tensile cracks can be spotted originating at the interface: crack (5) at 13.72MPa and crack (6) at 16.08MPa. In Fig. 3.25 (b), one can observe that two other tensile cracks (7) and (8) initiate at the interface, under a compressive loading of 16.67 MPa. Tensile cracks (9) and (10) appears at the interface, respectively, at 18.33 MPa and 20.38 MPa. Crack (6) reaches the inside tip of the bottom flaw at 20.21 MPa, and crack (7) reaches the inside tip of the upper flaw at 21.78 MPa, which can be seen in Fig. 3.25 (c). Coalescence takes place at 29.94 MPa through cracks (6), (10) and (11).

3.2.5 Analyses of the results

3.2.5.1 Crack initiation stress

The initiation stresses of specimens with and without interface are tabulated on Tables 3.2 and 3.3. It is possible to observe that the specimens without interface present higher initiation stress values than those with interface. This may indicate that the presence of interface in the specimens reduces crack initiation stress.

Figure 3.26 is a plot of crack initiation stresses originated from flaws (i.e. only tensile cracks initiated at the tips) from the 16 different types of specimens with interface that were tested (i.e. specimens with different interface roughness, interface inclination angle and flaw geometries), including the repeatability tests. The crack initiation stresses obtained from the tests, when compared with the repeatability tests, are within errors of 15%. The figure shows that the specimens with a smooth interface presented a crack initiation stress higher than the specimens with a rough interface. It is important to mention that specimens with a horizontal interface (i.e. 90° from the vertical) presented higher magnitudes of crack initiation stresses than those with an

inclined interface (i.e. 80° and 70° from the vertical). This may indicate that the increase of both roughness and inclination of an interface reduce crack initiation stress.

Regarding whether the variation in roughness or inclination of the interface facilitated the initiation of cracks at the interface, it is possible to observe in sections 3.2.4.1 – 3.2.4.16 that no trend was detected in the initiation stress of the first crack originated at the interface from all the specimens tested.

3.2.5.2 *Interaction between cracks and the interface*

Tensile cracks are always the first cracks to appear in the experiments, and start at the tip or near the tip of the pre-existing flaws or at the interface. In contrast to the experiments without interface (See Fig. 3.7 - 3.9) that showed that the flaws are the most important source for new cracks, the experiments with an interface (See Fig. 3.10 – 3.25) indicate that the interface itself is an important contributor to new cracks. While the type of cracks that initiate from a flaw can be tensile or shear, those observed in the experiments emanating from the interface are all tensile.

As depicted in Table 3.4, which is a list of the smallest angle between the cracks initiated at the interface and the interface plane, for all types of specimen tested, changes in interface roughness or inclination angle do not seem to affect the angles at which cracks initiate at the interface. For the majority of the specimens tested, such angles ranged from 70° to 90° .

One can also observe in Fig. 3.10 – 3.25 that there is no trend in the number of cracks initiating at a smooth or rough interface, meaning that the interface roughness does not seem to affect the production of cracks. The same conclusion is reached for specimens with different interface inclination angles, since no trend was found between the interface inclination and the number of cracks initiating at the interface.

Table 3.5 shows the angle at which tensile and shear cracks reach the interface and how those cracks interact with the interface (i.e. whether they arrest or cross the interface). This angle is the smallest angle between the interface plane and the incident crack path. This is called the incident angle, as depicted in Fig. 3.27. The Table shows that tensile cracks that meet the interface at 30° to 60° angle get arrested, while those at or above 70° cross the interface with an offset of 0 – 1.2 mm. Shear cracks that meet the interface at 20° to 63° angles get arrested at the interface, while those at or above 70° cross the interface with an offset in the range of 0 – 1.76 mm. It is relevant to mention that this observation is independent of the roughness or inclination of the

interface. These results are similar to the findings obtained by Roy Xu et al. (2003), where they observed that the angle between the incident crack plane and the interface affects whether an incident crack will penetrate an interface or be arrested.

3.2.5.3 Coalescence

Coalescence stresses of specimens with and without interface are tabulated in Tables 3.2 and 3.3. For specimens with geometry 2aa30° and 3a030°, the presence of the interface leads to a decrease of the crack coalescence stress. However, this is not the case for specimens with geometry 0-2a30°. It seems that the effect of an interface, on crack coalescence, depends on flaw geometry, interface roughness and interface inclination angle.

Fig. 3.28 shows crack coalescence stresses in all specimens tested with an interface. The results do not show any trend with the change in interface roughness or interface inclination. Tables 3.2 and 3.3 also indicate that the presence of the interface does not induce any trend in the coalescence stress.

Table 3.6 shows the coalescence patterns observed on the specimens tested with an interface and Table 3.7 presents the coalescence patterns on specimens without interface. It is possible to observe that the presence of interfaces causes the number of cracks that produce coalescence to increase when compared to specimens without interface.

An important difference between crack behavior between specimens with and without interface is that the presence of the interface leads to different crack coalescence patterns. Another relevant observation is that the variation in interface inclination angle and roughness may change the location where the cracks that produce coalescence originate. For example, in specimens with geometry 2aa30° with rough interface inclined 90° from the loading direction (See Type 12 – Table 3.6), coalescence is produced by two tensile cracks that both originate at the interface and propagate towards the outside tip of the upper flaw and to the inside tip of the bottom flaw, respectively. When the interface inclination is changed to 80° from the loading direction (See Type 14 of Table 3.6), coalescence occurs by a tensile crack that originates at the inside tip of the bottom flaw that crosses the interface with an offset of 1.2 mm and reaches the upper flaw near its middle. One can also notice that in specimens with geometry 3a030° with a smooth interface inclined 80° from the vertical (See Type 7 – Table 3.6), coalescence occurs when a tensile crack initiated at the interface connects with an oblique shear crack above the interface while a shear crack originated

at the tip of the bottom flaw reaches the interface. When the interface roughness is increased (See Type 8 – Table 3.6), coalescence occurs when a tensile crack initiated at the interface connects with an oblique shear crack above the interface and, at the same time, another tensile crack initiated at the interface links with an oblique shear crack below the interface.

In the cases with a left-stepping geometry, it is possible to observe that a rougher interface prevented coalescence. This can be seen by comparing coalescence type 1 with 2 or type 3 with 4 in Table 5.6.

However, the cases with overlapping and right-stepping geometries promoted the same trend in coalescence patterns: coalescence in tension was favored by both the increase in roughness and in inclination of the interface (from horizontal to 70° from the vertical) in a smooth interface. The first can be observed in Table 5.6 by comparing coalescence type 5 with 6, 7 with 8, or 9 with 10 for the right-stepping geometry; and type 11 with 12, 13 with 14, or 15 with 16 for the overlapping geometry. The latter by the comparison between coalescence types 5, 7 and 9 for the right-stepping geometry; and between types 11, 13 and 15 for the overlapping geometry.

3.2.5.4 General observations

After comparing and analyzing the results obtained from specimens with different flaw geometries with and without an interface (See Fig. 3.17 – 3.25), it is possible to make the following general observations:

1. The interface itself is an important contributor to new tensile cracks;
2. The presence of interface in the specimens reduces tensile crack initiation stress;
3. An increase in both roughness and inclination of an interface (i.e. from horizontal to 70° from the vertical) reduces tensile crack initiation stress;
4. Changes in interface roughness or inclination angle do not affect the angles at which tensile cracks initiate at the interface. The angle of initiation ranged from 70° to 90° ;
5. Tensile cracks that meet the interface at 30° to 60° angle get arrested, while those at angles larger than 70° cross the interface with an offset of 0 – 1.2 mm. Shear cracks that meet the interface at 20° to 63° angles get arrested at the interface, while those at angles larger than 70° cross the interface with an offset range of 0 – 1.76 mm. This behavior is independent of roughness or inclination angle of the interface;

6. The presence of interfaces causes the number of cracks that produce coalescence to increase when compared to specimens without interface, and consequently causes changes in coalescence patterns;
7. Variation in the interface inclination angle and roughness may change the location where cracks that produce coalescence originate.

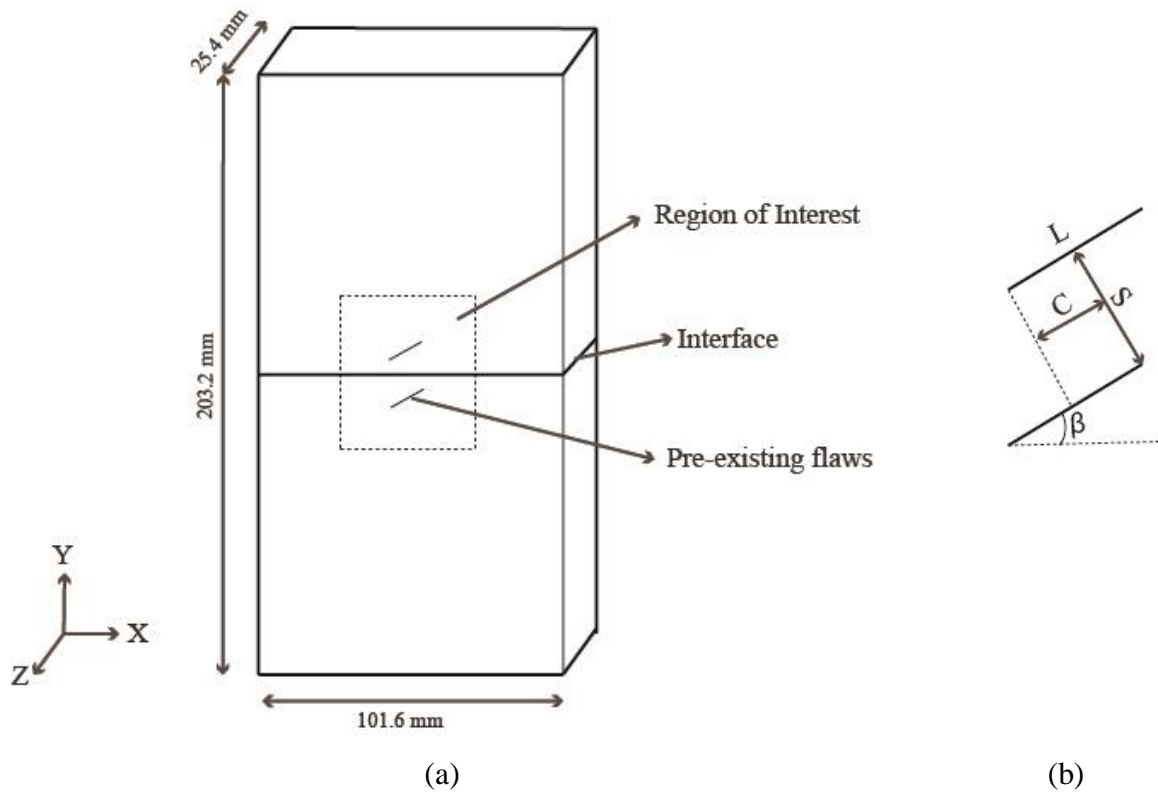


Figure 3.1. Geometry of (a) specimen and (b) flaws.



(a)



(b)



(c)



(d)

Figure 3.2. Preparation of pre-cracked specimens with interface. (a) mold with pvc block; (b) sandpaper attached to block; (c) greased steel shim inserted through one of the PMMA slits; (d) specimen with rough interface.

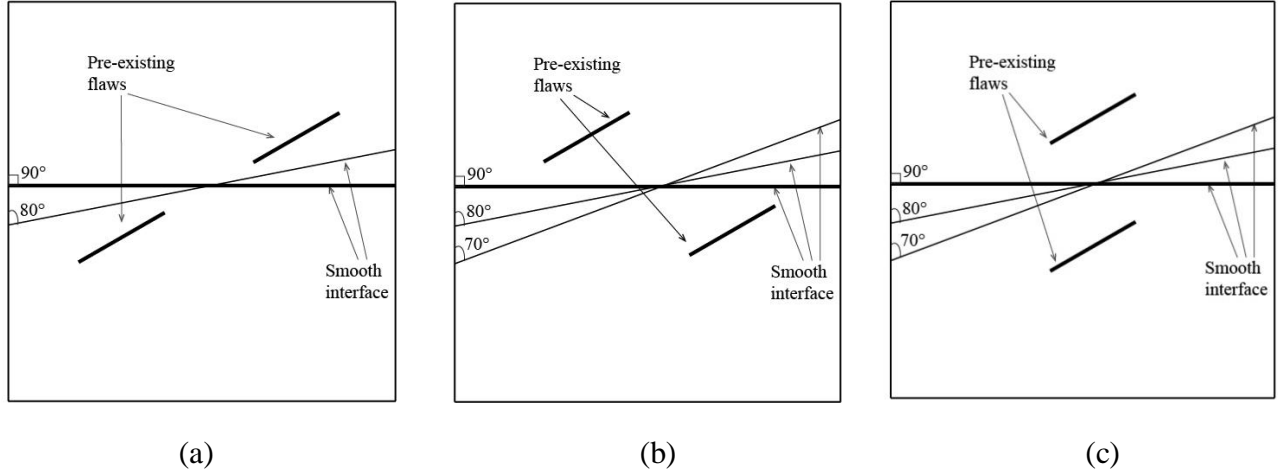


Figure 3.3. Flaw geometries with smooth interface for 70°, 80° and 90° interface inclination angles. (a) $S=0$, $C=-2a$, $\beta=30^\circ$; (b) $S=3a$, $C=0$, $\beta=30^\circ$; (c) $S=2a$, $C=a$, $\beta=30^\circ$.

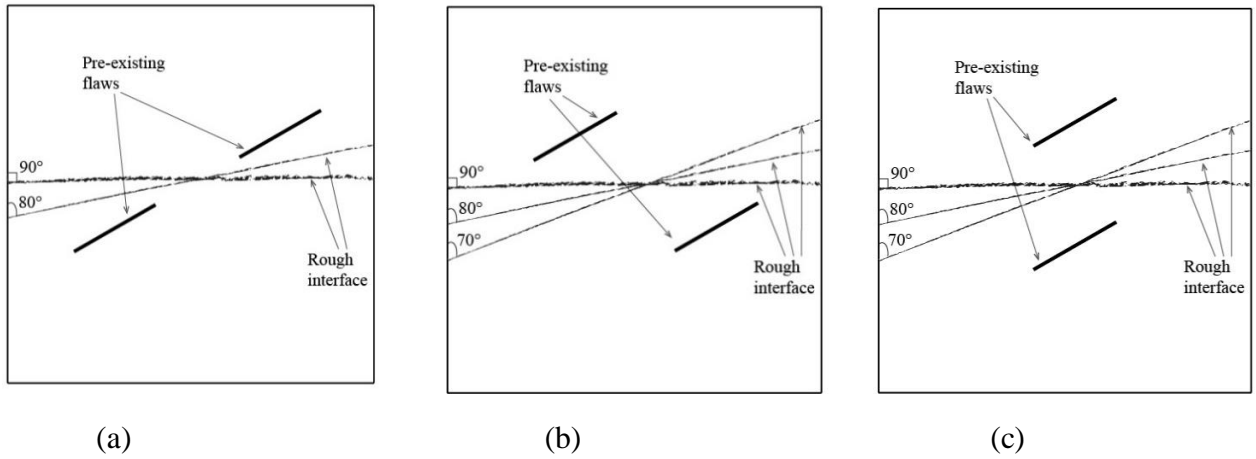


Figure 3.4. Flaw geometries with rough interface (made with sandpaper grit #36) for 70°, 80° and 90° interface inclination angles. (a) $S=0$, $C=-2a$, $\beta=30^\circ$; (b) $S=3a$, $C=0$, $\beta=30^\circ$; (c) $S=2a$, $C=a$, $\beta=30^\circ$.

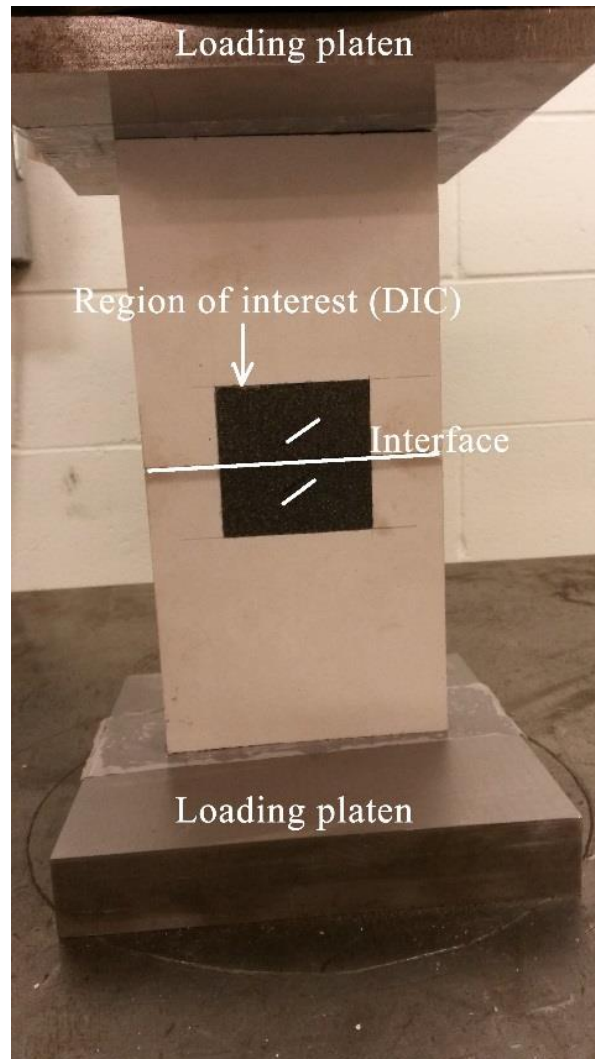


Figure 3.5. Gypsum specimen

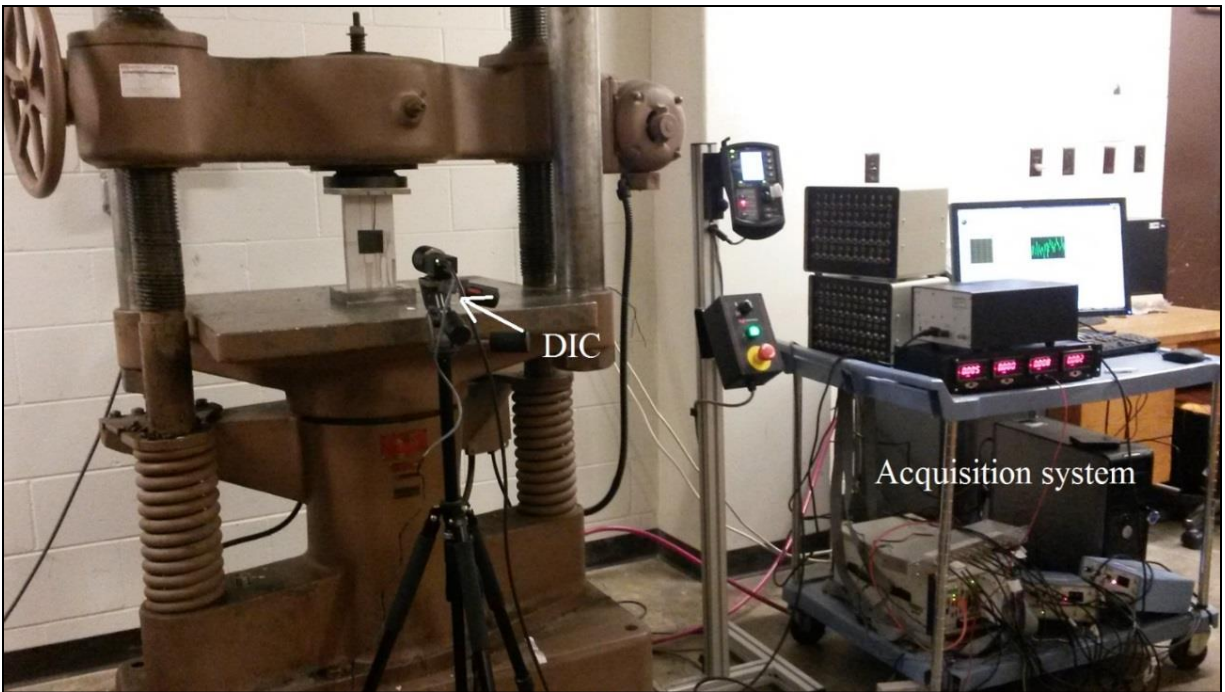
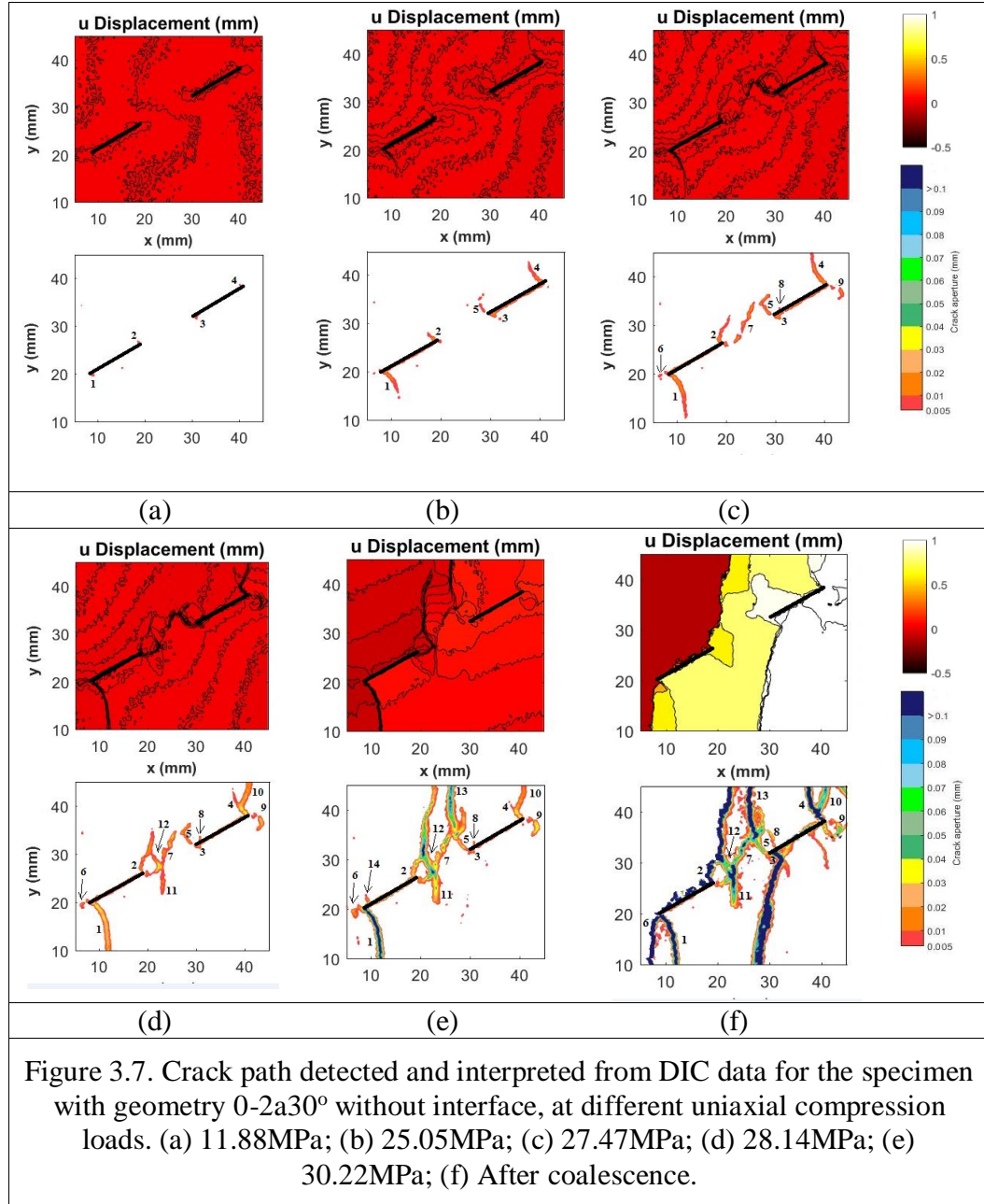


Figure 3.6. Experimental setup



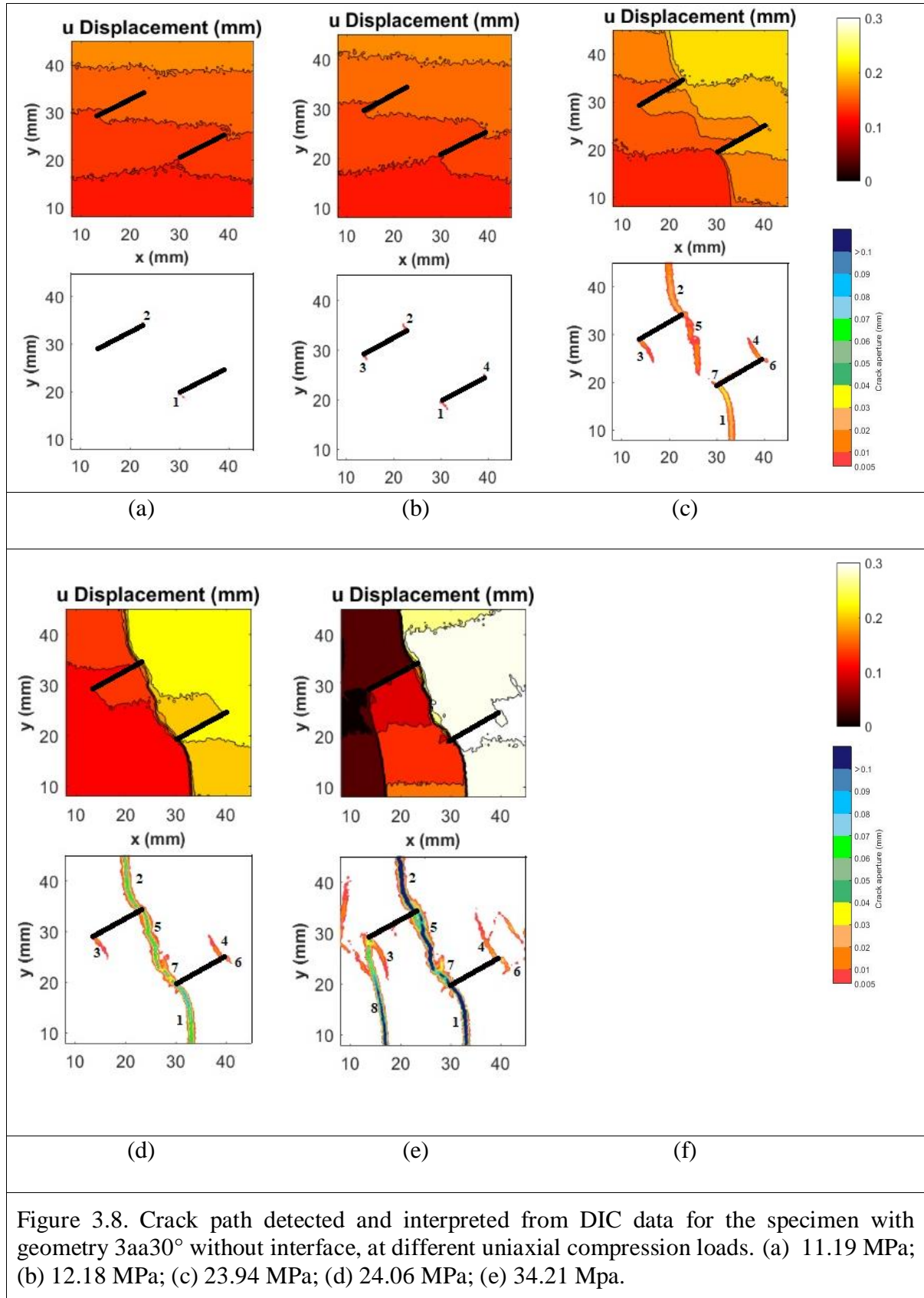
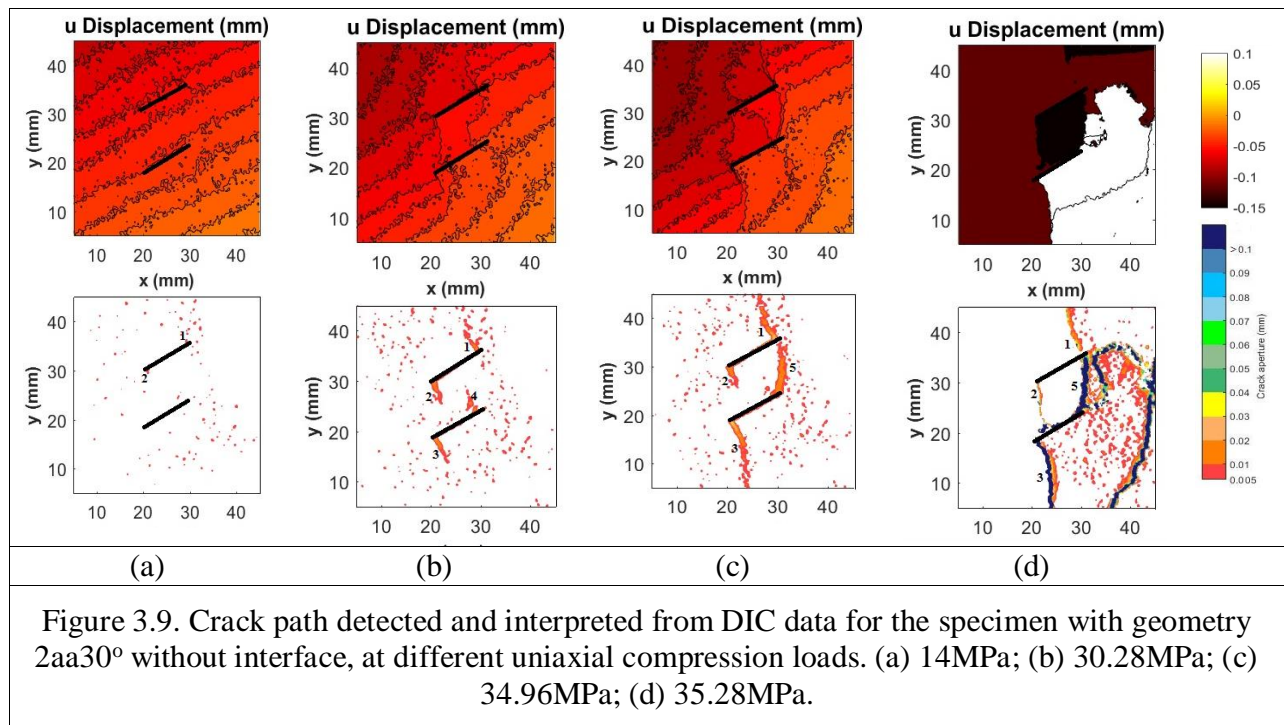
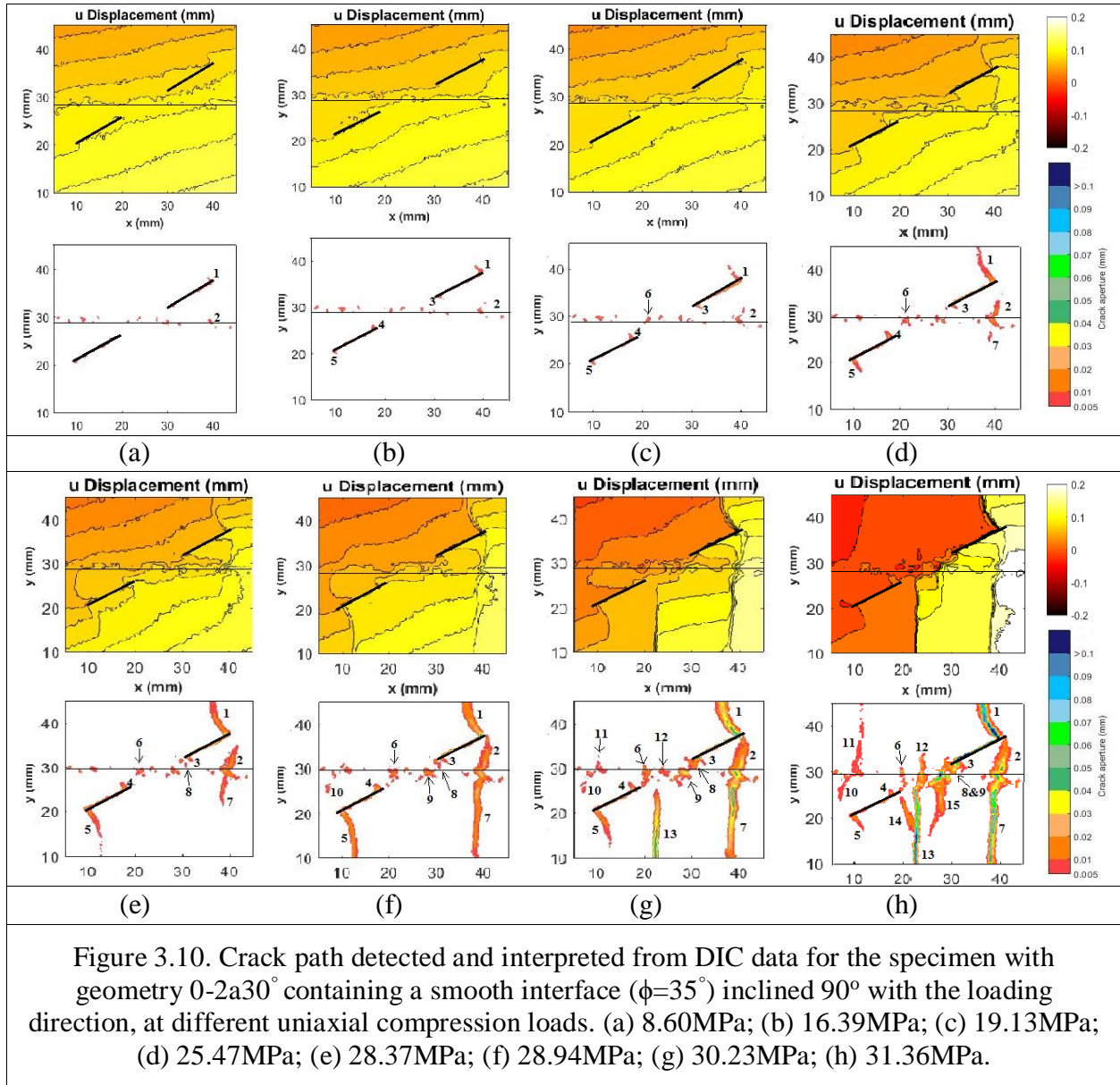
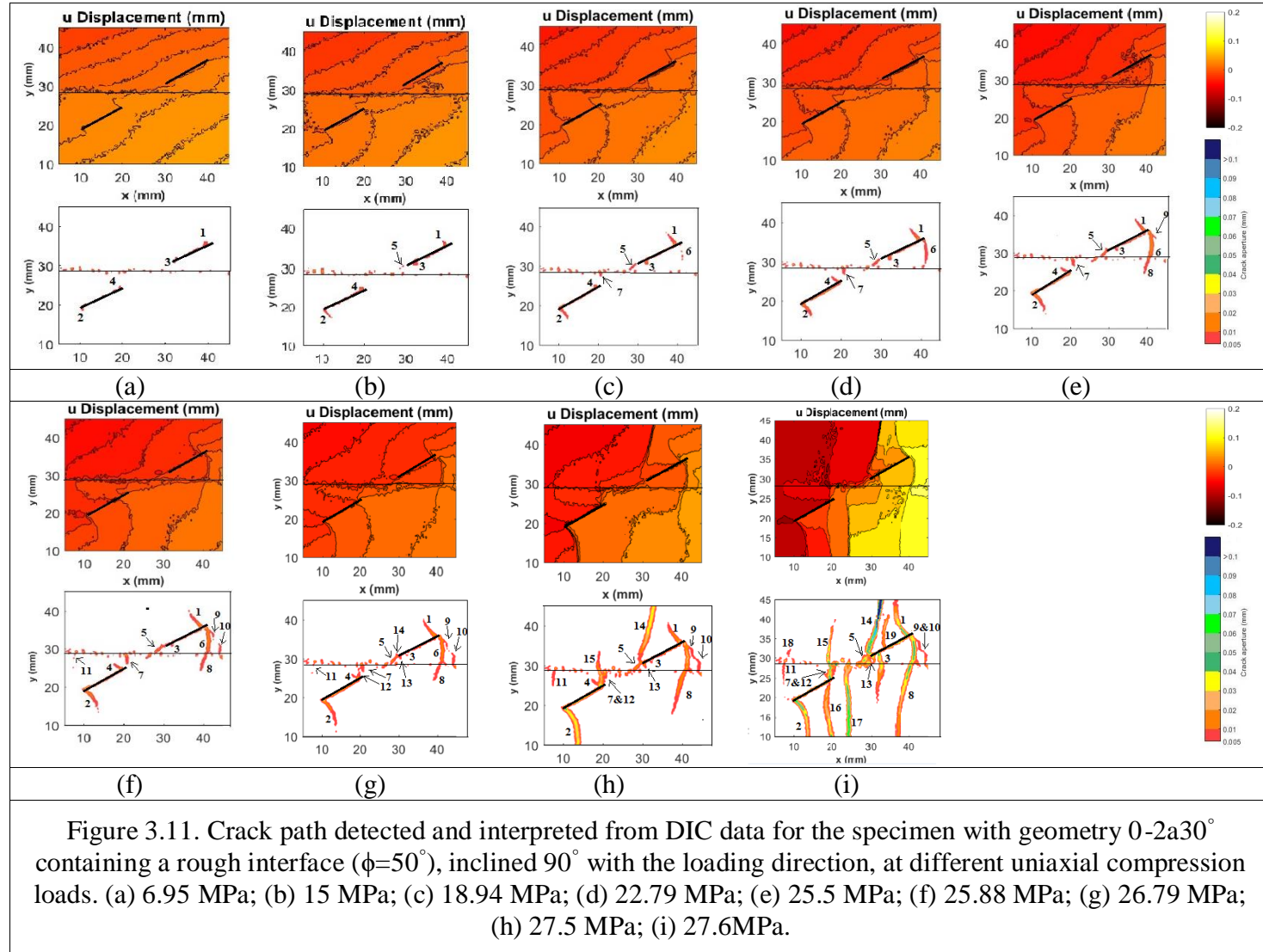


Figure 3.8. Crack path detected and interpreted from DIC data for the specimen with geometry 3aa30° without interface, at different uniaxial compression loads. (a) 11.19 MPa; (b) 12.18 MPa; (c) 23.94 MPa; (d) 24.06 MPa; (e) 34.21 MPa.







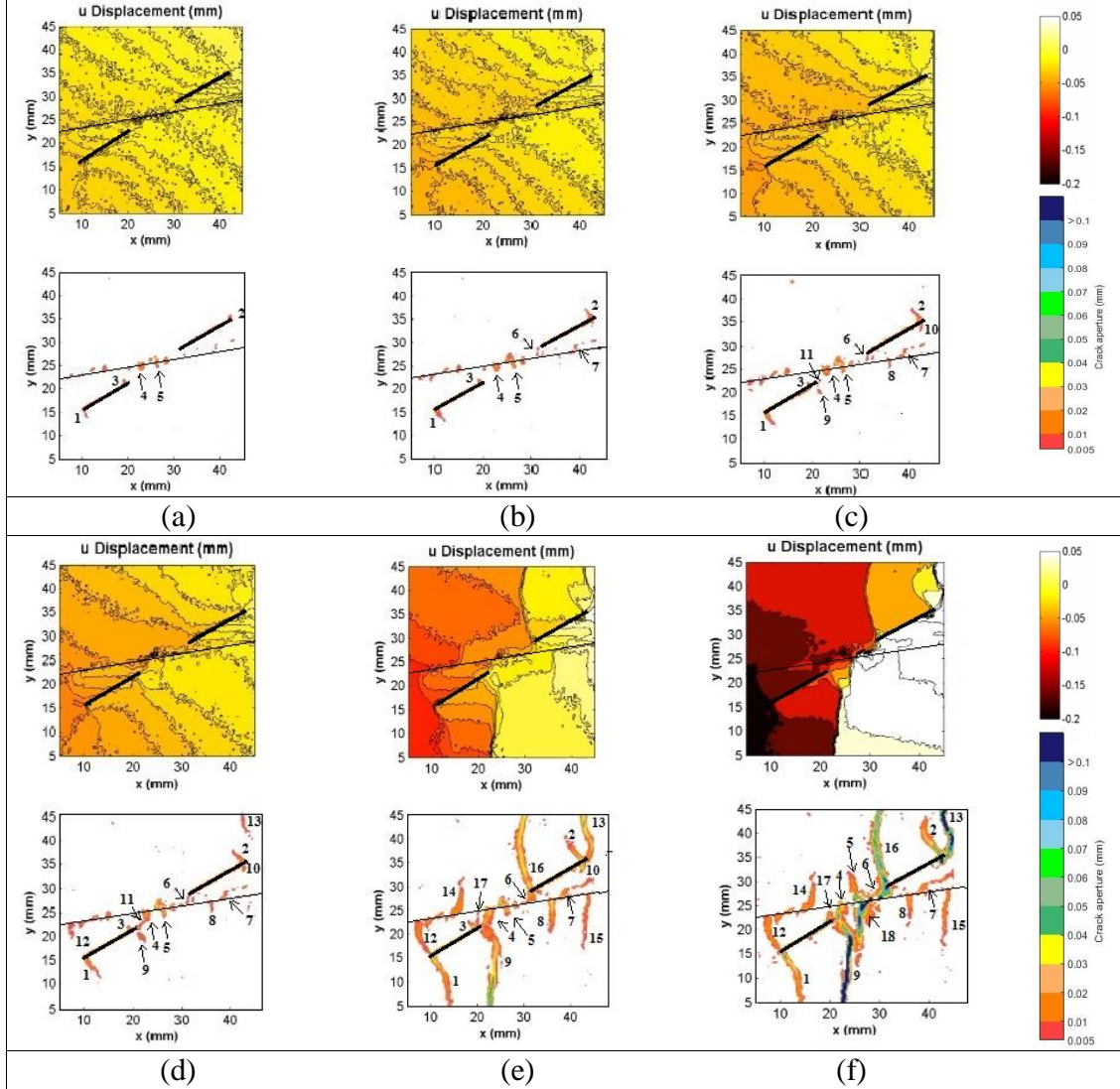
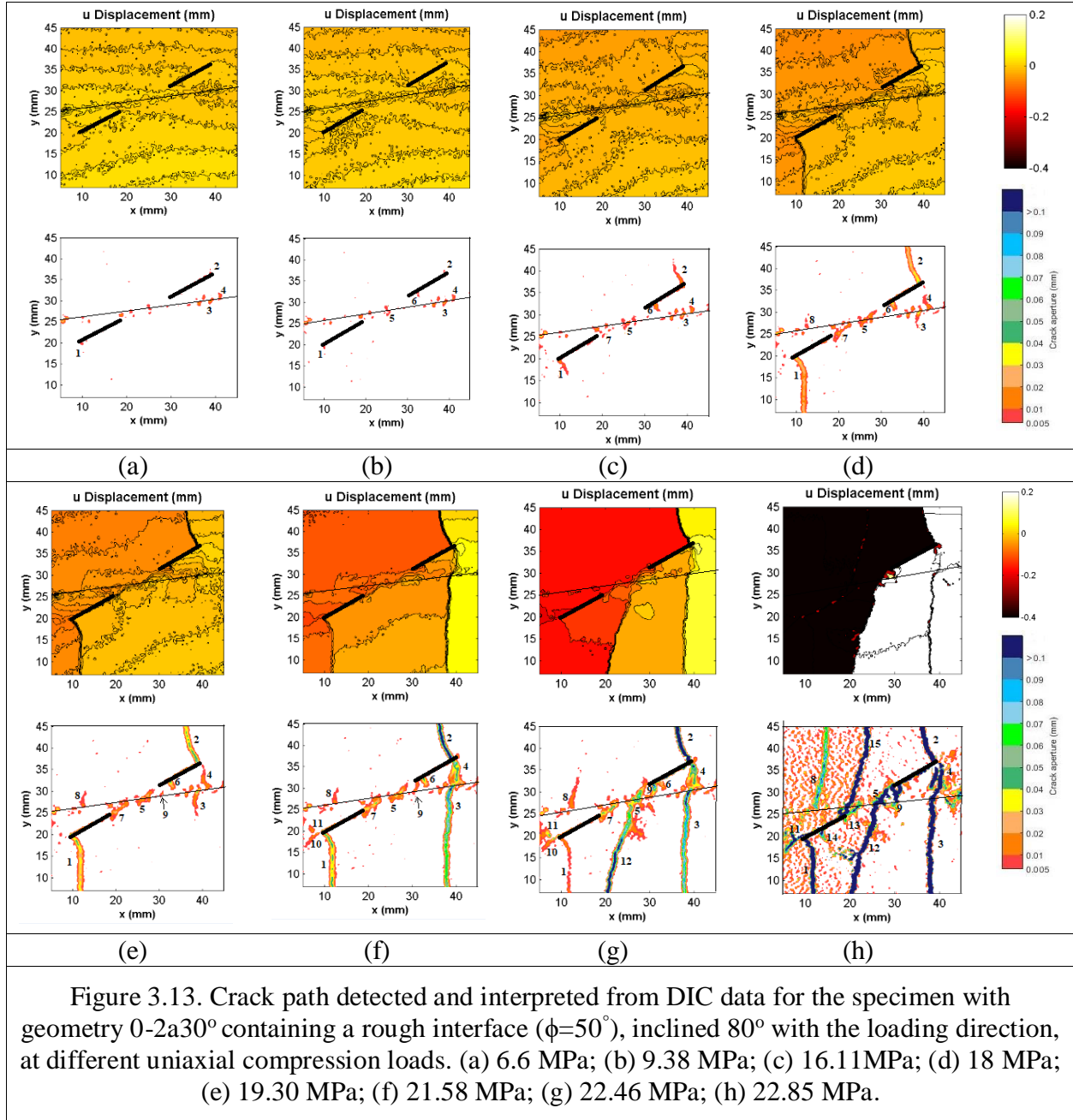
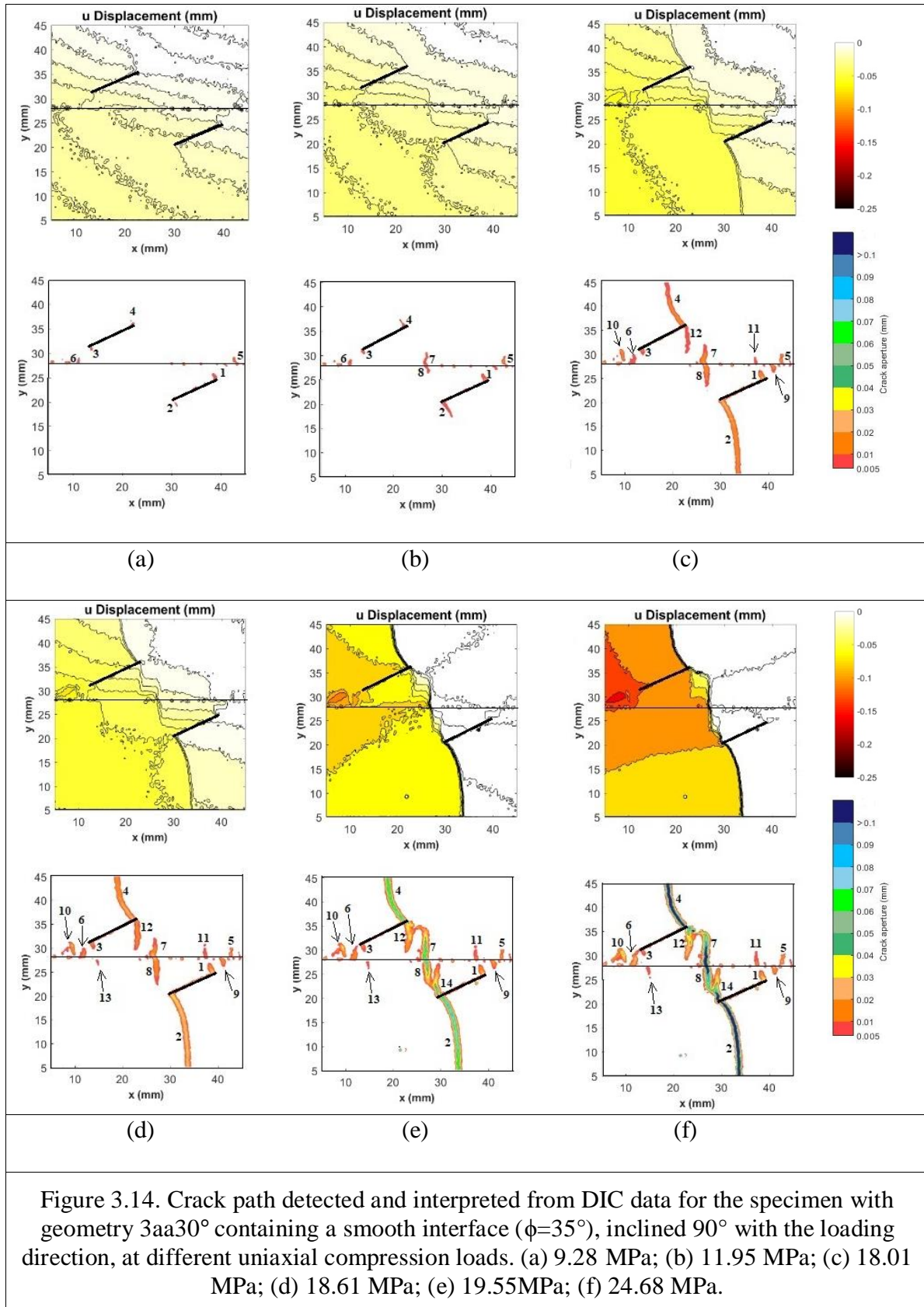


Figure 3.12. Crack path detected and interpreted from DIC data for the specimen with geometry 0-2a30° containing a smooth interface ($\phi=35^\circ$), inclined 80° with the loading direction, at different uniaxial compression loads. (a) 8.5 MPa; (b) 16.98MPa; (c) 20.87MPa; (d) 23.05MPa; (e) 23.92MPa; (f) 23.95MPa.





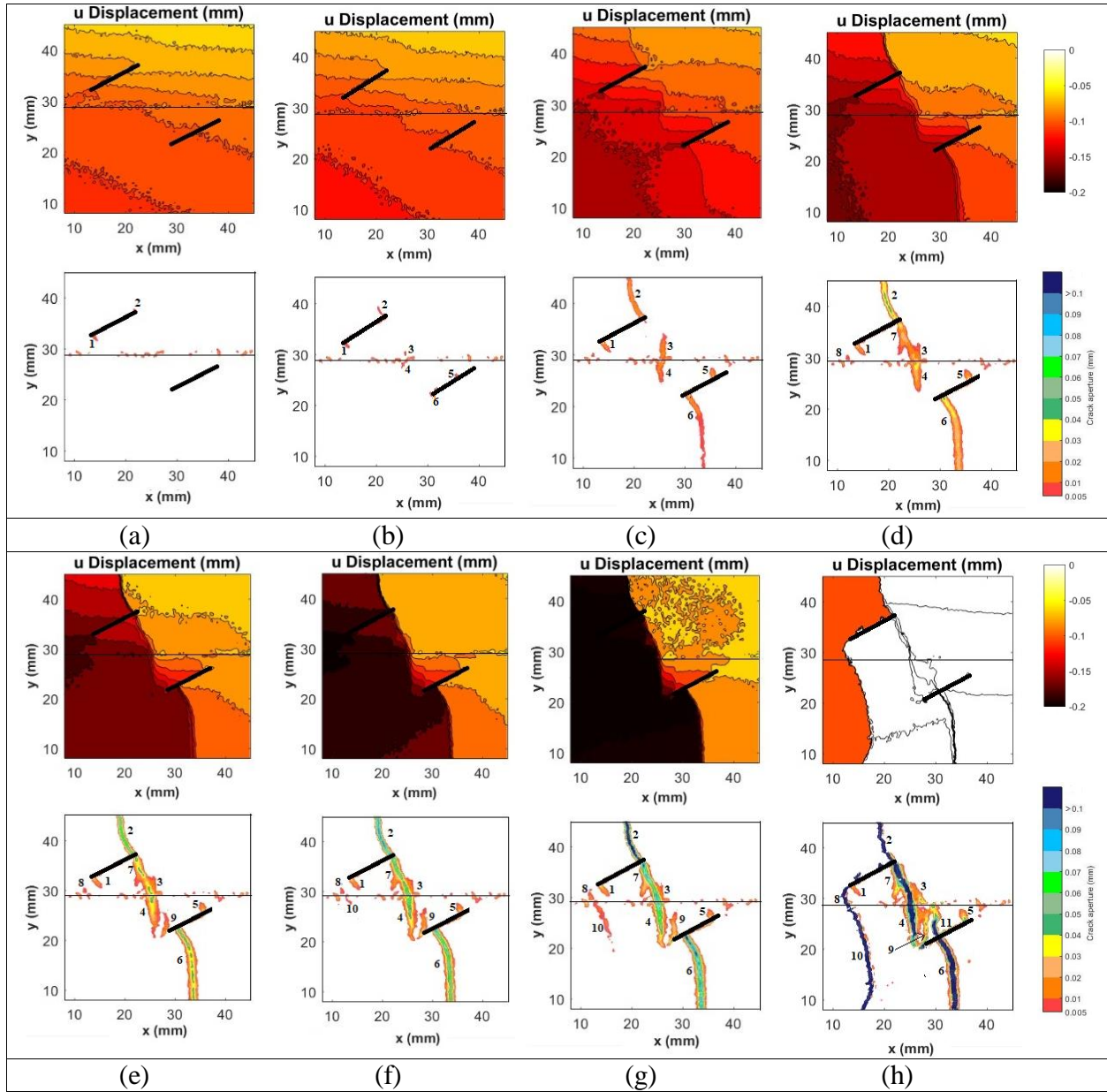
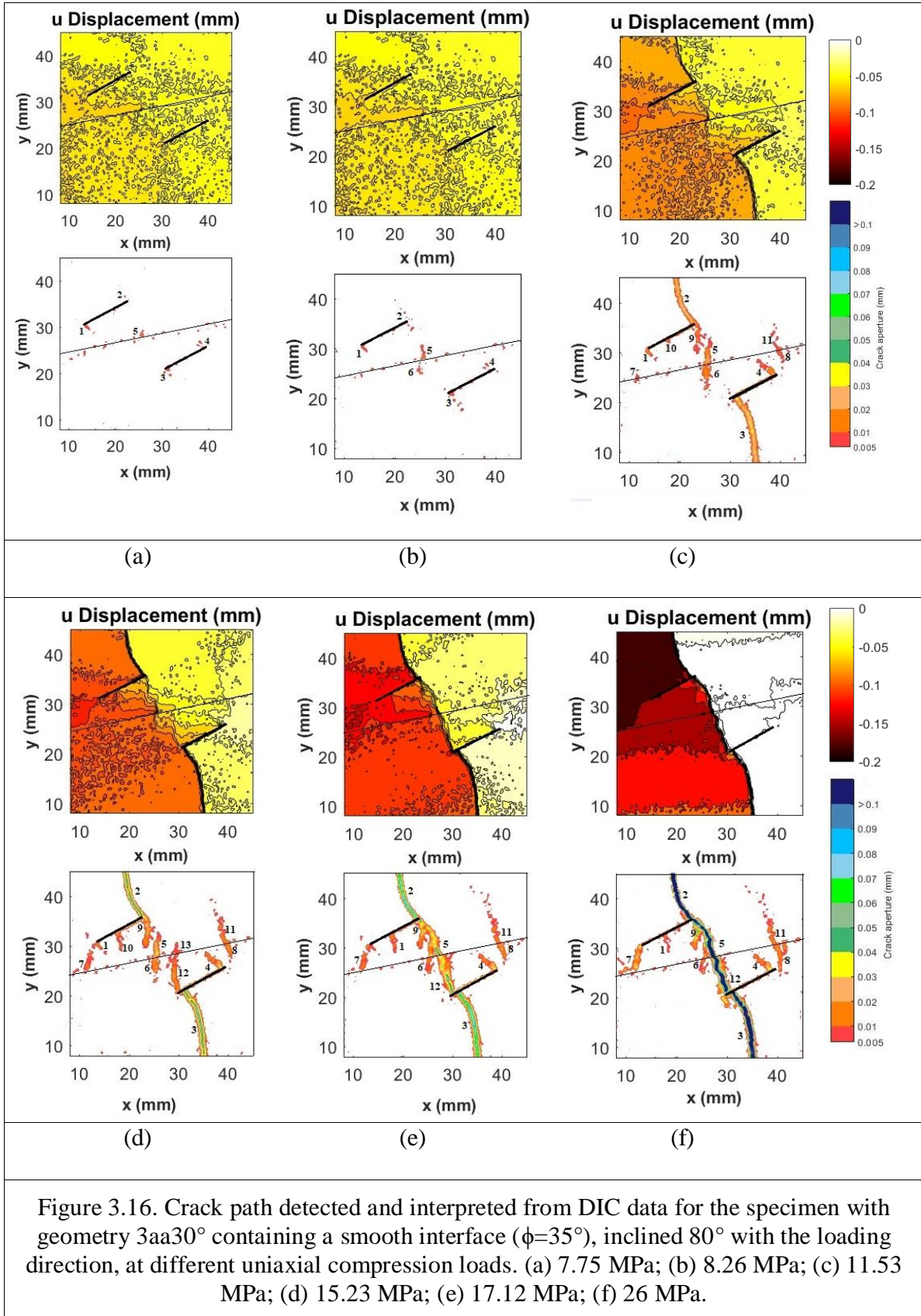
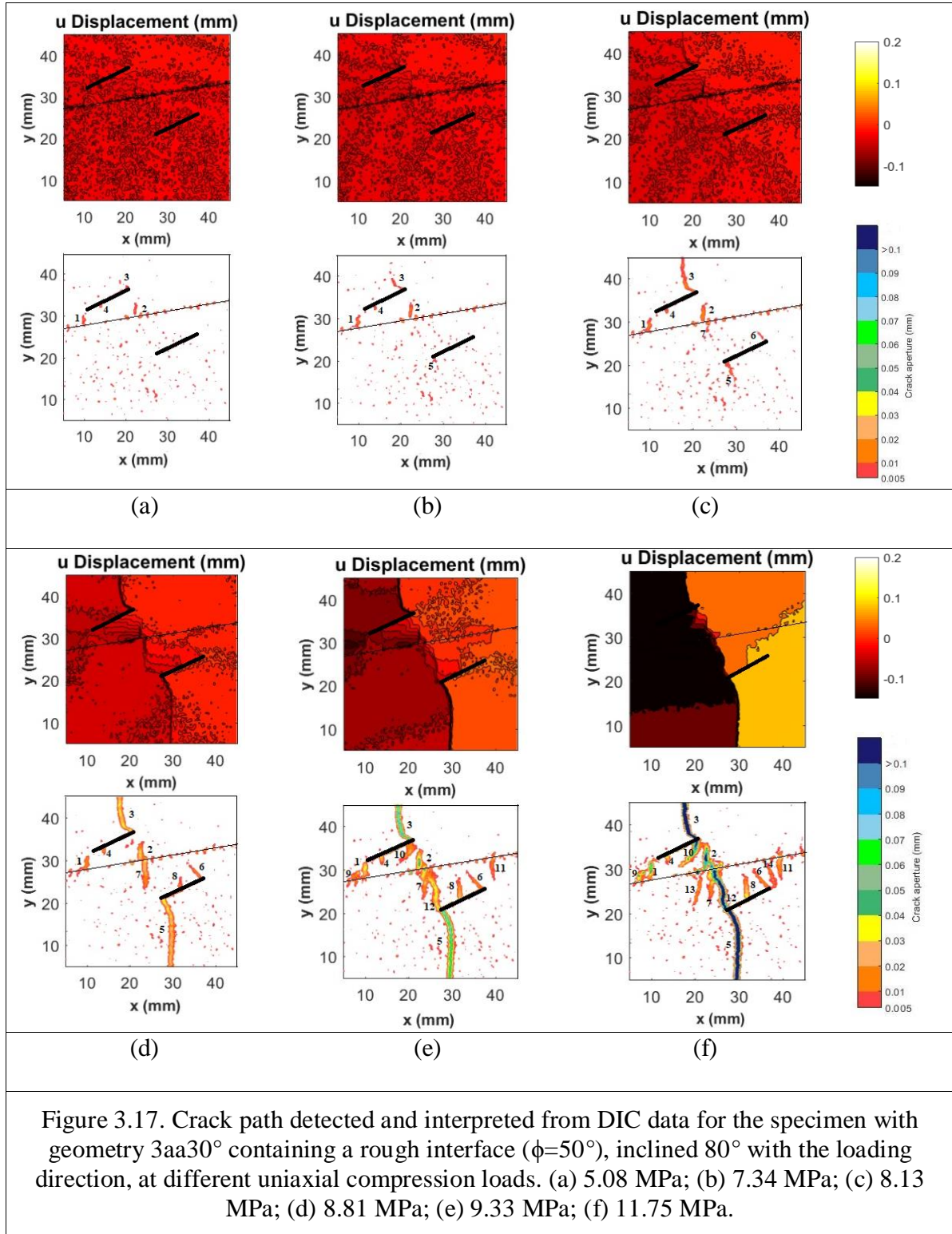


Figure 3.15. Crack path detected and interpreted from DIC data for the specimen with geometry 3aa30° containing a rough interface($\phi=50^\circ$), inclined 90° with the loading direction, at different uniaxial compression loads. (a) 5.45 MPa; (b) 6.78 MPa; (c) 16.14 MPa; (d) 16.15 MPa; (e) 16.29 MPa; (f) 18.06 Mpa; (g) 22.38 MPa; (h) 22.34 MPa.





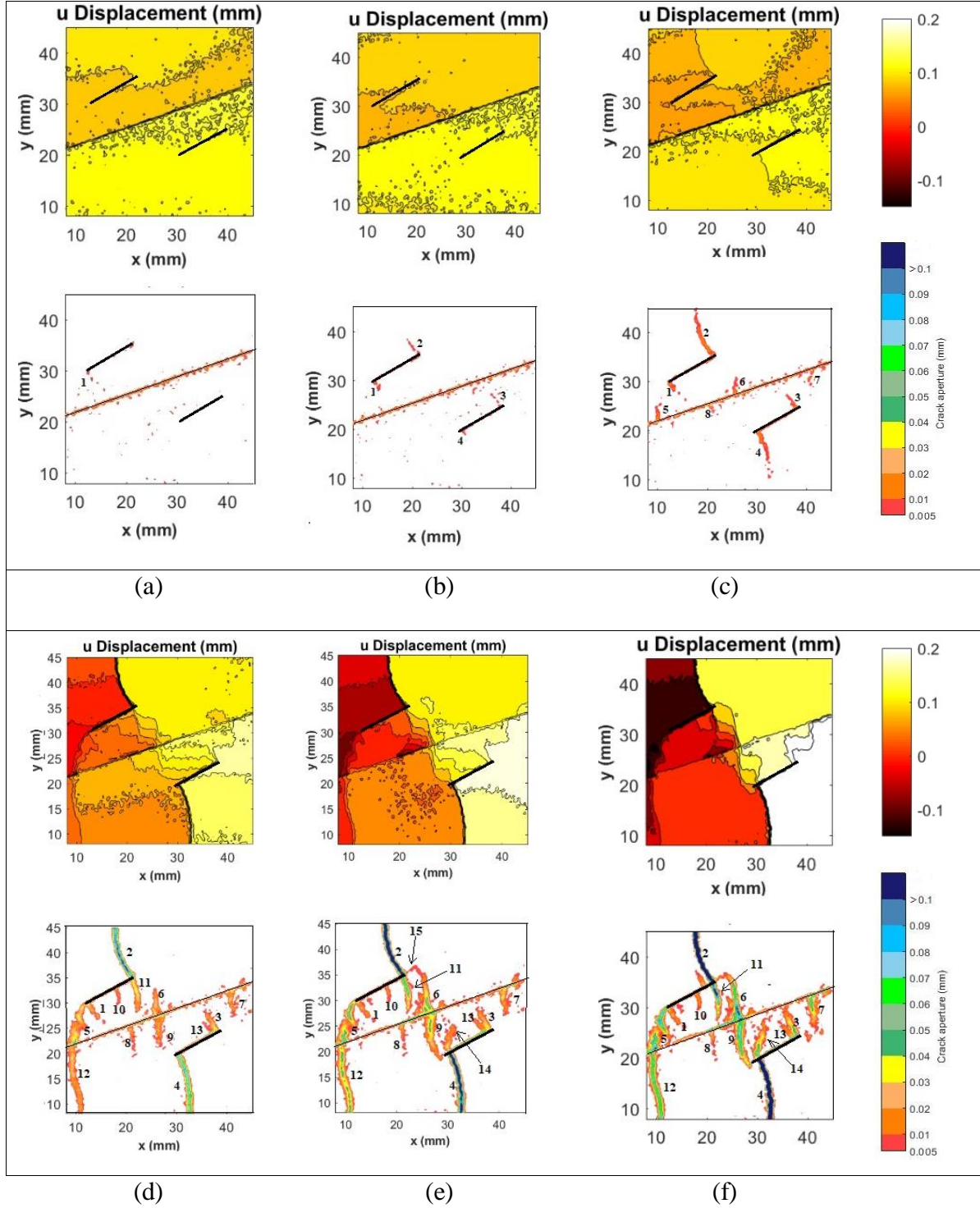


Figure 3.18. Crack path detected and interpreted from DIC data for the specimen with geometry 3aa30° containing a smooth interface ($\phi=35^\circ$), inclined 70° with the loading direction, at different uniaxial compression loads. (a) 6.68 MPa; (b) 9.21 MPa; (c) 10.5 MPa; (d) 10.5 MPa; (e) 11.5 MPa; (f) 14.34 MPa.

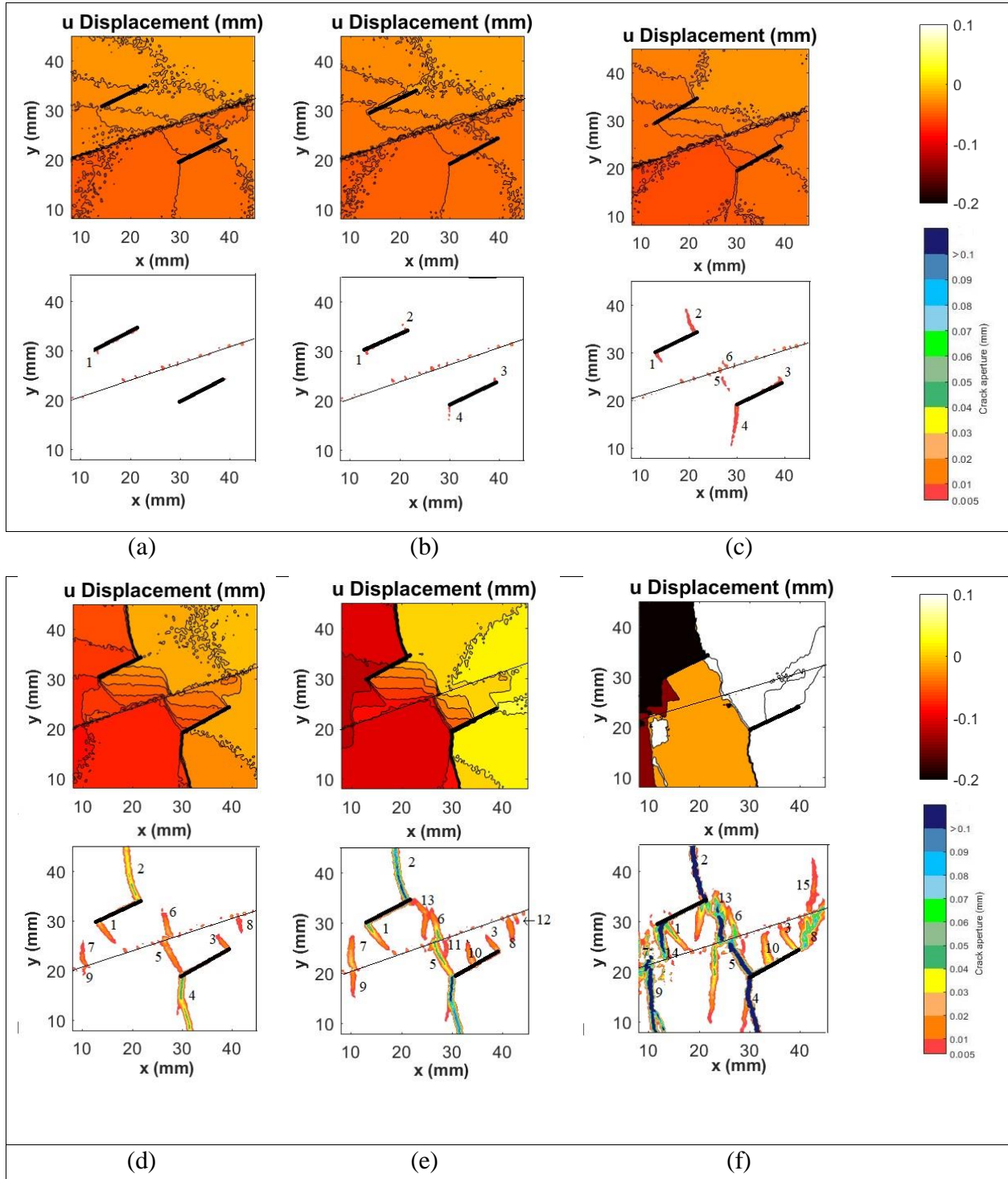


Figure 3. 19. Crack path detected and interpreted from DIC data for the specimen with geometry 3aa30° containing a rough interface ($\phi=50^\circ$), inclined 70° with the loading direction, at different uniaxial compression loads. (a) 5 MPa; (b) 6.06 MPa; (c) 7.73 MPa; (d) 8.11 MPa; (e) 10.58 MPa; (f) 13.56 MPa.

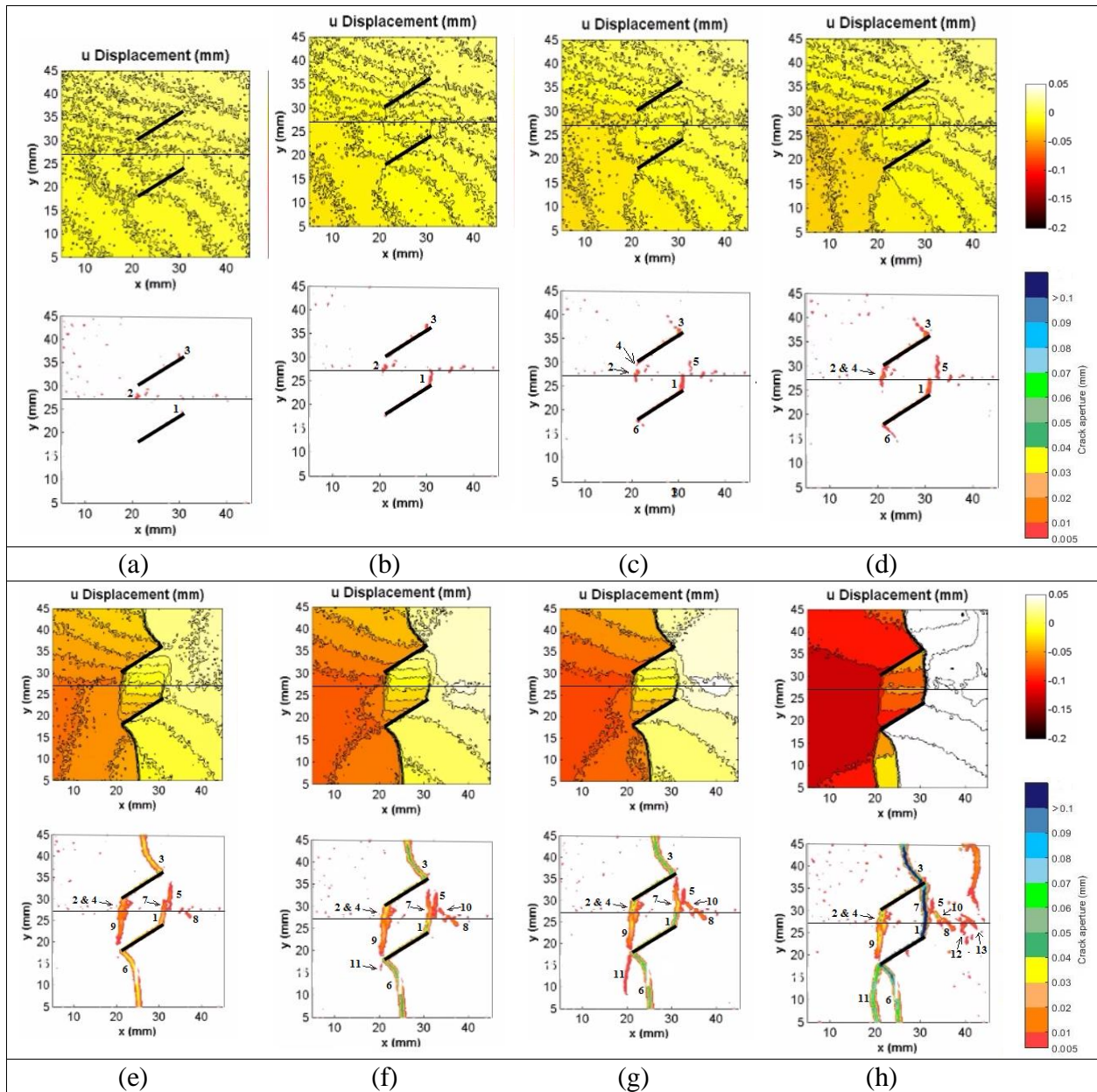
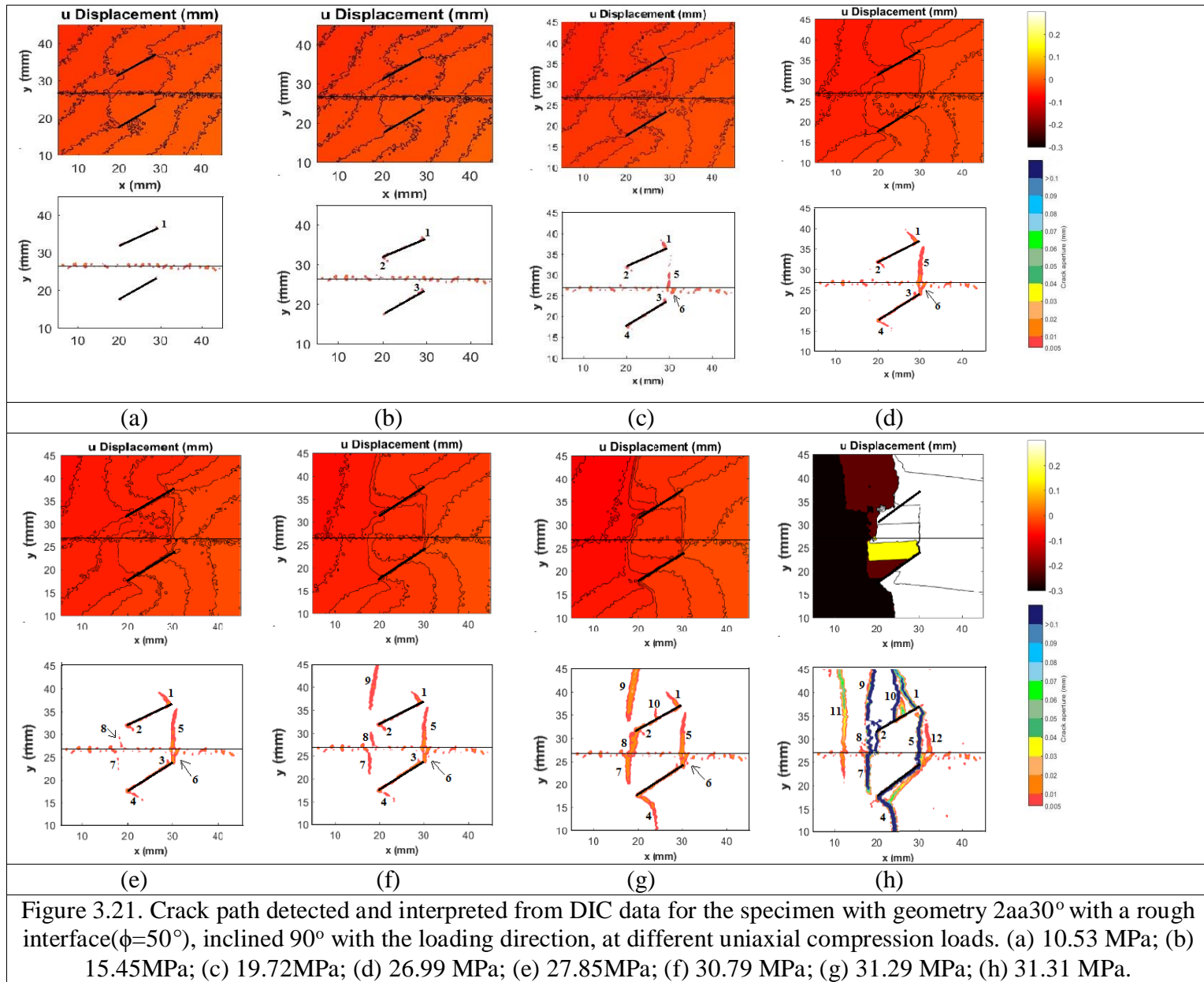
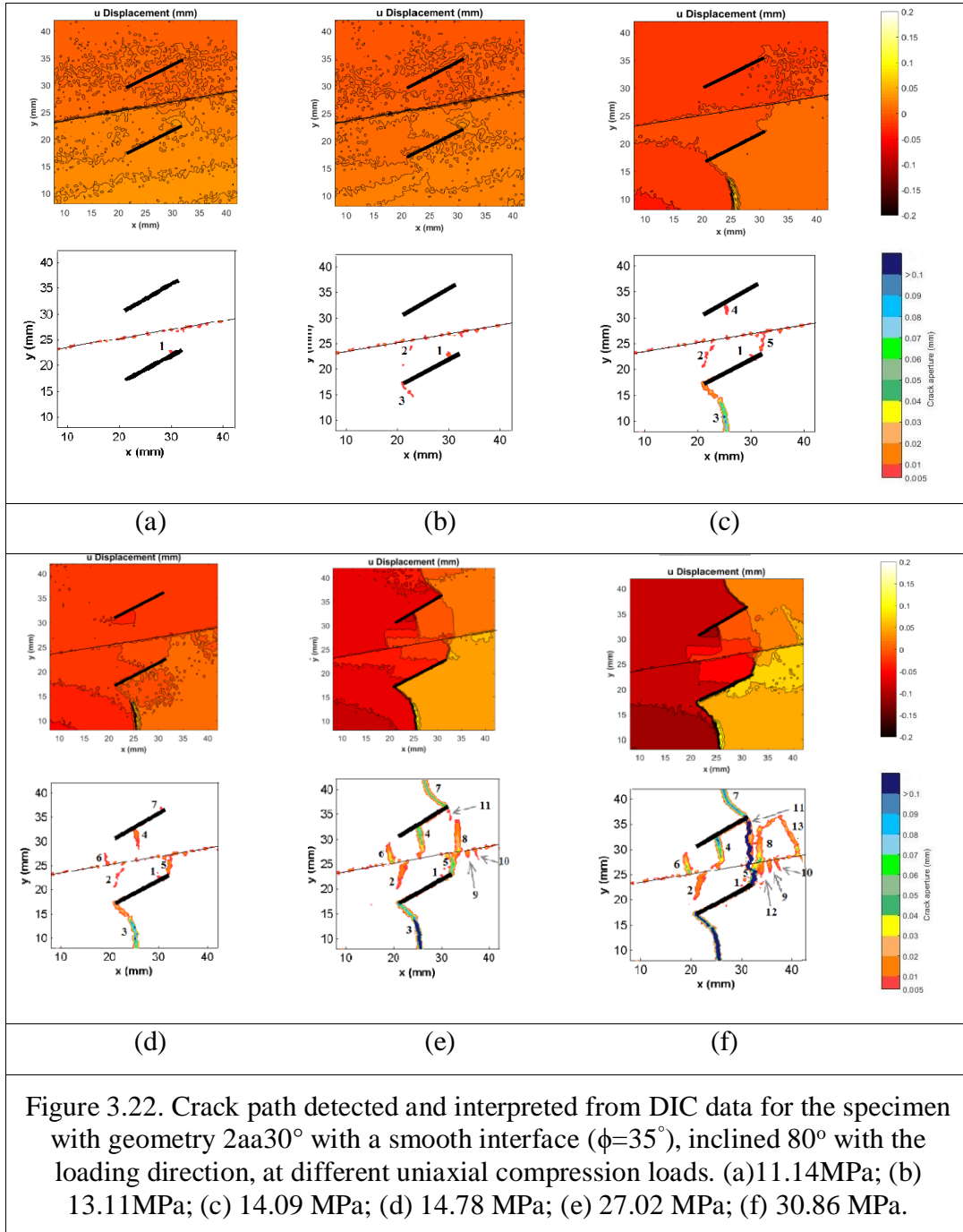
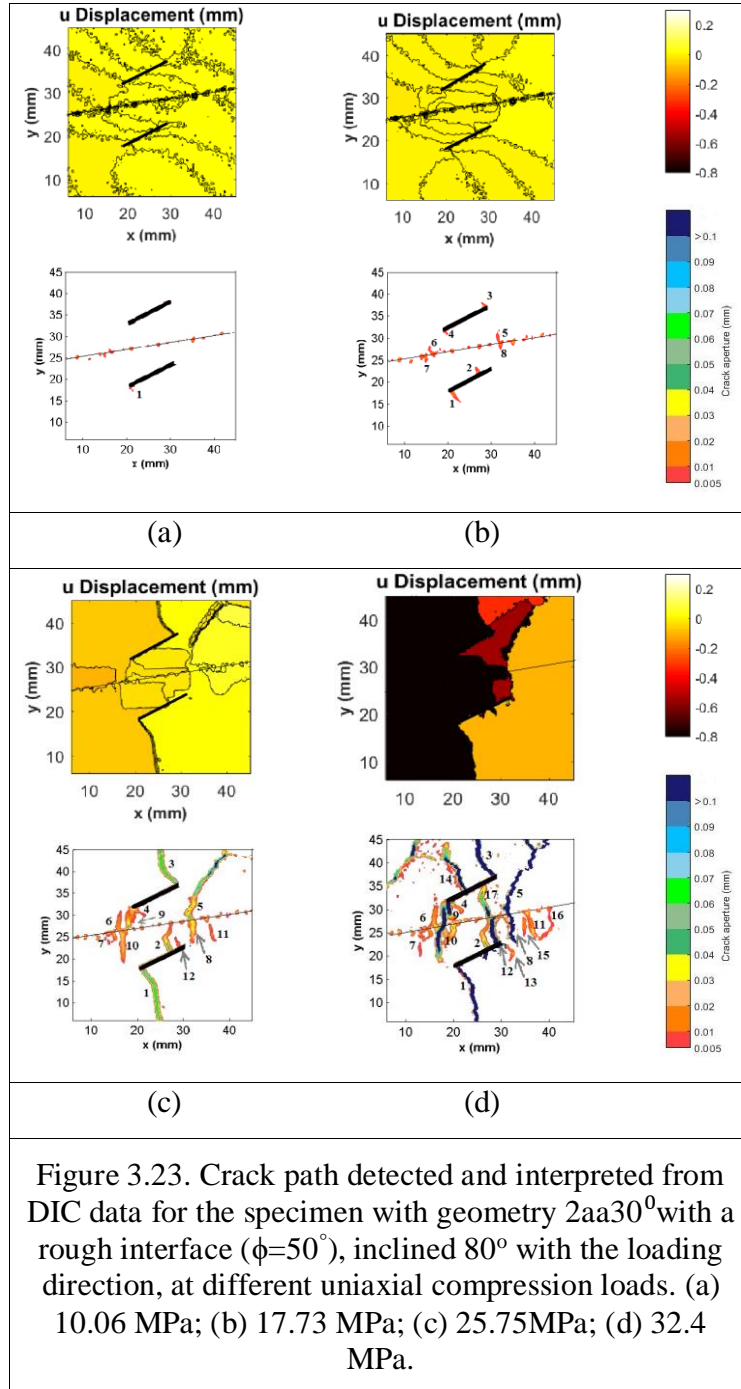


Figure 3.20. Crack path detected and interpreted from DIC data for a specimen with geometry 2aa30°, with a smooth interface ($\phi=35^\circ$) inclined 90° with the loading direction, at uniaxial compression loads: (a) 11.6 MPa; (b) 15.51 MPa; (c) 17.44 MPa; (d) 19.34 MPa; (e) 23.67 MPa; (f) 24.24 MPa; (g) 27.2 MPa; (h) 30.36 MPa.







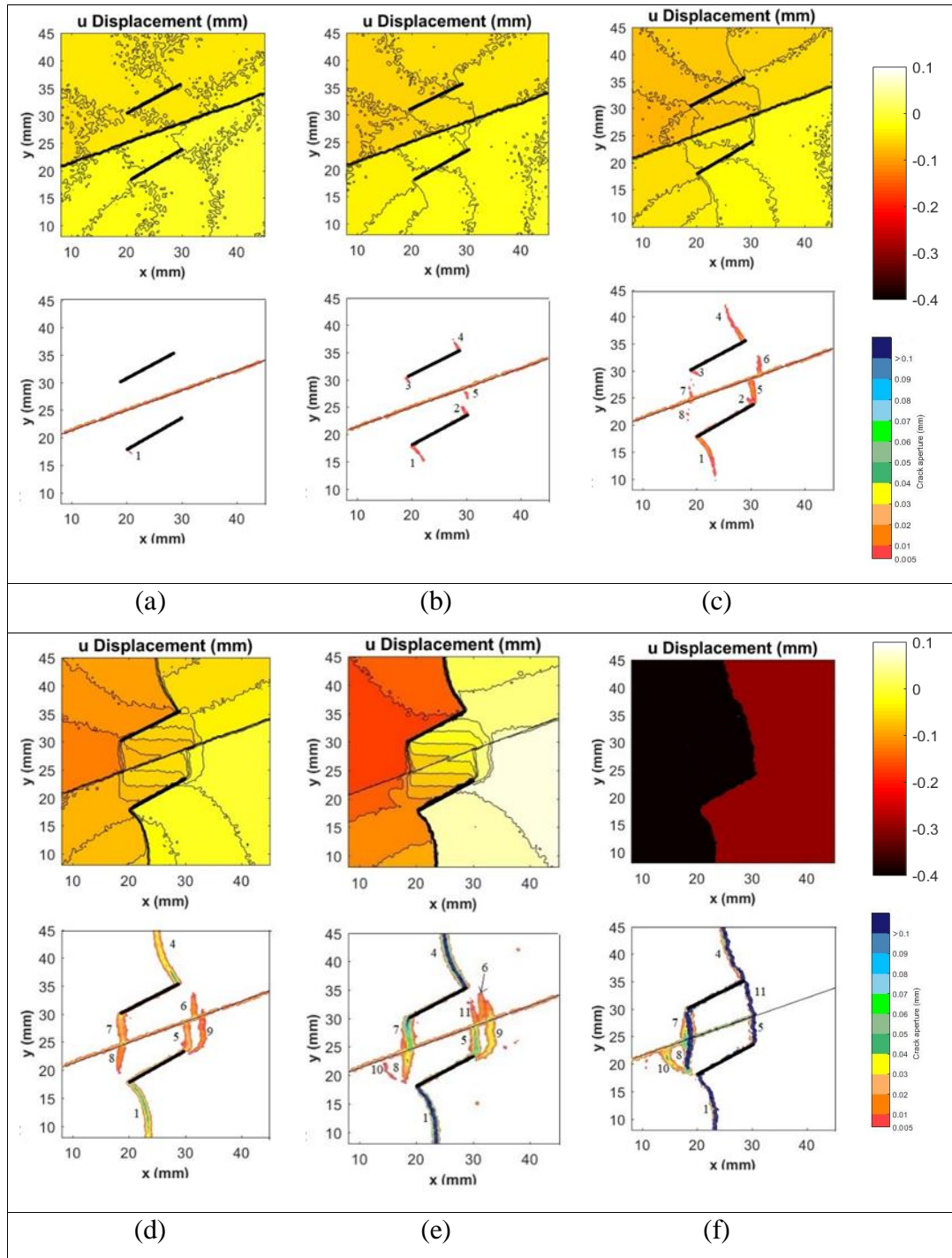
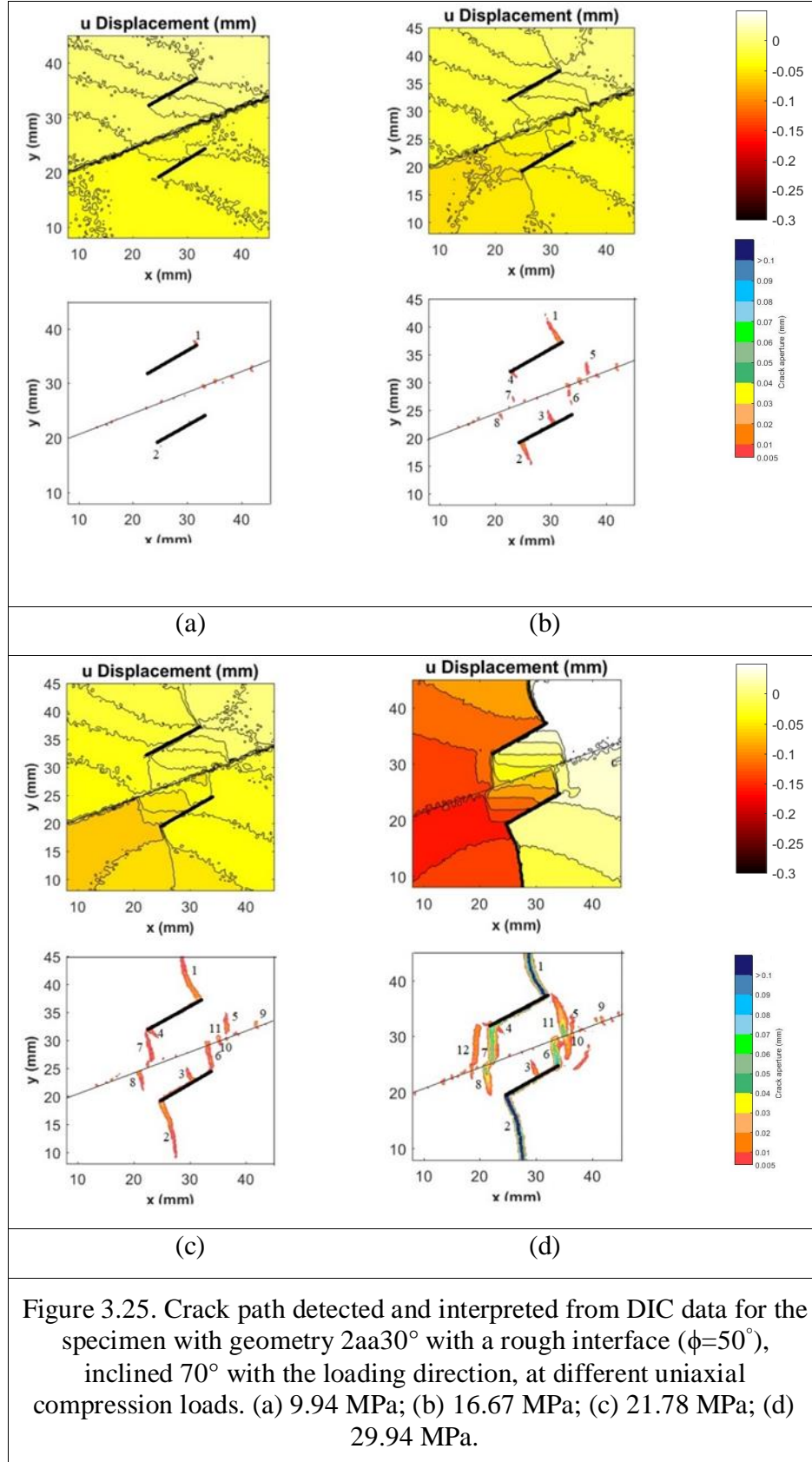


Figure 3.24. Crack path detected and interpreted from DIC data for the specimen with geometry 2aa30° with a smooth interface ($\phi=35^\circ$), inclined 70° with the loading direction, at different uniaxial compression loads. (a) 10.58 MPa; (b) 15.31 MPa; (c) 21.11 MPa; (d) 26.56 MPa; (e) 29.42 MPa; (f) 29.43 MPa.



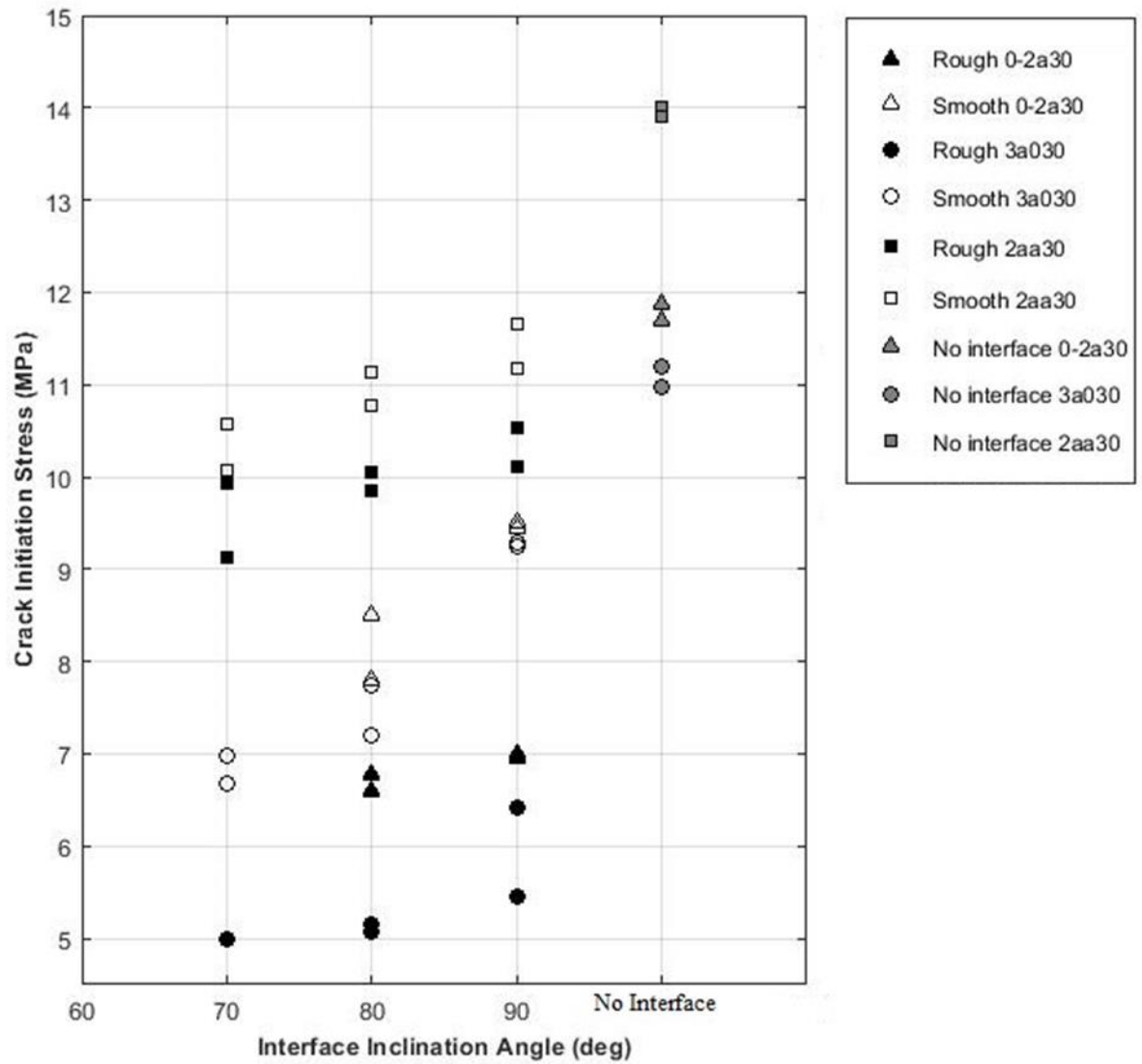


Figure 3.26. Crack initiation stresses in specimens with interface and without interface for different geometries (including repeatability specimens)

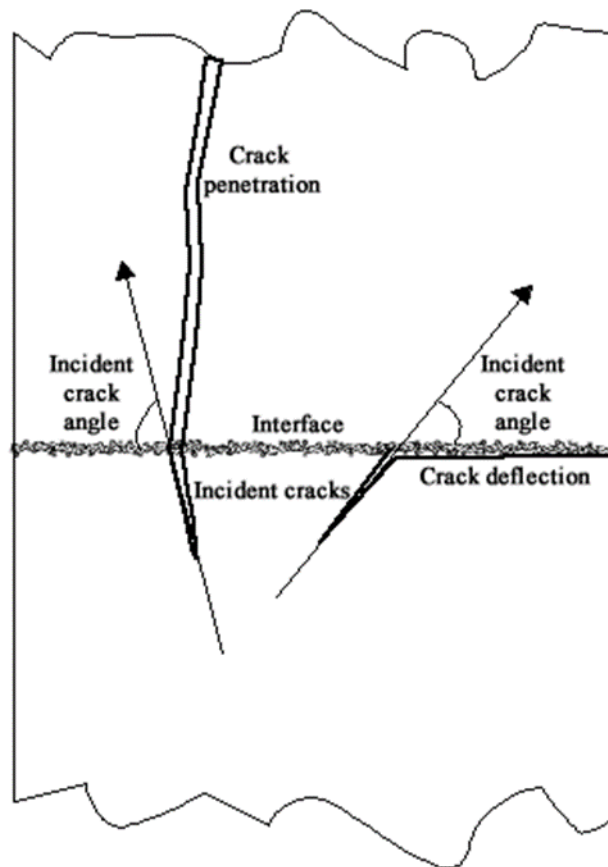


Figure 3.27. Angle between crack path and the interface

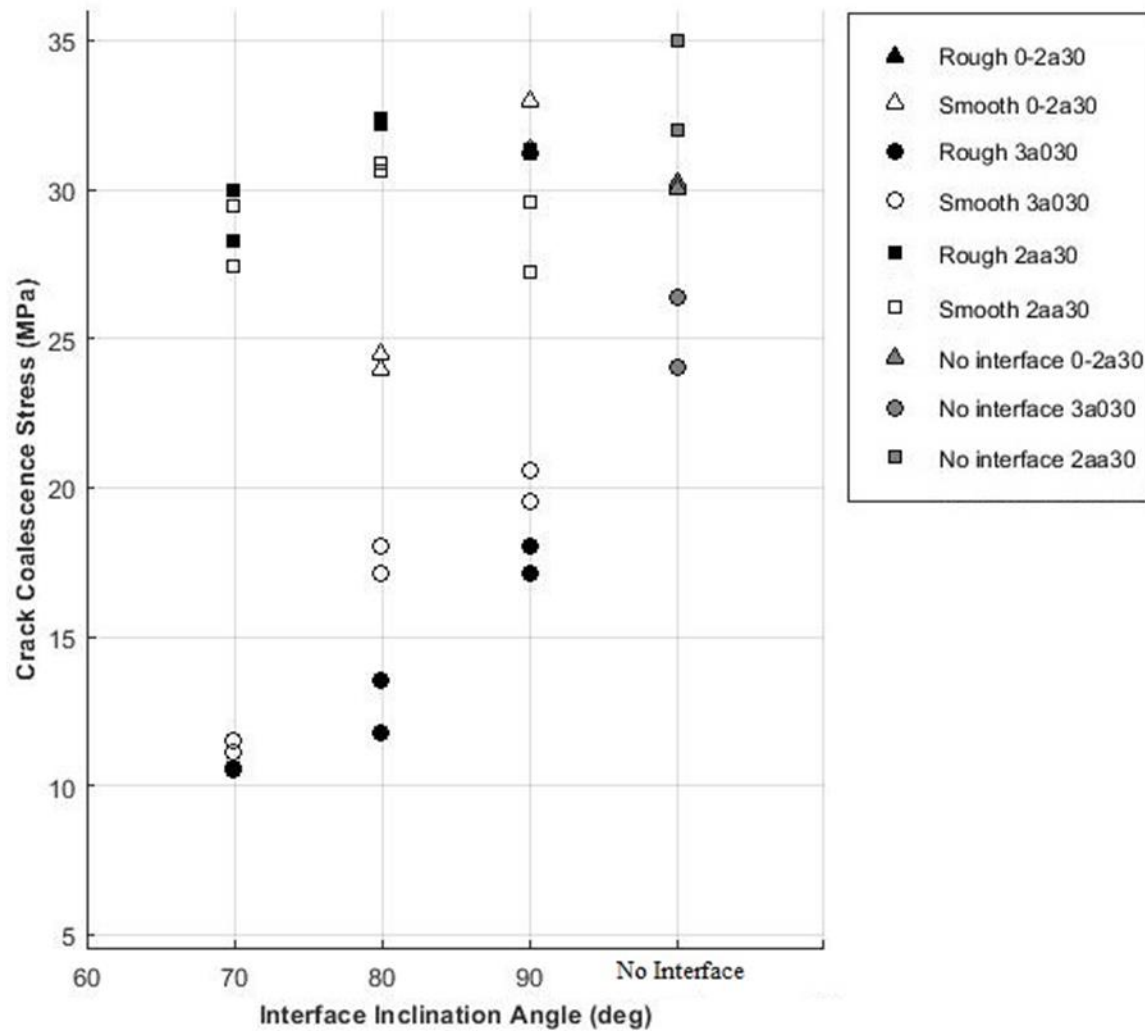


Figure 3.28. Crack coalescence stresses in specimens with interface for different geometries (including repeatability specimens)

Table 3.2. Crack initiation and coalescence stresses for the different tested specimens.

Flaw geometry	Interface roughness	Interface angle (from vertical)	Crack initiation stress (MPa)	Crack Coalescence stress (MPa)
0-2a30°	Smooth	90°	9.5	31.36
	$\phi=35^\circ$	80°	8.5	23.95
	Rough	90°	6.95	No coalescence
	$\phi=50^\circ$	80°	6.6	No coalescence
	No interface	-	11.88	30.22
3a030°	Smooth	90°	9.28	19.55
	$\phi=35^\circ$	80°	7.75	17.12
		70°	6.68	11.5
	Rough	90°	5.45	18.06
	$\phi=50^\circ$	80°	5.08	11.75
		70°	5	10.58
	No interface	-	11.19	24.06
2aa30°	Smooth	90°	11.65	27.2
	$\phi=35^\circ$	80°	11.14	30.86
		70°	10.58	29.43
	Rough	90°	10.53	31.31
	$\phi=50^\circ$	80°	10.06	32.4
		70°	9.94	29.94
	No interface	-	14	34.96
OBS: Cracks initiate at the flaw tips.				

Table 3.3. Crack initiation and coalescence stresses for the specimens tested for repeatability.

Flaw geometry	Interface roughness	Interface angle (from vertical)	Crack initiation stress (MPa)	Crack Coalescence stress (MPa)
0-2a30°	Smooth	90°	9.45	32.96
	$\phi=35^\circ$	80°	7.8	24.51
	Rough	90°	7	No coalescence
	$\phi=50^\circ$	80°	6.78	No coalescence
	No interface	-	11.7	30.05
3a030°	Smooth	90°	9.24	20.58
	$\phi=35^\circ$	80°	7.20	18.02
		70°	6.98	11.13
	Rough	90°	6.42	17.12
	$\phi=50^\circ$	80°	5.16	13.54
		70°	4.06	10.51
	No interface	-	10.97	26.35
2aa30°	Smooth	90°	11.17	29.6
	$\phi=35^\circ$	80°	10.78	30.61
		70°	10.08	27.43
	Rough	90°	10.12	31.19
	$\phi=50^\circ$	80°	9.85	32.16
		70°	9.12	28.29
	No interface	-	13.9	32
OBS: Cracks initiate at the flaw tips.				

Table 3.4. Smallest angle between cracks initiated at the interface and interface plane

Type	Geometry	Crack number	Smallest angle between crack and interface plane
1	0-2a30° Smooth interface 90° from vertical	#2	80°
		#7	72°
		#6	70°
		#9	90°
		#10	65°
		#11	85°
2	0-2a30° Rough interface 90° from vertical	#7	90°
		#10	90°
		#11	80°
		#18	70°
3	0-2a30° Smooth interface 80° from vertical	#4	90°
		#8	90°
		#12	90°
		#14	65°
		#15	80°
4	0-2a30° Rough interface 80° from vertical	#3	75°
		#4	90°
		#8	80°
5	3a030° Smooth interface 90° from vertical	#5	90°
		#6	75°
		#7	75°
		#8	90°
		#9	70°
		#10	75°
		#11	70°
		#13	80°

Table 3.4 continued

Type	Geometry	Crack number	Smallest angle between crack and interface plane
6	3a030° Rough interface 90° from vertical	#3	90°
		#4	70°
		#8	70°
		#10	70°
7	3a030° Smooth interface 80° from vertical	#5	80°
		#6	75°
		#8	70°
		#11	70°
8	3a030° Rough interface 80° from vertical	#1	70°
		#2	75°
		#7	75°
		#9	70°
		#11	65°
		#14	75°
9	3a030° Smooth interface 70° from vertical	#5	75°
		#6	80°
		#7	60°
		#8	90°
		#12	70°
10	3a030° Rough interface 70° from vertical	#5	80°
		#6	90°
		#7	75°
		#8	80°
		#9	70°
		#15	70°

Table 3.4 continued

Type	Geometry	Crack number	Smallest angle between crack and interface plane
11	2aa30° Smooth interface 90° from vertical	#2	75°
		#5	90°
		#8	60°
		#9	90°
		#12	75°
12	2aa30° Rough interface 90° from vertical	#5	90°
		#6	75°
		#7	60°
		#8	80°
13	2aa30° Smooth interface 80° from vertical	#2	70°
		#6	90°
		#9	90°
		#10	80°
		#12	80°
14	2aa30° Rough interface 80° from vertical	#5	90°
		#6	75°
		#7	90°
		#8	80°
		#9	80°
		#10	85°
		#11	80°
		#16	90°
15	2aa30° Smooth interface 70° from vertical	#5	80°
		#6	75°
		#7	80°
		#8	70°

Table 3.4. continued

Type	Geometry	Crack number	Smallest angle between crack and interface plane
16	2aa30° Rough interface 70° from vertical	#5	75°
		#6	70°
		#7	90°
		#8	90°
		#9	80°
		#10	90°
		#11	90°

Table 3.5. Angle at which tensile and shear cracks reach the interface from the interface plane and interaction with the interface (i.e. Arrest at interface – A, Cross the interface– C, Arrest right after crossing the interface - CA)

Flaw geometry	Interface roughness	Interface angle(from vertical)	Tensile cracks		Shear cracks	
			Crack number/ Incident angle	Interaction w/ interface: Cross (C), Arrest (A) or Arrest right after crossing (CA)	Crack number/ Incident angle	Interaction w/ interface: Cross (C), Arrest (A) or Arrest right after crossing (CA)
0-2a30°	Smooth $\phi=35^\circ$	90°	#3 / 40°	A	-	-
			#13 / 70°	C – No offset	-	-
		80°	-	-	#6 / 75° #11 / 55°	C – 1.756 mm A
	Rough $\phi=50^\circ$	90°	#3 / 75°	C – No offset	#5 / 35° #6 / 80° #12 / 75°	CA – 0.95 mm C – No offset C – No offset
		80°	-	-	#7 / 20° #13 / 75°	A C – No offset
3a030°	Smooth $\phi=35^\circ$	90°	-	-	#14 / 63°	A
		80°	-	-	-	-
		70°	#3 / 50°	A	-	-
	Rough $\phi=50^\circ$	90°	#11 / 60°	A	#9 / 75°	C – No offset
		80°	-	-	-	-
		70°	#1 / 55°	A	#13 / 75°	C – 1.5 mm
2aa30°	Smooth $\phi=35^\circ$	90°	-	-	#1 / 80° #4 / 80°	C - No offset C - No offset
		80°	#4 / 30°	A	#5 / 75°	C – 1.559 mm
		70°	-	-	#9 / 70°	C - No offset
	Rough $\phi=50^\circ$	90°	-	-	-	-
		80°	#12 / 75°	C – 1.2 mm	-	-
		70°	-	-	-	-

Table 3.6. Coalescence patterns for specimens with interface

Type	Geometry	Interface inclination (from vertical)	Interface roughness	Coalescence patterns	Short description
1	0-2a30°	90°	Smooth		Indirect coalescence by multiple cracks (T and S). Tensile crack (T) initiated at the interface reaches the upper flaw. Another Tensile crack (T) at the interface, which turns into shear (S), connects to a tensile crack (T) coming from the ROI that bifurcates and reaches the bottom flaw.
2	0-2a30°	90°	Rough		No coalescence

Table 3.6. continued

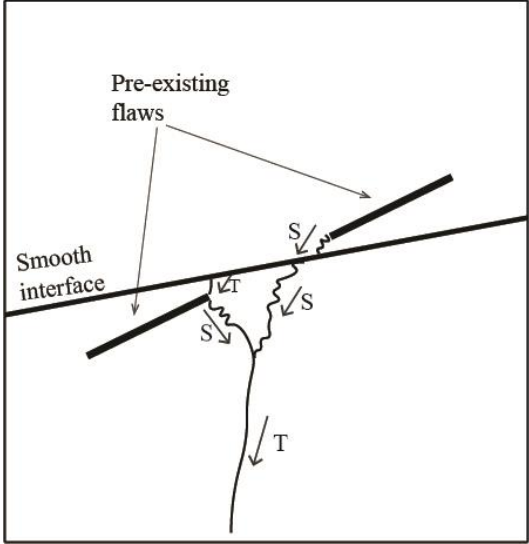
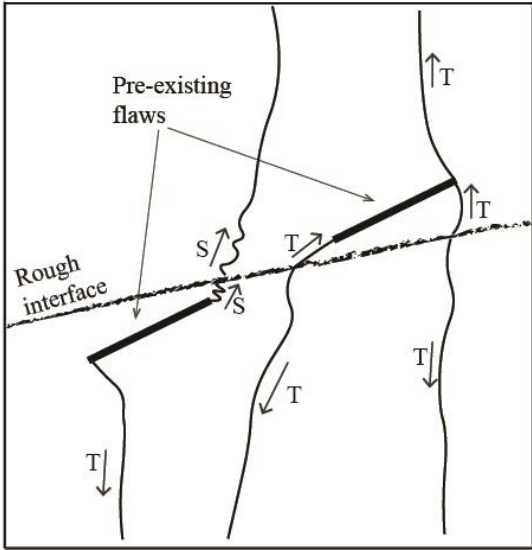
Type	Geometry	Interface inclination (from vertical)	Interface roughness	Coalescence patterns	Short description
3	0-2a30°	80°	Smooth		Indirect coalescence by a shear crack (S) originated at the upper flaw tip that crosses the interface with an offset and reaches a tensile crack (T) which originated initially as a shear crack (S) at the other flaw tip.
4	0-2a30°	80°	Rough		No coalescence

Table 3.6. continued

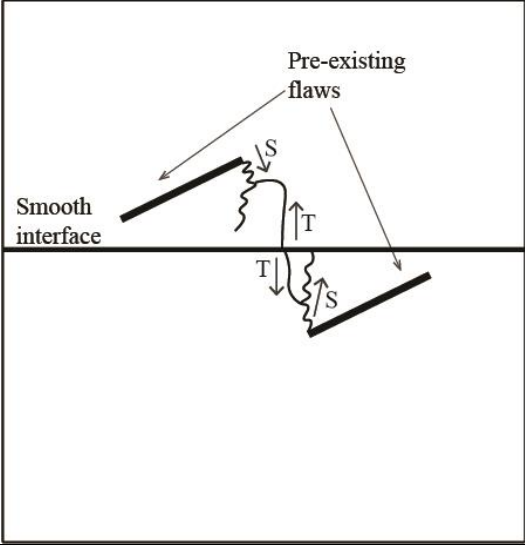
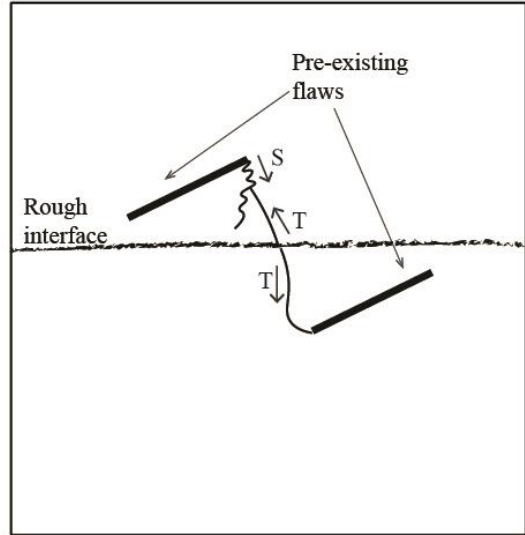
Type	Geometry	Interface inclination (from vertical)	Interface roughness	Coalescence patterns	Short description
5	3aa30°	90°	Smooth		Coalescence occurs when a tensile crack (T) connects with an oblique shear crack (S) above the interface; at the same time, another tensile crack (T) links with an oblique shear crack (S) below the interface
6	3aa30°	90°	Rough		Coalescence occurs when a tensile crack (T) connects with an oblique shear crack (S) above the interface; at the same time, another tensile crack (T) links with the inner tip of the bottom flaw below the interface

Table 3.6. continued

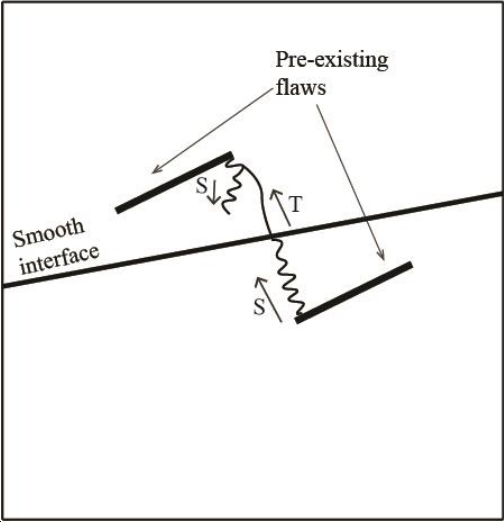
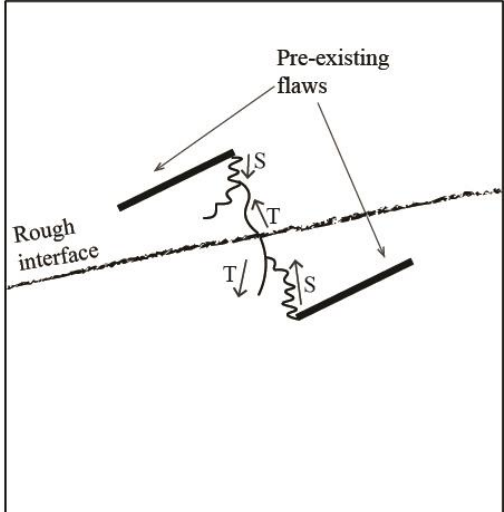
Type	Geometry	Interface inclination (from vertical)	Interface roughness	Coalescence patterns	Short description
7	3aa30°	80°	Smooth		Coalescence occurs when a tensile crack (T) connects with an oblique shear crack (S) above the interface; while a shear crack (S) originated at the tip of the bottom flaw reaches the interface.
8	3aa30°	80°	Rough		Coalescence occurs when a tensile crack (T) connects with an oblique shear crack (S) above the interface; at the same time, another tensile crack (T) links with an oblique shear crack (S) below the interface

Table 3.6. continued

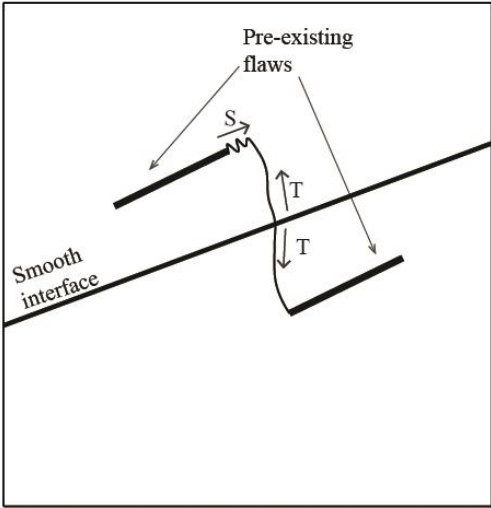
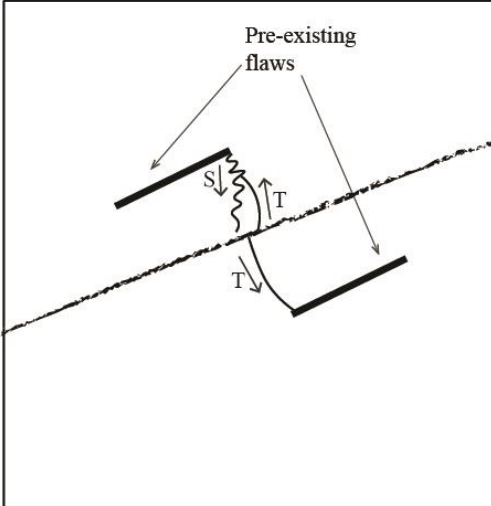
Type	Geometry	Interface inclination (from vertical)	Interface roughness	Coalescence patterns	Short description
9	3aa30°	70°	Smooth		Coalescence is produced when a tensile crack (T) connects with a coplanar shear crack (S) above the interface, and a tensile crack (T) reaches the inside tip of the bottom flaw.
10	3aa30°	70°	Rough		Coalescence is produced when a tensile crack (T) connects with an oblique shear crack (S) above the interface, and a tensile crack (T) reaches the inside tip of the bottom flaw.

Table 3.6. continued

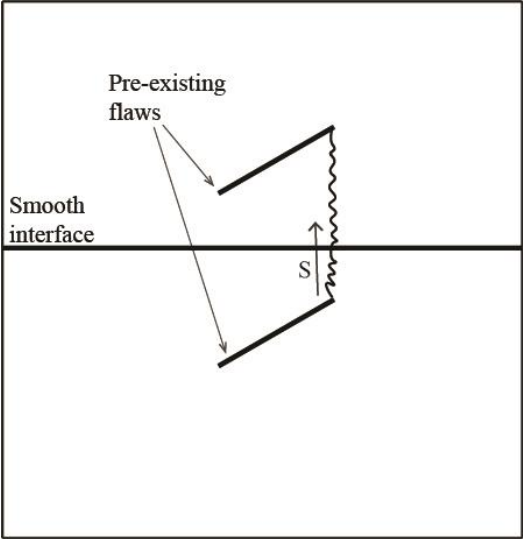
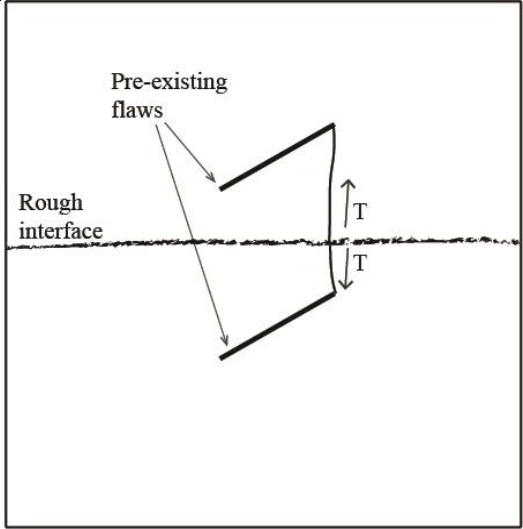
Type	Geometry	Interface inclination (from vertical)	Interface roughness	Coalescence patterns	Short description
11	2aa30°	90°	Smooth		Flaws tips on the same side linked by a shear crack (S) originated at the bottom flaw that crosses the interface and propagates towards the upper flaw.
12	2aa30°	90°	Rough		Flaw tips on the same side linked by tensile cracks (T) initiated at the interface.

Table 3.6. continued

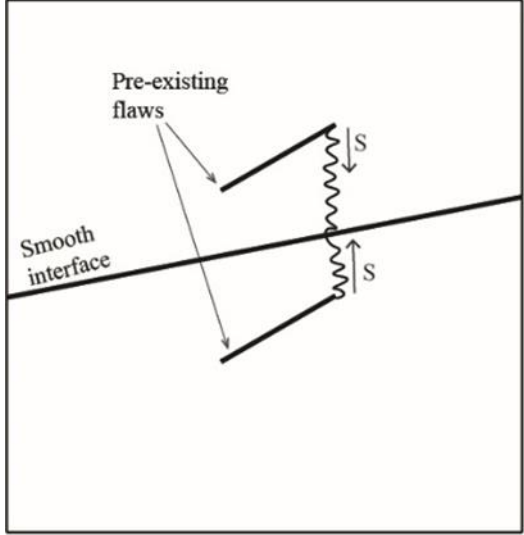
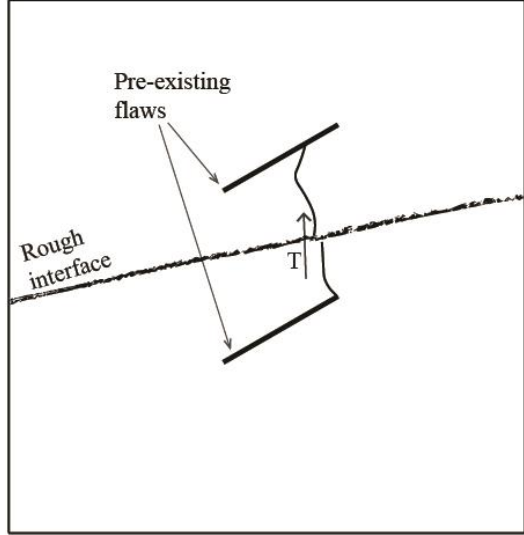
Type	Geometry	Interface inclination (from vertical)	Interface roughness	Coalescence patterns	Short description
13	2aa30°	80°	Smooth	 <p>The diagram shows a smooth interface line. Two pre-existing flaws, represented by angled lines, are located on either side of the interface. Two shear cracks, labeled 'S', originate from the tips of these flaws and meet at the interface, forming a zig-zag pattern.</p>	Flaws tips on the same side linked by shear cracks (S) that connect to one another at the interface
14	2aa30°	80°	Rough	 <p>The diagram shows a rough interface line. Two pre-existing flaws, represented by angled lines, are located on either side of the interface. A tensile crack, labeled 'T', originates from the tip of one flaw, crosses the rough interface with an offset, and reaches the middle of the other flaw.</p>	Flaws linked by a tensile crack (T) initiated at a flaw tip that crosses the interface with an offset and reaches the middle of the other flaw.

Table 3.6. continued

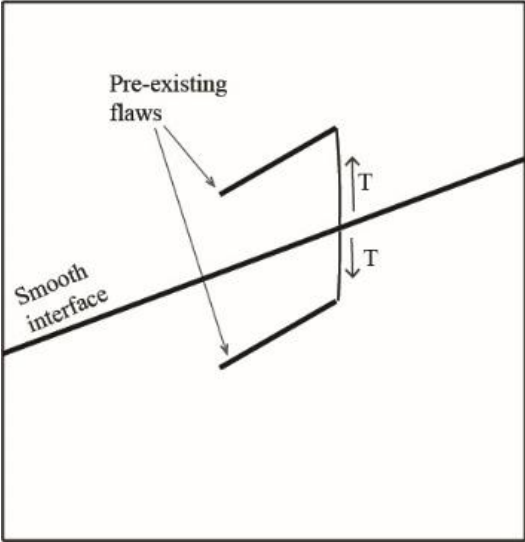
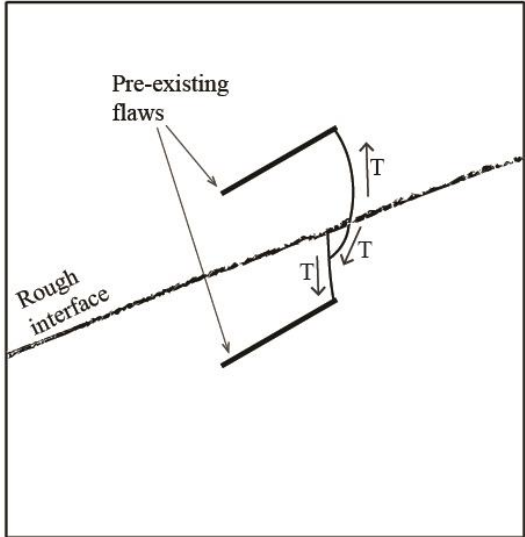
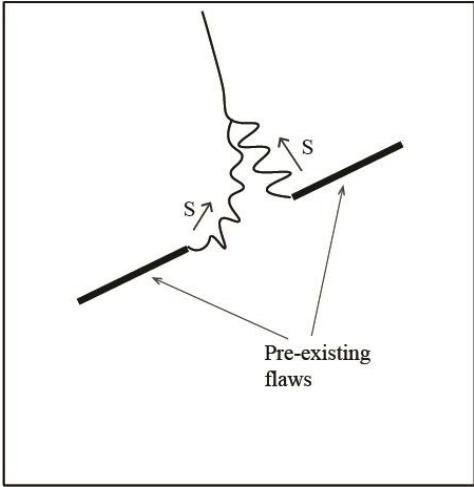
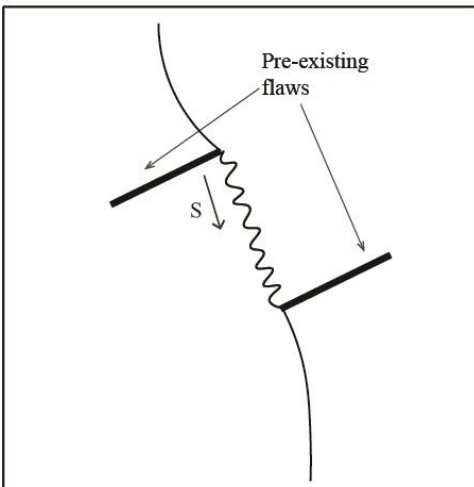
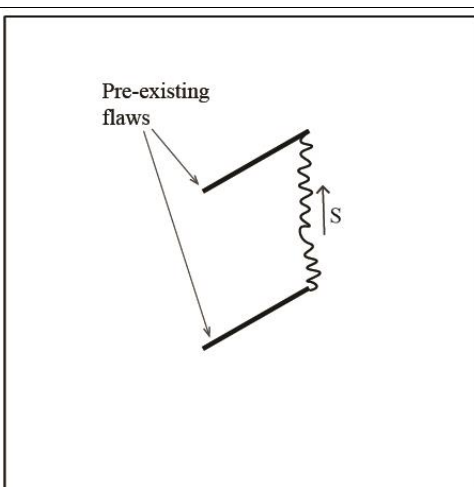
Type	Geometry	Interface inclination (from vertical)	Interface roughness	Coalescence patterns	Short description
15	2aa30°	70°	Smooth		Flaw tips on the same side linked by tensile cracks (T) initiated at the interface.
16	2aa30°	70°	Rough		Flaw tips on the same side linked by tensile cracks (T) initiated at the interface.

Table 3.7. Coalescence patterns for specimens without interface

Type	Geometry	Coalescence patterns	Short description
17	0-2a30°		Indirect coalescence by a shear crack (S) originated at the upper flaw tip that connects with a Shear crack (S) originated at the other flaw tip outside of the bridge area.
18	3aa30°		Shear crack (S) initiated at the inside tip of the upper flaw propagates towards the inside tip of the bottom flaw
19	2aa30°		Flaws tips on the same side linked by a shear crack (S) originated at the bottom flaw that propagates towards the upper flaw.

4. NUMERICAL INVESTIGATION: BACKGROUND

4.1 Introduction

Various numerical methods have been used to simulate crack initiation and propagation in rocks or rock-like materials. These numerical methods include the finite element method (FEM), extended finite element method (XFEM), boundary element method (BEM), discrete element method (DEM), and discontinuous deformation analysis (DDA), which are arguably the methods used the most by the rock mechanics community. Li and Wong (2012) and Goncalves da Silva (2012) conducted simulations using finite element codes to investigate crack behavior; Rannou et al. (2010) and Zhuang et al. (2014) used extended finite element codes for predicting tensile cracks; Bobet and Einstein (1998a) and Goncalves da Silva and Einstein (2013) were able to predict both tensile and shear fracturing using FROCK, which is a code based on the boundary element method (BEM); Lee and Jeon (2011) and Liu and Wang (2017) simulated cracks under mixed-mode I-II loading conditions using the particle flow code (PFC), which is based on DEM; and Yuyong et al. (2007) performed a study on rock crack propagation using the discontinuous deformation analysis method (DDA). Each of these numerical methods incorporate one or more of the several criteria for crack initiation and propagation that have been developed throughout the decades.

The main goal of this chapter is to provide a background on previous studies conducted by other researchers on Fracture Mechanics. Firstly, theoretical concepts of fracture mechanics will be discussed in Section 4.2. Then, different criteria for crack initiation and propagation in brittle materials will be briefly explained in section 4.3. Finally, criteria for cracks interacting with an interface will be briefly explained in section 4.4.

4.2 Fracture mechanics

The field of fracture mechanics basically derives from the classic investigations of Griffith (1920) and Irwin (1958), where cracks, as stress concentrators, are given their rightful importance in controlling brittle fracture. Fracture mechanics is a powerful tool to address the mechanisms as well as the mechanics of crack growth (Atkinson, 1987).

Griffith (1921) proposed a relationship between fracture stress and crack size. He considered an infinite cracked plate of unit thickness with a central through crack of length $2a$, subjected to a

stress σ (See Fig. 4.1). Griffith stated that crack propagation from length a to $a+da$ will occur if the energy release upon crack growth was sufficient to provide all the energy that required for crack growth; this can be expressed as:

$$\frac{dU}{da} = \frac{dW}{da} \quad (4.1)$$

where U is the elastic potential energy supplied by the internal strain energy and the external forces, and W is the energy required for crack growth. From the stress field analysis by Inglis

(1913), Griffith obtained $\frac{dU}{da} = \frac{2\pi\sigma^2a}{E}$ per unit plate thickness, where E is the Young's modulus.

Usually $\frac{dU}{da}$ is replaced by $G = \frac{\pi\sigma^2a}{E}$, which is the elastic energy release rate or the crack driving force.

G needs to be at least equal to the energy consumed in crack propagation (i.e. crack resistance $R = \frac{dW}{da}$) so that crack propagation can occur. Hence, the stress σ_c required for a fracture to propagate in a plate, with a crack of size $2a$ is:

$$\sigma_c = \sqrt{\frac{EG_{Ic}}{\pi a}} \quad (4.2)$$

where G_{Ic} is the critical energy release rate.

A crack can be loaded in three different modes, as illustrated in Fig. 4.2. Normal stresses give rise to mode I, also known as “opening mode”, in which the displacements of the crack surfaces are perpendicular to the crack plane (See Fig. 4.2a). In-plane shear gives rises to mode II, also known as “sliding mode”, in which the displacement of the crack surfaces is on the plane of the crack and perpendicular to the leading edge of the crack (See Fig. 4.2b). Finally, mode III, also known as “tearing mode”, is caused by out-of-plane shear (See Fig. 4.2c). In mode III, crack surface displacements are on the plane of the crack and parallel to the leading edge of the crack (Broek, 1986).

Based on Griffith's investigation, Irwin (1957) developed the stress intensity factor (SIF) concept. The SIFs define the stress and displacement fields close to the crack tip, for the three different modes. The following equations can be used for analytical SIF calculations for mode I (K_I) and mode II (K_{II}):

For open flaws:

$$K_I = \frac{\sqrt{\pi a}}{2} [(1 + k) + (1 - k)\cos 2\beta] \sigma_v \quad (4.3)$$

$$K_{II} = \frac{-\sqrt{\pi a}}{2} (1 - k) \sin 2\beta \sigma_v \quad (4.4)$$

For closed flaws:

$$K_I = 0 \quad (4.5)$$

$$K_{II} = \frac{-\sqrt{\pi a}}{2} [(1 - k) \sin 2\beta - \mu[(1 + k) + (1 - k) \cos 2\beta]] \sigma_v \quad (4.6)$$

where a is half of the flaw length, β is the flaw inclination angle, k is the ratio of horizontal to vertical applied load, and μ is the friction coefficient for closed flaws.

Assuming cylindrical coordinates, r , Θ , and z , as shown in Fig. 4.3, linear elastic stress analysis and an isotropic medium under uniaxial or biaxial stress state, the stresses around the tip of a single crack can be calculated as follows:

$$\begin{bmatrix} \sigma_r \\ \sigma_\theta \\ \sigma_{r\theta} \end{bmatrix} = \frac{K_I}{\sqrt{2\pi r}} \cos \frac{\theta}{2} \begin{bmatrix} 1 + \sin^2 \frac{\theta}{2} \\ \cos^2 \frac{\theta}{2} \\ \sin \frac{\theta}{2} \cos \frac{\theta}{2} \end{bmatrix} + \frac{K_{II}}{\sqrt{2\pi r}} \begin{bmatrix} \sin \frac{\theta}{2} (1 - 3\sin^2 \frac{\theta}{2}) \\ -3 \sin \frac{\theta}{2} \cos^2 \frac{\theta}{2} \\ \cos \frac{\theta}{2} (1 - 3\sin^2 \frac{\theta}{2}) \end{bmatrix} \quad (4.7)$$

In the above formulation, σ_r , σ_θ , and $\sigma_{r\theta}$ are the radial, tangential, and shear stresses, respectively.

Most materials are not perfectly brittle, as assumed by Griffith theory, but display ductility after reaching their strength limit. This creates a fracture process zone at the crack tip, where micro cracking and void initiation occur, resulting in plastic deformations. Outside this zone, the material is still elastic. Linear elastic fracture mechanic concepts can be only assumed if the fracture process zone is small enough compared to the geometry of the crack. In this case, small scale yielding (SSY) can be assumed, which occurs if the condition in equation 4.8 is satisfied (Whittaker et al., 1992).

$$\left\{ \frac{a}{L - a} \right\} \geq (1.5 \text{ to } 2.0) \left(\frac{K_{IC}}{\sigma_t} \right)^2 \quad (4.8)$$

where $L - a$ is the distance from the external boundary of the specimen to the tip of the flaw (See Fig. 4.4), K_{IC} is the critical stress intensity factor K_I (i.e. mode I fracture toughness), and σ_t is the tensile strength of the material.

The Griffith stress approach is only able to predict initiation of tensile cracks under tensile or compressive stresses (only if the crack remains open). Shear crack initiation cannot be predicted through this approach.

For the past few decades, several criteria have been proposed to predict crack initiation following Griffith's stress approach. These criteria can be classified into three families: stress-

based, strain-based and energy-based. In section 4.3 of this chapter, the most relevant criteria for crack propagation will be explained. From the stress-based family, the maximum tangential stress criterion (σ_θ – criterion), the Bobet’s stress-independent failure criterion and the Goncalves da Silva’s exact stress-dependent criterion will be looked into. From the strain-based family, the Goncalves da Silva’s strain-based criterion will be discussed. Finally, from the energy-based family, the maximum energy release rate criterion (G-criterion) and the minimum strain energy density criterion (S-criterion) will be explained.

Furthermore, as the objective of this thesis is to investigate the interaction between cracks approaching an interface, criteria for predicting crack propagation through interfaces will be discussed in section 4.4. Most of the criteria developed so far apply only for mode-I loading cases, for example the energy release rate criterion for crack penetration or deflection at the interface (He and Hutchinson criterion), the stress-based crack reinitiation criterion (Lemaitre’s criterion), the stress-based criteria for orthogonal and non-orthogonal crack propagation across unbonded frictional interfaces (Renshaw and Pollard’s, and Gu and Weng’s criteria), and the maximum principal tensile stress criterion. A criterion for crack interacting with an interface under mixed-mode I-II conditions will also be presented in that section (i.e. the traction-separation criterion, also known as cohesive zone model).

4.3 Criteria for crack initiation and propagation at flaw tips

4.3.1 Maximum tangential stress criterion (σ_θ – criterion)

The first of the mixed-mode I-II theories to be discussed was formulated by Erdogan and Sih (1963). In this criterion, the parameter that controls cracking is the maximum tangential stress, $\sigma(\theta)_{max}$, near the crack tip. The $\sigma(\theta)_{max}$ criterion states the following:

1. Crack initiation starts at the flaw tip and in a radial direction which forms an angle θ with the flaw plane
2. Crack initiation starts in a direction in which $\sigma(\theta)$ is maximum, meaning:

$$\frac{\partial \sigma(\theta)}{\partial \theta} = 0 \quad (4.9)$$

and

$$\frac{\partial^2 \sigma(\theta)}{\partial \theta^2} < 0 \quad (4.10)$$

3. Crack initiation begins when $\sigma(\theta)_{max}$ reaches a critical, material-constant value

$$(\sigma_{\theta})_{maximum} = (\sigma_{\theta})_{critical} \quad (4.11)$$

4. Crack initiates in a direction that is perpendicular to the direction of the maximum tangential stress $(\sigma_{\theta})_{max}$

Considering a crack under mixed-mode conditions, the stress state near its tip can be expressed in cylindrical coordinates (See Fig. 4.5) in terms of the stress intensity factors K_I and K_{II} as shown in Equation 4.7.

This criterion yields good predictions for mixed mode I-II loading in tension; however the predictions for compressive load cases are not satisfactory (i.e. shear cracks cannot be predicted through this criterion). Another limitation of this criterion is that it is only valid for LEFM conditions, when small scale yielding applies (Whittaker et al., 1992).

4.3.2 Maximum strain energy release rate (G - criterion)

This criterion is based on Griffith's failure criterion (1921). It was extended to cases of inclined cracks embedded in a plate under tensile stresses. The G-criterion is expressed in terms of the strain energy release rate G and it follows the premises below:

1. Crack initiation takes place at the tip of the flaw at an angle θ with respect to the flaw plane
2. Crack initiates in the direction of maximum energy release rate, G_{max}

$$\frac{\partial G(\theta)}{\partial \theta} = 0 \text{ and } \frac{\partial^2 G(\theta)}{\partial \theta^2} < 0 \quad (4.12)$$

3. Crack starts propagating at a critical value of the strain energy release rate, G_{max} , which is material dependent

$$G_{maximum} = G_{critical} \quad (4.13)$$

The strain energy release rate, $G(\theta)$, can be evaluated according to equation 4.14. E^* is the elastic modulus for plain strain conditions and can be obtained by making $E^* = \frac{E}{1-\nu^2}$, where E is the Young's modulus and ν is the Poisson's ratio. $K_I'(\theta)$ and $K_{II}'(\theta)$ are the stress intensity factors for mode I and mode II of a new crack forming from a pre-existing flaw, respectively.

$$G(\theta) = \frac{1}{E^*} [K_I'^2(\theta) + K_{II}'^2(\theta)] \quad (4.14)$$

Hussain et al. (1974) provided a solution for the stress intensity factors for a new crack forming from a pre-existing flaw, which is shown in equation 4.15.

$$\begin{bmatrix} K_I'(\theta) \\ K_{II}'(\theta) \end{bmatrix} = \left(\frac{4}{3 + \cos^2 \theta} \right) \left(\frac{1 - \frac{\theta}{\pi}}{1 + \frac{\theta}{\pi}} \right)^{\frac{\theta}{2\pi}} \begin{bmatrix} K_I \cos \theta + \frac{3}{2} K_{II} \sin \theta \\ K_{II} \cos \theta - \frac{K_I}{2} \sin \theta \end{bmatrix} \quad (4.15)$$

where θ is the angle that the new crack makes with the horizontal plane. K_I and K_{II} are the stress intensity factors for the pre-existing crack, which can be obtained by Equations 4.3, 4.4 and 4.5, 4.6, for cases of open cracks or closed cracks, respectively.

The maximum strain energy release rate criterion can only be applied for cases under LEFM conditions. Another limitation of this criterion is that it cannot predict cracks under compressive loads since its predictions do not match with observations from experimental results (Whittaker et al., 1992).

4.3.3 Minimum strain energy density criterion (S-criterion)

The S criterion is a mixed-mode cracking theory that was formulated by Sih (1974). The parameter that governs cracking is the strain density near the crack tip. The energy density per unit volume is expressed by:

$$S = \frac{1}{16G} \left[\frac{k}{2G} (\sigma_r + \sigma_\theta)^2 - \sigma_r \sigma_\theta + \sigma_{r\theta}^2 \right] \quad (4.16)$$

where the shear modulus $G = \frac{E}{2(1+\nu)}$, E is the Young's modulus and ν is the Poisson's ratio. For plain strain, $k = (3 - 4\nu)$ and for plain stress, $k = \frac{3-\nu}{1+\nu}$. σ_r , σ_θ and $\sigma_{r\theta}$ correspond to the stress state near the crack tip in cylindrical coordinates. Sih (1974) showed that the strain energy density at a distance r from a crack tip is:

$$S = \frac{1}{r} (a_{11} K_I^2 + 2a_{12} K_I K_{II} + a_{22} K_{II}^2) \quad (4.17)$$

where:

$$\begin{bmatrix} a_{11} \\ a_{12} \\ a_{22} \end{bmatrix} = \frac{1}{16\pi G} \begin{bmatrix} (1 + \cos \theta)(k + \cos \theta) \\ \sin \theta [2\cos \theta - (k - 1)] \\ (k + 1)(1 - \cos \theta) + (1 + \cos \theta)(3\cos \theta - 1) \end{bmatrix} \quad (4.18)$$

Unlike the two criteria discussed previously, the results obtained from the S-criterion are a function of the Poisson's ratio (Atkinson, 1987).

The S-criterion criterion proposes the following:

1. Crack extension occurs at the flaw tip, making an angle θ with respect to the flaw plane

2. Crack extension occurs in the direction θ_{min} along which the strain energy density possesses a minimum value

$$\frac{\partial S(\theta)}{\partial \theta} = 0 \text{ and } \frac{\partial^2 S(\theta)}{\partial \theta^2} > 0 \quad (4.19)$$

3. Crack initiates when the strain energy density reaches a critical value which is material dependent

$$S_{maximum} = S_{critical} \quad (4.20)$$

Similarly to the σ_θ and G criteria, the S-criterion should only be used for LEFM applications and provides satisfactory results when it comes to predictions of tensile cracks in tension and in compression (Bobet, 1997). Summing up, shear cracks could not be properly predicted by any of these three criteria (Goncalves da Silva, 2009).

Other criteria and models worth mentioning include the Stress independent failure criterion by Bobet (1997), and the Strain-based and Exact stress dependent criteria by Goncalves da Silva (2009).

4.3.4 Bobet's criterion (Stress independent failure criterion)

The criterion for crack initiation, formulated by Bobet (1997), is based on the local stress relative to the strength of the material rather than on the Stress Intensity factors. That being said, should the calculated stress exceed the strength of the material, crack initiation occurs (Bobet, 1998b). A fracture process zone of radius r_0 is assumed to form at the tip of the crack at an angle θ with respect to the flaw plane (See Fig. 4.3) due to the fact that the stresses at the crack tips are much larger than the strength of the material.

Bobet's criterion makes predictions for both tensile and shear cracks for mixed mode I and II loading. A tensile crack initiates along the direction perpendicular to the direction of maximum tensile stress (i. e. $\frac{\partial \sigma(\theta)}{\partial \theta} = 0$ and $\frac{\partial^2 \sigma(\theta)}{\partial \theta^2} > 0$) when the tangential tensile stress σ_θ ($r = r_0$) reaches the critical tensile strength of the material $\sigma_{\theta crit}$. A shear crack initiates in the direction of the maximum shear stress (i. e. $\frac{\partial \tau(\theta)}{\partial \theta} = 0$ and $\frac{\partial^2 \tau(\theta)}{\partial \theta^2} < 0$) when the shear stress τ ($r = r_0$) reaches the critical shear strength of the material.

The main advantage of this criterion is that it yields satisfactory results for both tensile and shear cracks predictions. The results obtained from this criterion were consistent with the experimental observations for various flaw geometries, as one can observe in Fig. 4.6.

However, an investigation conducted by Wong (2008) showed that this criterion failed to predict crack formation in some geometries, for instance $S=0$ $C=-2a$ $\beta=75^\circ$ and $S=0$ $C=-a$ $\beta=30^\circ$, given that the spacing (S) between flaws, continuity (C), and inclination angle, measured from the horizontal, (β) define the geometry of the flaws. The reason behind the poor results in some geometries is possibly because of the simplifications that were taken for the criterion, for example the independence between the critical shear stress and the normal stress (or radial stress). In this criterion, the only requirement for a shear crack to occur is that the shear stress reaches the failure envelope (see Fig. 4.6e), meaning that the radial stress σ_r is not considered, as it is normally the case for frictional materials.

Another limitation of this criterion is that it cannot explain cracks formed by the linkage of en-echelon cracks (i.e. arrays of microcracks that do not develop in a radial direction from the flaw tip) since Bobet's criterion only predicts cracks that develop radially from the flaw tip.

4.3.5 Goncalves da Silva's criterion

4.3.5.1 Goncalves da Silva's evaluation of existing crack initiation criteria

Goncalves da Silva (2013) conducted a qualitative study using FEM in ABAQUS to analyze stress-, strain- and energy- based criteria for cracking mechanisms. His investigation indicated that only stress- or strain-based approaches were able to differentiate tensile from shear cracks.

The methodology of this approach is that the order of initiation of cracks follows the stress, strain or energy levels at the flaw tip. This means that the first crack occurs in the direction in which the stresses, strains or energy are the highest; the second crack occurs in the direction in which the stresses, strains or energy are the second highest, and so on (Goncalves da Silva, 2013).

A circular path was created around a flaw tip, and stresses and strains were obtained at several points along the path (See Fig. 4.7a). In order to interpret the results more efficiently, the circular path was divided into areas where the different types of cracks were most likely to occur and this was done based on the investigations performed by Bobet (1997) and Wong (2008). The

path was then divided into tensile crack, coplanar shear crack and oblique shear crack regions (See Fig. 4.7b).

As discussed in the introduction section, there is an area around the flaw tip where a plastic behavior is observed. In this area, the stresses tend to infinity. Therefore, Goncalves da Silva and Einstein (2013) placed the path, where the stresses were measured, at a distance of twice the radius of the flaw tip ($r=0.7\text{mm}$).

The maximum principal stresses (σ_I) and the maximum shear stress (τ_{12}^{max}) were obtained along the predefined path. The maximum principal stresses (σ_I) were extracted from ABAQUS output and analyzed for tensile cracking. The maximum shear stresses (τ_{12}^{max}) were used in the investigation of shear cracks and calculated as follows: $\tau_{12}^{max} = \frac{1}{2}(\sigma_I - \sigma_{III})$, where σ_I is the maximum principal stress and σ_{III} is the minimum principal stress, both obtained directly from ABAQUS output. One can observe that the maximum shear stress is the radius of the Mohr circle of stresses.

In the strain-based approach, the maximum principal strain (ϵ_I) was used to characterize tensile cracks, and the maximum shear strain (γ_{12}^{max}) was used to investigate shear crack initiation. The maximum shear strains were calculated as $\gamma_{12}^{max} = (\epsilon_I - \epsilon_{III})$, where ϵ_I is the maximum principal strain and ϵ_{III} is the minimum principal strain, both obtained from ABAQUS. However, the maximum shear strains results were displayed as $\epsilon_{12}^{max} = \frac{1}{2}(\epsilon_I - \epsilon_{III})$, which is equivalent to the radius of the Mohr circle of strains. It is expected that the shear stresses and strains plots match, since there is a linear dependence between shear stresses and strains given by $\gamma_{12} = \frac{\tau_{12}}{G}$, where G is the shear modulus.

In ABAQUS, positive results correspond to tensile stresses and elongation strains, while negative results correspond to compressive stresses and contraction strains.

As mentioned earlier, both stress and strain approaches yielded very good predictions for the direction and type of cracks that were observed in experimental tests. Based on these findings, Goncalves da Silva and Einstein (2009) proposed the two criteria that will be discussed in subsections 4.3.5.2 and 4.3.5.3.

4.3.5.2 Strain based criterion

Similarly to the stress-independent based criterion (i.e. Bobet's criterion), the strain based criterion also predicts both tensile and shear cracks. In the Goncalves da Silva's strain based criterion (See Fig. 4.8), a tensile crack initiates at the crack tip along the direction θ in which the tangential strain is maximum $\mathcal{E}_{\theta max}$ (i.e. $\frac{\partial \mathcal{E}(\theta)}{\partial \theta} = 0$ and $\frac{\partial^2 \mathcal{E}(\theta)}{\partial \theta^2} > 0$) when the tangential strain $\mathcal{E}_{\theta max}$ reaches the critical strain of the material $\mathcal{E}_{\theta crit}$. A shear crack initiates at the crack tip in the direction θ in which the shear strain is maximum $\mathcal{E}_{\gamma \theta max}$ (i.e. $\frac{\partial \gamma(r\theta)}{\partial \theta} = 0$ and $\frac{\partial^2 \gamma(r\theta)}{\partial \theta^2} < 0$) when the shear strain $\gamma_{r\theta max}$ reaches the critical shear strain of the material $\gamma_{r\theta crit}$.

The Goncalves da Silva's criterion yielded better results than the Bobet's criterion, meaning that successful results were achieved even in coplanar flaw geometries (i.e. $S=0$ $C=-2a$ $\beta=75^\circ$ and $S=0$ $C=-a$ $\beta=30^\circ$) where Bobet's criterion did not work well. However, for geometries such as $S=0$ $C=-2a$ $\beta=30^\circ$, shear cracks predicted through this criterion were too steep and inconsistent with experimental results, which suggests that this criterion does not accurately estimate the direction of initiation of shear cracks.

4.3.5.3 Exact stress dependent criterion

Goncalves da Silva (2013) proposed a failure criterion that introduced friction in the stress failure criterion, to consider the dependence between the resisting shear stress and the normal shear stress, which he named "exact stress dependent" criterion. Figure 4.9 shows the difference between the failure envelopes for the confinement stress independent criterion by Bobet (1997) and the exact stress dependent criterion by Goncalves da Silva (2013). In both criteria, tensile failure occurs when the Mohr circle reaches and is tangential to the tensile strength of the material $\sigma_{\theta crit}$. Shear failure occurs when the Mohr circle reaches and is tangential to the horizontal (i.e. $\phi=0$ in Bobet's criterion) or inclined (i.e. $\phi \neq 0$ in Goncalves de Silva's criterion) envelope failure.

In the exact stress dependent criterion, the cracks are not required to be radial since the principal stress directions are not necessarily radial. In contrast to Bobet's criterion, this criterion takes into consideration the three stresses (i.e. tangential, radial and shear) for tensile and shear failures. Regarding crack initiation, Bobet's and Goncalves da Silva's criteria yield reasonable results. When it comes to crack propagation, the results were always poor for the Goncalves da

Silva's criterion; however good results were observed for cases with low friction angles (i.e. between 0 and 10 degrees).

4.4 Criteria for cracks interacting with an interface

4.4.1 Energy release rate criterion for crack penetration or deflection at the interface (He and Hutchinson's criterion)

He and Hutchinson (1989) used linear elastic fracture mechanics to investigate a crack impinging a bimaterial interface in a normal direction. The authors conducted a comprehensive analytical work in which they examined the competition between penetration and deflection of a crack approaching a bimaterial interface under remote static loading.

For a tensile crack subjected to a remote static stress defined with the stress intensity factor (K_I^S), it will continuously pass through the interface (See Fig. 2.4b in Chapter 2) when the mode-I static crack energy release rate (G_I^S) reaches the fracture toughness Γ_{IC}^{MA} of the material, i.e.

$$G_I^S = \frac{1-\nu^2}{E} (K_I^S)^2 = \Gamma_{IC}^{MA} \quad (4.21)$$

The toughness of an interface is basically the energy required to separate two adjoining materials, usually quantified in terms of a critical energy release rate for crack extension along the interface, measured in units of energy per unit area.

However, a crack will deflect (i.e. kink) at the interface (See Fig. 2.4a in Chapter 2) when the static energy release rate of the kinked crack tip (G^{sk}) reaches or exceeds the fracture toughness of the interface (Γ_c^{IT}), i.e.

$$G^{sk} = \frac{1-\nu^2}{E} [(K_I^{sk})^2 + (K_{II}^{sk})^2] = \Gamma_c^{IT} \quad (4.22)$$

where K_I^{sk} , K_{II}^{sk} are, respectively, the static mode-I and mode-II stress intensity factors for the kinked mixed-mode crack (Hutchinson and Suo, 1992).

$$K_I^{sk} = K_I^S \left(\frac{3}{4} \cos \frac{\beta}{2} + \frac{1}{4} \cos \frac{3\beta}{2} \right) \quad (4.23)$$

$$K_{II}^{sk} = K_I^S \left(\frac{1}{4} \sin \frac{\beta}{2} + \frac{1}{4} \sin \frac{3\beta}{2} \right) \quad (4.24)$$

where β is the kink angle.

The two scenarios can be assessed through the ratio of equations (4.22) and (4.21), and so: A crack will penetrate and cross the interface when

$$\frac{G^{sk}}{G_I^S} < \frac{\Gamma_c^{IT}}{\Gamma_{IC}^{MA}} \quad (4.25)$$

A crack will deflect/kink at the interface when

$$\frac{G^{sk}}{G_I^S} \geq \frac{\Gamma_c^{IT}}{\Gamma_{IC}^{MA}} \quad (4.26)$$

One can observe from equations (4.22) and (4.21) that the ratio of the two energy release rates (*i.e.* $\frac{G^{sk}}{G_I^S}$) depends only on the kink angle β and not on magnitude of the stress intensity factors or material properties:

$$\frac{G^{sk}}{G_I^S} = \frac{1}{16} \left[\left(\frac{3}{4} \cos \frac{\beta}{2} + \frac{1}{4} \cos \frac{3\beta}{2} \right)^2 + \left(\frac{1}{4} \sin \frac{\beta}{2} + \frac{1}{4} \sin \frac{3\beta}{2} \right)^2 \right] \quad (4.27)$$

The equation shown above holds for both plane strain and plane stress analyses.

As for limitations, this criterion does not address the debonding length which is the distance along the interface between the incident crack and the location where the crack propagates on the other side of the interface. The next criterion addresses the debonding length as well as a damage equivalent stress that governs crack re-initiation.

4.4.2 Stress-based crack re-initiation criterion (Lemaitre's criterion)

Lemaitre et al. (1996) investigated the conditions for a mode I crack, 12mm long, in one of the layers of a bimaterial (*i.e.* layer A), which reaches the interface normally, to reinitiate in the opposite layer (*i.e.* layer B) under remote stress σ_∞ (corresponding to the remote strain ϵ_∞), as shown in Fig. 4.10. The authors observed in their experiments in PMMA (See Fig. 4.11) that re-initiation started at the tips of the debonding. They also conducted an analytical investigation of the failure of multimaterials to predict the shear stress distribution in interface problems.

The debonding length l_D is defined as the interface crack length where the stress intensity factor or the strain energy release rate reaches a steady state magnitude equal to their critical value. It may also be defined as the length of the interface for which the damage equivalent stress at the interface is larger than its critical value (*i.e.* when the shear stress at the interface σ_{12}^I is larger than the critical debond shear strength τ_c). In this criterion, the damage equivalent stress is the stress at which a crack reinitiates across the interface.

Considering layers A and B under pure tension and zero thickness interface between layers in pure shear, and their thickness being equal as well as their Young's modulus, *i.e.* $h_A = h_B = h$,

$E_A = E_B = E$. h_A and h_B are half of the thickness of layers A and B. E_A and E_B are the Young's modulus of layers A and B;

Lemaitre demonstrated that the debond length l_D could be calculated by using the following equation:

$$\frac{l_D}{2h} = \frac{1}{\sqrt{2}} \left(\frac{E}{G_I} \right)^{1/2} \ln \left(\sqrt{2} \frac{\sigma_\infty}{\tau_c} \left(\frac{G_I}{E} \right)^{1/2} \right) \quad (4.28)$$

where G_I is the elastic shear modulus of the interface and $\sigma_\infty = \sigma_\infty^B = E_B \mathcal{E}_\infty$

In order to determine the stress field at the critical end point of the debond (i.e. point at which a crack will reinitiate), Lamaitre et al.(1996) applied a damage law in the uncracked layer B to predict the crack re-initiation in B. According to this criterion, the damage equivalent stress σ^* governs the crack re-initiation in layer B at the location of its maximum. The damage equivalent stress σ^* is calculated as the mises equivalent stress σ_{eq} multiplied by the square root of the triaxiality factor R_v , as shown in Equation 4.29.

$$\sigma^* = \sigma_{eq} R_v^{1/2}, \quad R_v = \frac{2}{3} (1 + \nu_B) + (1 - 2\nu_B) \left(\frac{\sigma_H}{\sigma_{eq}} \right)^2 \quad (4.29)$$

The triaxiality factor is a function of the ratio between the hydrostatic stress σ_H (i.e. average of uniaxial stresses along three orthogonal axes) and the mises stress σ_{eq} , shown in Equations 4.30 and 4.31.

$$\sigma_{eq} = \sqrt{\frac{3}{2} \sigma_{ij}^D \sigma_{ij}^D}, \quad (4.30)$$

$$\sigma_H = \frac{1}{3} \sigma_{kk} \quad (4.31)$$

$$\sigma_{ij}^D = \sigma_{ij} - \sigma_H \delta_{ij} \quad (4.32)$$

where δ_{ij} is the Kronecker delta and ν_B is the poisson ratio of layer B.

Lamaitre et al.(1996) also showed that the damage equivalent stress σ^* is maximum at $x_1 = l_D$ which indicates the location where a crack may initiate:

$$\sigma^*(x_1 = l_D) = \sigma_\infty \left(\left(1 + \frac{h_A}{h_B} \right)^2 + 12\lambda^2 h_A^2 \right)^{1/2} \times \left(\frac{2}{3} (1 + \nu_B) + 3(1 - 2\nu_B) \left(\frac{\sigma_H}{\sigma_{eq}} \right)^2 \right)^{1/2} \quad (4.33)$$

where

$$\text{the elastic parameter } \lambda = \sqrt{\frac{G_I E_\infty}{2h_A h_B E_A E_B}} \quad (4.34)$$

Crack re-initiation in layer B will not occur if σ^* remains smaller than the ultimate stress of the material B, σ_u^B .

Both criteria for cracks approaching an interface discussed so far consider cracks orthogonal to the interface. The following criterion applies to propagation of an impinging non-orthogonal crack.

4.4.3 Stress-based criterion for orthogonal and non-orthogonal crack propagation across unbonded frictional interfaces

First, Renshaw and Pollard's criterion for orthogonal cracks will be discussed, followed by the Gu and Weng's criterion for non-orthogonal cracks.

Renshaw and Pollard (1995) states that when a low compressive stress is acting normal to the interface, slip and opening along the interface reduce the stress concentration levels at the approaching crack tip (Fig. 4.12), which results in the termination of propagation. On the other hand, when compressive stresses are high enough to inhibit slip and opening along the interface, then the crack propagation through the interface occurs and a new crack reinitiate on the other side of the interface.

Renshaw and Pollard's assumptions and conditions, based on their experimental observations, were the following:

1. Crack crossing occurs through re-initiation of the crack on the opposite side of the interface that contains the impinging crack rather than through continuous propagation through the interface, as shown in Fig. 4.13. Re-initiation should likely occur at a small asperity or notch along the surface of the frictional interface
2. Continuous propagation requires greater compressive stress acting on the interface than the discontinuous
3. The direction of the approaching crack is perpendicular to the maximum tensile stress
4. The frictional interface does not affect the propagation direction of the fracture
5. The loss of stress singularity at the crack tip once it reaches the interface leads to a considerably reduction in stress concentration ahead of the crack tip. This suggests that crack re-initiation on the opposite side of the interface may occur prior to contact when the stress singularity at the approaching crack still exists. As shown in Fig. 4.12, the authors

consider the investigated geometry just prior to crack-interface contact, in which the crack tip is at a distance δ from the interface where $\delta \ll a$ for an approaching crack length of $2a$

6. The maximum stress field that act along the frictional interface can be obtained by setting $\theta = \pm \frac{\pi}{2}$, since this criterion applies only for cracks making an orthogonal angle with the interface, and $r = r_c \left(\pm \frac{\pi}{2} \right)$, since $\delta \ll r_c$ where r_c is the critical radius within which the stresses allow inelastic fracture processes to occur
7. For crack re-initiation to occur, the stresses acting on the interface must not induce slip of the interface, since slip would lead to crack termination at the interface according to this criterion. Thus, the condition for slip not to take place along a frictional interface is:

$$|\tau_{xy(max)}| < \mu \sigma_{xx(max)} \quad (4.35)$$

where $\tau_{xy(max)}$ and $\sigma_{xx(max)}$ are the maximum shear and normal stresses along the interface, respectively (See Fig. 4.14)

8. For a crack to begin to propagate on the other side of the interface, the tensile stress $\sigma_{yy(max)}$ created by the approaching crack must be equal to the tensile strength T_0 of the material on the opposite side of the interface:

$$\sigma_{yy(max)} = T_0 \quad (4.36)$$

Renshaw and Pollard (1995)'s criterion stated that in order for crack crossing to occur:

$$\frac{-\sigma_H}{T_0 - \sigma_V} > \frac{0.35 + \frac{0.35}{\mu}}{1.06} \quad (4.37)$$

where μ is the coefficient of friction, σ_H and σ_V are the far-field stresses.

According to Renshaw and Pollard (1995), interface slip and subsequent fracture termination are more likely to occur at low values of the coefficient of friction.

The stress-based criterion for an impinging non-orthogonal crack crossing an interface, developed by Gu and Weng (2010), is an extension of the Renshaw and Pollard (1995)'s criterion for predicting whether a crack will terminate or propagate across an unbonded frictional interface orthogonal to the incident crack. Similarly to Renshaw and Pollard's approach, this criterion also looks into the stress field near both the crack tip and along the interface, and relates the far-field normal stresses to the tensile strength of the rock and to the interface friction. Both criteria are based on the linear elastic fracture mechanics solution for the stresses near the crack tip, and they

aim to determine the minimum stress that prevent slip along the interface at the moment when the stress on the opposite portion of the interface is sufficient to initiate a crack (Renshaw and Pollard, 1995).

In the Gu and Weng (2010)'s criterion, the authors extended Renshaw and Pollard's criterion so that it could be applied to cracks crossing frictional interfaces at non-orthogonal angles. This criterion is more realistic because natural cracks or interfaces are often not aligned with the principal in-situ stress directions in the rock formation, which means that the intersection angle of the crack approaching the interface may be between 0° and 90° . Considering the scheme in Fig. 4.15 that shows a crack approaching an interface with an intersection angle β , the assumptions and conditions followed by Gu and Weng (2010)'s criterion are:

1. Crack re-initiation is based on the maximum principal stress. The maximum principal stress σ_1 on the opposite side of the interface at $r = r_c$, considering $\theta = \beta$ or $\theta = \beta - \pi$ (i.e. non-orthogonal), is obtained by:

$$\sigma_1 = \frac{\sigma_x + \sigma_y}{2} + \sqrt{\left(\frac{\sigma_x - \sigma_y}{2}\right)^2 + \tau_{xy}^2} \quad (4.38)$$

2. The direction of the maximum principal stress is determined by:

$$\tan 2\theta_p = \frac{2\tau_{xy}}{\sigma_x - \sigma_y} \quad (4.39)$$

Thus, the direction of the reinitiated crack is considered perpendicular to the σ_1 direction. The new crack will eventually turn and propagate in a direction governed by the remote stresses.

3. The maximum tensile stress σ_1 created by the approaching crack must be equal to the tensile strength T_0 of the material on the opposite side of the interface:

$$\sigma_1 = T_0 \quad (4.40)$$

which implies that, for crack crossing in this criterion:

$$\frac{\frac{c_o - \sigma_H}{\mu} - \sigma_v}{T_0 - \sigma_v} > \frac{0.35 + \frac{0.35}{\mu}}{1.06} \quad (4.41)$$

where μ is the coefficient of friction, σ_H and σ_v are the far-field stresses.

4. A crack will re-initiate only if the stresses acting on the interface do not cause slip of the interface, so that the stresses can be transmitted across the interface. For frictional interfaces, the condition for slip to not occur along the interface is:

$$|\tau_\beta| < c_o - \mu \sigma_{\beta y} \quad (4.42)$$

where c_o is the cohesion of the interface, μ is the coefficient of friction, τ_β and $\sigma_{\beta y}$ are the shear and normal stresses on the interface, respectively.

If the shear stress at the interface exceeds its shear strength, interface slip takes place and there is no propagation through the interface (i.e. the crack arrests).

For the case of interfaces without cohesion, Equation 4.41 reduces to Equation 4.37 (i.e. the original criterion by Renshaw and Pollard). The increase in cohesion is expected to increase the tendency of crossing.

Equations 4.43, 4.44, 4.45, 4.46, and 4.47 can be used to compute stresses in the geometry under investigation, as follows.

The combined stress field of the far-field stresses σ_H and σ_v and the fracture tip stresses:

$$\begin{bmatrix} \sigma_x \\ \sigma_y \\ \tau_{xy} \end{bmatrix} = \begin{bmatrix} \sigma_H + \frac{K_I}{\sqrt{2\pi r}} \cos \frac{\theta}{2} \left(1 - \sin \frac{\theta}{2} - \sin \frac{3\theta}{2}\right) \\ \sigma_V + \frac{K_I}{\sqrt{2\pi r}} \cos \frac{\theta}{2} \left(1 + \sin \frac{\theta}{2} - \sin \frac{3\theta}{2}\right) \\ \frac{K_I}{\sqrt{2\pi r}} \sin \frac{\theta}{2} \cos \frac{\theta}{2} \cos \frac{3\theta}{2} \end{bmatrix} \quad (4.43)$$

where K_I is the stress intensity factor, and r and θ are the polar coordinates at the crack tip.

The stresses projected on the interface from the far-field stresses σ_H and σ_v :

$$\begin{bmatrix} \sigma_{r,\beta x} \\ \sigma_{r,\beta y} \\ \tau_{r,\beta} \end{bmatrix} = \begin{bmatrix} \frac{\sigma_H + \sigma_V}{2} + \frac{\sigma_H - \sigma_V}{2} \cos 2\beta \\ \frac{\sigma_H + \sigma_V}{2} - \frac{\sigma_H - \sigma_V}{2} \cos 2\beta \\ -\frac{\sigma_H - \sigma_V}{2} \sin 2\beta \end{bmatrix} \quad (4.44)$$

The fracture tip stresses projected on the interface:

$$\begin{bmatrix} \sigma_{tip,\beta x} \\ \sigma_{tip,\beta y} \\ \tau_{tip,\beta} \end{bmatrix} = \begin{bmatrix} K - K \sin \frac{\theta}{2} \sin \frac{3\theta}{2} \cos 2\beta + K \sin \frac{\theta}{2} \cos \frac{3\theta}{2} \sin 2\beta \\ K + K \sin \frac{\theta}{2} \sin \frac{3\theta}{2} \cos 2\beta - K \sin \frac{\theta}{2} \cos \frac{3\theta}{2} \sin 2\beta \\ K \sin \frac{\theta}{2} \sin \frac{3\theta}{2} \sin 2\beta + K \sin \frac{\theta}{2} \cos \frac{3\theta}{2} \cos 2\beta \end{bmatrix} \quad (4.45)$$

The combined shear stress on the interface:

$$\tau_\beta = \tau_{tip,\beta} + \tau_{r,\beta} = K \sin \frac{\theta}{2} \sin \frac{3\theta}{2} \sin 2\beta + K \sin \frac{\theta}{2} \cos \frac{3\theta}{2} \cos 2\beta - \frac{\sigma_H - \sigma_V}{2} \sin 2\beta \quad (4.46)$$

The combined normal stress on the interface:

$$\sigma_{\beta y} = \sigma_{tip,\beta y} + \sigma_{r,\beta y} = K + K \sin \frac{\theta}{2} \sin \frac{3\theta}{2} \cos 2\beta - K \sin \frac{\theta}{2} \cos \frac{3\theta}{2} \sin 2\beta + \frac{\sigma_H + \sigma_V}{2} - \frac{\sigma_H - \sigma_V}{2} \cos 2\beta \quad (4.47)$$

The authors also stated, from experimental observations, that the smaller the intersection angle β , the more unlikely crack propagation through the interface occurs and the more likely that the interface slips.

Even though the stress-based criterion for crack propagation across a frictional interface proposed by Renshaw and Pollard (1995) pointed out that the crossing crack is more likely to occur with an offset from the original crack plane (i.e. creating a step-over crack), the authors did not explore conditions for step-over.

The next criterion to be discussed addresses the step-over cracks at interfaces.

4.4.4 Maximum principal tensile stress criterion for predicting step-over cracks at the interface

Cooke and Underwood (2001) investigated crack step-over at interfaces using the maximum principal tensile stress criterion as the crack approaches the contact. According to this criterion, the distribution of maximum tensile stress near a crack tip highlights the potential for crack initiation off the plane of the parent crack (i.e. the impinging crack that reaches the interface). As depicted in Fig. 4.16, the greatest value of maximum tension occurs about 1.5 cm to either side of the parent fracture. Two hypothetical daughter fractures are sketched perpendicular to the maximum tension in these locations ahead of the parent fracture tip. The authors stated that new cracks commonly initiate off the plane of the parent crack, resulting in fracture jogs or step-overs. However, if the tensile stresses at the interface are not large enough to initiate new step-over cracks, the parent crack may terminate at the interface.

Dollar and Steif (1989) suggested that re-initiation of the crack on the opposite side of the interface may occur when the stress singularity at the approaching crack tip still exists, i.e. prior to reaching the interface. Therefore, in Cooke and Underwood's analysis, which simulated a crack approaching a bonded contact, the maximum principal tensile stress along the intact side of the interface (i.e. the side that did not contain the approaching crack) for different crack tip-interface distances was examined. The authors observed that the two locations of greatest principal tensile stress that exist at either side of the crack (Figure 4.17) are most pronounced when the crack is within 1 cm of the interface and tensile stress peaks occur along the interface within 1 cm of $x = 0$, where x is the point of contact with the interface.

Furthermore, the investigation conducted by Helgeson and Aydin (1991) indicated that greater distance from the parent crack (i.e. the crack approaching the interface) to the position of greatest maximum tensile stress at the interface promotes the development of crack step-overs rather than crack propagation through the interface.

The different criteria discussed so far were either energy-based or strength-based. The next criterion to be presented, known as the cohesive zone, bridges these two historically distinct approaches for crack initiation prediction. Unlike the crack-interface criteria mentioned previously, the cohesive zone model can predict the behavior of both tensile and shear cracks since it considers mixed mode I-II conditions.

4.4.5 Traction-separation criterion (cohesive zone model)

The cohesive zone approach has its origins in the early models of Dugdale (1960) and Barenblatt (1962) whose investigations considered the effects of finite stresses at a crack tip. It was later adapted within the finite element framework by Needleman (1987). This approach may be used when the fracture process zone is not sufficiently small compared to other dimensions (i.e. LEFM does not apply) and cohesive forces that exist in the process zone must be taken into consideration.

A cohesive zone model (CZM) incorporates a region in front of the crack (i.e. the cohesive zone) where a traction-separation criterion describes the fracture process. The size of the cohesive zone is related to the material ductility. Among different cohesive zone models, the exponential traction-separation criterion developed by Xu and Needleman (1994) is the most popular in fracture simulation.

CZM can only model material damage in the crack propagation direction. The damage zone is simplified into a thin strip (i.e. zero-thickness elements represented by the dashed line in Fig. 4.18). There is a stress-displacement relation across this strip plane which represents the degradation mechanisms in the fracture process zone (Fig. 4.18).

In this criterion, the tractions across the crack plane increase with displacement up to a maximum cohesive strength, and then decay to zero at a critical opening displacement. When the critical displacement is attained, the material in the cohesive zone is assumed to have failed, and

the crack advances. That means that a crack is a gradual phenomenon in which the separation of elements occurs across the cohesive zone and is resisted by cohesive tractions.

A traction vector T acting on a cohesive surface, which is function of an interfacial potential φ , is composed of normal and tangential components T_n and T_t , respectively.

$$T = \frac{\partial \varphi(\Delta)}{\partial(\Delta)} \quad (4.48)$$

with $\Delta = (\Delta_n, \Delta_t)$

where $\Delta_n = n \cdot \Delta$ and $\Delta_t = t \cdot \Delta$; n and t are, respectively, unit vectors normal and tangent to the cohesive surface at a given point.

The interfacial potential can be expressed as (Xu and Needleman, 1994):

$$\varphi(\Delta_n, \Delta_t) = \varphi_n + \varphi_n \exp\left(-\frac{\Delta_n}{\delta_n}\right) \left\{ \left[1 - r + \frac{\Delta_n}{\delta_n}\right] \frac{1-q}{r-1} - \left[q + \left(\frac{1-q}{r-1}\right) \frac{\Delta_n}{\delta_n}\right] \exp\left(-\frac{\Delta_t^2}{\delta_t^2}\right) \right\} \quad (4.49)$$

where δ_n and δ_t represent characteristic lengths, which are defined as the normal and $\frac{\sqrt{2}}{2}$ times the relatively tangent displacement of the cohesive surfaces at the maximum normal and shear cohesive forces, respectively.

$$T_n(\delta_n) = \sigma_{max} \quad (4.50)$$

and

$$T_t\left(\frac{\delta_n}{\sqrt{2}}\right) = \tau_{max} \quad (4.51)$$

where σ_{max} and τ_{max} are the maximum values of normal traction and shear traction of the cohesive surface, respectively.

Furthermore,

$$q = \frac{\varphi_t}{\varphi_n} \quad (4.52)$$

and

$$r = \frac{\Delta'_n}{\delta_n} \quad (4.53)$$

where $r = \Delta'_n$ is the value of Δ_n when complete shear separation of elements across the cohesive zone has occurred without resulting in normal tension (i.e. $T_n = 0$). q and r are assumed to be equal to zero.

The resulting equations for normal and shear tractions are then written as:

$$T_n = -\frac{\varphi_n}{\delta_n} \exp\left(-\frac{\Delta_n}{\delta_n}\right) \left[\frac{\Delta_n}{\delta_n} \exp\left(-\frac{\Delta_t^2}{\delta_t^2}\right) + \frac{1-q}{r-1} \left[1 - \exp\left(-\frac{\Delta_t^2}{\delta_t^2}\right) \left[r - \frac{\Delta_n}{\delta_n} \right] \right] \right] \quad (4.54)$$

$$T_t = 2 \left(-\frac{\varphi_n \Delta_t}{\delta_t^2} \right) \left[q + \left(\frac{r-q}{r-1} \right) \frac{\Delta_n}{\delta_n} \right] \exp \left(-\frac{\Delta_n}{\delta_n} \right) \exp \left(-\frac{\Delta_t^2}{\delta_t^2} \right) \quad (4.55)$$

φ_n and φ_t , respectively, represent the normal and shear amount of work necessary to complete separation.

Without loss of generality, it is also assumed in the computation that $q=1$ and $r=0$, and assuming that

$$T_n = T_n(\Delta_n, \Delta_t = 0) \quad (4.56)$$

and

$$T_t = T_t(\Delta_n = 0, \Delta_t) \quad (4.57)$$

the uncoupled tractions are obtained.

Finally, by using equations 4.58 and 4.59, the following relations for the fracture energy φ_n and φ_t resulting, respectively, from normal and tangential separation are calculated as:

$$\varphi_n = \sigma_{max} \exp(1) \delta_n \quad (4.58)$$

$$\varphi_t = \sqrt{\frac{\exp(1)}{2}} \tau_{max} \delta_n \quad (4.59)$$

T_n and T_t are CZMs for mode-I (i.e. tensile) and mode-II (i.e. shear) loading, respectively. Mixed-mode effects are modeled by combining normal and shear displacements into a single parameter that is used in a traction-separation law to indicate overall load-carrying ability (Tvergaard and Hutchinson, 1993).

The traction–separation laws are prescribed independently, thus they need to be coupled through a mixed-mode failure criterion.

Parmigiani and Thouless (2006) used CZM to analyze the problem of crack deflection or penetration at interfaces. As shown in Fig. 4.19, one can observe the sets of cohesive elements ahead of an impinging orthogonal crack and along the interface. A layer of thickness h and with an elastic modulus of E_f and a Poisson's ratio of ν_f is bonded to a substrate of thickness d , where $d = 1/4 \cdot 10h$. The substrate has an elastic modulus of E_s and a Poisson's ratio of ν_s . A crack extends from the top surface to the interface, and is normal to the interface. Sets of cohesive elements exist ahead of the crack in the substrate and along the interface. There is a plane of symmetry along the crack, and the system is loaded by a uniform displacement applied to the ends of the specimen.

In Parmigiani and Thouless' study, a linear failure criterion of the form

$$\frac{G_I}{\Gamma_I} + \frac{G_{II}}{\Gamma_{II}} = 1 \quad (4.60)$$

was used, where G_I is the mode-I energy release rate, Γ_I is the mode-I toughness, G_{II} is the mode-II energy release rate, and Γ_{II} is the mode-II toughness.

The use of Equation 4.60 in cohesive-zone analyses can mimic mixed-mode fracture criteria for linear-elastic fracture mechanics (LEFM). The phase angle is defined as

$$\psi = \arctan \frac{G_{II}}{G_I} \quad (4.61)$$

where ψ has its usual definition under LEFM conditions of

$$\psi = \arctan \frac{K_{II}}{K_I} \quad (4.62)$$

and K_I and K_{II} are the mode-I and mode-II stress intensity factors at the crack tip (Hutchinson and Suo, 1992). The general forms of the mode-I and mode-II traction-separation laws used in Parmigiani and Thouless (2006)'s study are shown in Fig. 4.20. The mode-I cohesive strength is $\hat{\sigma}$, the mode-II cohesive strength is $\hat{\tau}$, the mode-I toughness is Γ_I , and the mode-II toughness is Γ_{II} . Generalized forms for the traction–separation laws were used, as the precise shape does not generally have a significant effect on fracture. The strength and toughness (area under the curve in Fig. 4.20) are the two dominant parameters that control fracture, and cracks can propagate only if both the stress and energy criteria are met.

In the case shown in Fig 4.19, if the impinging tensile crack propagates, it will do so under pure mode-I conditions. The mode-I substrate toughness is designated as G_s , and the mode-I strength is designated as $\hat{\sigma}_s$. The interface fails under mixed-mode conditions due to the linear failure criterion used in this study, and a mixed-mode analysis is required for crack propagation along the interface. Parmigiani and Thouless (2006) observed that no matter how tough an interface is, crack deflection can always be induced if the strength of the interface is low enough compared to the strength of the medium.

One main limitation of using CZM for predicting crack penetration or deflection at the interface is that it does not take into consideration the possibility of step-over cracks (i.e. a crack that can deflect out of an interface after delamination of the interface).

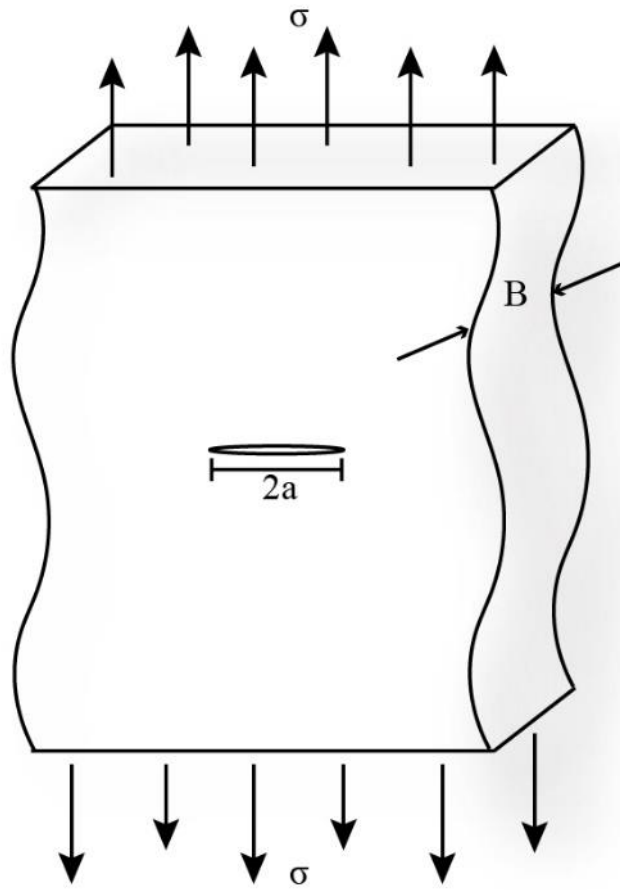


Figure 4.1 Infinite plate with a central elliptical crack

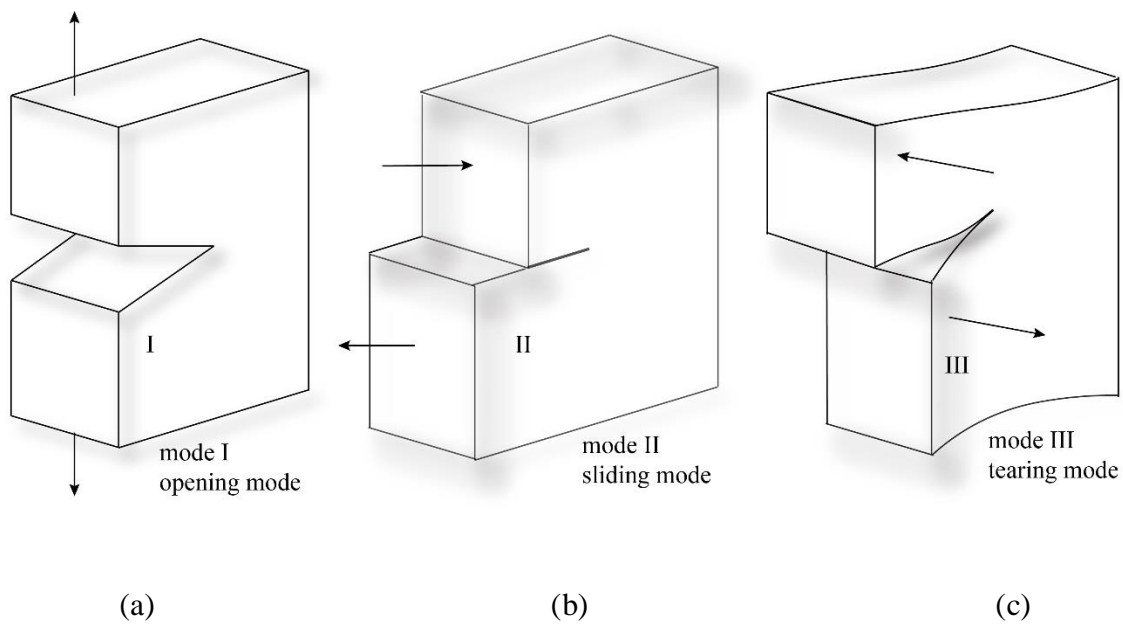


Figure 4.2 The three modes of loading. a) mode I; b) mode II; mode III

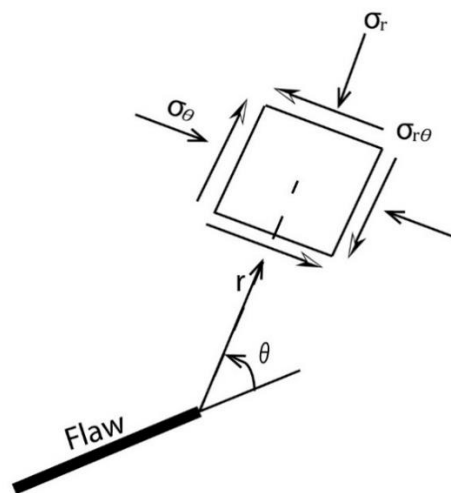


Figure 4.3 Cylindrical stresses of an element near crack tip

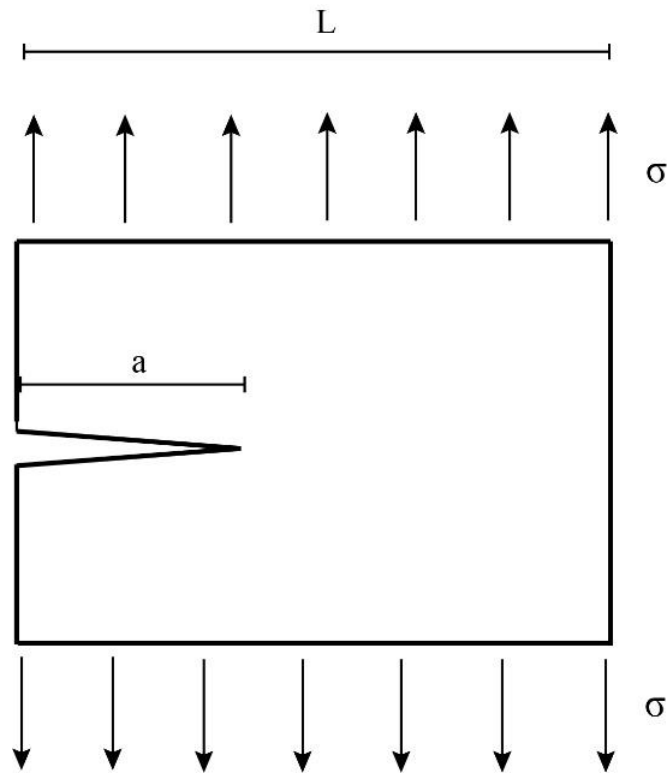


Figure 4.4 Specimen length L and crack length a in a single edge crack

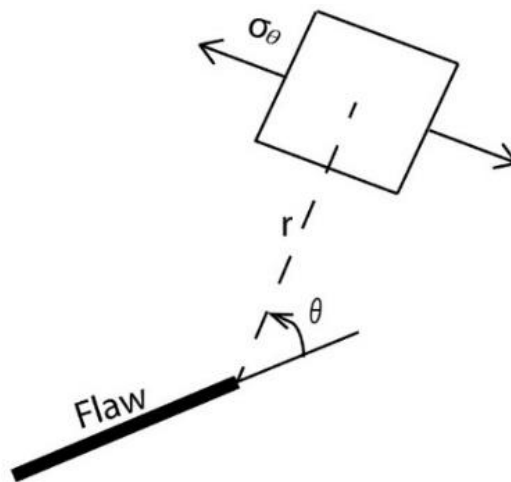
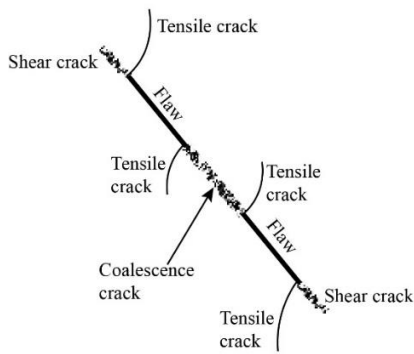
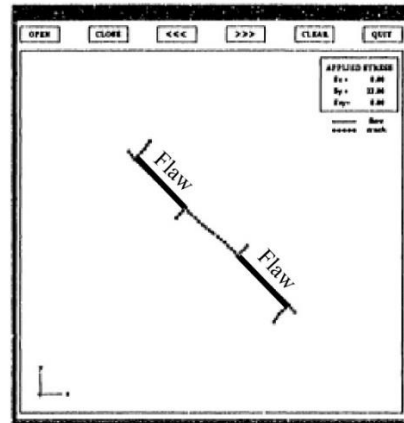


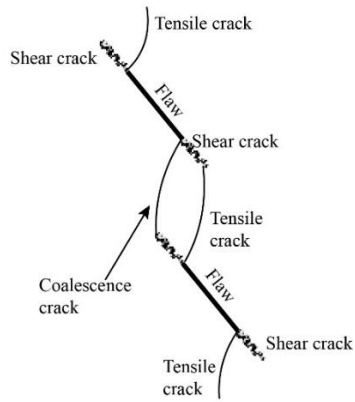
Figure 4.5 Tangential stresses around a flaw tip



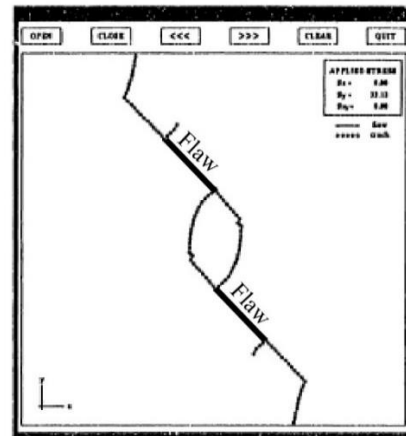
(a)



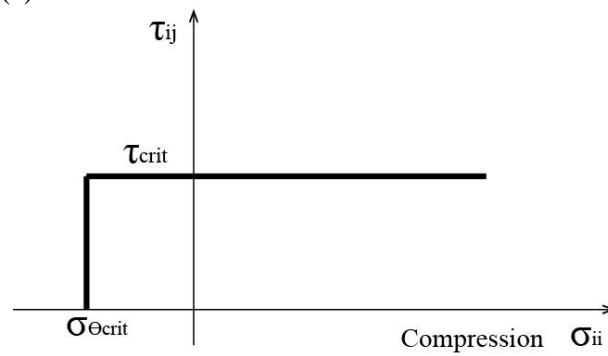
(b)



(c)



(d)



(e)

Figure 4.6 Bobet's investigation in gypsum under uniaxial compression. (a) Experimental and (b) Numerical results for a flaw geometry $S=0$ $C=-2a$ $\beta=45^\circ$; (c) Experimental and (d) Numerical results for a flaw geometry $S=-2a$ $C=-2a$ $\beta=45^\circ$; (e) Failure envelope for Bobet's criterion
Adapted from Bobet, 1997

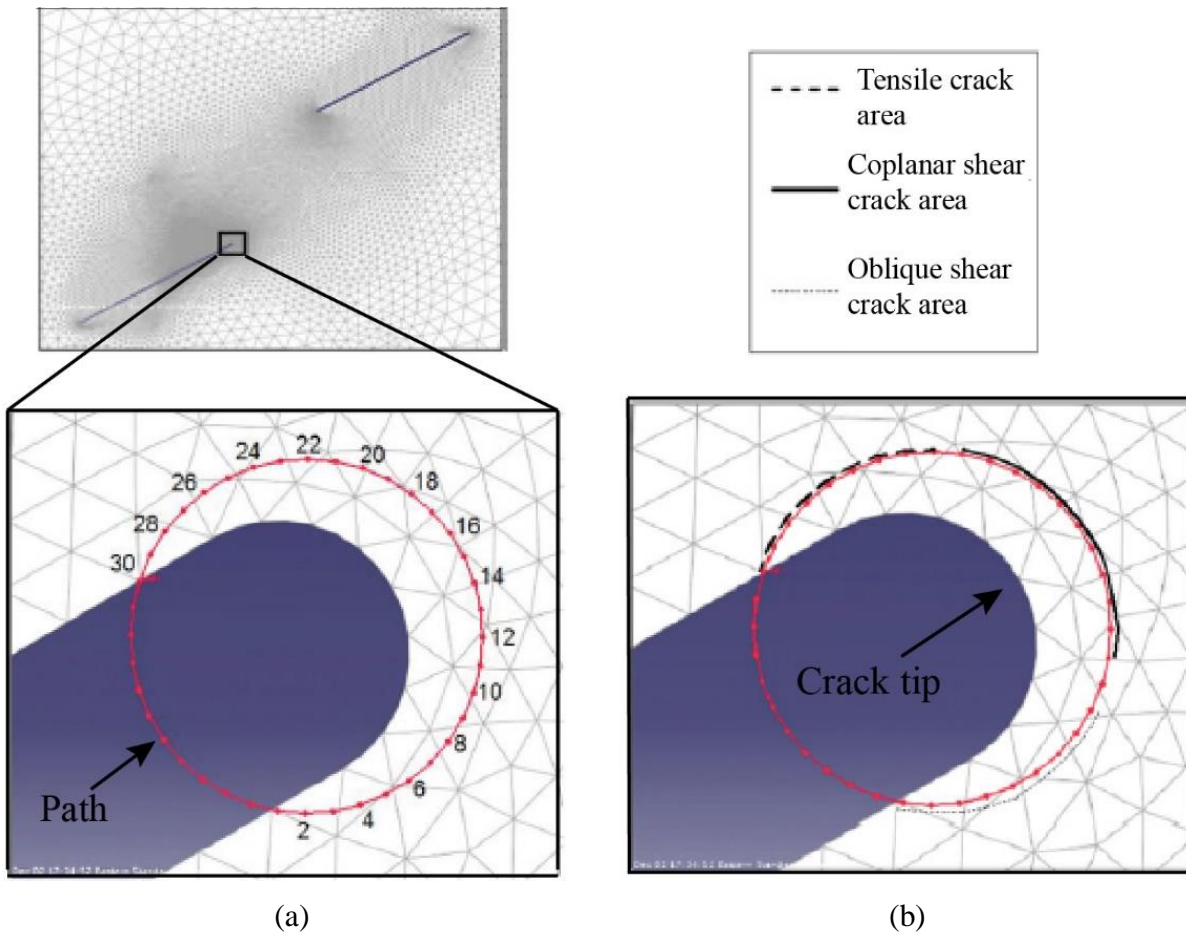


Figure 4.7 Goncalves da Silva (2013)'s investigation. (a) path and point IDs; (b) Areas considered in the studied path. Source: Adapted from Goncalves da Silva (2013)

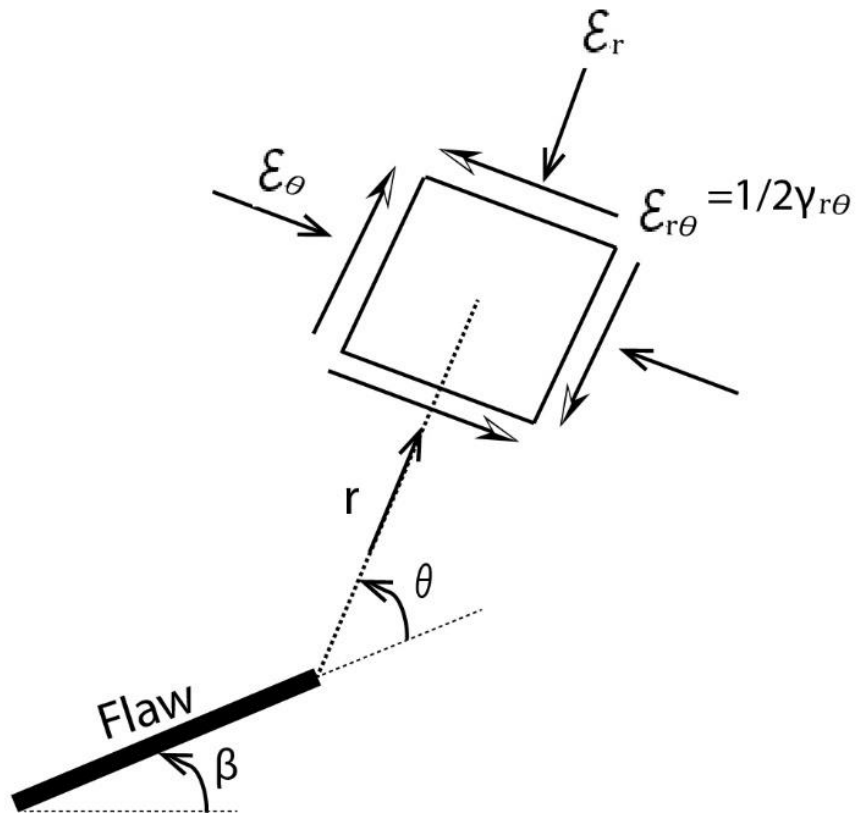


Figure 4.8 Strain field around a crack tip/ cylindrical strains of an element radial to the flaw tip

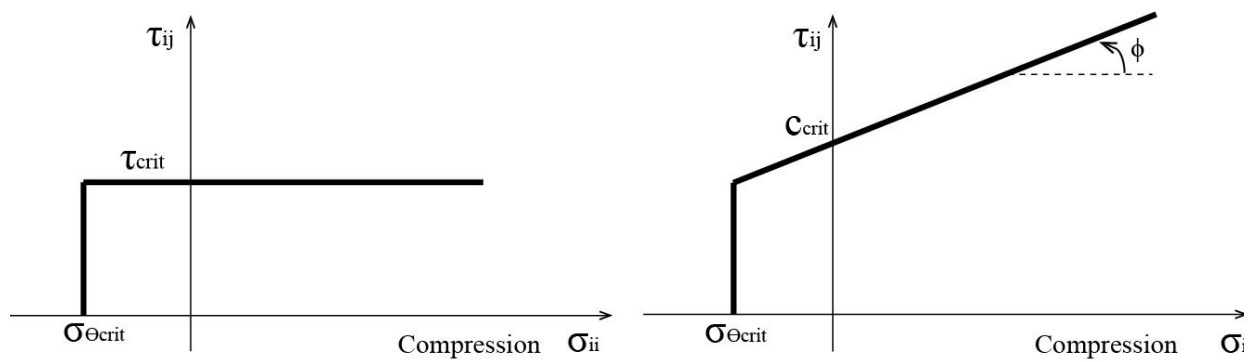


Figure 4.9 Failure envelope for: (a) Bobet's criterion; (b) Goncalves da Silva's criterion (after Goncalves da Silva, 2012)

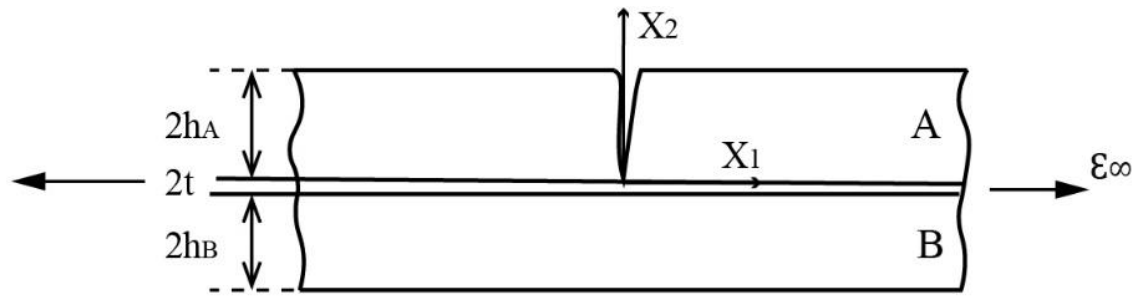


Figure 4.10 Schematic problem of a crack reaching an interface investigated by Lemaitre et al. (1996)

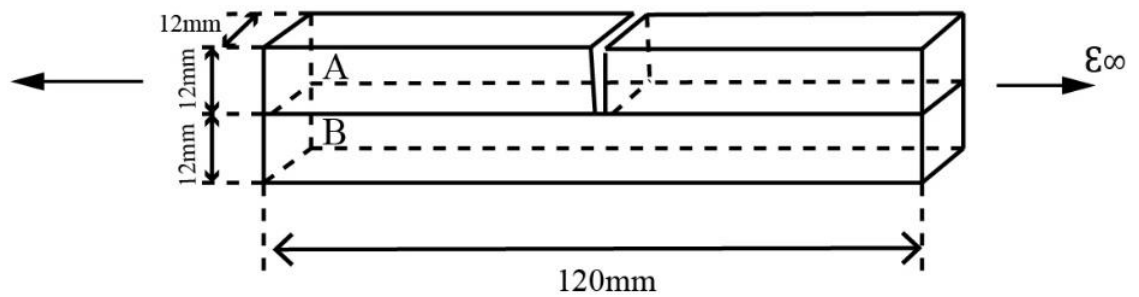


Figure 4.11 PMMA Specimen investigated by Lemaitre et al. (1996)

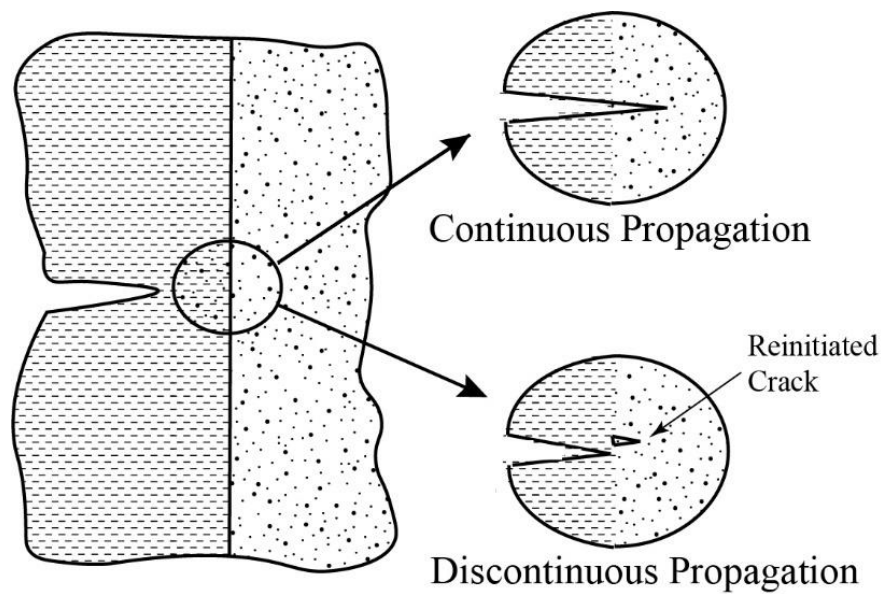


Figure 4.13 Continuous vs discontinuous propagation across an interface. In the top model, propagation across the interface is continuous (i.e. as if the interface was not there). In the bottom model, crossing occurs when the stresses ahead of the approaching crack tip reinitiate a new crack on the other side of the interface. In Renshaw and Pollard's criterion, crossing is a discontinuous process.

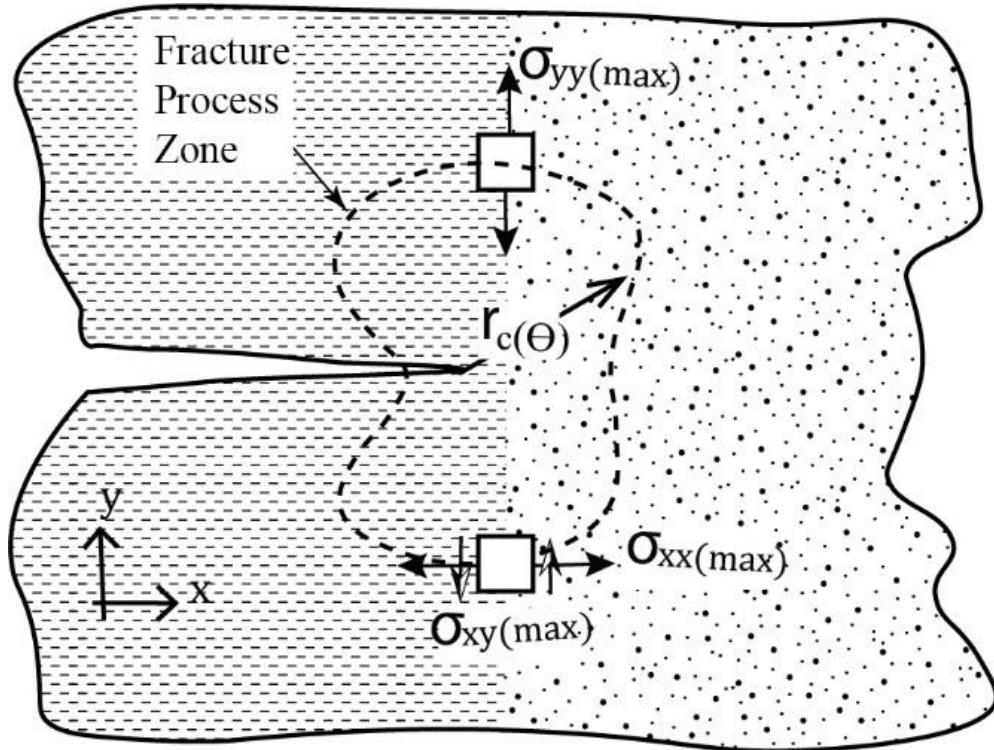


Figure 4.14 Geometry and stresses of the fracture process zone. Stresses within this zone are assumed to be equal or less than the stresses calculated from the stress field (Equation 4.7) at a distance $r_c(\theta)$. The approximate maximum magnitude of the components of stress $\sigma_{ij(\max)}$ acting along the interface can thus be calculated using the stress field equations with $\theta = \pm \frac{\pi}{2}$ and

$$r = r_c\left(\pm \frac{\pi}{2}\right)$$

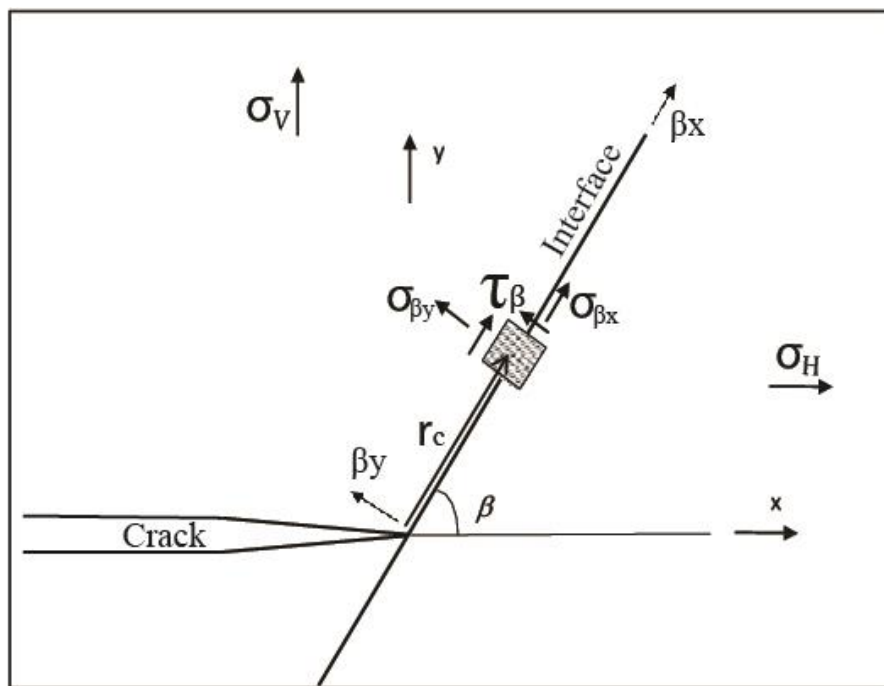


Figure 4.15 Schematic of fracture approaching interface in Gu and Weng (2010)'s criterion

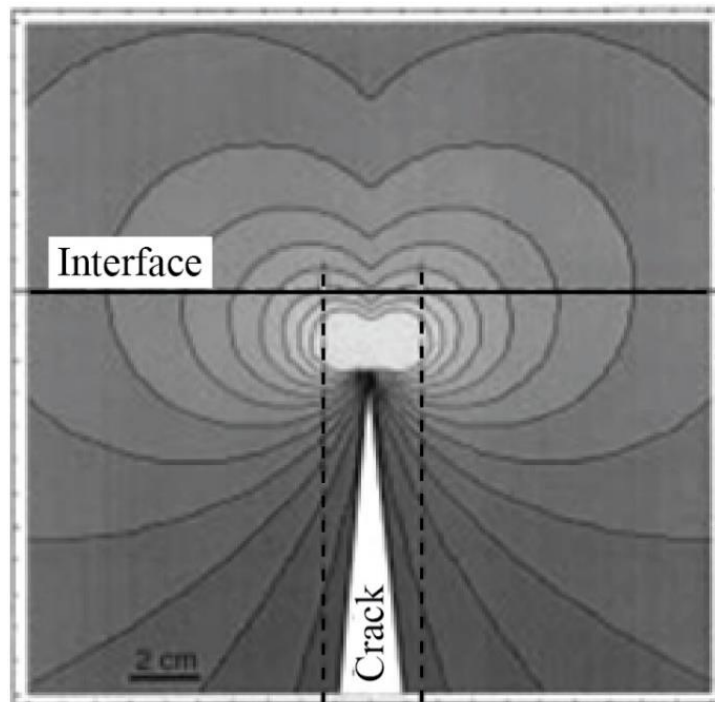


Figure 4.16 Maximum tension (principal stress) around the tip of a 1m vertical crack under 5MPa remote isotropic tension. Contours range from 2 to 24 MPa (tension is positive). Along a bonded interface 2 cm ahead of the crack, the greatest value of maximum tension occurs about 1.5 cm to either side of the parent fracture. Two hypothetical daughter fractures are sketched perpendicular to the maximum tension in these locations ahead of the parent fracture tip.

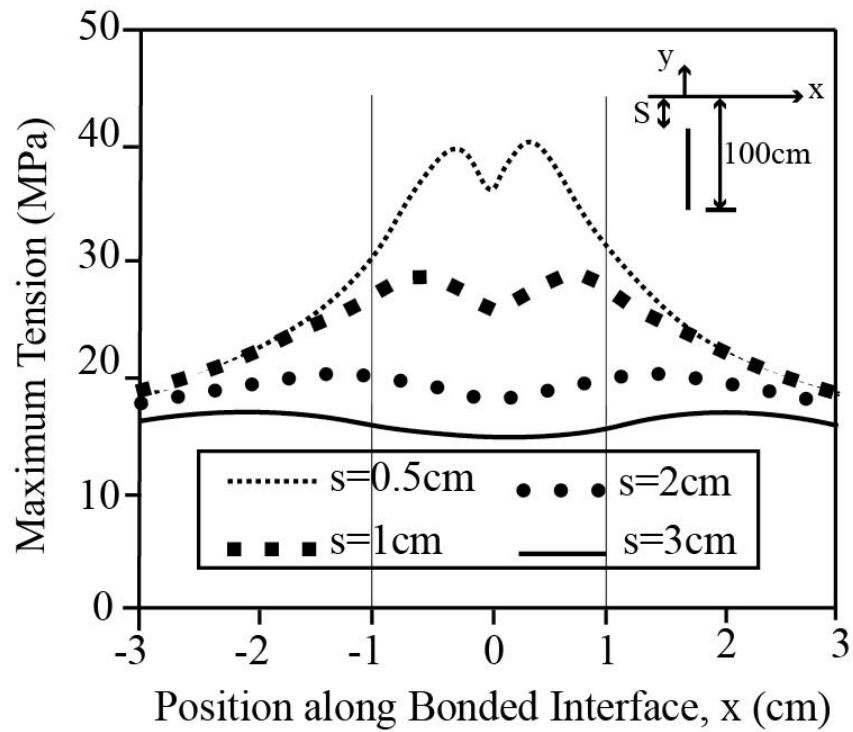


Figure 4.17 Maximum tensile stress along a bonded interface. Maximum tension increases as the crack approaches the interface. The greatest tension occurs to either side of the parent fracture and moves closer to $x=0$ as the fracture approaches the interface.

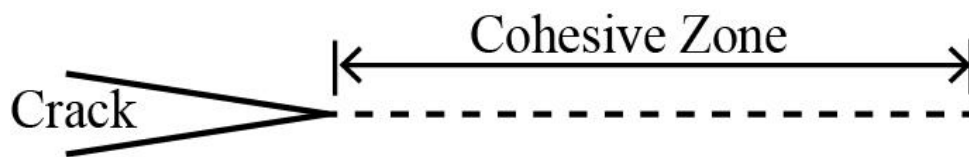


Figure 4.18 Cohesive Zone ahead of a crack

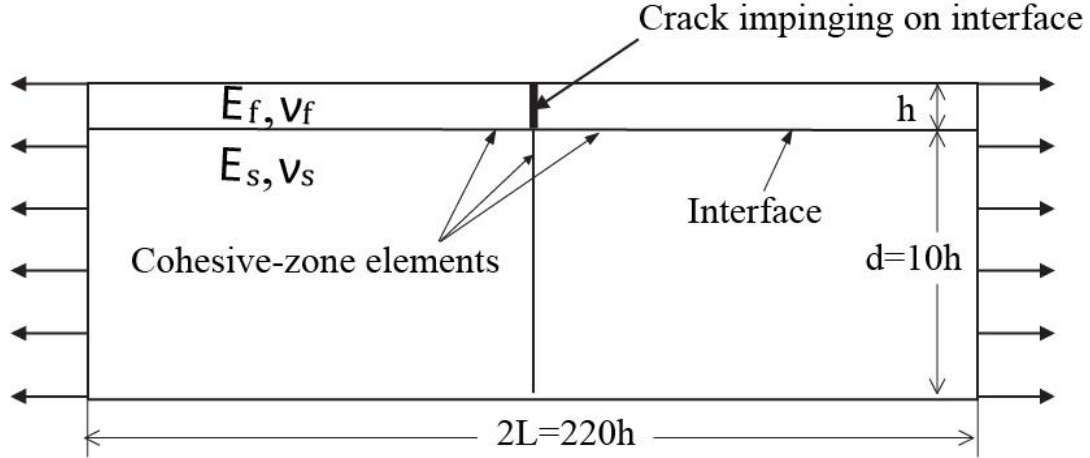


Figure 4.19 The laminated geometry used to study crack deflection in this paper. A layer of thickness h and with an elastic modulus of E_f and a Poisson's ratio of ν_f is bonded to a substrate of thickness d , where $d \approx 10h$. The substrate has an elastic modulus of E_s and a Poisson's ratio of ν_s . There is a crack that extends from the top surface to the interface, and is normal to the interface. Sets of cohesive elements exist ahead of the crack in the substrate and along the interface. There is a plane of symmetry along the crack, and the system is loaded by a uniform displacement applied to the ends of the specimen.

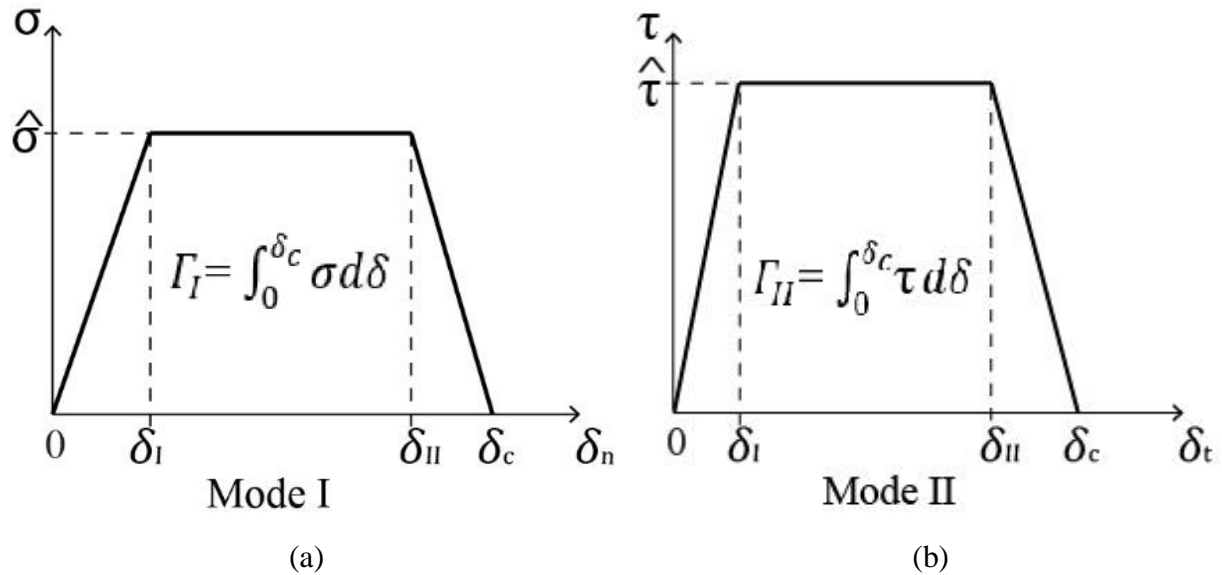


Figure 4.20 Schematic illustration of the (a) mode I, and (b) mode II traction-separation laws used for the cohesive zone model in Parmigiani and Thouless (2006)'s study.

5. NUMERICAL INVESTIGATION: METHODOLOGY AND RESULTS

5.1 Introduction

In addition to the experimental investigation, a numerical study was conducted using the Extended Finite Element Method (XFEM) on ABAQUS, to further investigate the fracture behavior observed in the experiments at different loading stages and, more specifically, the influence of the different types of interfaces. The objective of this chapter is to conduct an extensive investigation of the stress fields around the tips of the flaws and new cracks, as well as along the interface in the modeled specimens, to determine if there is any relationship between stresses and crack initiation and propagation (i.e. type and direction of cracks).

In addition to this Introduction, the Chapter has two more Sections. Section 5.2 includes the methodology used for the numerical investigation, and Section 5.3, the numerical results.

5.2 Methodology

5.2.1 Model Description for XFEM simulations in ABAQUS

In order to validate the fracture predictions from XFEM, a comparison between tangential stresses at the crack tip of a flaw inclined 45° from the horizontal, obtained both analytically and numerically (i.e. from ABAQUS), was performed. In Fig. 5.1, one can observe that the XFEM's numerical predictions are in good agreement with the analytical results, which supports the validity of the numerical model.

As mentioned in Section 3.2.5.4, when it comes to crack initiation from flaws and interfaces, as well as to the behavior of tensile and shear cracks interacting with different types of interfaces, all three types of flaw geometries (i.e. left-stepping, right-stepping and overlapping) tested experimentally yielded similar observations, namely:

1. The interface itself is an important contributor to new cracks;
2. The presence of an interface in the specimens reduces crack initiation stress;
3. An increase in both roughness and inclination of the interface (i.e. from horizontal to 70° from the vertical) reduces crack initiation stress;

4. Changes in interface roughness or inclination angle do not affect the angles at which cracks initiate at the interface. Those angles ranged from 70° to 90° ;
5. Tensile cracks that meet the interface at 30° to 60° angle get arrested, while those at angles greater than 70° cross the interface with an offset of 0 – 1.2 mm. Shear cracks that meet the interface at 20° to 60° angles get arrested at the interface, while those at 70° angle or larger cross the interface with an offset range of 0 – 1.76 mm.

Given the general findings for all types of flaw geometries, the numerical investigation focused on one of the three flaw geometries in the experiments, as representative of the other cases. Models with a coplanar flaw geometry $0-2a30^\circ$, with two open flaws and a frictional interface, were then used in the simulations with ABAQUS, as shown in the Fig. 5.2. This geometry was selected among the others for the numerical investigation because it presented experimental observations similar to the other geometries, as discussed (see also Chapter 3).

In the models, the material (i.e. gypsum) is considered homogeneous, isotropic and linear elastic. The following material properties are used in the simulations: Young's modulus $E=13,800\text{MPa}$; and Poisson's ratio $\nu=0.15$. These values were obtained from uniaxial compression tests on intact gypsum specimens.

Similarly to the specimens tested experimentally, the dimensions of the modeled specimens are: 203.2mm high and 101.6mm wide. An interface that splits the model in two may have either a 90° or 80° angle from the vertical. Furthermore, two different interface roughness are investigated; that is, interface friction angles of 35° and 50° .

The two pre-existing flaws are inclined 30° from the horizontal and have a 12.7mm length, which corresponds to the specimens used in the experiments. The flaws are assumed having no opening, but to remain open in compression; that is, the normal and shear stresses at the faces of the flaws are zero. Any new cracks may be either open or close, depending on whether they are tensile or shear, or may open or close during the simulations.

Figure 5.2 shows the geometry of one of the modeled specimens in ABAQUS. The bottom boundary of the model is fixed in all direction while the top boundary is allowed to move. The load is then applied to the top boundary of the model, as a uniform pressure.

The mesh around the cracks is finer than at any other regions in the model, with elements of size 0.05mm. This element size is selected since it provides a refined mesh with good precision

to capture stresses in the vicinity of the cracks. As observed in Fig. 5.1, numerical predictions of stresses in ABAQUS using such element size are in good agreement with analytical solutions. Furthermore, the element type used in the simulations is CPE4R; that is, 4-node bilinear plane strain quadrilateral element, which is widely used by researchers who conduct investigations in XFEM. In the simulations, the tips of the flaws are assumed as sharp.

In order to investigate the interaction between the interface and the flaws or the new cracks, specific observations made during the experiments were modeled using XFEM, which included all the cracks observed in the experiments at different loading stages.

For tensile cracks, a frictionless tangential behavior is adopted. For shear cracks, a frictional interface is adopted, with a coefficient of friction of 0.3. The value of the coefficient of friction is decided by trial and error, by comparing model predictions with experiments. This value is in agreement with that obtained by Bobet (1997).

The friction characteristics of the interface is included as a “surface-to-surface” interaction. The contact interaction is defined by a coefficient of friction (which depends on the roughness of the interface) to describe tangential behavior, and a “hard-contact pressure-overclosure” to describe normal behavior.

5.2.2 Methodology used in the numerical analysis

The approach used in this study is stress-based, in which the order of initiation of cracks is decided by the stress levels at the flaw tip. This means that the first tensile and shear cracks occur in the direction in which the tensile and shear stresses, respectively, are the highest; the second tensile and shear crack occurs in the direction in which the tensile and shear stresses, respectively, are the second highest, and so on. This criterion was selected for this investigation because it yielded very good predictions for simulations of pre-cracked specimens without interfaces, as discussed in Section 4.3.5.1 in Chapter 4.

Initially, a circular path is created around a flaw tip, and stresses are obtained at several points along the path (See Fig. 5.3a), similar to the approach discussed in section 4.3.5.1.

A sensitivity analysis is conducted to select the radius of the circular path where the stresses are measured. Path radii ranging from 0.2 to 0.7mm are found to be the best fit for the analysis.

The maximum principal stresses (σ_I) and the maximum shear stress (τ_{12}^{max}) are then obtained along the predefined path (See Fig. 5.3b). In ABAQUS, positive results correspond to

tensile stresses, while negative results correspond to compressive stresses. The maximum tensile stresses (σ_I) were extracted from the ABAQUS output and used to determine the direction of initiation of tensile cracks. The maximum shear stresses (τ_{12}^{max}) were used for the direction of initiation of shear cracks and is calculated as follows: $\tau_{12}^{max} = \frac{1}{2}(\sigma_I - \sigma_{III})$, where σ_I is the maximum principal stress and σ_{III} is the minimum principal stress, both obtained directly from the ABAQUS output.

In Fig. 5.3b, the maximum principal stresses (σ_I), plotted along the studied path, shows a maximum, corresponding to point 1. However, since point 1 is at the intersection between the flaw and the path, it is also necessary to investigate the maximum principal stress vectors to find the direction of the tensile crack.

Maximum principal stresses in the proximity of the flaw are shown in Fig. 5.4 (maximum principal stress contour - σ_I) and Fig. 5.5 (σ_I vectors). By analyzing these figures, one can observe that there is a region over the upper face of the flaw tip where tensile stress occurs. This is the region where a tensile crack is most likely to initiate, and in a direction that is perpendicular to the maximum principal stress direction. The prediction of the tensile cracks initiation direction using this approach is in accordance with experimental observations, as it will be shown later in Section 5.3.

The maximum shear stress (τ_{12}^{max}) plot reveals two maxima (Fig. 5.3b), corresponding to point 20 (making a 50° angle with the flaw plane) —global maximum—; and point 5 (making a -130° angle with the flaw plane). The fact that the shear stress at point 20 is higher than the shear stress at point 5 means that the predicted shear crack at point 20 would occur first (See Fig. 5.6). This is in accordance with experimental observations, as it will be presented later in Section 5.3.

The maximum principal tensile stress criterion is also used to predict crack step-over at the interfaces, as the crack approaches the contact. As mentioned in Section 4.4.5, in this criterion, the distribution of maximum tensile stress near a crack tip highlights the potential for crack initiation off the plane of the parent crack (i.e. the crack that reaches the interface). Previous researchers (e.g. Cooke and Underwood, 2001; Dollar and Steif, 1989) indicated that re-initiation of the crack on the opposite side of the interface (i.e. the side without the approaching crack) may occur prior to contact when the stress singularity at the approaching crack tip still exists. In this study, the distance between the approaching crack and the interface ranged between 1 to 2 mm. A linear path is created on the opposite side of the interface (i.e. the side that does not contain the approaching

crack) to obtain the maximum principal tensile stresses within a distance of 0.1mm from the interface (See Fig. 5.7). These distances were selected based on the discussion in Section 4.4.5 in Chapter 4. In the example shown in Fig. 5.7, the crack that reinitiated across the interface is predicted to be located at a distance of 1mm from the plane of the approaching crack, which corresponds to the distance from the approaching crack plane to the greatest maximum principal tensile stress. In this case, the distance of 1mm is not large enough to promote tensile crack step-over at the interface, a fact that is supported by the experimental findings since crack step-overs were only observed in cases with distances, between the reinitiated crack and the approaching crack, starting at 1.2mm. It is expected that larger distances from the crack approaching the interface to the position of greatest maximum tensile stress will promote crack step-overs, rather than crack propagation through the interface. The distance for crack step-over was calibrated by the experimental findings: If the distance between the approaching crack plane and the point of maximum tensile stress at the interface is smaller than the minimum step-over distances observed in the experiments, then the approaching crack makes a curve before reaching the point of maximum tensile stress at the interface and crosses the interface without promoting step-over). However, if the distance between the approaching crack plane and the point of maximum tensile stress at the interface exceeds the minimum step-over distances observed in the experiments, then the approaching crack reaches the interface and reinitiates across the interface with an offset (i.e. step-over).

5.3 Numerical Simulation Results

The numerical simulation results section consists of 5 sub-sections. Sections 5.3.1 through 5.3.4 present numerical predictions of initiation direction of cracks originated at the flaw tips and at the interface for specimens with geometry $0-2a30^\circ$ containing different interface characteristics, as well as a comparison of these numerical findings with those of the experiments. Section 5.3.5 then provides a discussion about the effects of interface roughness and inclination angle on crack initiation and interaction with an interface.

5.3.1 Geometry 0-2a30° with interface inclined 90° with the vertical and contact friction angle of 50°

Table 5.1 sums up the results from the analysis for the prediction of direction of cracks initiation and interaction with the interface. The results are based on the stress-based approach described earlier, for a specimen with geometry 0-2a30° with interface inclined 90° with the vertical and contact friction angle of 50°. The table also shows the crack paths observed experimentally using digital image correlation (DIC). The following observations are made:

5.3.1.1 Tensile cracks initiating from flaws

For the tensile cracks initiated at the outside tips of the pre-existing flaws (i.e. cracks 1 and 2) and those originated at the inside tips of the pre-existing flaws (i.e. 3 and 4) at 6.64MPa, it is numerically predicted that they all initiate in a direction perpendicular to the pre-existing flaw plane, which is in accordance with the crack directions observed in experiments (See Table 5.1(a) for comparison between the cracks direction obtained numerically and experimentally). To exemplify this, one can refer to Fig. 5.5, which shows that tensile crack 4 in Table 5.1(a) is likely to originate in a direction that is perpendicular to the maximum principal stress direction (i.e. 90° from the flaw plane in this case).

5.3.1.2 Shear cracks initiating from flaws

Shear cracks 12, shown in Table 5.1(g), originated at the inside tip of the pre-existing bottom flaw at 26.79MPa is predicted to initiate at 80° from the horizontal through the numerical approach. While another shear crack 16, depicted in Table 5.1(i), that originated at the same flaw tip at 27.6MPa is predicted to make a -130° angle with the flaw plane. Fig. 5.6 illustrates the results for cracks 12 and 16 using the stress approach. They yielded predictions of direction are in good agreement with the experimental results, which can be seen in Table 5.1(g) and 5.1(i).

A shear crack 6, in Table 5.1(c), observed at the outside tip of the upper flaw at a load of 18.94MPa is predicted to make an angle of -90° from horizontal using the maximum shear stress approach, matching its experimental result which is also shown in the table.

5.3.1.3 Tensile cracks initiating (or crossing) the interface

Tensile crack 7 was observed originating at the interface at 18.94MPa, illustrated in Table 5.1(c). In Fig. 5.8, one can observe that the region along the interface where tensile crack 7 initiated can be associated with a region of tension. This region of tension is due to the stresses generated by the approaching tensile crack 4, which originated at the inner tip of the bottom flaw, as shown in Table 5.1(c). The direction of initiation of crack 7 numerically predicted (i.e. -85° from the horizontal) is found to be perpendicular to the maximum principal stress vectors, as depicted in Fig. 5.9, which is very close to that from DIC observations (i.e. -90° from the horizontal). The difference is viewed within experimental error.

Crack 6, shown in Table 5.1(c), originated as a shear crack at the outer tip of the upper flaw at 25.5 MPa. The crack turned into a tensile crack with further loading as it approached the interface. The model predicts that the crack reinitiates across the interface without an offset since the distance between the approaching crack plane and the reinitiated crack was 1mm (See Fig. 5.10), which is lower than the minimum distance of 1.2mm observed in the DIC crack paths that promoted tensile crack step-over. Consequently, the crack is predicted to curve before reaching the point of greatest maximum tensile stress at the interface, where reinitiation of the crack across the interface occurs. The stress-approach indicates that crack 6 makes an angle of -100° with the horizontal, while in the experimental observations, from the DIC, the angle was -110° .

More tensile cracks (i.e. marked as 10 and 11 in Table 5.1(f)) were observed initiating at the interface at a load of 25.8MPa. Fig. 5.11 shows the regions of tension where those cracks initiated. The tension in these regions is thought to be developed due to the presence of surrounding cracks that either approach or cross the interface (i.e. cracks 4 and 6 in Table 5.1(f)). The direction of initiation of tensile cracks 10 and 11 was predicted by the stress-approach to be 90° and -95° from the horizontal, respectively. These predictions are illustrated in Fig. 5.12 and 5.13, which show that the direction of those cracks is perpendicular to the maximum principal stress. This is in good agreement with the DIC observations, since cracks 10 and 11 originated at angles of 90° and -100° , respectively, from the horizontal in the experiments.

5.3.1.4 Shear cracks crossing the interface

Shear cracks 12, shown in Table 5.1(h), which originated at the inside tip of the pre-existing bottom flaw, crosses the interface at 27.5MPa without an offset (from the DIC results). The direction of re-initiation of crack 12 after crossing the interface is numerically predicted to make an angle of 90° with the horizontal without an offset, since the distance between the plane of the approaching crack and the point of maximum shear stress across the interface was smaller than the minimum distance of 0.95mm observed in the experiments for shear crack step-over (See Fig. 5.14). Therefore, the approaching shear crack is predicted to make a curve before reaching the point of greatest maximum shear stress at the interface and finally cross it without an offset. The predicted direction of crack re-initiation matches with that of the experimental observations, as shown in Table 5.1(h).

5.3.2 Geometry 0-2a30° with interface inclined 90° with the vertical and contact friction angle of 35°

Table 5.2 sums up the results for the prediction of cracks direction based on the stress approach described earlier, for a model with geometry 0-2a30°, with interface inclined 90° with the vertical and contact friction angle of 35° . The table also shows the crack paths extracted experimentally using the digital image correlation technique (DIC). The following observations are made:

5.3.2.1 Tensile cracks initiating from flaws

Similarly to the previous case, the tensile cracks that initiated at the crack tips (i.e. cracks 1, 3, 4 and 5 shown in Table 5.2(b)) did so in a direction that was either perpendicular or very close to perpendicular to the flaw planes. The stress-approach model confirmed that behavior, as it can be seen in Table 5.2(a) and (b).

No shear cracks at the flaw tips are observed in this geometry.

5.3.2.2 Tensile cracks initiating (or crossing) the interface

Tensile crack 2, initiated at the interface at 19.13MPa, is numerically predicted to make an angle of 82° with the horizontal, which is very close to the experimental observations (i.e. 80° from the horizontal), as shown in Table 5.2(a).

Regarding the direction from the horizontal of several other tensile cracks that initiated at the interface, obtained through the stress-based approach, one can observe that in Table 5.2(c-f): crack 6 initiated at a 70° angle; crack 7 at a -105° angle; Crack 8 initiated at approximately 90° ; crack 9 at -90° ; Crack 10 at -105° ; and crack 11 at 85° . Fig. 5.15 depicts the predicted direction of tensile crack 10, which is perpendicular to the maximum principal stress vectors or at -105° with the horizontal, as with the experiments. The predictions from the numerical approach match closely the experimental observations for the tensile cracks that initiated at the interface, as it can be seen in Table 5.2 (c-f).

The only crack crossing the interface captured by the DIC was tensile crack 13. The crack originated in the ROI and crossed the interface with an angle of 90° from the horizontal, as listed in Table 5.2(g). This crack could not be numerically predicted because the models created for the stress-approach were developed for loading stages up until right before coalescence and this crack only crossed the interface at coalescence.

5.3.3 Geometry 0-2a30° with interface inclined 80° with the vertical and contact friction angle of 50°

Table 5.3 lists the results from the numerical predictions for a model with geometry 0-2a30° with interface inclined 80° from the vertical and contact friction angle of 50° . The table also includes observations from experiments, for comparison. The following observations apply:

5.3.3.1 Tensile cracks initiating from flaws

The tensile cracks initiated at the crack tips follow a direction that is perpendicularly to the flaw plane (i.e. cracks 1, 2 and 6, as shown in Table 5.3(a-b)). Similar to the previous cases, the stress-approach indicates that these cracks originate in a direction that is perpendicular to the maximum principal stress direction; that is, at 90° with the flaw.

5.3.3.2 Shear cracks initiating from flaws

At 16.11MPa, Table 5.2(c), a coplanar shear crack (crack 7 in the Table) is seen initiating at the inner bottom flaw at a 50° angle from the horizontal. The stress-based approach prediction indicates that crack 7 should initiate at an inclination of 52° from the horizontal.

At 19.3MPa, shear cracks 10 and 11, that initiated at the outside tip of the bottom flaw, can be observed making angles of -150° and 120° from the horizontal, respectively; see Table 5.3(f). They are numerically predicted to make, respectively, -135° and 125° from the horizontal.

5.3.3.3 Tensile cracks initiating (or crossing) the interface

At 6.6MPa, tensile cracks 3 and 4 are observed initiating at the interface at angles of -105° and 90° from the horizontal, respectively, as shown in Table 5.3(a). The numerical approach estimates that tensile cracks 3 and 4 originate at the interface at angles of -100° and 90° with the horizontal, respectively.

Another tensile crack 8 is seen originating at the interface with an angle of 100° from the horizontal, when the load reached 18MPa (Table 5.3(d)). By performing an analysis of the maximum principal tensile stress vectors in the region of concentration of tension (See Fig. 5.16), it is possible to observe that the stress-approach prediction for the direction of crack 8 matches the experimental findings. It is believed that the region of tension developed due to the change of stress caused by the coplanar shear crack 7 approaching the interface, as seen in Table 5.3(d).

5.3.4 Geometry 0-2a30° with interface inclined 80° with the vertical and contact friction angle of 35°

Table 5.4 provides findings from the prediction of cracks direction based on the stress-based approach described earlier, for a model with geometry 0-2a30° with interface inclined 80° from the vertical and contact friction angle of 35° . The table also presents observations from experiments, for comparison. The following observations can be made:

5.3.4.1 Tensile cracks initiating from flaws

Tensile cracks were observed initiating at the flaw tips (e.g. cracks 1, 2 and 3) at 9.4MPa, as seen in Table 5.4(a). It was found through the stress-based approach that these tensile cracks

should be all perpendicular to the pre-existing flaw plane, which is in good agreement with experiments.

5.3.4.2 Shear cracks initiating from flaws

Shear crack 9, in Table 5.4(c), that originated at the inside tip to the bottom flaw at 20.87MPa, is estimated to make a -75° angle with the horizontal. The DIC crack path shows that the crack makes an angle of -70° with the horizontal.

At the same load (Table 5.4(c)), shear crack 10 can be observed initiating at the outside tip of the upper flaw at a -90° angle from the horizontal, while the numerical prediction suggests that the crack should be at -80° with the horizontal.

5.3.4.3 Tensile cracks initiating (or crossing) the interface

Tensile cracks 7 and 8 can be seen originating at the interface in Table 5.4(b-c). In Fig. 5.17, one can observe that the regions along the interface where tensile cracks 7 and 8 initiate are located in a region of tension. The predicted direction of crack 7, at 80° with the horizontal, is perpendicular to the maximum principal stress vectors, as shown in Fig. 5.18. Similarly, crack 8 should be at -90° with the horizontal. These predictions are consistent with the observations from experiments. See Table 5.4(b-c).

5.3.4.4 Shear cracks crossing the interface

Shear Crack 6, originated at the inside tip of the upper flaw, crossed the interface at an angle of -105° with the horizontal with an offset of 1.56mm, as shown in Table 5.4(b).

The direction of re-initiation of crack 6, after crossing the interface, is numerically predicted at an angle of -110° with the horizontal with an offset of 1.2mm. The agreement between experiments and predictions is reasonable and is within experimental error.

5.3.5 Discussion

5.3.5.1 Effects of interface roughness and inclination angle on the initial stress state

For the specimens with the interface inclined 90° with the vertical, the interface roughness does not seem to affect the distribution of tensile and compressive zones in the specimen, as one can see in Fig. 5.20(a-b), which are contour plots of maximum principal stresses. In the contours, lighter gray means compressive stresses and darker grey means tensile stresses. However, a closer look into the region of interest (ROI) around the flaws, shown in Fig. 5.21 and Fig. 5.22, indicates that even though both specimens (i.e. with interface friction angles 50° and 35°) presented very similar distribution of tension and compression, the jump of compressive stress zone at the interface around the center of the modeled specimen is larger for the smoother interface (i.e. in the smooth interface case, the region of compression at the center of the specimen that coincides above and below the interface has a smaller length due to a larger jump of the compressive zone on both sides of the interface when compared to the rough interface). This slight difference in the stress state may be due to different magnitudes of slip at the interface. It was possible to extract from ABAQUS the maximum magnitude of slip along the rough and smooth interfaces inclined 90° with the vertical. Those were, respectively, $9.5 \cdot 10^{-4}$ and $1.2 \cdot 10^{-3}$ (i.e. the case with a smooth interface presented higher magnitudes of slip).

Differences between the contours of the maximum principal stresses for different levels of interface roughness are more noticeable when the interface is at 80° with the vertical. As it can be seen in Fig. 5.20(c) and Fig. 5.20(d), as well as in Fig. 5.23 and Fig. 5.24, the increase in roughness leads to a noticeable change in the stress state in the areas near the interface as well as in the ROI. One can observe in the figures that the jump of compressive stress zone above and below the interface around the center of the inclined interface is larger for the smoother interface (i.e. larger jump of the compressive zone promotes a smaller length along the interface where the compressive zones above and below the interface coincide). It is relevant to mention that the maximum magnitude of slip along the rough and smooth interfaces inclined 80° with the vertical were, respectively, $1.3 \cdot 10^{-3}$ and $7.6 \cdot 10^{-2}$ (i.e. the specimen with a smooth interface presented higher magnitudes of slip). This may indicate that a smooth interface facilitates slip as well as causes considerable changes in the stress state of the specimen.

Furthermore, a comparison between the contour plots of the major principal stress indicate that the increase in interface inclination (i.e. from horizontal to inclined), with a rough interface (i.e. 50° friction angle), show small differences in stresses; see Fig. 5.20(a) and 5.20(c). Larger changes are observed for the smoother interface (compare Fig. 5.20(b) and 5.20(d)). This may be explained by the fact that rougher interfaces mitigated slip along the interface, as indicated by the magnitudes of slip extracted from ABAQUS, as discussed. Plus, the increase of inclination of a smoother interface may likely cause slip, which may be a contributor to the changes in compression and tension distributions.

5.3.5.2 Effects of interface roughness and inclination angle on the initiation of tensile cracks at the flaw tips

As discussed in sections 5.3.1-5.3.4, the majority of tensile cracks that initiated at the flaw tips were perpendicular to the flaw, and perpendicular to the maximum principal stress. Experimental results indicate that the decrease in interface roughness leads to an increase in crack initiation stress at the tips (See Section 3.251 in Chapter 3). The maximum tensile stress at the internal tip of the bottom flaw is investigated to understand this behavior.

The models with interface inclined 90° with the vertical and interface friction angles of 50° and 35° are shown in Tables 5.1 and 5.2. The numerical model predicts magnitudes of the maximum tensile stresses around the inside tip larger in specimens with 50° interface friction angle than with 35° . See Table 5.5. This may explain why tensile cracks initiated earlier in specimens with a rougher interface.

The effects of the inclination of the interface can also be observed in Table 5.5. First, an increase in friction along the interface is associated with an increase in maximum tensile stresses around the tip of the internal flaw; and second, a comparison of the magnitude of the major principal stresses shows that an inclined interface induces larger tensile stresses around the tip of the flaw. Thus, it is expected that tensile crack initiation at the internal tips of the flaws, would occur first in specimens with more inclined interfaces, which is supported by the experiment observations.

The increase in roughness and inclination angle of interfaces seem to produce a similar effect on tensile crack initiation at the outside flaw tips. One can observe that in the specimens with an interface inclined 80° with the vertical, the rougher interface (See Table 5.3(a)) promoted

crack initiation at the outside tip of the upper flaw at 6.6MPa, while the smoother interface case (See Table 5.4(a)) produced crack initiation at 8.5MPa, at the same location; furthermore, the crack initiation at the outside tip of the upper flaw for the rough interface case with a horizontal interface was found to be 6.95MPa (See Table 5.1(a)). This indicates that, similarly to the inside flaw tips, the increase in roughness and inclination angle of an interface also leads to a reduction in crack initiation stress at the outside flaw tips. Therefore, changes in the interface also affect the outside tips of the flaws, which may be explained by the fact that those tips are still within the influence of the interface.

Similarly to the results on the inside tip, the numerical model predicts magnitudes of the maximum tensile stresses around the outside tip larger in specimens with 50° interface friction angle than with 35°, as shown in Table 5.6. In addition to that, a comparison of the magnitude of the major principal stresses in Table 5.6 shows that an inclined interface induces larger tensile stresses around the tip of the flaw, indicating that tensile crack initiation at the internal tips of the flaws would occur first in specimens with more inclined interfaces, which is supported by the experiment observations.

5.3.5.3 Effects of roughness and inclination angle on shear crack initiation at the flaw tips

As previously discussed in Sections 5.3.1.2, 5.3.3.2 and 5.3.4.2, the direction of shear cracks initiation at the flaw tips is well predicted. Even though the initiation direction of these cracks coincides well with experiments, no trend correlating crack initiation stresses at the inside flaw tips and the order of initiation of shear cracks is found for cases with different roughness and inclination angle of interfaces. One can observe that in the specimens with interface inclined 90° from the vertical, the specimen with the rougher interface (See Table 5.1(b)) promoted crack initiation at the inside tip of the upper flaw at 15MPa, while no shear crack initiated for the smoother interface (See Table 5.2). Moreover, in the specimens with interface inclined 80° from the vertical, the rougher interface (See Table 5.3) did not promote crack initiation at the inside tip of the upper flaw, while for the smoother interface case (See Table 5.4(b)), a shear crack initiated at 16.98MPa.

The same conclusion is achieved for shear crack initiation at the outside flaw tips. It is possible to observe that in specimens with interface inclined 90° from the vertical, the rougher interface (See Table 5.1(g)) promoted crack initiation at the outside tip of the upper flaw at

18.94MPa, while no shear crack initiated for the smoother interface (See Table 5.2). Furthermore, in the specimens with interface inclined 80° from the vertical, the rougher interface (See Table 5.3(a)) did not result in crack initiation at the outside tip of the upper flaw, while for the smoother interface (See Table 5.4(c)) a shear crack initiated at 20.87MPa. Therefore, no trend correlating shear crack initiation stresses at the inside or outside flaw tips is found.

5.3.5.4 Effects of roughness and inclination angle on the initiation of cracks at the interface

All cracks predicted to originate at the interface were tensile. The different roughness or inclination angles of the interface do not seem to affect the predicted initiation angles of tensile cracks that initiate at the interface. This can be ascertained by looking at the results of the numerical model shown in Figures 5.9, 5.12, 5.13, 5.15, 5.16 and 5.18. These are plots of maximum principal stress for specimens containing an interface with different roughness and inclination angles, which would show the location and direction of tensile cracks. The predicted tensile cracks in the figures correspond to crack 7 in Table 5.1(c), cracks 10 and 11 in Table 5.1(e), crack 10 in Table 5.2(e), crack 8 in Table 5.3(d) and crack 7 in Table 5.4(b-c). One can observe that the smallest angle between any of the predicted tensile cracks at the interface and the interface ranged from 70° to 90° , irrespective of the roughness or inclination of the interface. This is in good agreement with the experimental findings, which were presented in section 3.2.5.2 in Chapter 3.

5.3.5.5 Effects of roughness and inclination angle on cracks approaching the interface

Irrespective of the roughness or the inclination of the interface, the reinitiation of cracks that crossed the interface was predicted to occur at the point of greatest maximum tensile stress, for tensile cracks, or maximum shear stress, for shear cracks, as previously discussed in sections 5.3.1.3 and 5.3.1.4. All cracks that reinitiated across the interface were in a direction that was perpendicular to the maximum tensile stress or the direction of the maximum shear stress in locations ahead of the approaching crack.

5.3.5.6 Summary

A comparison of the numerical results and subsequent analysis (See Tables 5.1-5.4), has resulted in the following general observations:

1. The stress-based approach used in this study yields predictions of tensile and shear cracks location and initiation direction that are in good agreement with experimental results;
2. The model predicts that the direction of initiation of the tensile cracks at the flaw tips is perpendicular to the maximum principal stress vectors, which are perpendicular to the flaws. This is consistent with experimental observations;
3. Rougher horizontal interfaces induced slightly higher tensile stresses around the interior and exterior flaw tips than smoother interfaces, which may explain why tensile cracks at these locations initiated earlier in specimens with a rough interface;
4. Inclined interfaces induced higher tensile stresses around the interior and exterior flaw tips than horizontal interfaces, which may justify that, in the experiments, inclined interfaces promoted crack initiation earlier than horizontal interfaces.
5. The roughness or inclination of the interface do not seem to affect the angles of initiation of the tensile cracks that initiate at the interface. The numerical model predicts initiation angles in the range 70° to 90° , which is in good agreement with experimental findings;
6. The numerical prediction of crack re-initiation after crossing an interface does not seem to be affected by the roughness or the inclination of the interface. In the model, the reinitiation of cracks that crossed the interface was predicted to occur at the point of greatest maximum tensile stress, for tensile cracks, or maximum shear stress, for shear cracks. All cracks that reinitiated across the interface were in a direction that was perpendicular to the maximum tensile stress or in the direction of the maximum shear stress in locations ahead of the approaching crack.

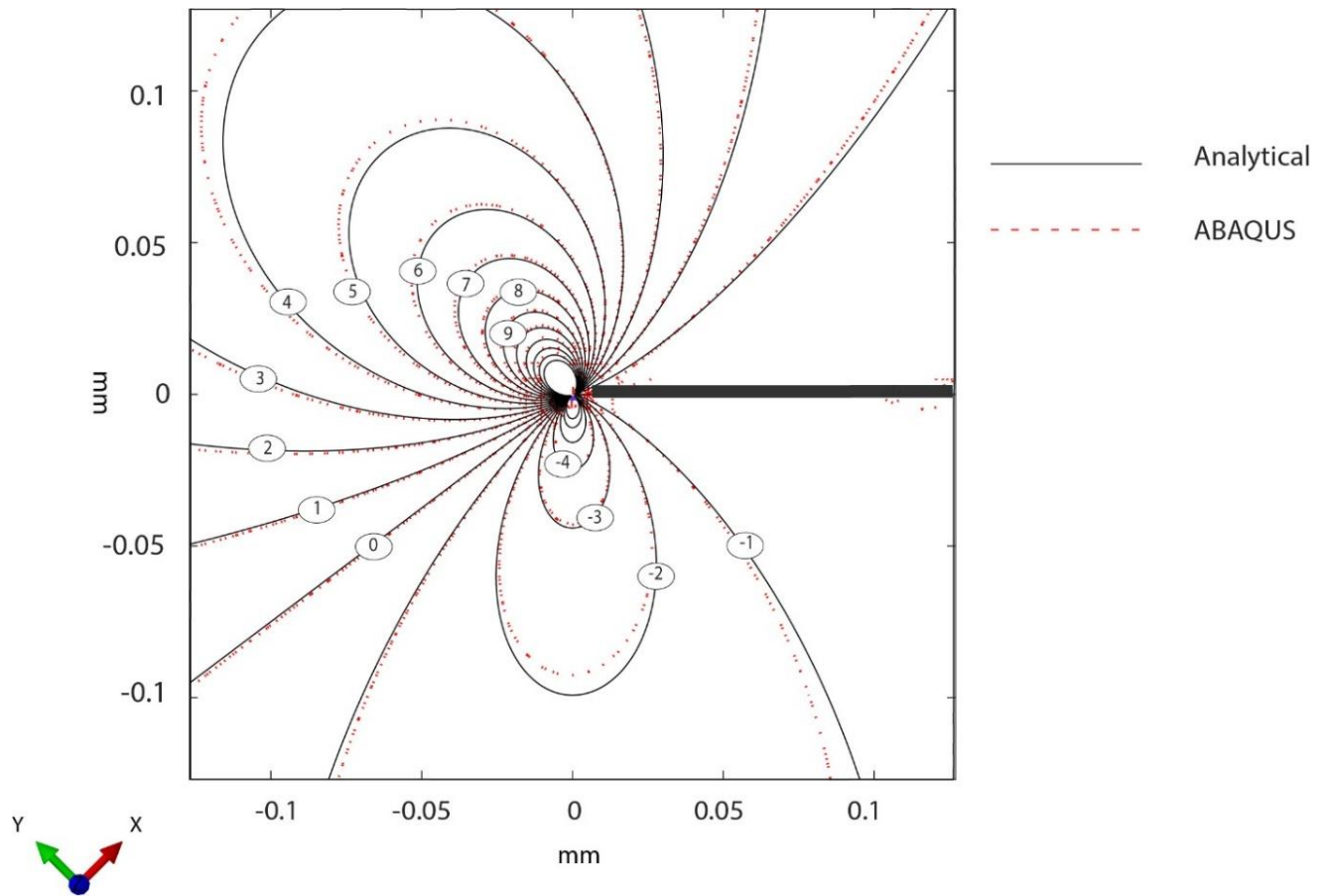


Figure 5.1. Contour of the tangential stress (MPa) near a pre-existing flaw tip with 45° inclination in a specimen under uniaxial compression of 1 MPa.

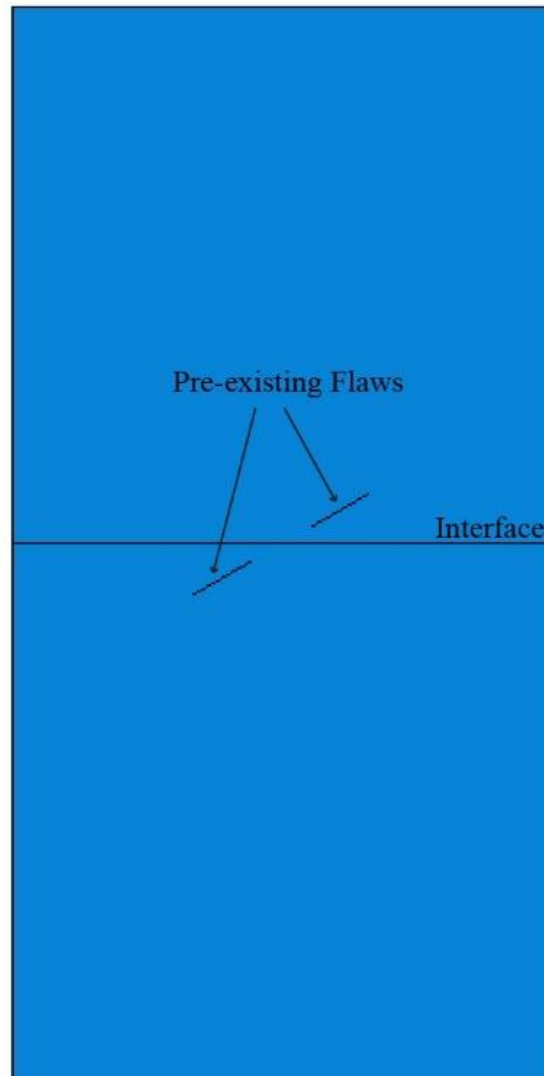
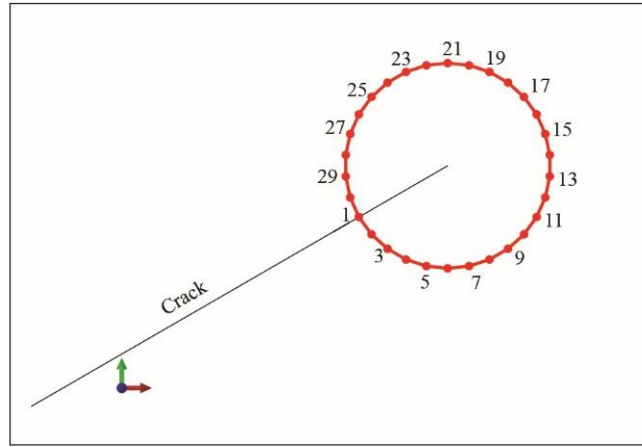
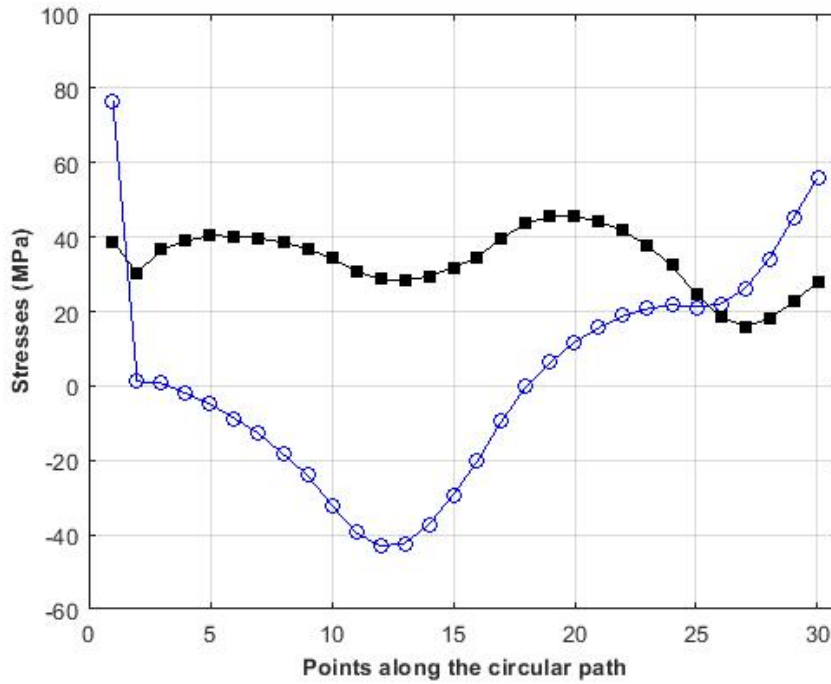


Figure 5.2. Example of specimen geometry used in ABAQUS



(a)



(b)

Figure 5.3. Path used in the investigation of existing crack initiation at the inside tip of the bottom flaw of the $-2a030^\circ$ geometry, with $\phi=50^\circ$ interface inclined 90° from vertical. a) point IDs along the path; b) σ_I (blue full circles) and τ_{12}^{max} (orange hollow circles) along the path

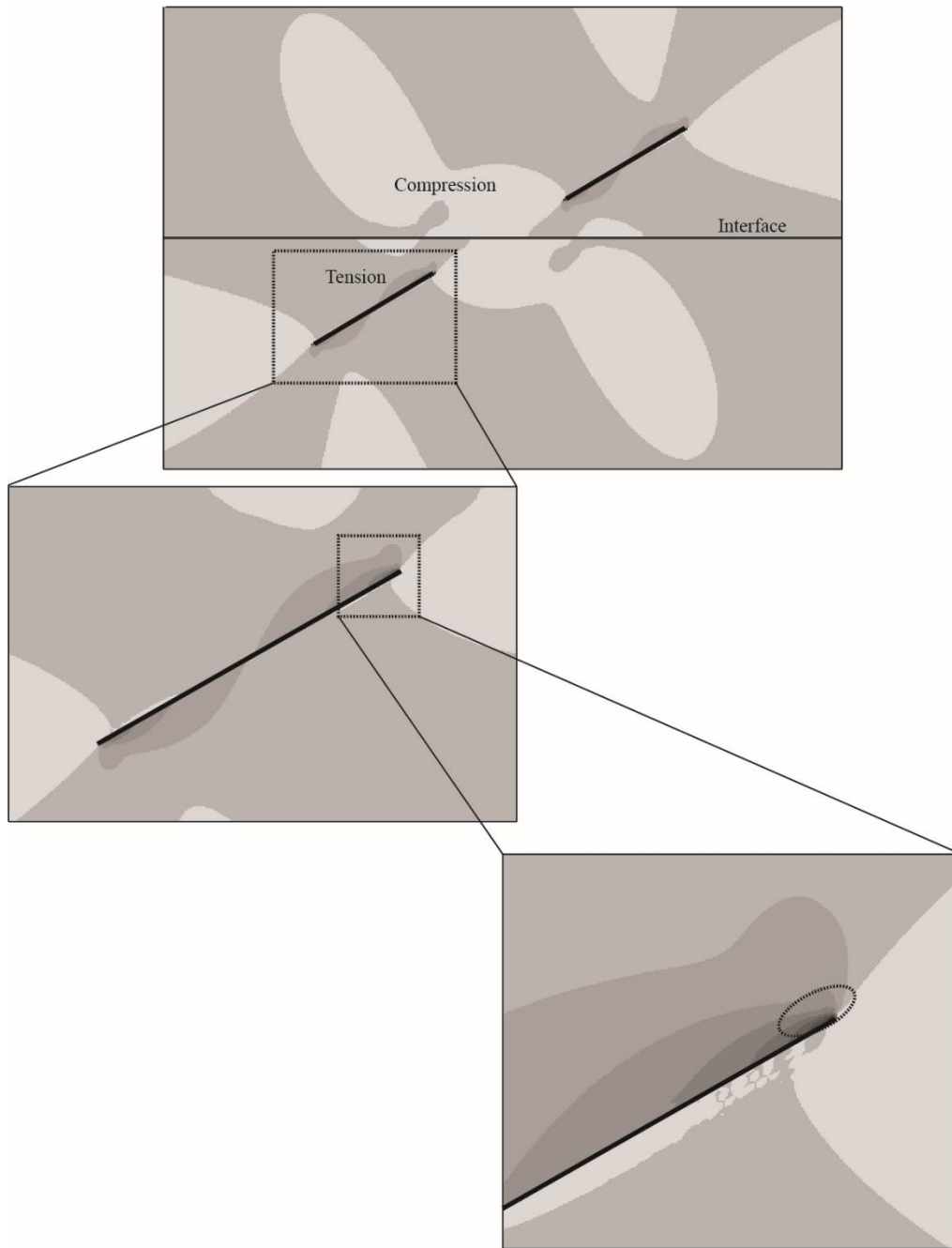


Figure 5.4. Maximum principal stress around a flaw (top and middle) for a model with geometry $0-2a30^\circ$ with interface inclined 90° with the vertical and interface friction angle 50° . The elliptical area (bottom) indicates the region where tensile cracks are most likely to initiate – lighter gray indicates compression and darker grey tension.

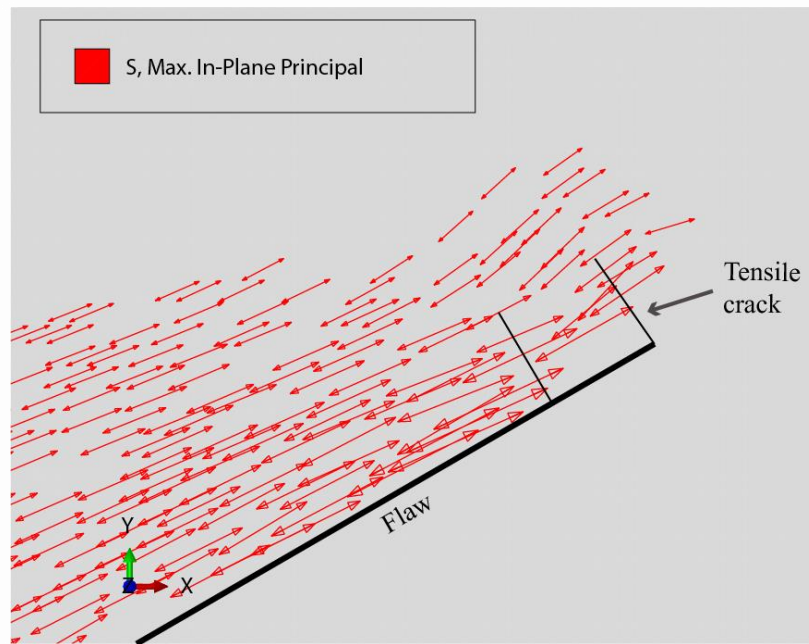


Figure 5.5. Possible directions of tensile cracks according to the stress field analysis

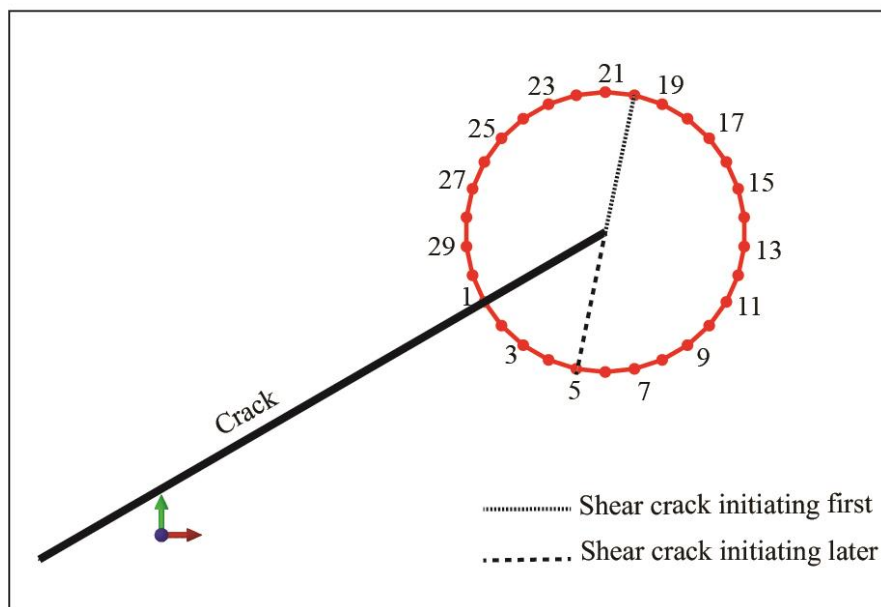


Figure 5.6. Illustration of the results obtained using the Stress Approach. The dashed lines indicate the order by which the shear cracks are most likely to initiate.

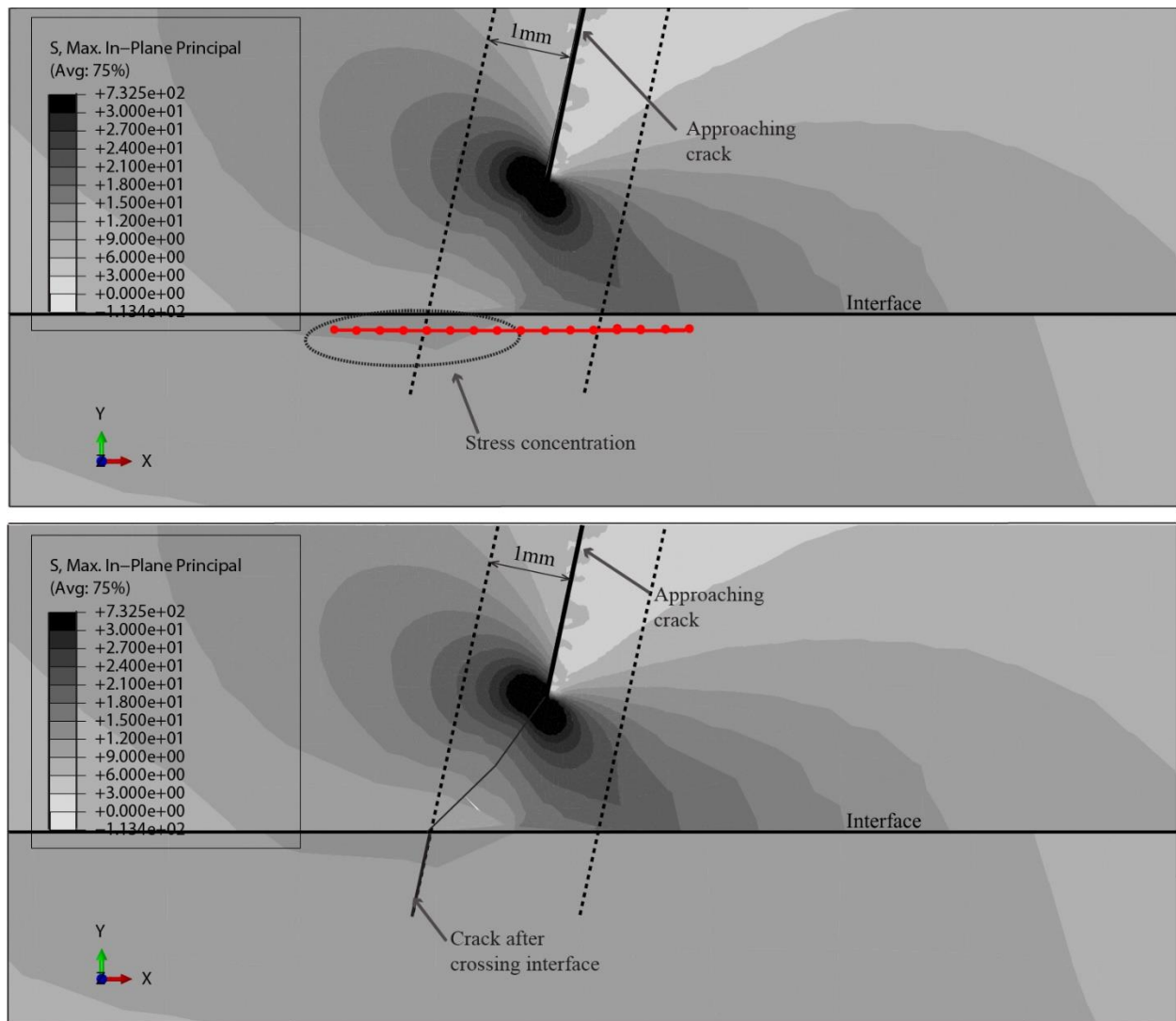


Figure 5.7. Prediction of tensile crack's direction of initiation after crossing the interface, using the approach described in section 4.4.5 (MPa).

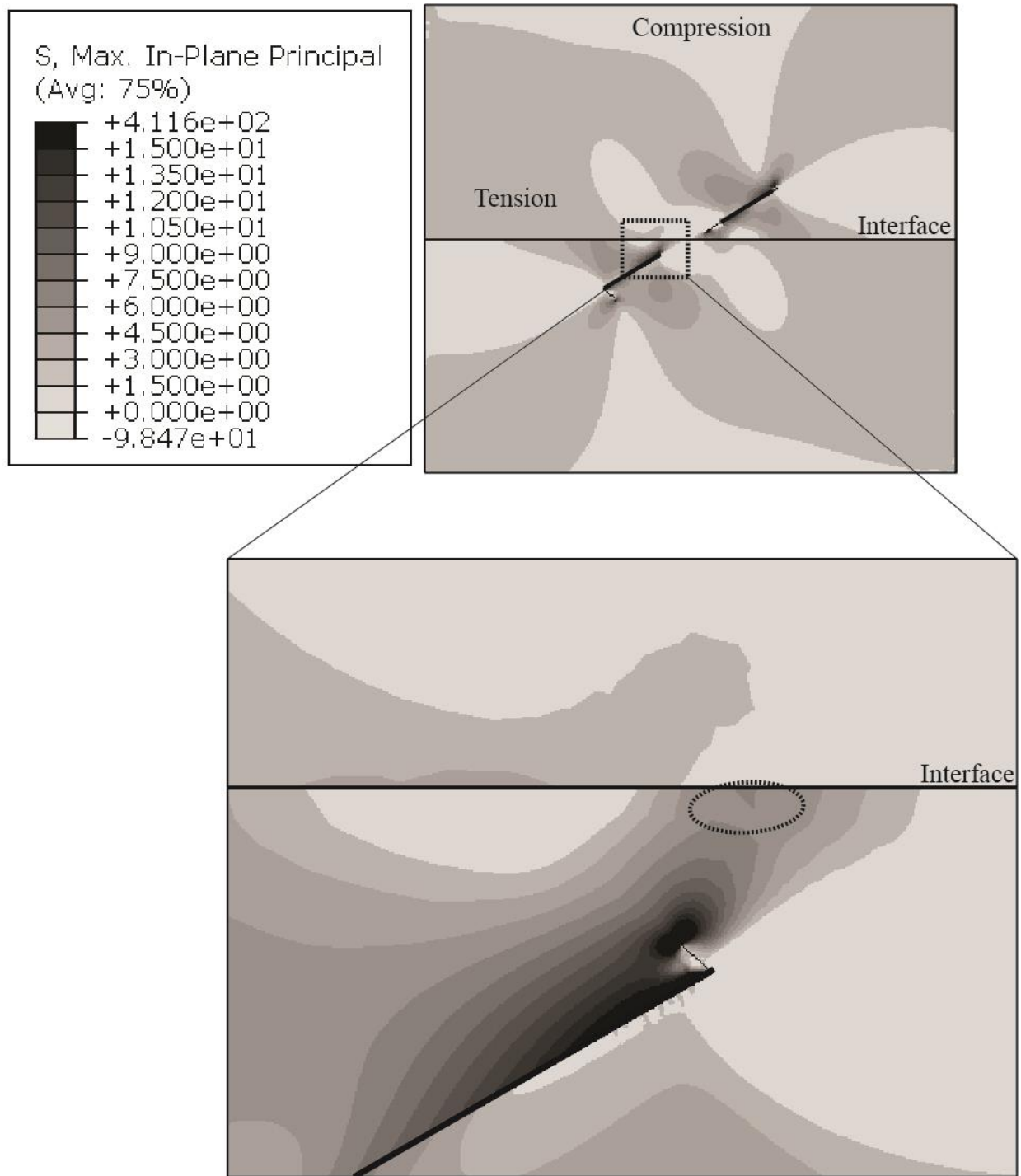


Figure 5.8. Crack 7 in Table 5.1(c). Maximum principal stress contours at 15MPa, for a model with geometry 0-2a30° with interface inclined 90° with the vertical and friction angle 50°. The elliptical area (bottom) indicates the region where a tensile crack is most likely to initiate – lighter gray means compression and darker grey tension.

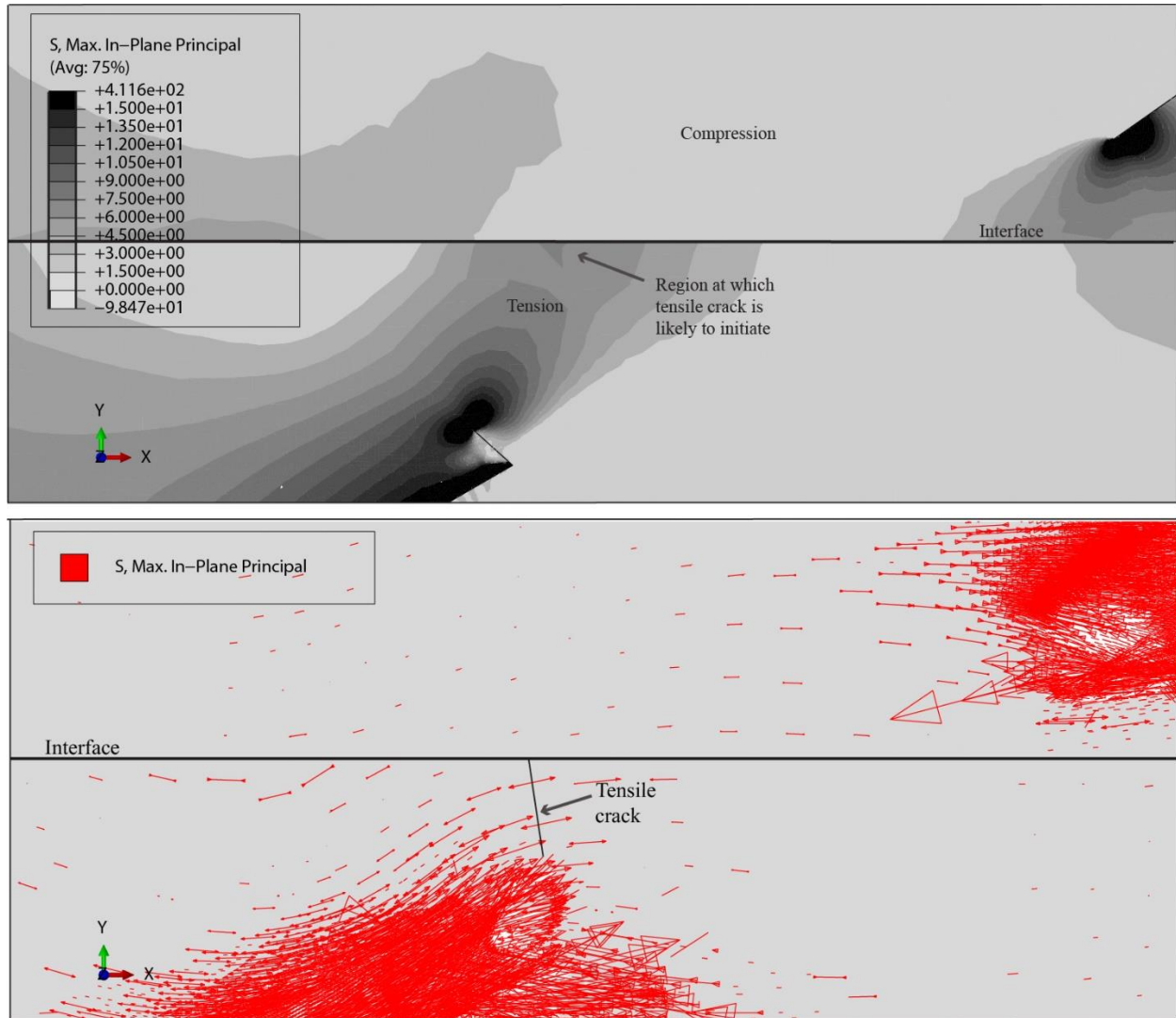


Figure 5.9. Crack 7, Table 5.1(c). Prediction of crack 7 initiation, for the geometry 0-2a30° with interface inclined 90° with the vertical and friction angle of 50°. Top: Region where crack is more likely to initiate. Bottom: Direction - perpendicular to the maximum principal stress vectors (bottom), MPa.

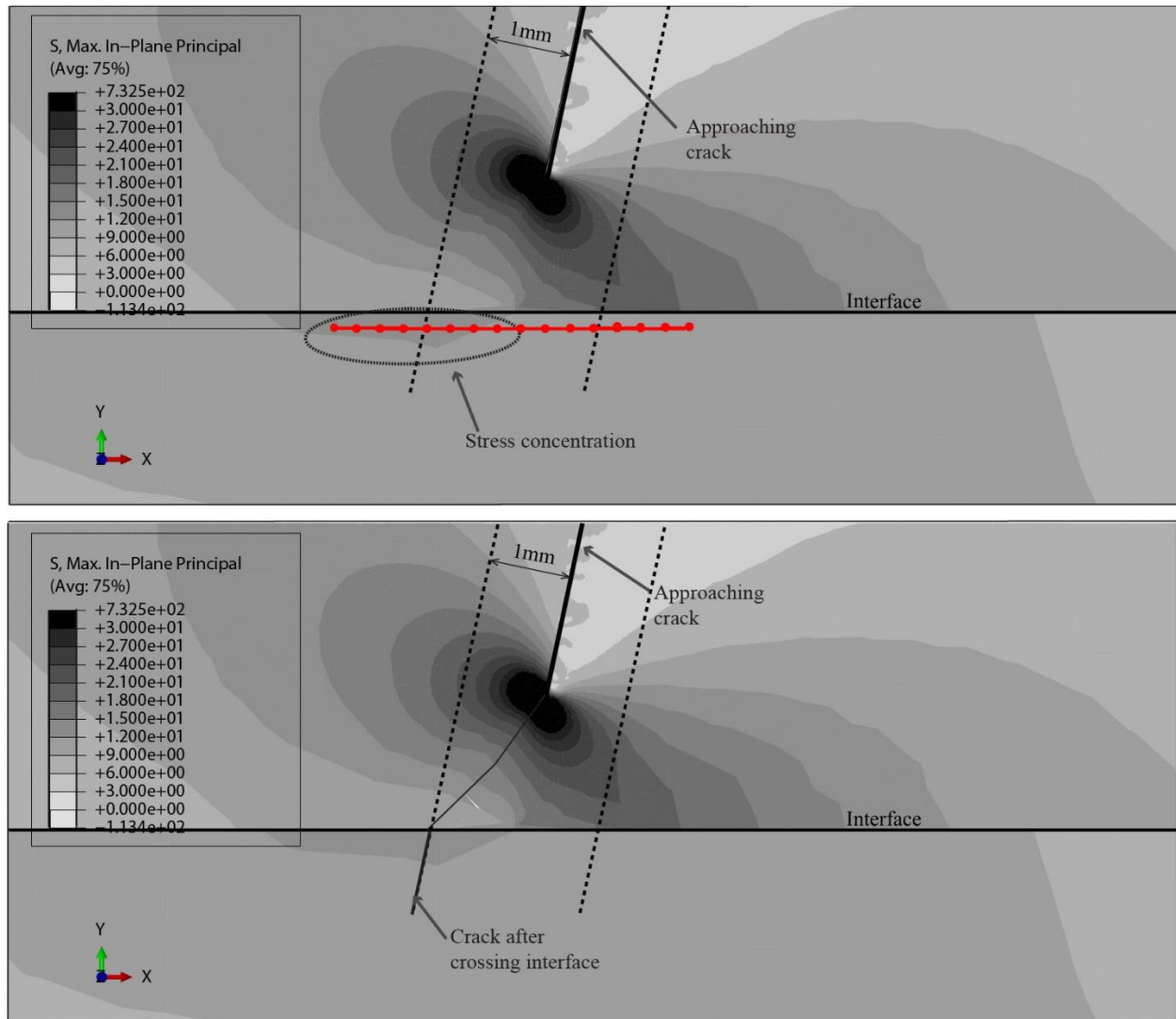


Figure 5.10. Crack 6, Table 5.1(d). Prediction of crack 6 direction of initiation after crossing the interface, using the approach described in section 4.4.5. Specimen with geometry 0-2a30° with interface inclined 90° with the vertical and contact friction angle 50° (MPa).

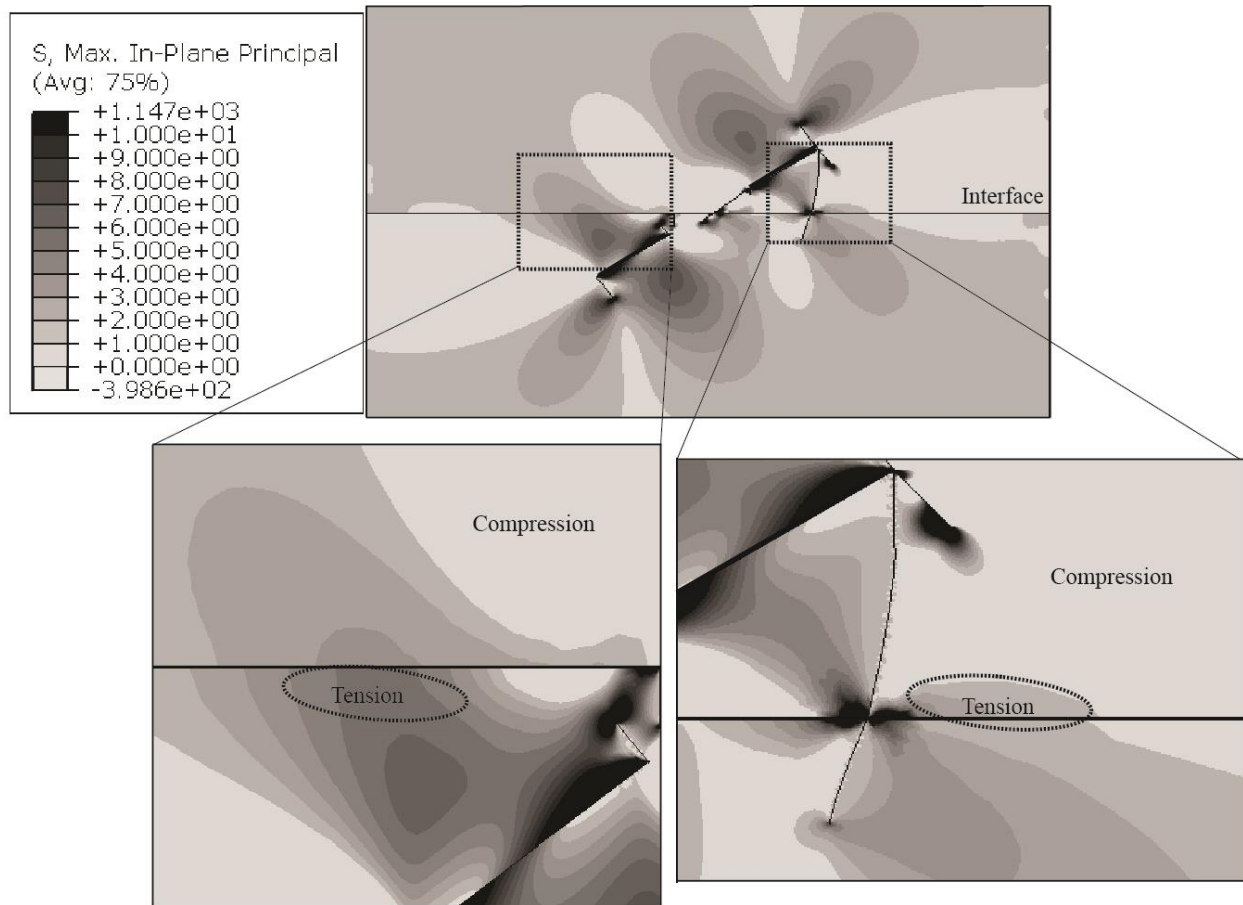


Figure 5.11. Cracks 10 and 11, Table 5.1(e). Maximum principal stress contours at 25.5MPa, for a 0-2a30° specimen with interface inclined 90° with the vertical and interface friction angle of 50°. The elliptical areas (bottom) indicate the regions at the interface where a tensile crack is most likely to initiate – lighter gray means compression and darker grey tension. (Crack 10 originates in the region shown on the right and crack 11 on the left).

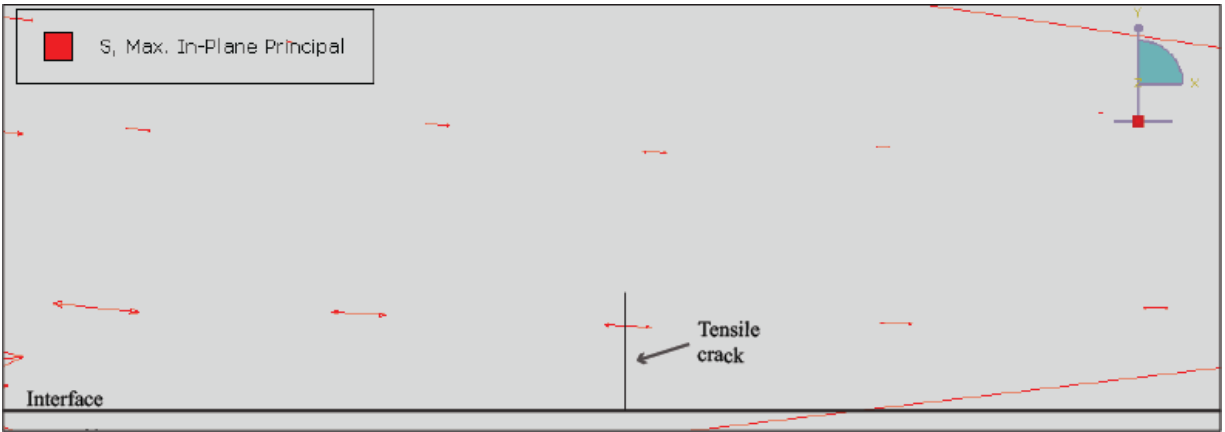


Figure 5.12 Crack 10, Table 5.1(e) Prediction of tensile crack 10 for a specimen geometry 0-2a30° with interface inclined 90° with the vertical and interface friction angle of 50°. Direction of crack: perpendicular to the maximum principal stress (MPa).

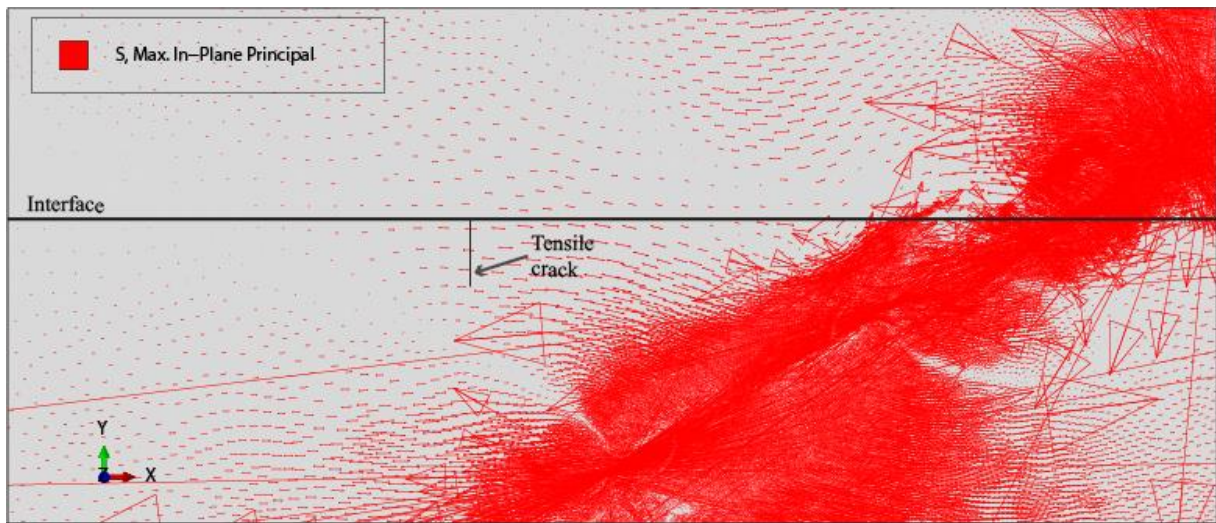


Figure 5.13. Crack 11, Table 5.1(e). Prediction of tensile crack 11 for a specimen geometry 0-2a30° with interface inclined 90° with the vertical and interface friction angle of 50°. Direction of crack: perpendicular to the maximum principal stress (MPa).

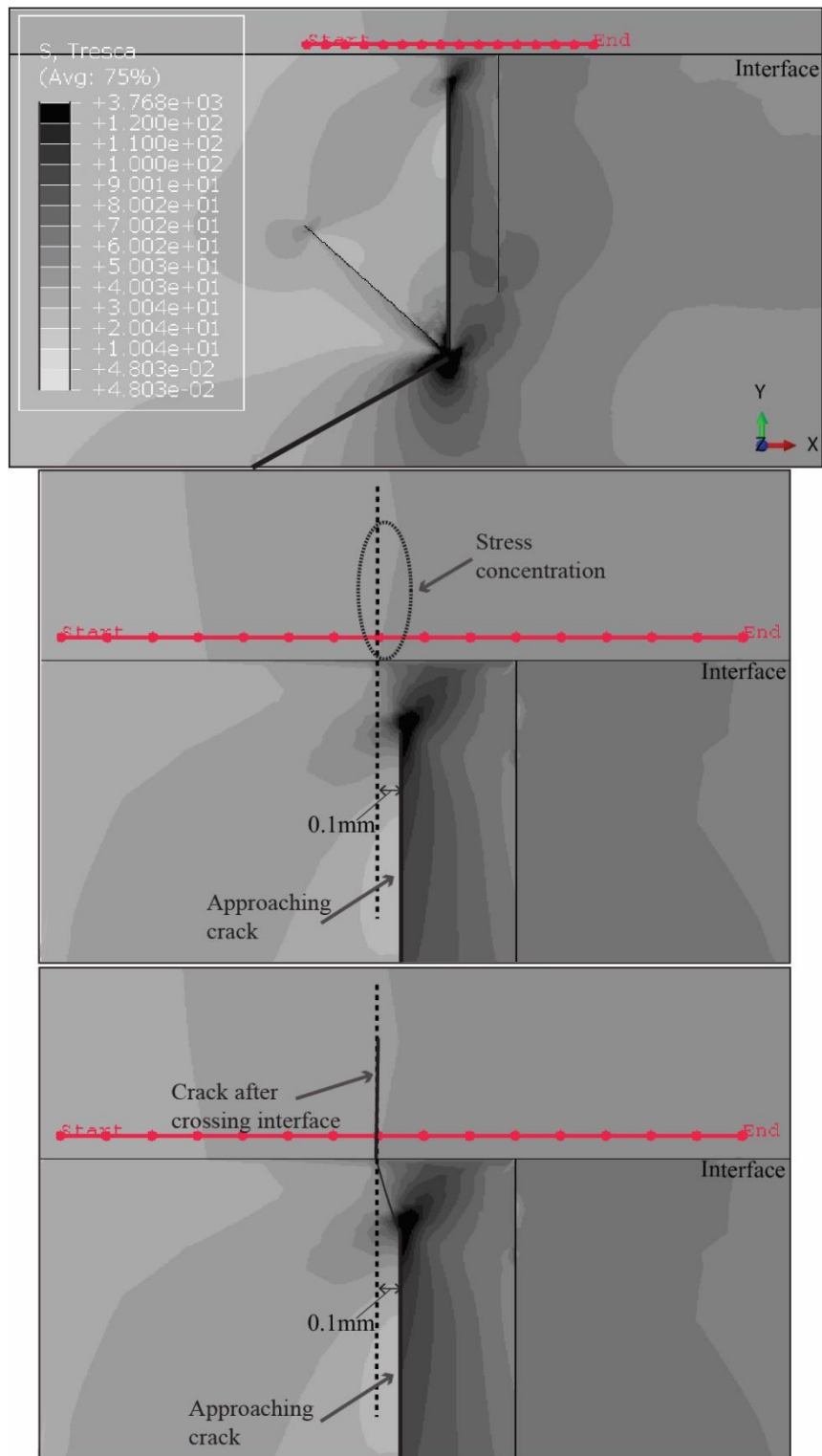


Figure 5.14. Crack 12, Table 5.1(h). Prediction of crack 12 direction of initiation after crossing the interface, using the approach described in section 4.4.5. Specimen with geometry 0-2a30° with interface inclined 90° with the vertical and contact friction angle 50° (MPa).

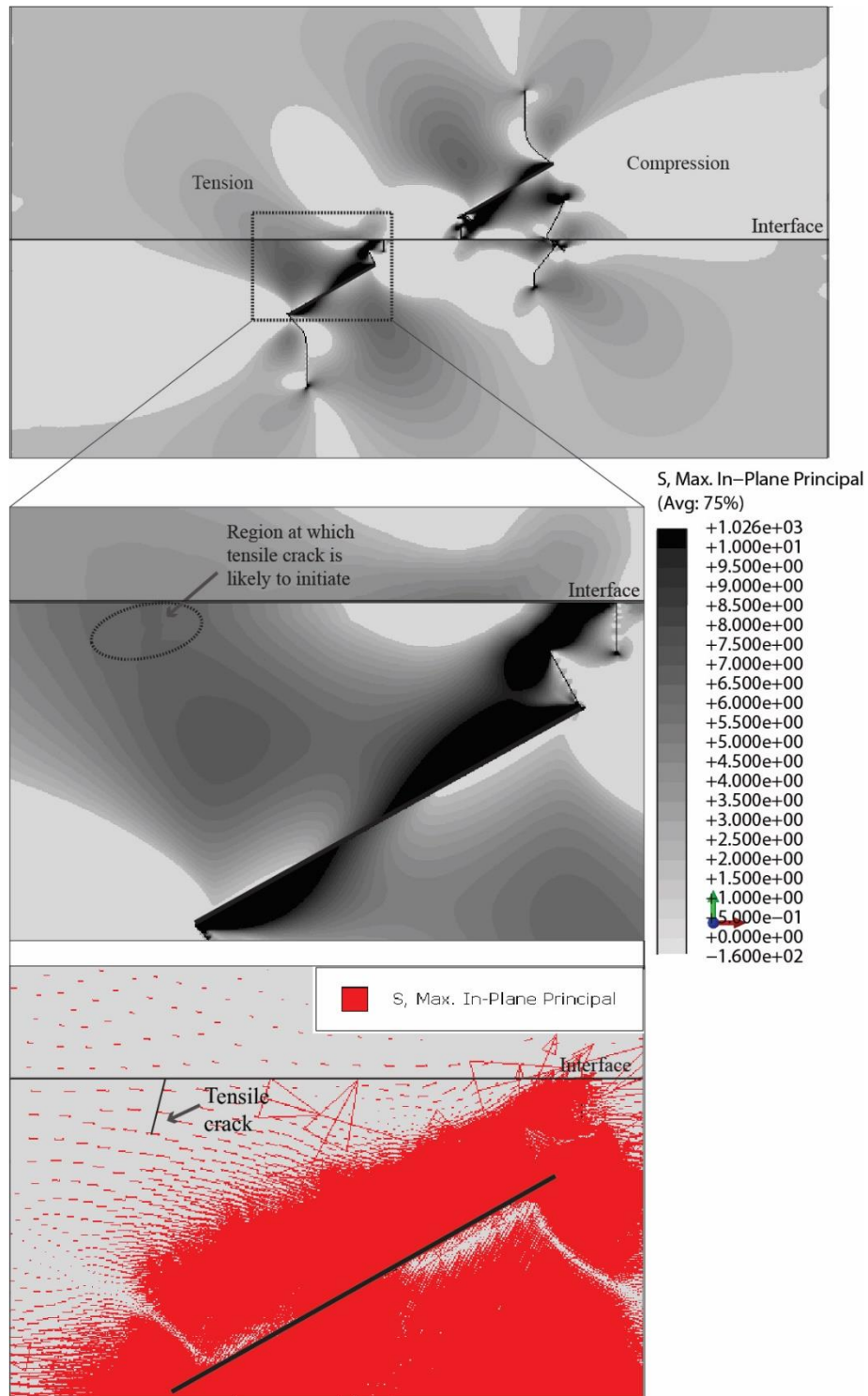


Figure 5.15. Crack 10, Table 5.2(e). Prediction of tensile crack 10 for a specimen 0-2a30° with interface inclined 90° with the vertical and interface friction angle of 35°. Direction of crack: perpendicular to the maximum principal stress vectors (MPa).

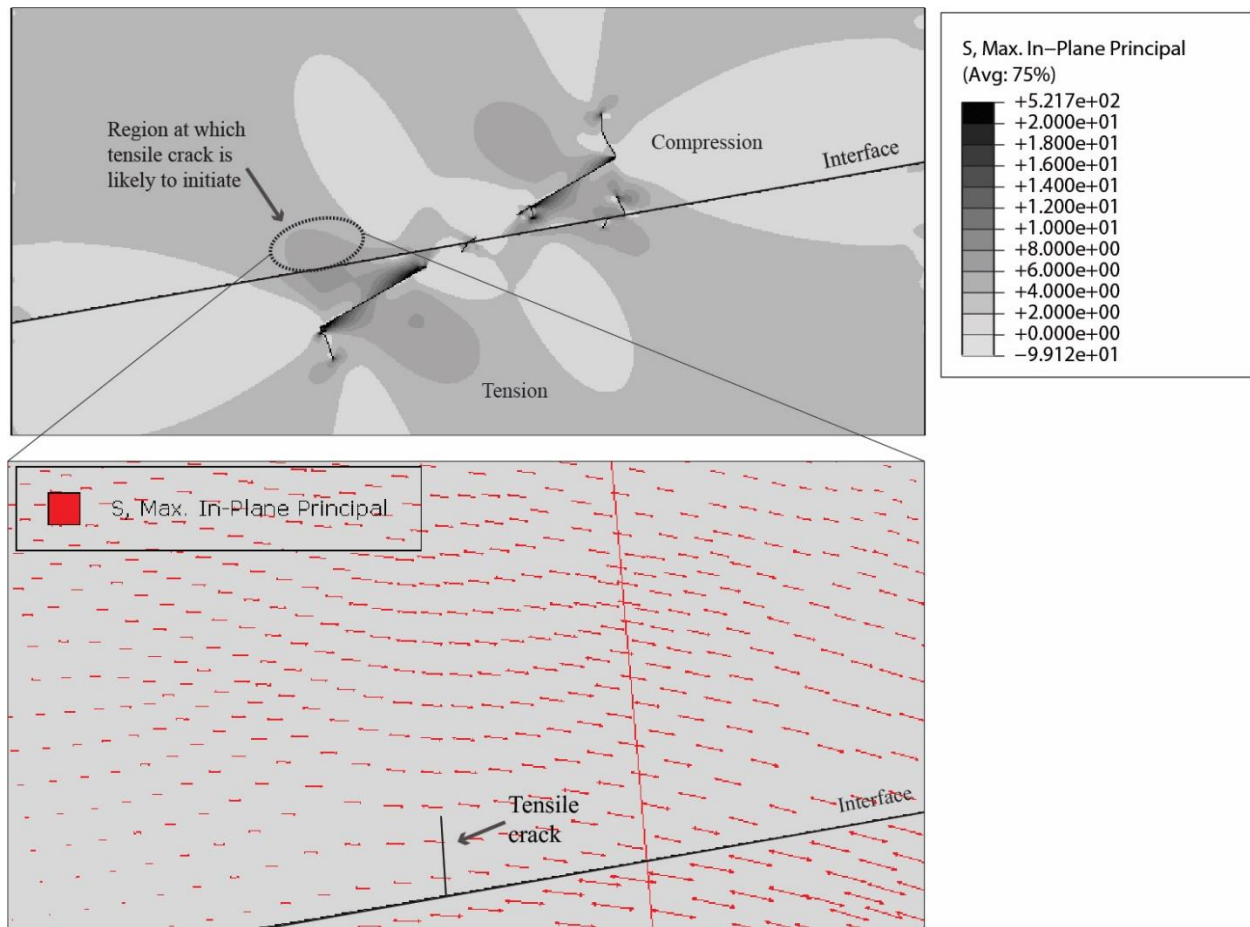


Figure 5.16. Crack 8, Table 5.3(d). Prediction of tensile crack 8 for 0-2a30° specimen with interface inclined 80° with the vertical and interface friction angle of 50°. Direction of crack: perpendicular to the maximum principal stress vectors (MPa).

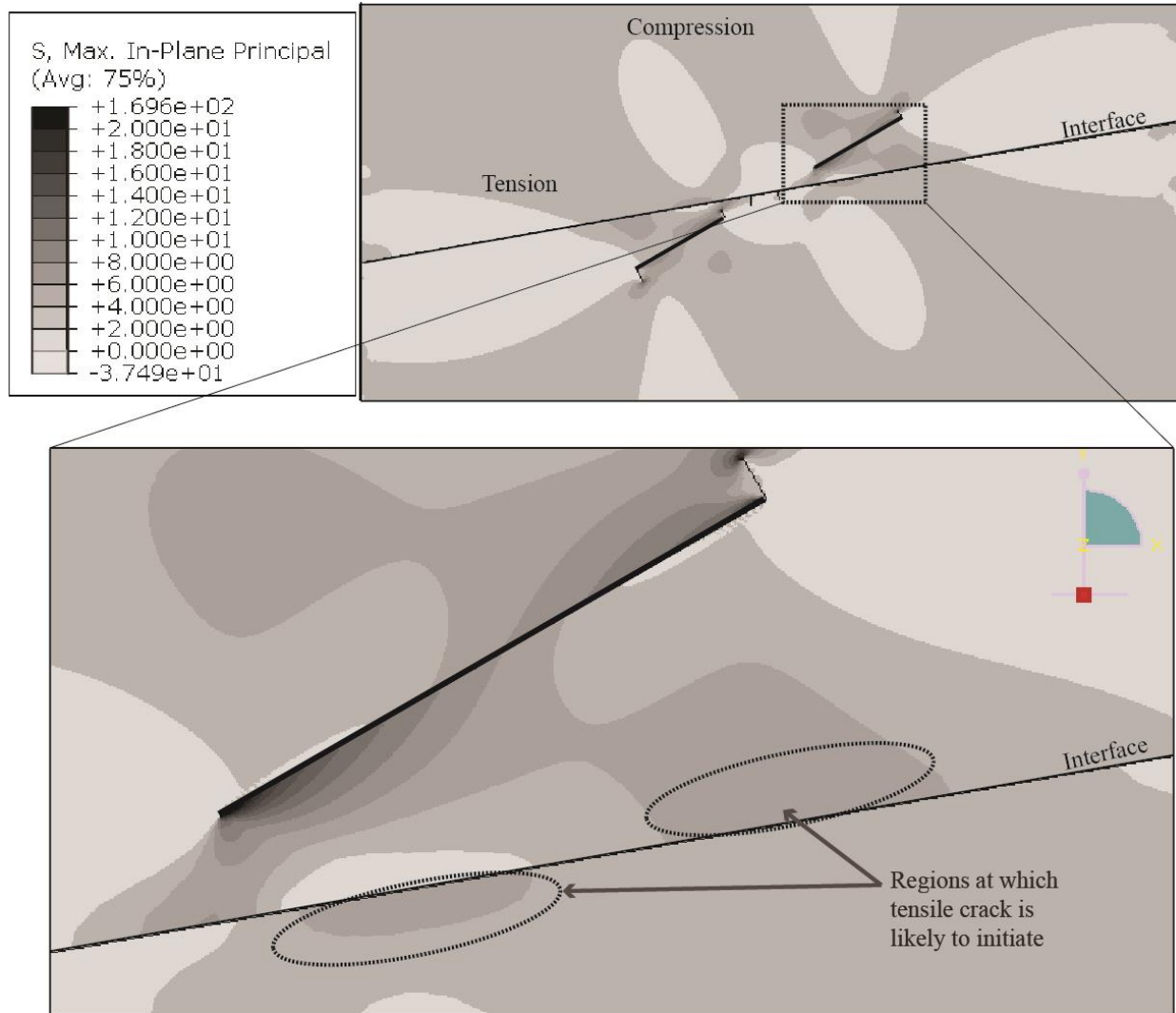


Figure 5.17. Cracks 7 and 8, Table 5.4(b-c). Maximum principal stress contour at 8.5MPa for a specimen with geometry 0-2a30°, interface inclined 80° with the vertical and interface friction angle of 35°. The elliptical areas (bottom) indicate regions at the interface where a tensile crack is most likely to initiate – lighter gray means compressive stress and darker grey means tensile stresses. (Crack 7 originates in the region shown above the interface and crack 8 originates on the region below the interface).

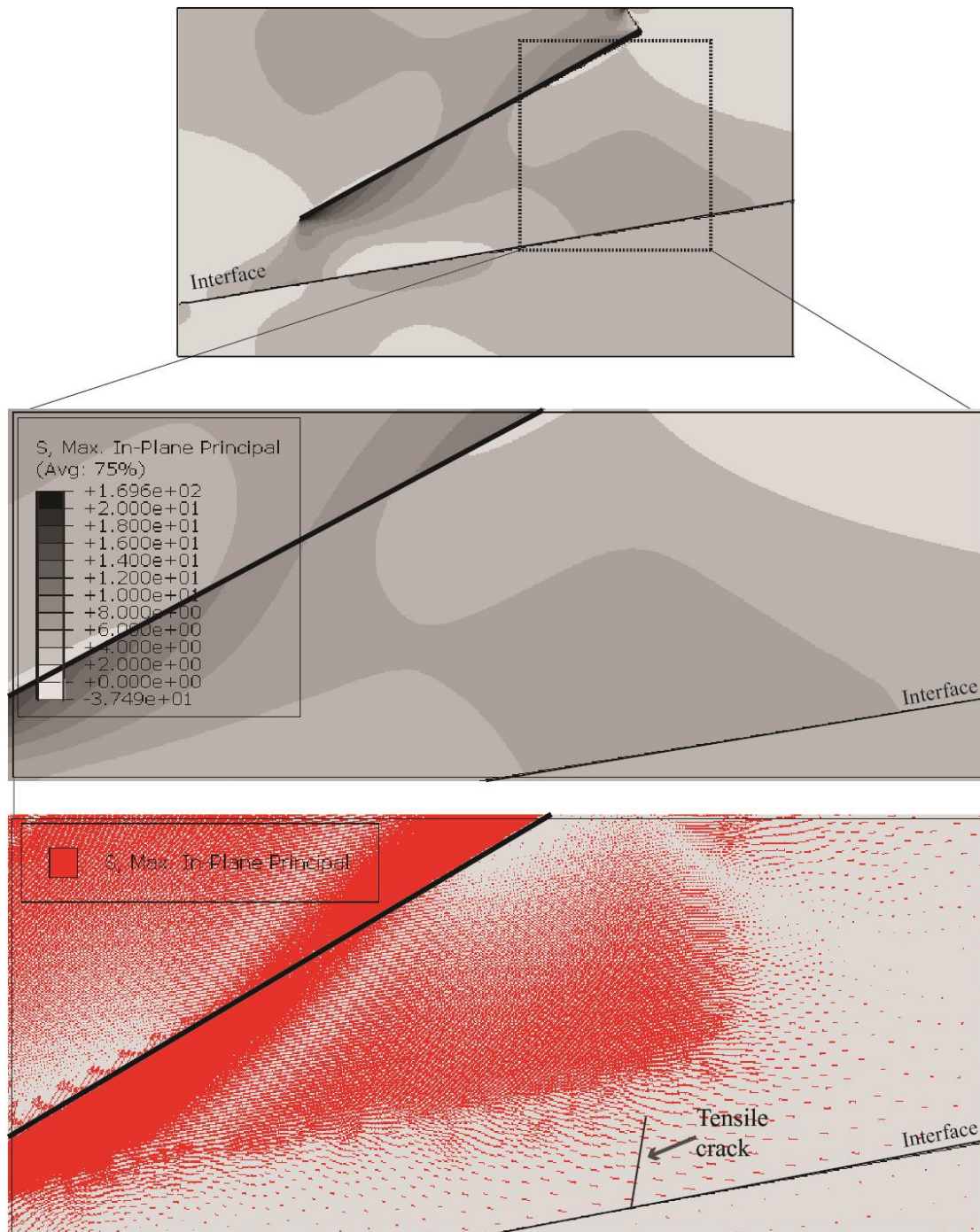


Figure 5.18. Crack 7, Table 5.4(b-c). Prediction of tensile crack 7 in geometry 0-2a30° with interface inclined 80° with the vertical and interface friction angle of 35°. Direction of crack: perpendicular to the maximum principal stress vectors (MPa).

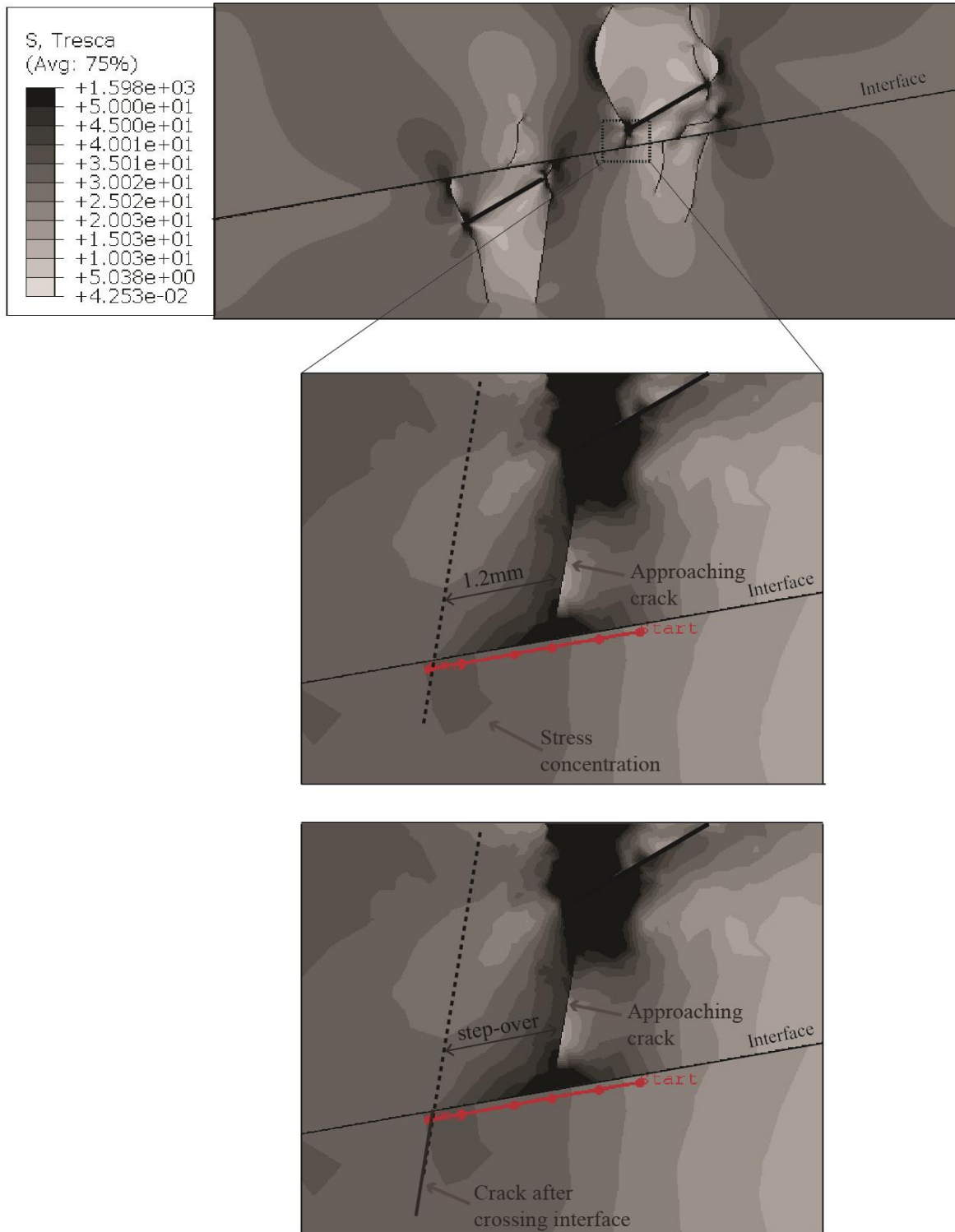


Figure 5.19. Crack 6, Table 5.4(f). Prediction of crack direction of re-initiation after crossing the interface with an offset, using the approach described in section 4.4.5. Specimen with geometry 0-2a30° with interface inclined 80° with the vertical and contact friction angle 35° (MPa).

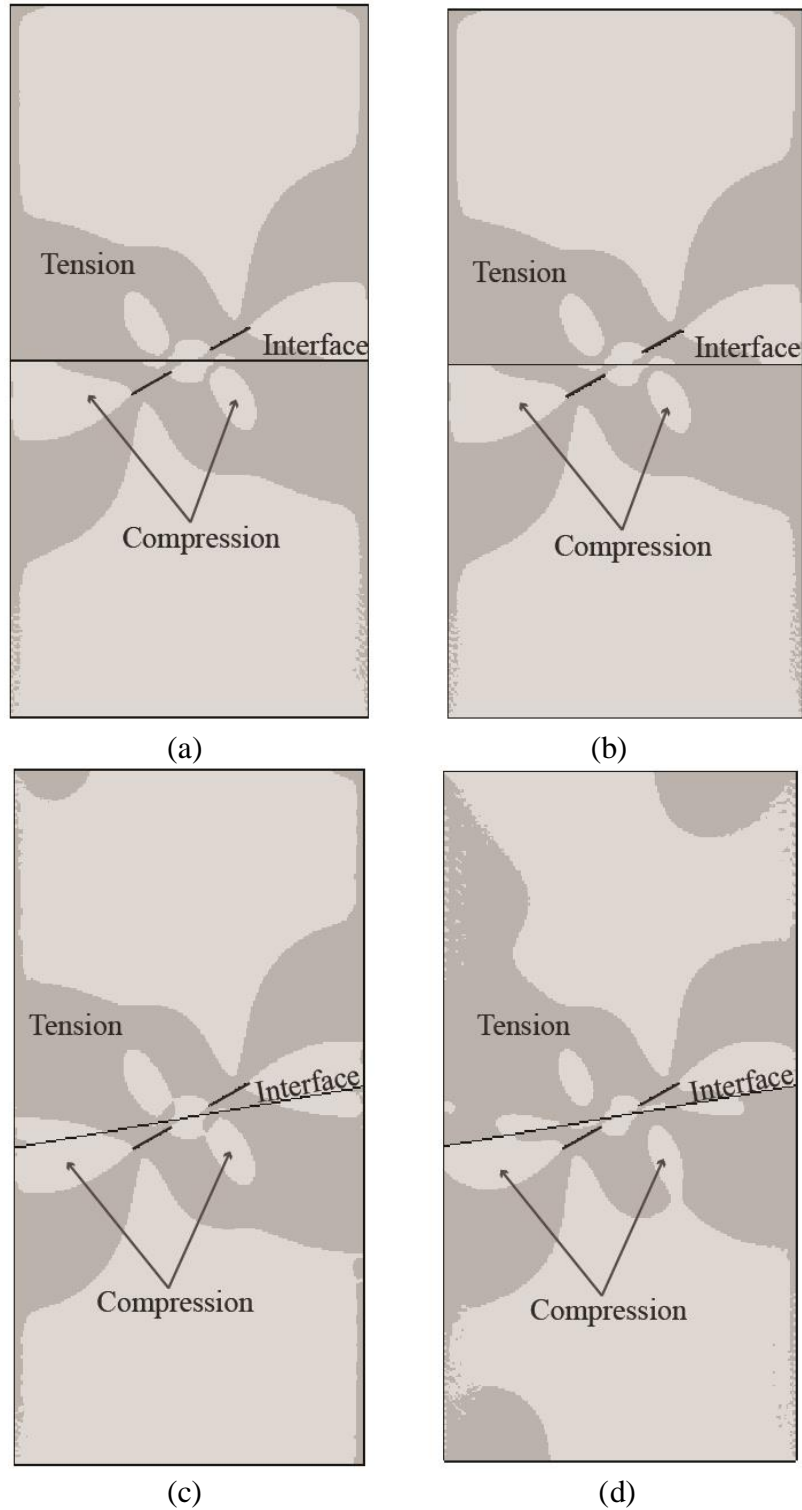


Figure 5.20. Effects of interface roughness and inclination angle. Tension and Compression zones in specimen 0-2a30°. a) horizontal interface with 50° friction angle; b) horizontal interface with 35° friction angle; c) inclined interface with 50° friction angle; d) inclined interface with 35° friction angle.

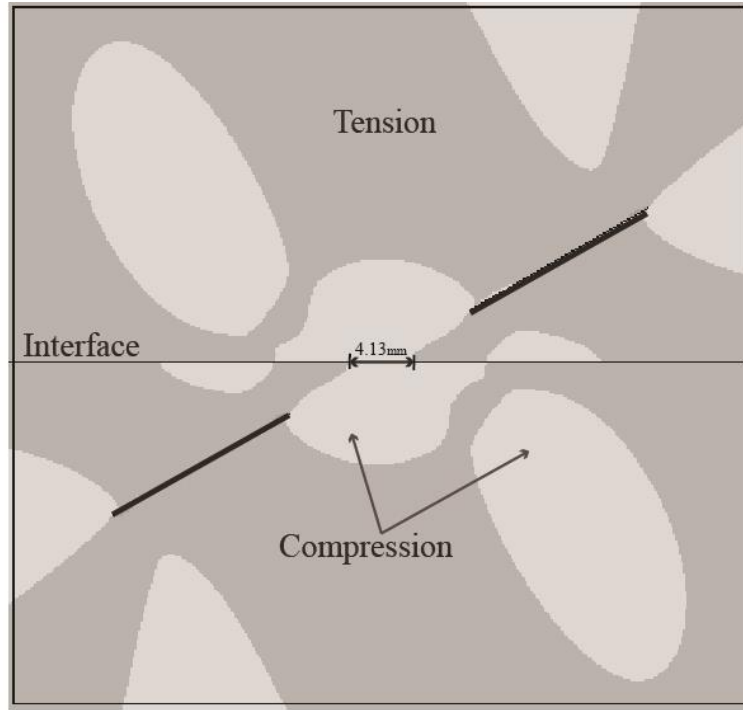


Figure 5.21. Effects of interface roughness and inclination angle. Tension and Compression zones in the area of interest for specimen 0-2a30° with interface inclined 90° with the vertical and interface friction angle of 50° (at a compression of 6.64MPa)

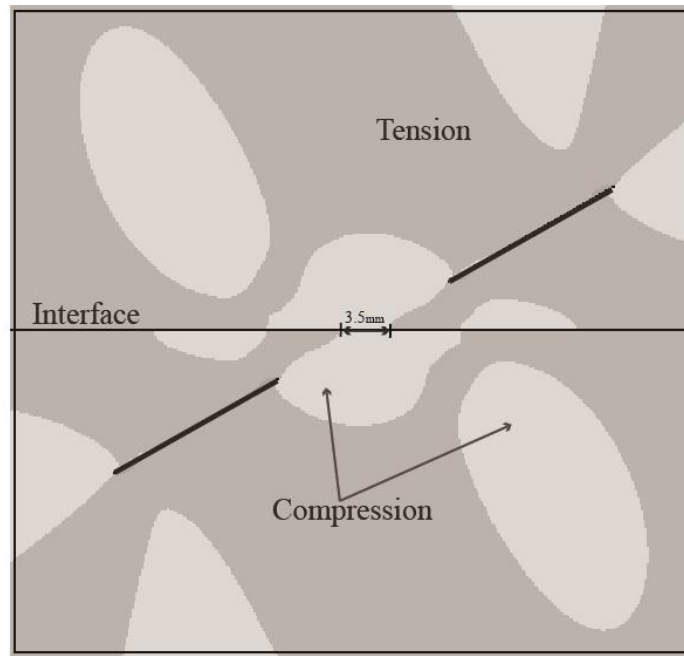


Figure 5.22. Effects of interface roughness and inclination angle. Tension and Compression zones in the area of interest for specimen 0-2a30° with interface inclined 90° with the vertical and interface friction angle of 35° (at a compression of 6.64MPa)

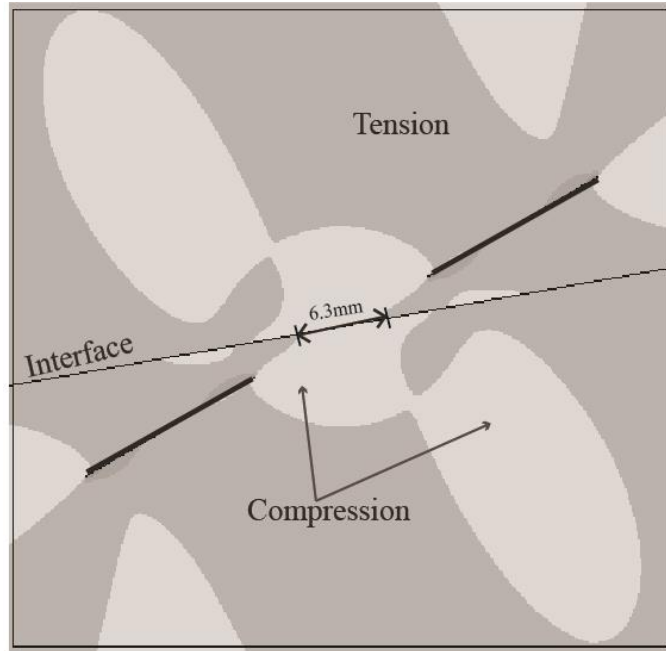


Figure 5.23. Effects of interface roughness and inclination angle. Tension and Compression zones in the area of interest for specimen 0-2a30°, interface inclined 80° and friction angle 50° (at a compression of 6.64MPa)

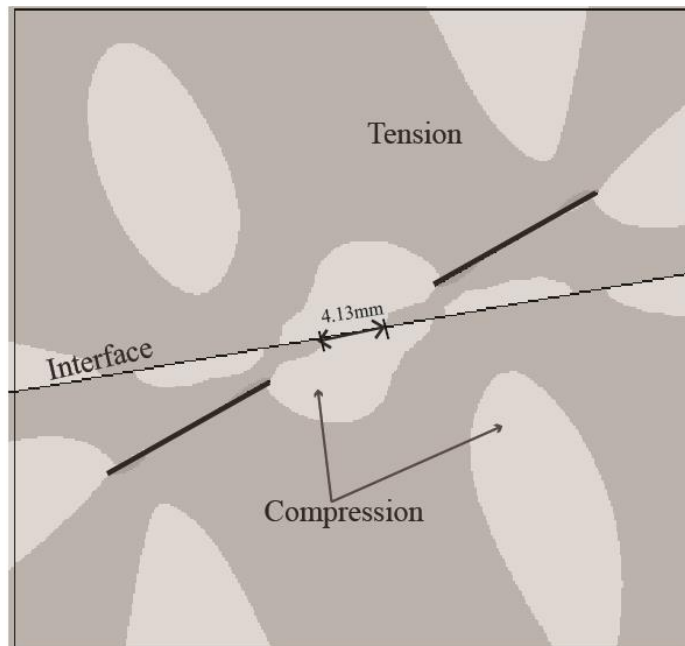


Figure 5.24. Effects of interface roughness and inclination angle. Tension and Compression zones in the area of interest for specimen 0-2a30°, interface inclined 80° friction angle 35° (at a compression of 6.64MPa).

Table 5.1. Geometry 0-2a30° with interface inclined 90° from the vertical and friction angle of 50°

Load (MPa)	Crack path detected by DIC	Observations of crack direction from experiments	Numerical simulation in ABAQUS	Prediction of crack direction using stress approach
(a) Initial - 6.64		<p>Crack 1: ~perpendicular to the flaw plane</p> <p>Crack 2: ~perpendicular to the flaw length</p> <p>Crack 3: ~perpendicular to the flaw length</p> <p>Crack 4: ~perpendicular to the flaw length</p>		<p>Crack 1: perpendicular to the flaw length</p> <p>Crack 2: perpendicular to the flaw length</p> <p>Crack 3: ~perpendicular to the flaw length</p> <p>Crack 4: perpendicular to the flaw length</p>
(b) 15		<p>Crack 5: ~140° from horizontal</p>		<p>Crack 5: ~130° from horizontal</p>

Table 5.1. Geometry 0-2a30° with interface inclined 90° from the vertical and friction angle of 50°

Load (MPa)	Crack path detected by DIC	Observations of crack direction from experiments	Numerical simulation in ABAQUS	Prediction of crack direction using stress approach
(c) 18.94		Crack 6: -90° from horizontal		Crack 6: -90° from horizontal
(d) 22.79		Crack 7: -90° from horizontal		Crack 7: -85° from horizontal

Table 5.1. Geometry 0-2a30° with interface inclined 90° from the vertical and friction angle of 50°

Load (MPa)	Crack path detected by DIC	Observations of crack direction from experiments	Numerical simulation in ABAQUS	Prediction of crack direction using stress approach
(e) 25.5		<p>Crack 5 crossing interface: 0.95mm offset to the left</p> <p>Crack 6 crossing the interface: no offset/-110° from the horizontal</p>		<p>Crack 5 crossing interface: 1 mm offset</p> <p>Crack 6 crossing the interface: no offset/-100° from the horizontal</p>
(f) 25.88		<p>Crack 9: crack 6 bifurcates</p> <p>Crack 10: 90° from horizontal</p>		<p>Crack 10: 90° from horizontal</p>

Table 5.1. Geometry 0-2a30° with interface inclined 90° from the vertical and friction angle of 50°

Load (MPa)	Crack path detected by DIC	Observations of crack direction from experiments	Numerical simulation in ABAQUS	Prediction of crack direction using stress approach
(g) 26.79		<p>Crack 11: -100° from horizontal</p> <p>Crack 12: 80° from horizontal</p> <p>Crack 13: -78° from horizontal</p> <p>Crack 14: perpendicular to flaw plane</p>		<p>Crack 11: -95° from horizontal</p> <p>Crack 12: 80° from horizontal</p> <p>Crack 13: -78° from horizontal</p> <p>Crack 14: could not be predicted</p>
(h) 27.5		<p>Crack 15 (Crack 12 crossing the interface): no offset/ 90° from horizontal</p>		<p>Crack 15 (Crack 12 crossing the interface): no offset/ 90° from horizontal</p>

Table 5.1. Geometry 0-2a30° with interface inclined 90° from the vertical and friction angle of 50°

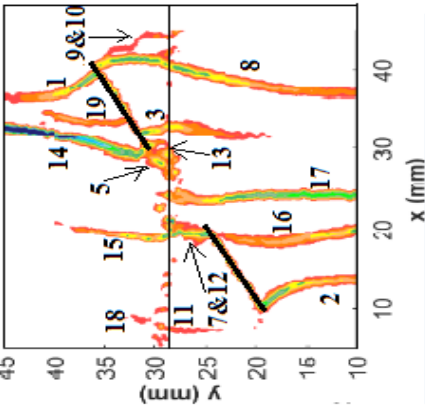
Load (MPa)	Crack path detected by DIC	Observations of crack direction from experiments	Numerical simulation in ABAQUS	Prediction of crack direction using stress approach
(i) 27.6		<p>Crack 16: -130° from the flaw plane</p> <p>Crack 17: originated in the ROI</p>	---	<p>Crack 16: -130° from the flaw plane</p> <p>Crack 17: could not be predicted</p>

Table 5.2. Geometry 0-2a30° with interface inclined 90° from the vertical and friction angle of 35°

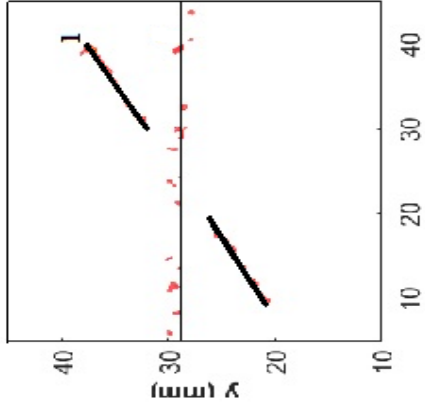
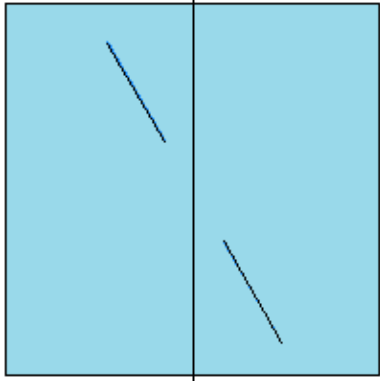
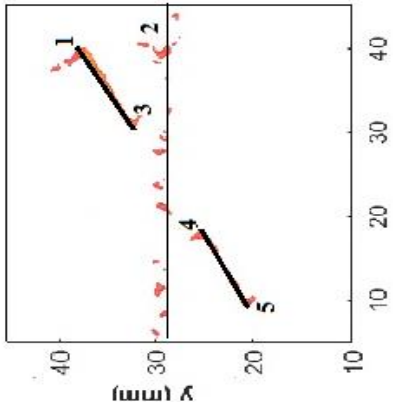
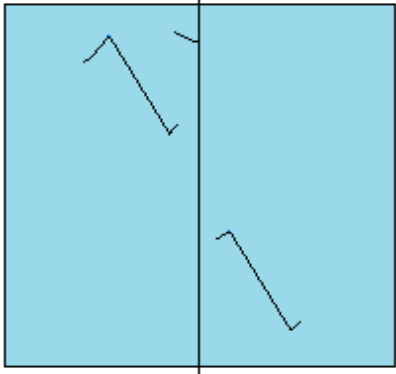
Load (MPa)	Crack path detected by DIC	Observations of crack direction from experiments	Numerical simulation in ABAQUS	Prediction of crack direction using stress approach
(a) Initial – 9.5		Crack 1: perpendicular to the flaw plane		Crack 1: perpendicular to the flaw plane
(b) 19.13		Crack 2: 80° from the horizontal Crack 3: 78° from flaw plane Crack 4: perpendicular to the flaw plane Crack 5: perpendicular to the flaw plane		Crack 2: 82° from the horizontal Crack 3: 78° from flaw plane Crack 4: perpendicular to the flaw plane Crack 5: perpendicular to the flaw plane

Table 5.2. Geometry 0-2a30° with interface inclined 90° from the vertical and friction angle of 35°

Load (MPa)	Crack path detected by DIC	Observations of crack direction from experiments	Numerical simulation in ABAQUS	Prediction of crack direction using stress approach
(c) 25.47		<p>Crack 6: 70° from the horizontal</p> <p>Crack 7: -108° from the horizontal</p>		<p>Crack 6: 70° from the horizontal</p> <p>Crack 7: -105° from the horizontal</p>
(d) 28.37		<p>Crack 8: 90° from the horizontal</p>		<p>Crack 8: ~90° from the horizontal</p>

Table 5.2. Geometry 0-2a30° with interface inclined 90° from the vertical and friction angle of 35°

Load (MPa)	Crack path detected by DIC	Observations of crack direction from experiments	Numerical simulation in ABAQUS	Prediction of crack direction using stress approach
(e) 28.94		<p>Crack 9: -90° from the horizontal</p> <p>Crack 10: -115° from the horizontal</p>		<p>Crack 9: -90° from the horizontal</p> <p>Crack 10: -105° from the horizontal</p>
(f) 30.23		<p>Crack 11: 85° from the horizontal</p> <p>Crack 12: damage zone</p>		<p>Crack 11: 85° from the horizontal</p> <p>Crack 12: damage zone</p>

Table 5.2. Geometry 0-2a30° with interface inclined 90° from the vertical and friction angle of 35°

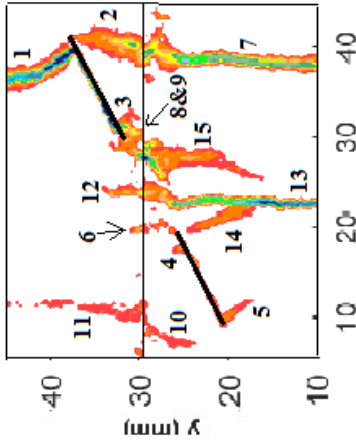
Load (MPa)	Crack path detected by DIC	Observations of crack direction from experiments	Numerical simulation in ABAQUS	Prediction of crack direction using stress approach
(g) 31.36		Crack 13 crossing the interface: no offset/ 90° from the horizontal	---	Crack 13 crossing the interface: could not be predicted

Table 5.3. Geometry 0-2a30° with interface inclined 80° from the vertical and friction angle of 50°

Load (MPa)	Crack path detected by DIC	Observations of crack direction from experiments	Numerical simulation in ABAQUS	Prediction of crack direction using stress approach
(a) Initial – 6.6MPa		<p>Crack 1: perpendicular to the flaw plane</p> <p>Crack 2: perpendicular to the flaw plane</p> <p>Crack 3: -105° from horizontal</p> <p>Crack 4: 90° from horizontal</p>		<p>Crack 1: perpendicular to the flaw plane</p> <p>Crack 2: perpendicular to the flaw plane</p> <p>Crack 3: -100° from horizontal</p> <p>Crack 4: 90° from horizontal</p>
(b) 9.38		<p>Crack 5: damage zone</p> <p>Crack 6: perpendicular to the flaw plane</p>		<p>Crack 5: damage zone</p> <p>Crack 6: perpendicular to the flaw plane</p>

Table 5.3. Geometry 0-2a30° with interface inclined 80° from the vertical and friction angle of 50°

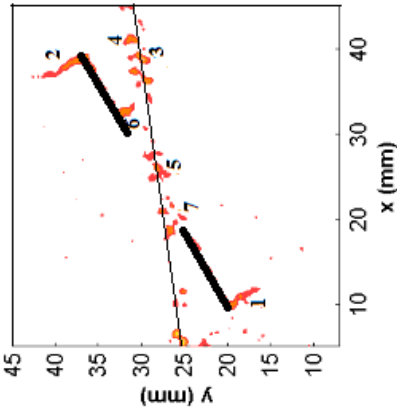
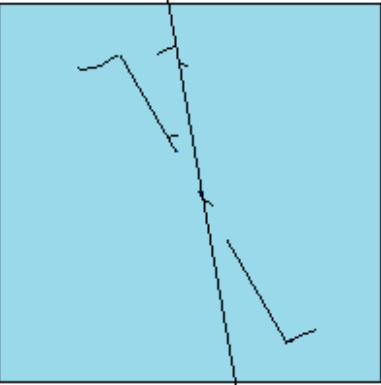
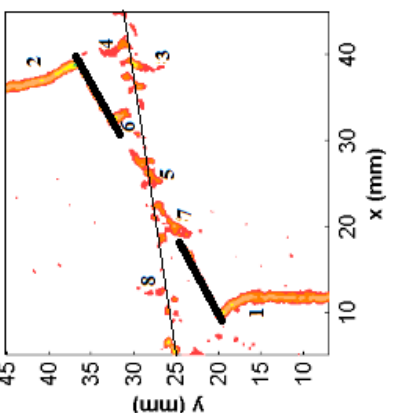
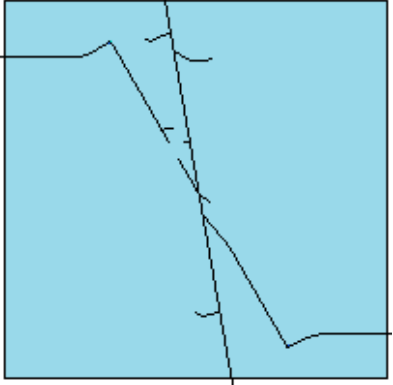
Load (MPa)	Crack path detected by DIC	Observations of crack direction from experiments	Numerical simulation in ABAQUS	Prediction of crack direction using stress approach
(c) 16.11		Crack 7: 50° from horizontal		Crack 7: 52° from horizontal
(d) 18		Crack 8: 100° from horizontal		Crack 8: 100° from horizontal

Table 5.3. Geometry 0-2a30° with interface inclined 80° from the vertical and friction angle of 50°

Load (MPa)	Crack path detected by DIC	Observations of crack direction from experiments	Numerical simulation in ABAQUS	Prediction of crack direction using stress approach
(e) 19.3		Crack 9: 70° from the horizontal		Crack 9: 85° from the horizontal
(f) 21.58		Crack 10: -150° from the horizontal Crack 11: 120° from the horizontal		Crack 10: -135° from the horizontal Crack 11: 125° from the horizontal

Table 5.3. Geometry 0-2a30° with interface inclined 80° from the vertical and friction angle of 50°

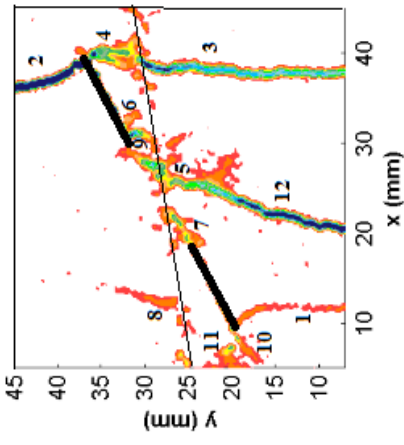
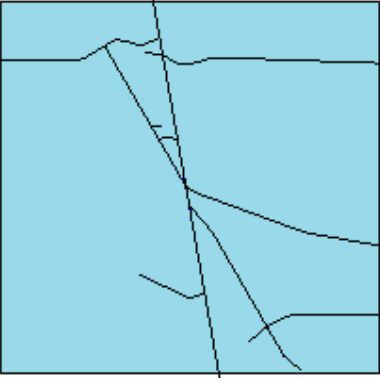
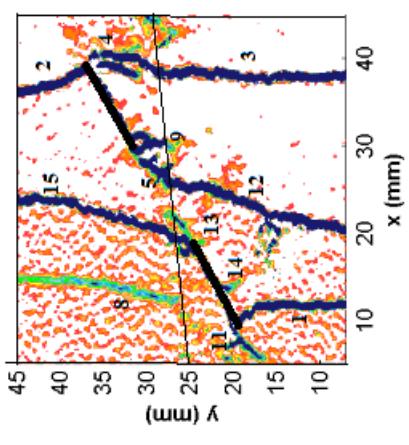
Load (MPa)	Crack path detected by DIC	Observations of crack direction from experiments	Numerical simulation in ABAQUS	Prediction of crack direction using stress approach
(g) 22.46		Crack 12: originated in the ROI		Crack 12: could not be predicted
(h) 22.85		Crack 15 (Crack 13 crossing the interface): no offset/ 70° from the horizontal	---	Crack 15 (Crack 13 crossing the interface): could not be predicted

Table 5.4. Geometry 0-2a30° with interface inclined 80° from the vertical and friction angle of 35°

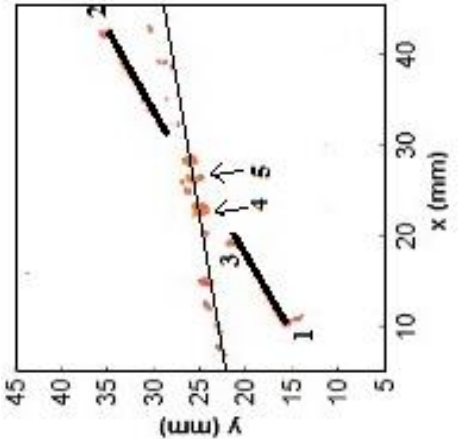
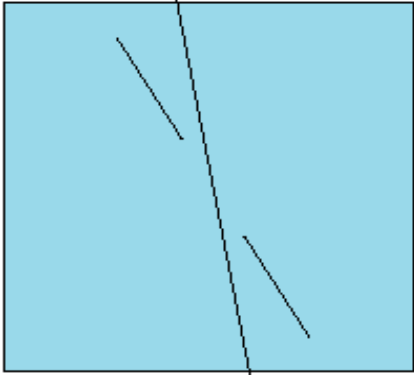
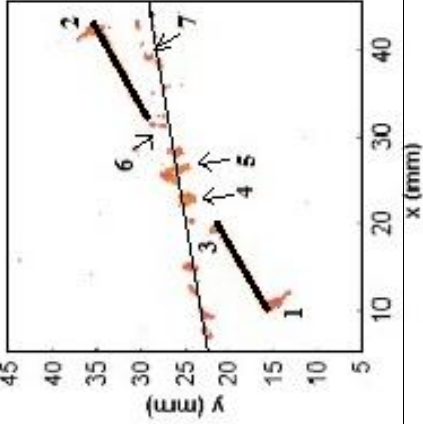
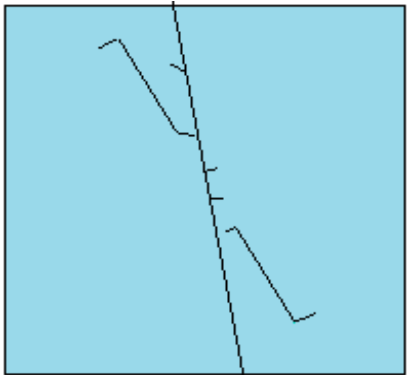
Load (MPa)	Crack path detected by DIC	Observations of crack direction from experiments	Numerical simulation in ABAQUS	Prediction of crack direction using stress approach
(a) Initial – 9.4		Crack 1: perpendicular to the flaw plane Crack 2: perpendicular to the flaw plane Crack 3: perpendicular to the flaw plane Crack 4: -90° from the horizontal Crack 5: damage zone		Crack 1: perpendicular to the flaw plane Crack 2: perpendicular to the flaw plane Crack 3: perpendicular to the flaw plane Crack 4: -90° from the horizontal Crack 5: damage zone
(b) 16.98		Crack 6: -105° from the horizontal Crack 7: 75° from the horizontal		Crack 6: -105° from the horizontal Crack 7: 80° from the horizontal

Table 5.4. Geometry 0-2a30° with interface inclined 80° from the vertical and friction angle of 35°

Load (MPa)	Crack path detected by DIC	Observations of crack direction from experiments	Numerical simulation in ABAQUS	Prediction of crack direction using stress approach
(c) 20.87		Crack 8: -90° from the horizontal Crack 9: -70° from the horizontal Crack 10: -90° from the horizontal Crack 11: 40° from the horizontal		Crack 8: -90° from the horizontal Crack 9: -75° from the horizontal Crack 10: -80° from the horizontal Crack 11: 55° from the horizontal
(d) 23.05		Crack 12: -90° from the horizontal Crack 13: originated in the ROI		Crack 12: -90° from the horizontal Crack 13: could not be predicted

Table 5.4. Geometry 0-2a30° with interface inclined 80° from the vertical and friction angle of 35°

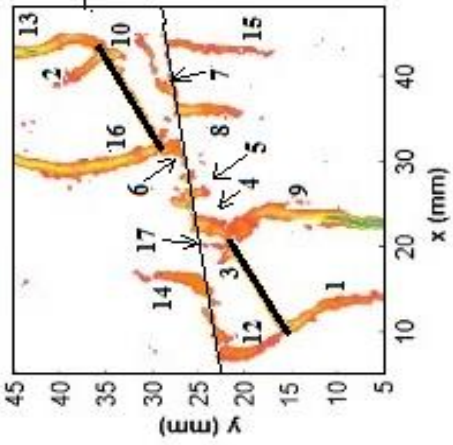
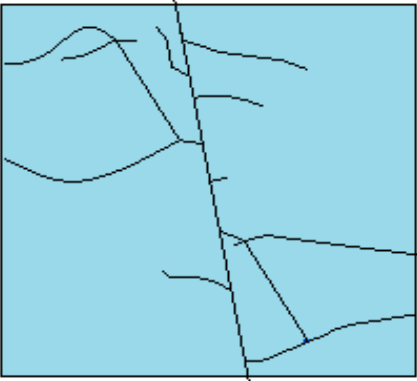
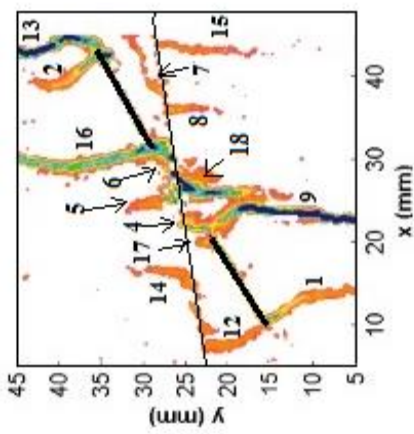
Load (MPa)	Crack path detected by DIC	Observations of crack direction from experiments	Numerical simulation in ABAQUS	Prediction of crack direction using stress approach
(e) 23.92		Crack 14: 65° from horizontal Crack 15: -100° from horizontal Crack 16: -132° from horizontal Crack 17: -90° from horizontal		Crack 14: 70° from the horizontal Crack 15: -97° from the horizontal Crack 16: -140° from the horizontal Crack 17: could not be predicted
(f) 23.95		Crack 18 (crack 6 crossing the interface): 1.56mm offset/ -105° from the horizontal	---	Crack 18 (crack 6 crossing the interface): 1.2mm offset/ -110° from the horizontal

Table 5.5. Effects of interface roughness and inclination angle on the initiation of tensile cracks at an inside flaw tip. Maximum principal stress for a crack path radius of 0.2mm from the internal crack tip of the bottom flaw for different interface roughness and inclination angles in a specimen with geometry 0-2a30°

Interface inclination (from vertical)	Interface roughness	
	Rough	Smooth
90°	28.71	28.58
80°	42.1	41.88

Table 5.6. Effects of interface roughness and inclination angle on the initiation of tensile cracks at an outside flaw tip. Maximum principal stress for a crack path radius of 0.2mm from the internal crack tip of the bottom flaw for different interface roughness and inclination angles in a specimen with geometry 0-2a30°

Interface inclination (from vertical)	Interface roughness	
	Rough	Smooth
90°	21.32	21.26
80°	27.54	27.52

6. CONCLUSIONS AND RECOMMENDATIONS

6.1 Conclusions

The study of crack behavior in rock-like specimens containing an interface is very relevant to rock mechanics, specifically to geology, engineering of rock masses, gas and oil extraction, and to the behavior of brittle materials. Proper knowledge of how cracks interact with an interface may lead to better and more economical designs in layered rock masses.

Extensive experimental and numerical research has been conducted on crack initiation, propagation and coalescence in homogeneous brittle materials containing pre-existing flaws under compression. Previous studies show that there are two types of cracks that are commonly found in brittle materials: tensile and shear. However, there is not much information in the literature on the influence of interfaces on crack behavior.

Uniaxial compression tests were conducted on prismatic specimens of gypsum, used as a rock-model material, that contained two open flaws and a frictional interface that separated the two flaws. The specimens are 203.2mm high, 101.6mm wide, and 25.4mm thick. The two flaws, with 0.1 mm aperture and 12.7 mm length (2a), were created through the thickness of the specimen. Spacing (S), continuity (C), and flaw inclination angle (β) define the geometry of the tests. The specimens discussed in this investigation had three flaw geometries, defined as: $S=0$, $C=-2a=-12.7\text{mm}$, $\beta=30^\circ$ (i.e. a left-stepping geometry); $S=2a=12.7\text{ mm}$, $C=a=6.35\text{ mm}$, $\beta=30^\circ$ (i.e. an overlapping geometry) and $S=3a=19.05\text{mm}$, $C=0$, $\beta=30^\circ$ (i.e. a right-stepping geometry). Different interface inclination angles were investigated, namely: 70° , 80° and 90° with respect to the vertical axis of the specimen. A Digital Image Correlation (DIC) technique was used to monitor crack initiation and propagation on the specimen surface.

A numerical study was conducted using the Extended Finite Element Method (XFEM) to investigate the fracture behavior observed in the experiments. A coplanar flaw geometry with $S=0$, $C=-2a$ (2a is the flaw length), $\beta=30^\circ$, in a specimen 203.2mm high and 101.6mm wide was modeled using ABAQUS. The specimen had a frictional interface with one flaw on each side. The cracks that were observed during the experiments were re-created in the numerical model. A stress-based crack initiation approach, where cracks initiate in the direction of maximum principal and

maximum shear stresses, was used to estimate the direction of crack initiation from the flaws and from the interface. The cracks initiating or crossing the interface were also investigated.

A brief summary of the most important experimental observations from the uniaxial compression tests, as well as the most relevant findings from the numerical investigation are presented in the following sections. Specifically, Section 6.1.1 lists the most relevant experimental findings, which are taken from Chapter 3. Section 6.1.2 describes the most salient results from the numerical model, which can be found in Chapter 5.

6.1.1 Experimental Work

A series of experiments on homogeneous gypsum specimens containing an interface has been performed. The work addressed how cracks interact with interfaces and how different variables (i.e. flaw geometry, interface inclination angle and interface roughness) affect crack behavior in homogeneous materials with an interface. The major results obtained from the uniaxial compression test series can be summarized as follows:

1. Three different types of cracks have been detected in the experiments: tensile, coplanar shear and oblique shear. Tensile cracks are always the first to appear and start at/near the tips of the flaws or at the interface. Shear cracks appear later than the tensile cracks and emanate from the tips of the flaws.
2. The interface itself is an important contributor to new tensile cracks;
3. The presence of an interface reduces tensile crack initiation stress;
4. An increase in both roughness and inclination of the interface (i.e. from horizontal to 70° from the vertical) reduces tensile crack initiation stress;
5. Changes in interface roughness or inclination angle do not affect the angles at which tensile cracks initiate at the interface. The angle of initiation ranged from 70° to 90° ;
6. Tensile cracks that meet the interface at 30° to 60° angle get arrested, while those at angles larger than 70° cross the interface with an offset of 0 – 1.2 mm. Shear cracks that meet the interface at 20° to 63° angles get arrested at the interface, while those at angles larger than 70° cross the interface with an offset of 0 – 1.76 mm. This behavior is independent of roughness or inclination angle of the interface;

7. The presence of interfaces causes the number of cracks that produce coalescence to increase when compared to specimens without interface, and consequently causes changes in coalescence patterns;
8. Variation in the interface inclination angle and roughness may change the location where cracks that produce coalescence originate.

6.1.2 Numerical work

A numerical study was conducted using the Extended Finite Element Method (XFEM) feature in ABAQUS, to further investigate the fracture behavior observed in the experiments; more specifically, the influence of the different types of interfaces. An extensive investigation of the stress fields around the tips of the flaws and of the new cracks, as well as along the interface was performed to determine whether there was any relationship between stresses and crack initiation and propagation (i.e. type and direction of cracks). The main conclusions obtained from the numerical investigation are:

1. The stress-based approach used in this study yields predictions of tensile and shear cracks location and initiation direction that are in good agreement with experimental results;
2. The model predicts that the direction of initiation of the tensile cracks at the flaw tips is perpendicular to the maximum principal stress vectors, which are perpendicular to the flaws. This is consistent with experimental observations.;
3. Rougher horizontal interfaces induced slightly higher tensile stresses around the interior and exterior flaw tips than smoother interfaces, which may explain why tensile cracks at these locations initiated earlier in specimens with a rough interface;
4. Inclined interfaces induced higher tensile stresses around the interior and exterior flaw tips than horizontal interfaces, which may justify that, in the experiments, inclined interfaces promoted crack initiation earlier than horizontal interfaces.
5. The roughness or inclination of the interface do not seem to affect the angles of initiation of the tensile cracks that initiate at the interface. The numerical model predicts initiation angles in the range 70° to 90° , which is in good agreement with experimental findings;
6. The numerical prediction of crack re-initiation after crossing an interface does not seem to be affected by the roughness or the inclination of the interface. In the model, the reinitiation of cracks that crossed the interface was predicted to occur at the point of greatest maximum

tensile stress, for tensile cracks, or maximum shear stress, for shear cracks. All cracks that reinitiated across the interface were in a direction that was perpendicular to the maximum tensile stress or maximum shear stress in these locations ahead of the approaching crack.

6.2 Recommendations for future research

While the investigation completed has contributed to a better understanding of the fracturing processes in rock materials containing an interface, more work is needed. The following are recommendations for further research, to address some of the questions that arose from the work completed:

1. Additional flaw arrangements. All the specimens tested in this research had two flaws with the same inclination angle. Additional experimental research on specimens with different inclination angles is suggested, since there is evidence in literature that changes in inclination angle leads to differences in crack behavior;
2. Bonded interfaces. All the specimens tested under uniaxial compression contained an unbonded interface. Future investigations on specimens with bonded interface should be helpful because bonded interfaces may induce changes in crack behavior when compared to unbonded interfaces;
3. Other materials. The crack patterns observed in the research conducted were obtained in specimens made of gypsum. A systematic experimental series, similar to the one undertaken in this dissertation, on other materials is necessary to compare results obtained with the conclusions from this dissertation.
4. Different flaw lengths. All the experiments have been conducted on specimens with a constant flaw length of 12.7mm. Thus, the fact that there were cases in which cracks initiated at the inside and outside flaw tips at the same time may be favored by the short length of the flaws used in the specimens. It is suggested to explore the effect of different flaw lengths on the experimental and numerical results.
5. Different type of pre-existing flaw. In the present investigation, all pre-existing cracks were open. Studying cases with closed pre-existing flaws would be advisable for comparison.

REFERENCES

- Amann, F., E. Button, K. Evans, V. Gischig & M. Blümel (2011). Experimental Study of the Brittle Behavior of Clay Shale in Rapid Unconfined Compression. *Rock Mech Rock Eng*, 44, 415-430.
- Atkinson, B.K. *Fracture Mechanics of Rock* (1987). Academic Press Geology series. London. ISBN 0-12-066265-5.
- Barenblatt, G.I. (1962). The mathematical theory of equilibrium cracks in brittle fracture. *Adv. Appl. Mech.* 7, 55–129.
- Bobet, A. (1997) *Fracture Coalescence in Rock Materials: Experimental Observations and Numerical Predictions*, Sc. D. Thesis, Massachusetts Institute of Technology.
- Bobet A, Einstein HH (1998a) Numerical modeling of fracture coalescence in a model rock material. *Int J Fract* 92:221–252.
- Bobet A, Einstein HH (1998b) Fracture coalescence in rock-type materials under uniaxial and biaxial compression. *Int J Rock Mech Min Sci* 35(7):863–888.
- Broek, D. (1984). *Elementary Engineering Fracture Mechanics*. Fourth revised edition. Kluwer Academic Publishers. Galena, OH, USA.
- Chang, X., Y. Shan, Z. Zhang, C. Tang & Z. Ru (2015) Behavior of propagating fracture at bedding interface in layered rocks. *Engineering Geology*, 197, 33-41.
- Cooke, M. L. & C. A. Underwood (2001). Fracture termination and step-over at bedding interfaces due to frictional slip and interface opening. *Journal of Structural Geology*, 23, 223-238.

- Dollar, Anna S., and Paul S. Steif. A (1989). Tension Crack Impinging upon Frictional Interfaces. *Journal of Applied Mechanics, Transactions ASME* 56.2 (1989): 291-98.
- Dugdale, D.S., (1960). Yielding of sheets containing slits. *J. Mech. Phys. Solids* 8, 100–104.
- Einstein, H. H., and Hirschfeld, R. C. (1970). Model studies on mechanics of jointed rocks. *ASCE Journal of the Geotechnical Division*, 99, 229-248.
- Erdogan, F. and Sih, G.C. (1963) On the crack extension in plates under plane loading and transverse shear, *Journal of Basic Engineering*, 85, pp. 305-321.
- Gonçalves da Silva B (2009) Modeling of crack initiation, propagation and coalescence in rocks. S.M, Thesis, Massachusetts Institute of Technology.
- Gonçalves da Silva, B., Einstein, H.H. (2013). Modeling of crack initiation, propagation and coalescence in rocks. *Int. J. Fract.* 182 (2), 167–186.
- Griffith, A.A. (1921) The phenomenon of rupture and flow in solids. *Philosophical Transactions, Series A*, 221, pp. 163-198.
- Gu, H. and Weng, X (2010). Criterion for Fractures Crossing Frictional Interfaces at Non-orthogonal Angles. 44th US Rock Mechanics Symposium. Salt Lake City, UT June 27–30.
- Haeri, H. (2014). On the Strength and Crack Propagation Process of the Pre-Cracked Rock-Like Specimens under Uniaxial Compression. *Strength of Materials*, 46, 140-153.
- He, M.-Y. & J. W. Hutchinson (1989). Kinking of a crack out of an interface. *Journal of Applied Mechanics, Transactions ASME*, 56, 270-278.
- He, M.Y., Hutchinson, J.W. (1989). Crack deflection at an interface between dissimilar elastic materials. *Int. J. Solids Struct.* 25 (9), 1053–1067.

- Hedayat, A. (2013). Mechanical and geophysical characterization of damage in rocks. ed. E. Purdue University. Civil. Thesis (Ph.D.), Indiana, USA.
- Helgeson, D.E., Aydin, A. (1991). Characteristics of joint propagation across layer interfaces in sedimentary rocks. *Journal of Structural Geology* 13, 897±991.
- Hou, J., Q. Li, G. Liu & H. Zuo (2016). Fundamental solutions of a crack impinging upon an interface slippage in laminated anisotropic bodies. *Archive of Applied Mechanics*, 86, 687-700.
- Hutchinson, J. & Z. Suo (1990). Interface crack between two elastic layers. *International Journal of Fracture*, 43, 1-18.
- Hutchinson, J.W., Suo, Z. (1992). Mixed mode cracking in layered materials. *Adv. Appl. Mech.* 29, 63–191.
- Inglis. (1913) Stresses in a plate due to the presence of cracks and sharp comers, *Inst. Naval Architecture, London*, 55, pp 219-230.
- Irwin. (1956) Onset of fast crack propagation in high strength steel and aluminum alloys. *Sagamore Research Conference Proceedings*, 2, pp 289-305.
- Ko, T. Y., Einstein, H.H., and Kemeny, J. (2006). Crack Coalescence in Brittle Material under Cyclic Loading”, *Golden Rocks 2006, 41st U.S. Symposium on Rock Mechanics (USRMS)*, ARMA/USRMS 06-930.
- Larsen, B. et all. (2010). Effects of sedimentary interfaces on fracture pattern, linkage, and cluster formation in peritidal carbonate rocks. *Marine and Petroleum Geology*, 27, 1531-1550.
- Lee, H., Jeon, S. (2011). An experimental and numerical study of fracture coalescence in pre-cracked specimens under uniaxial compression. *Int. J. Solids Struct.* 48 (6), 979–999.

- Leguillon, D., C. Lacroix & E. Martin (2000) Interface debonding ahead of a primary crack. *Journal of the Mechanics and Physics of Solids*, 48, 2137-2161.
- Lemaitre, J., R. Desmorat, M. Vidonne & P. Zhang (1996). Reinitiation of a crack reaching an interface. *International Journal of Fracture*, 80, 257-276.
- Li, H.Q., Wong, L.N.Y. (2012). Influence of flaw inclination angle and loading condition on crack initiation and propagation. *Int. J. Solids Struct.* 49, 2482–2499.
- Liu, L. (2011). Strain-rate effects on deflection/penetration of crack terminating perpendicular to bimaterial interface under dynamic loadings. *International Journal of Fracture*, 167, 135-146.
- Liu, Jie & Wang, Jun. (2018). Stress Evolution of Rock-Like Specimens Containing a Single Fracture Under Uniaxial Loading: a Numerical Study Based on Particle Flow Code. *Geotechnical and Geological Engineering*. 36. 1-14. 10.1007/s10706-017-0347-0.
- Morgan, S. (2013) Cracking processes in Barre granite: fracture process zones and crack coalescence. *International Journal of Fracture*, 180, 177-205.
- Modiriasari, A. (2017). Active Seismic Monitoring of Crack Initiation, Propagation, and Coalescence in Rock. *Rock Mechanics & Rock Engineering*, 50, 2311-2326.
- Needleman (1987). A continuum model for void nucleation by inclusion debonding, *Journal of Applied Mechanics*, 54 (3) (1987) 525-531.
- Parmigiani, J.P., Thouless, M.D. (2006). The roles of toughness and cohesive strength on crack deflection at interfaces. *Journal of the Mechanics and Physics of Solids* 54 (2006) 266–287.

- Park, C. H. & A. Bobet (2009). Crack coalescence in specimens with open and closed flaws: A comparison. *International Journal of Rock Mechanics and Mining Sciences*, 46, 819-829.
- Park, C. H. & A. Bobet (2010). Crack initiation, propagation and coalescence from frictional flaws in uniaxial compression. *Engineering Fracture Mechanics*, 77, 2727-2748.
- Rannou, J. et al. (2010). Three dimensional experimental and numerical multiscale analysis of a fatigue crack. *Comput. Meth. Appl. Mech. Eng.* 199 (21–22), 1307–1325.
- Reyes, O. and H. H. Einstein. 1991. Failure mechanisms of fractured rock: A fracture coalescence model. *Int. Proceedings of the Seventh International Congress on Rock Mechanics*, Vol. 1, p. 333–40.
- Renshaw, C. E. & D. D. Pollard (1995). An experimentally verified criterion for propagation across unbounded frictional interfaces in brittle, linear elastic materials. *International Journal of Rock Mechanics and Mining Sciences and Geomechanics Abstracts*, 32, 237-249.
- Roy Xu, L., Y. Y. Huang & A. J. Rosakis (2003). Dynamic crack deflection and penetration at interfaces in homogeneous materials: experimental studies and model predictions. *Journal of the Mechanics and Physics of Solids*, 51, 461-486.
- Sagong, M. & A. Bobet (2002). Coalescence of multiple flaws in a rock- model material in uniaxial compression. *International Journal of Rock Mechanics and Mining Sciences*, 39, 229-241.
- Shen, B., O. Stephansson, H. Einstein & B. Ghahreman (1995). Coalescence of fractures under shear stresses in experiments. *J. Geophys. Res.-Solid Earth*, 100, 5975-5990.
- Siegmund, T. & A. Needleman (1997). A numerical study of dynamic crack growth in elastic-viscoplastic solids. *International Journal of Solids and Structures*, 34, 769-787.

- Sih. (1974) Strain-energy-density factory applied to mixed mode crack problems. *International Journal of Fracture*, 10(3), 305-321.
- Suo, Z. & J. Hutchinson (1990). Interface crack between two elastic layers. *International Journal of Fracture*, 43, 1-18.
- Sundaram, B. M. & H. V. Tippur (2016). Dynamic Crack Growth Normal to an Interface in Bi-Layered Materials: An Experimental Study Using Digital Gradient Sensing Technique. *An International Journal*, 56, 37-57.
- Sundaram, B. M. & H. V. Tippur (2016). Dynamic Crack Growth Normal to an Interface in Bi-Layered Materials: An Experimental Study Using Digital Gradient Sensing Technique. *An International Journal*, 56, 37-57.
- Sutton MA, Yan JH, Tiwari V, et al (2008). The effect of out-of-plane motion on 2D and 3D digital image correlation measurements. *Optics and Lasers in Engineering* 46:746–757. doi: 10.1016/j.optlaseng.2008.05.005.
- Takeuchi, K (1991). Mixed-Mode Fracture Initiation in Granular Brittle Materials. M.S. Thesis, Massachusetts Institute of Technology, Cambridge, U.S.A.
- Tvergaard, V., Hutchinson, J.W. (1993). The influence of plasticity on mixed mode interface toughness. *J. Mech. Phys. Solids* 41, 1119–1135.
- Whittaker, B. N., Singh, R.N., Sun, G. (1992). *Rock Fracture Mechanics: Principles, Design and Applications*. Elsevier Science Publishers, Amsterdam.
- Wong NY (2008). Crack coalescence in molded gypsum and Carrara marble. Ph.D. Thesis, Massachusetts Institute of Technology.

- Wong, L. & H. Einstein (2009). Crack Coalescence in Molded Gypsum and Carrara Marble: Part 1. Macroscopic Observations and Interpretation. *Rock Mechanics and Rock Engineering*, 42, 475-511.
- Wong, R., K. Chau, C. Tang & P. Lin (2001). Analysis of crack coalescence in rock-like materials containing three flaws—part I: experimental approach. *International Journal of Rock Mechanics and Mining Sciences*, 38, 909-924.
- Yang, S. (2012). An Experimental Study of the Fracture Coalescence Behaviour of Brittle Sandstone Specimens Containing Three Fissures. *Rock Mechanics & Rock Engineering*, 45, 563-583.
- Yuyong, J. et al. (2007). Simulation of rock crack propagation using discontinuous deformation analysis method. *Chinese Journal of Rock Mechanics and Engineering*. Vol.26(4), pp.682-691.
- Xu XP, Needleman A. (1994). Numerical simulations of fast crack growth in brittle solids. *J Mech Phys Solids* 1994; 42:1397–434.
- Zhou, X., H. Cheng & Y. Feng (2014). An Experimental Study of Crack Coalescence Behaviour in Rock-Like Materials Containing Multiple Flaws Under Uniaxial Compression. *Rock Mechanics and Rock Engineering*, 47, 1961-1986.
- Zhuang, X. et al. (2014). A comparative study on unfilled and filled crack propagation for rock-like brittle material. *Theoretical and Applied Fracture Mechanics*. 72, 110-120.

VITA

Danielli de Melo Moura earned her Bachelor's degree in Civil Engineering at Universidade de Pernambuco in 2010. Then, she obtained a highly competitive position in the Brazilian government where she supervised both construction and maintenance of earth-filled and concrete dams for three years. In 2014, she was granted the Science without Borders fellowship to fund her graduate studies at Purdue University. Danielli obtained her Master's degree in Civil Engineering from Purdue University in 2017. She continued at Purdue to pursue her Ph.D degree in Civil Engineering with focus in geotechnical engineering. The quality of her work has been recognized by the rock mechanics/geomechanics profession with the 2019 Best Poster Award at the 53rd US Rock Mechanics/Geomechanics Symposium in New York. During her Ph.D. degree, Danielli held the awarded positions Lyles Teaching Assistant and Lyles Teaching Fellow in the Department of Civil Engineering at Purdue University. She also received the Industrial Roundtable award in 2019 and the third-place award in the graduate and post-doc student poster competition at GIS Day 2019.